

**MODELING AND OPTIMIZATION OF THE PEM FUEL CELL CATALYST
LAYER**

by

Cankur Firat Cetinbas

A dissertation submitted to the Faculty of the University of Delaware in partial fulfillment of the requirements for the degree of Doctor of Philosophy in Mechanical Engineering

Summer 2014

© 2014 Cankur Firat Cetinbas
All Rights Reserved

UMI Number: 3642298

All rights reserved

INFORMATION TO ALL USERS

The quality of this reproduction is dependent upon the quality of the copy submitted.

In the unlikely event that the author did not send a complete manuscript and there are missing pages, these will be noted. Also, if material had to be removed, a note will indicate the deletion.



UMI 3642298

Published by ProQuest LLC (2014). Copyright in the Dissertation held by the Author.

Microform Edition © ProQuest LLC.

All rights reserved. This work is protected against unauthorized copying under Title 17, United States Code



ProQuest LLC.
789 East Eisenhower Parkway
P.O. Box 1346
Ann Arbor, MI 48106 - 1346

**MODELING AND OPTIMIZATION OF THE PEM FUEL CELL CATALYST
LAYER**

by

Cankur Firat Cetinbas

Approved:

Suresh G. Advani, Ph.D.
Chair of the Department of Mechanical Engineering

Approved:

Babatunde A. Ogunnaike, Ph.D.
Dean of the College of Engineering

Approved:

James G. Richards, Ph.D.
Vice Provost for Graduate and Professional Education

I certify that I have read this dissertation and that in my opinion it meets the academic and professional standard required by the University as a dissertation for the degree of Doctor of Philosophy

Signed:

Ajay K. Prasad, Ph.D.
Professor in charge of dissertation

I certify that I have read this dissertation and that in my opinion it meets the academic and professional standard required by the University as a dissertation for the degree of Doctor of Philosophy

Signed:

Suresh G. Advani, Ph.D.
Professor in charge of dissertation

I certify that I have read this dissertation and that in my opinion it meets the academic and professional standard required by the University as a dissertation for the degree of Doctor of Philosophy

Signed:

R. Valery Roy, Ph.D.
Member of dissertation committee

I certify that I have read this dissertation and that in my opinion it meets the academic and professional standard required by the University as a dissertation for the degree of Doctor of Philosophy

Signed:

Michael T. Klein, Ph.D.
Member of dissertation committee

ACKNOWLEDGMENTS

First, I would like to express my profound gratitude to my advisors: Dr. Prasad and Dr. Advani for giving me the chance to study at the University of Delaware Mechanical Engineering Department under their supervision.

I also like to thank to my family for their huge support and motivation throughout my entire life.

Finally, I would like to express my thanks to the US Federal Transit Administration for funding my graduate studies.

TABLE OF CONTENTS

LIST OF TABLES	viii
LIST OF FIGURES	ix
LIST OF SYMBOLS.....	xvii
ABSTRACT	xix
Chapter	
1 INTRODUCTION.....	1
1.1 Background.....	1
1.2 Proton Exchange Membrane (PEM) Fuel Cell.....	3
1.2.1 Operating Principles	4
1.2.2 PEM Fuel Cell Components	6
1.2.2.1 Polymer Electrolyte Membrane.....	6
1.2.2.2 Catalyst Layer.....	7
1.2.2.3 Gas Diffusion Layer (GDL)	8
1.2.2.4 Bi-polar Plates	9
1.2.3 Voltage Losses and Polarization Curve.....	9
1.3 Role of Modeling.....	11
1.4 Previous Work	12
1.4.1 Catalyst Layer Models.....	14
1.4.1.1 Microscale Models	15
1.4.1.2 Macroscale Models.....	17
1.4.2 Numerical Optimization and its Applications on CL Design.....	26
1.5 Motivation, Objectives and Contributions	28
1.6 Thesis Overview	30
2 INVESTIGATION OF THE SHORTCOMINGS OF THE CLASSICAL AGGLOMERATE APPROACH	32

2.1	PEM Fuel Cell Cathode Model	33
2.1.1	Model Description	33
2.1.2	Results and Discussion	40
2.2	Single Agglomerate Model.....	45
2.2.1	Model Description	45
2.2.2	Results and Discussion	47
2.3	Modeling the Effect of Discrete Catalyst Particles	52
2.3.1	Model Description	52
2.3.2	Model Verification	56
2.3.3	Results and Discussion	57
2.4	Summary.....	65
3	MODIFIED AGGLOMERATE MODEL WITH DISCRETE CATALYST PARTICLES.....	67
3.1	Modified Agglomerate Model	67
3.1.1	Classical Agglomerate Model Description with 2D Cylindrical Approach	68
3.1.2	Particle Agglomerate Model Description	72
3.1.3	Results and Discussion	74
3.2	3D Cathode Model using a Modified Agglomerate Approach	84
3.2.1	Cathode Model Description.....	85
3.2.1.1	Spherical Agglomerate Model.....	89
3.2.1.2	Modified Agglomerate Model	94
3.2.1.3	Macro-homogenous Model	97
3.2.1.4	Boundary Conditions and Model Parameters.....	98
3.2.2	Results and Discussion	98
3.3	Summary.....	106
4	IMPROVED AGGLOMERATE MODEL WITH ACCURATE SURFACE AREA CALCULATION BASED ON SPHERE PACKING APPROACH..	108
4.1	Model Description	110

4.1.1	Cathode Model	110
4.1.2	Physical Model for Effective Specific Surface Area.....	117
4.2	Validation	126
4.3	Results and Discussion	128
4.4	Summary.....	138
5	OPTIMIZATION OF FUNCTIONALLY GRADED PEM FUEL CELL CATALYST LAYER COMPOSITION.....	140
5.1	Investigation of Functionally Graded Catalyst Layer Composition.....	141
5.1.1	Results and Discussion	145
5.2	Optimization of Bidirectionally-Graded Catalyst Layer Composition .	160
5.2.1	Optimization Problem Formulation.....	161
5.2.2	Results and Discussion	164
5.3	Summary.....	181
6	CONCLUSIONS AND FUTURE WORK.....	183
6.1	Conclusions	183
6.2	Future Work.....	186
	REFERENCES	188
	Appendix	
A	COPYRIGHT PERMISSIONS	192

LIST OF TABLES

Table 2.1. Parameters used in 2D cathode model simulations with COMSOL.....	40
Table 2.2. Parameters used in single spherical agglomerate model simulations [56] .	47
Table 2.3. Parameters used for simulating the baseline case.....	55
Table 3.1. Parameters used in simulations [56].....	71
Table 3.2. Geometric parameters for the single channel computational domain.....	87
Table 3.3. Binary diffusivities at 1 atm and 298 K [98].....	88
Table 3.4. Parameters used in PEM fuel cell cathode model simulations	92
Table 4.1. Geometric parameters for the single channel computational domain.....	110
Table 4.2. Parameter values used in the cathode simulation for the baseline case....	117
Table 4.3. Characteristic properties of packing options used in this study	122
Table 5.1. Parameter values used in the cathode simulation for the baseline case....	145
Table 5.2. Baseline value and range for the three optimization variables	163

LIST OF FIGURES

Figure 1.1. History and projection of the world’s energy consumption (a) total consumption by year; (b) consumption by fuel [1]	1
Figure 1.2. Fuel cell car by Toyota, 2014 FCV	2
Figure 1.3. Anode-cathode reactions and PEM fuel cell operation	4
Figure 1.4. 2D schematic representation of the PEM fuel cell assembly	5
Figure 1.5. Schematic illustration of the cathode CL	8
Figure 1.6. Typical polarization curve of a PEM fuel cell	10
Figure 1.7. PEM fuel cell multiscale modeling chart	12
Figure 1.8. (a) Aggregation of C Pt particles; (b) idealized representation of a C Pt agglomerate; (c) 3D representation of PEM fuel cell cathode	20
Figure 2.1. Multiscale agglomerate approach description of the CL	33
Figure 2.2. 2D computational domain with half-cell section view	34
Figure 2.3. Cathode polarization curve for various Pt loadings	41
Figure 2.4. Influence of effective agglomerate surface area on cathode performance ($m_{Pt} = 0.4 \text{ mg/cm}^2$)	43
Figure 2.5. Influence of ionomer film thickness on cathode performance ($m_{Pt} = 0.4 \text{ mg/cm}^2$)	44
Figure 2.6. Spherically-symmetric, 1D computational domain and boundary conditions for the single agglomerate model	45
Figure 2.7. Effect of Pt loading on the agglomerate’s characteristic curve	48
Figure 2.8. Oxygen concentration in the ionomer film for various Pt loadings at $\eta=0.16 \text{ V}$	49
Figure 2.9. Oxygen concentration in the ionomer film for various Pt loadings at $\eta=0.40\text{V}$	50

Figure 2.10. Effect of Pt loading on the agglomerate’s characteristic curve when the ionomer film is removed in the single spherical agglomerate model	51
Figure 2.11. Computational domains for the two agglomerate constructions	53
Figure 2.12. Physical process and boundary conditions for the discrete particle model	54
Figure 2.13. Physical process and boundary conditions for the Pt layer assumption..	56
Figure 2.14. Comparison of 1D spherical symmetric analytical solution and 3D COMSOL model for uniform Pt layer assumption	57
Figure 2.15. Comparison of performance obtained with the uniform Pt layer and discrete Pt particle approaches	58
Figure 2.16. Effect of catalyst loading on performance obtained with (a) the uniform Pt layer approach, and (b) the discrete Pt particle approach	59
Figure 2.17. The effect of catalyst particle size on performance using the discrete particle approach	61
Figure 2.18. Concentration contours of reactant in mol/m ³ obtained for $\eta = -0.4$ V, $r_c = 20$ nm, and $r_{Pt} = 2$ nm.....	62
Figure 2.19. The effect of number of Pt particles on performance.....	62
Figure 2.20. The effect of Pt particle distribution on concentration contours in mol/m ³ for $\eta = -0.4$ V, $r_c = 20$ nm, and $r_{Pt} = 12$ nm.....	63
Figure 2.21. The effect of Pt particle distribution on performance	64
Figure 2.22. The effect of ionomer film thickness on performance	64
Figure 2.23. The effect of ionomer film thickness on performance	65
Figure 3.1. Representation of (a) catalyst agglomeration; (b) the homogenous mixture assumption; (c) randomly-located discrete Pt particles	68
Figure 3.2. Comparison between 2D (cylindrical) and 1D (spherically-symmetric) classical agglomerate models	72
Figure 3.3. Polarization curves for the particle, classical, and matched-thickness classical approaches ($m_{Pt} = 0.4$ [mg/cm ²]).....	74

Figure 3.4. Normalized concentration (C_{O_2}/C_0) contours for $\eta = 0.3 V$	75
Figure 3.5. Normalized concentration (C_{O_2}/C_0) contours for $\eta = 0.6 V$	76
Figure 3.6. Polarization curves for various diffusivities inside the agglomerate core for (a) the classical model, and (b) the particle model	78
Figure 3.7. Polarization curves for various Pt loadings in mg/cm^2 for (a) the classical model, and (b) the particle model	79
Figure 3.8. Polarization curves with the particle model showing the influence of particle size on performance.....	81
Figure 3.9. Distribution of 104 Pt particles with a higher concentration towards the periphery; r_{agg} is the agglomerate radius, and all particles are located outside the circle with radius = r_{in}	82
Figure 3.10. Effect of particle concentration towards the agglomerate periphery on the polarization curve	83
Figure 3.11. Polarization curves for uniform distributions of 104 and 207 Pt particles, and one non-uniform distribution of 104 particles with $r_{in}/r_{agg} = 0.9$	83
Figure 3.12. Computational domain for the 3D cathode model	85
Figure 3.13. 1D spherical agglomerate domain and boundary conditions	90
Figure 3.14. Agglomerate polarization curves from the modified approach for 20 different random particle distributions ($mPt = 0.4 mg/cm^2$)	95
Figure 3.15. Agglomerate polarization curves for various microscale models.....	97
Figure 3.16. Mass fraction distribution in the cathode at $V_c = 0.2 V$ (a) O_2 , and (b) H_2O . The cross-section includes the channel, the GDL, and the CL	99
Figure 3.17. Cathode overpotential (φ) distribution across the CL thickness from the modified agglomerate approach along the transverse ($x - z$) plane at $y = 0.95L_{ch}$. The bottom boundary of the plot corresponds to the CL/membrane interface.....	100
Figure 3.18. Volumetric current density along the membrane/CL interface ($x - y$ plane) [A/m^3].....	100

Figure 3.19. Comparison of polarization curves for the 3D cathode obtained with different CL modeling approaches	101
Figure 3.20. Comparison of current density distribution from different CL modeling approaches along a line at the membrane/CL interface at $y = 0.98L_{ch}$ and $I_{avg} = 0.4 A/cm^2$	103
Figure 3.21. Comparison of current density distribution from different CL modeling approaches along a line at the membrane/CL interface at $y = 0.98L_{ch}$ and $I_{avg} = 0.77A/cm^2$	105
Figure 3.22. Polarization curves for various Pt loadings (mPt) in mg/cm^2 predicted by the classical agglomerate model.....	105
Figure 3.23. Polarization curves for various Pt loadings (mPt) in mg/cm^2 predicted by the modified agglomerate model.....	106
Figure 4.1. 2D computational domain with 3D representation of cathode.....	110
Figure 4.2. Geometry of overlapping agglomerates and the spherical cap	120
Figure 4.3. Unit cell representation for (a) tetragonal, and (b) rhombohedral packing schemes.....	121
Figure 4.4. Representation of (a) the critical overlapping ratio, and (b) overlapping spherical caps	124
Figure 4.5. Effective surface area as a function of porosity for the two packing schemes considered here, and the expression provided by [55].....	125
Figure 4.6. Validation of the numerical model (with rhombohedral sphere packing) against the experimental data of [71]	126
Figure 4.7. Validation of the numerical model (using rhombohedral sphere packing) against the experimental data of [69] for $t_{cl} = 13 \mu m$ and $i_0 = 0.084 A/m^2$	127
Figure 4.8. Current density distribution along the membrane/CL interface for three values of cathode potential, V_c (using rhombohedral sphere packing).....	128
Figure 4.9. Effect of Pt loading with $NFP = 33\%$ and $Pt C = 20\%$ for effective surface area calculation with (a) Eq. 4.22 [55], (b) rhombohedral sphere packing, and (c) tetragonal sphere packing.....	131

Figure 4.10. Effect of Pt loading with $NFP = 33\%$ and $Pt C = 40\%$ for the rhombohedral packing scheme	132
Figure 4.11. Current density variation at $V_c = 0.6$ V for $Pt C = 20\%$ and 40%	132
Figure 4.12. Effect of $Pt C$ weight ratio on polarization curves for $m_{Pt} = 0.2$ mg/cm^2	133
Figure 4.13. Effect of NFP with $m_{Pt} = 0.325$ mg/cm^2 and $Pt C = 20\%$ for effective surface area calculation with (a) Eq. 4.22 [55], (b) rhombohedral sphere packing, and (c) tetragonal sphere packing	135
Figure 4.14. Current density variation at $V_c = 0.6$ V for $m_{Pt} = 0.325$ mg/cm^2 and $Pt C = 20\%$ with Eq. 4.22 [55], rhombohedral sphere packing, and tetragonal sphere packing	136
Figure 4.15. Effect of Pt loading on NFP with the rhombohedral packing scheme for $t_{cl} = 15$ μm ; (a) $m_{Pt} = 0.25$ mg/cm^2 , (b) $m_{Pt} = 0.5$ mg/cm^2	137
Figure 4.16. Effect of catalyst layer thickness with the rhombohedral packing scheme for $NFP = 30\%$ and $m_{Pt} = 0.2$ mg/cm^2	138
Figure 5.1. Schematic representation of graded CL composition in various directions.	144
Figure 5.2. O_2 mass fraction distributions in the CL for different operating regimes (spatially-uniform CL composition).	146
Figure 5.3. Absolute values of overpotential (V) distribution in the CL for different operating regimes (spatially-uniform CL composition).	147
Figure 5.4. Ionic potential (V) distribution in the CL for different operating regimes (spatially-uniform CL composition).	148
Figure 5.5. Reaction rate (mol/m^3s) distribution in the CL for different operating regimes (spatially-uniform CL composition).	149
Figure 5.6. Effect of NFP grading in the through-thickness direction on cathode performance; the average NFP is fixed at 30%	149
Figure 5.7. Effect of catalyst grading in the through-thickness direction on cathode performance; the average catalyst loading is fixed at 0.30 mg/cm^2	151

Figure 5.8. Effect of Pt C grading in the through-thickness direction on cathode performance for constant catalyst loading and NFP. The average Pt C is fixed at 0.25.	152
Figure 5.9. Effect of Pt C grading in the through-thickness direction on cathode performance for constant catalyst and Nafion loadings ($m_{Pt} = 0.3 \text{ mg/cm}^2$, $m_N = 0.514 \text{ mg/cm}^2$). The average Pt C is fixed at 0.25.	153
Figure 5.10. Effect of NFP grading in the in-plane direction on cathode performance; the average NFP is fixed at 30%.	154
Figure 5.11. Effect of catalyst grading in the in-plane direction on cathode performance; the average catalyst loading is fixed at 0.30 mg/cm^2 . ..	155
Figure 5.12. Effect of Pt C grading in the in-plane direction on cathode performance for constant catalyst loading and NFP. The average Pt C is fixed at 0.25.	156
Figure 5.13. Effect of Pt C grading in the in-plane direction on cathode performance for constant catalyst and Nafion loadings ($m_{Pt} = 0.3 \text{ mg/cm}^2$, $m_N = 0.514 \text{ mg/cm}^2$). The average Pt C is fixed at 0.25.	157
Figure 5.14. Effect of bidirectional NFP grading on performance; the average NFP is fixed at 30%.	158
Figure 5.15. Effect of bidirectional catalyst grading on performance; the average catalyst loading is fixed at 0.30 mg/cm^2	159
Figure 5.16. Optimum NFP distributions under different operating regimes for uniform Pt and C loadings.....	165
Figure 5.17. Performance improvement over the baseline case for two in-plane, through-thickness, and bidirectionally-optimized NFP distributions under different operating regimes for uniform Pt and C loadings	166
Figure 5.18. Reaction rate ($\text{mol/m}^3\text{s}$) distributions corresponding to the optimum NFP distributions in Fig. 5.16	167
Figure 5.19. Optimum Pt distributions under different operating regimes for uniform NFP and C loadings.....	168

Figure 5.20. Performance improvement over the baseline case for two in-plane, through-thickness, and bidirectionally-optimized Pt distributions under different operating regimes for uniform NFP and C loadings	169
Figure 5.21. Reaction rate (mol/m^3s) distributions corresponding to the optimum Pt distributions in Fig. 5.19	170
Figure 5.22. Optimum C distributions under different operating regimes for uniform NFP and Pt loadings	171
Figure 5.23. Performance improvement over the baseline case for two in-plane, through-thickness, and bidirectionally-optimized C distributions under different operating regimes for uniform NFP and Pt loadings	172
Figure 5.24. Reaction rate (mol/m^3s) distributions corresponding to the optimum C distributions in Fig. 5.22.....	173
Figure 5.25. Bidirectionally-optimized (a) Pt, and (b) NFP distributions under different operating regimes obtained by two-variable Pt/NFP optimization for uniform C loading.....	174
Figure 5.26. Performance improvement over the baseline case for single-variable Pt and NFP optimization, and two-variable NFP/Pt optimization under different operating regimes	175
Figure 5.27. Reaction rate (mol/m^3s) distributions corresponding to the optimum NFP/Pt distributions in Fig. 5.25	175
Figure 5.28. Bidirectionally-optimized (a) C, and (b) NFP distributions under different operating regimes obtained by two-variable C/NFP optimization for uniform Pt loading.....	176
Figure 5.29. Performance improvement over the baseline case for single-variable C and NFP optimization, and two-variable NFP/C optimization under different operating regimes	177
Figure 5.30. Reaction rate (mol/m^3s) distributions corresponding to the optimum NFP/C distributions in Fig. 5.28	178
Figure 5.31. Comparison of polarization curves for two Pt loadings while retaining all of the other constituent loading values in Table 5.2.....	179
Figure 5.32. Reaction rate distribution (mol/m^3s) for the spatially-uniform Pt loading of 0.1 mg/cm^2	180

Figure 5.33. Optimal Pt distribution at 0.6V for an average Pt loading of 0.1
mg/cm² 181

LIST OF SYMBOLS

A_0	active surface area per unit weight of Pt $cm^2 g^{-1}$
A_{agg}	specific surface area of an agglomerate $m^2 m^{-3}$
a_{Pt}	total effective reaction area $m^2 m^{-3}$
a_{agg}	effective surface area in CL $m^2 m^{-3}$
$a_{agg,cr}$	effective surface area at critical overlapping ratio $m^2 m^{-3}$
C_0	ionomer film surface oxygen concentration $mol m^{-3}$
$C_{O_2,ref}$	reference oxygen concentration $mol m^{-3}$
C_s	agglomerate surface oxygen concentration $mol m^{-3}$
$D_{i,j}$	binary diffusivities of i and j $m^2 s^{-1}$
$D_{i,j}^{eff}$	effective binary diffusivities of i and j $m^2 s^{-1}$
D	diffusivity of oxygen in ionomer $m^2 s^{-1}$
D_{eff}	effective diffusivity of oxygen in ionomer $m^2 s^{-1}$
D_p	particle diameter
E_r	effectiveness factor
E_{th}	Nernst voltage V
F	Faraday's constant $C mol^{-1}$
f	overlapping ratio
H	Henry's constant $atm m^3 mol^{-1}$
I_v^{agg}	current generation per unit volume of agglomerate $A m^{-3}$
I_v^{CL}	current generation per unit volume of CL $A m^{-3}$
i_0^{ref}	reference exchange current density $A cm^{-2}$
k_c	reaction rate constant s^{-1}
M_n	molecular weight of gas mixture $kg mol^{-1}$
M_j	molecular weight of species j $kg mol^{-1}$
m	number of contact points
m_{Pt}	Pt loading $mg cm^{-2}$
NFP	Nafion weight ratio
n	number of agglomerate per unit volume of CL
P	pressure atm
P_{O_2}	oxygen partial pressure atm
P_{H_2}	hydrogen partial pressure atm
$Pt C$	platinum carbon weight ratio
R	gas constant $mol cm^{-2} s^{-1}$

R_{O_2}	volumetric oxygen reaction rate $molm^{-3}s^{-1}$
R_{HO_2}	volumetric reaction rate for water vapor $molm^{-3}s^{-1}$
r_{agg}	agglomerate radius m
r_{Pt}	Pt particle radius m
T	temperature K
Th	Thiele modulus
t_{cl}	catalyst layer thickness m
V_s	volume agglomerates in unit cell m^3
V_{uc}	unit cell volume m^3
α_c	charge transfer coefficient
α_m	packing factor
α_{OD}	electroosmotic drag coefficient
δ	ionomer film thickness m
ϵ_{GDL}	porosity of GDL
ϵ_{Pt}	Pt volume fraction in CL
ϵ_C	C volume fraction in CL
ϵ_N	ionomer volume fraction in CL
$\epsilon_{V,cr}$	critical porosity
$\epsilon_{V,o}$	limiting porosity
ϵ_v	porosity of CL
ϵ_{agg}	ionomer volume fraction in agglomerate
η_{NCO}	nominal cathode overpotential V
λ	local water content
μ	dynamic viscosity $kgm^{-1}s^{-1}$
ρ	density kgm^{-3}
σ_s	electron conductivity Sm^{-1}
σ_s^{eff}	effective electron conductivity Sm^{-1}
σ_m	ionic conductivity Sm^{-1}
σ_m^{eff}	effective ionic conductivity Sm^{-1}
ϕ_s	electron potential V
ϕ_m	ionic potential V
ϕ_{RH}	local relative humidity
ω_i	mass fraction of species i

ABSTRACT

As the demand for clean energy grows rapidly, proton exchange membrane (PEM) fuel cell technology is seen as a viable candidate for an alternative energy conversion device. Despite much research progress in the past two decades, several remaining technical challenges must be overcome for the successful commercialization of PEM fuel cells. In particular, computational models play an important role in PEM fuel cell research by decreasing the dependence on expensive and time-consuming experimental approaches to develop a cost-effective and efficient PEM fuel cell.

The goal of this research study is to formulate multiscale catalyst layer (CL) modeling strategies to provide more accurate predictions for the effects of variations in the loading of platinum, carbon and ionomer, as well as porosity, within the catalyst layer. The ultimate goal is to provide guidelines for the design of an improved CL with better performance and lower cost.

The well-known agglomerate approach was chosen to model the CL. First, we conducted micro and macroscale numerical studies to investigate the shortcomings of the classical agglomerate approach which lead to unrealistic predictions of the effects of catalyst loading on performance. The investigation showed that the agglomerate model predictions can be improved either by employing relations between agglomerate parameters and compositional variables, or by accounting for discrete catalyst particles to capture local diffusion losses within the agglomerate core.

A novel multiscale approach was developed and employed within a 3D cathode model. The new approach incorporates local mass diffusion effects by representing the catalyst as a distribution of discrete particles in the agglomerate core. Unlike the classical approach, the discrete particle approach is shown to provide physically realistic results for the diffusion-limited region when the catalyst loading is varied. In addition, a framework is presented to incorporate numerical results from the discrete particle approach within the 3D cathode model.

The agglomerate model was further improved by incorporating a sphere-packing approach to analytically quantify the agglomerate surface area as a function of CL porosity. The importance of an accurate geometric model for the effective surface area was demonstrated by investigating the effect of CL composition on performance. The model was validated against experiments and the results show that the new method provides more realistic predictions for the effects of compositional variations in contrast to the existing approach.

Next, the improved agglomerate model was employed to investigate functionally-graded CL composition. In agreement with experimental observations, we found that a higher catalyst and/or ionomer loading at the membrane/CL interface improves performance especially in the ohmic loss regime. In addition, a bidirectionally-graded CL was investigated for the first time and further performance improvement was observed. Finally, the bidirectionally-graded CL constituent (Pt, C, and ionomer) distribution was optimized individually to maximize the current density under different operating regimes. The optimal distributions were found to depend significantly on the operating regime. In comparison to unidirectional grading, significantly higher performance was obtained with optimized CL compositions. In

addition, higher performance improvements were obtained with two-component optimization for the joint distributions of Pt with Nafion, and C with Nafion.

Chapter 1

INTRODUCTION

1.1 Background

Developments in technology and growing industrialization have increased our energy needs substantially. The world's energy demand is expected to increase by 1.7% per year between 2015 and 2030 [1]. Today, the lion's share of energy is supplied by carbon-based fossil fuels whose production will be increasingly unable to meet the future energy demand. In addition, the consumption of fossil fuels results in the release of large amounts of greenhouse gases which cause global warming. Hence, there has been a worldwide research effort to develop clean, sustainable energy sources, and to reduce the cost and increase the efficiency of clean energy technologies.

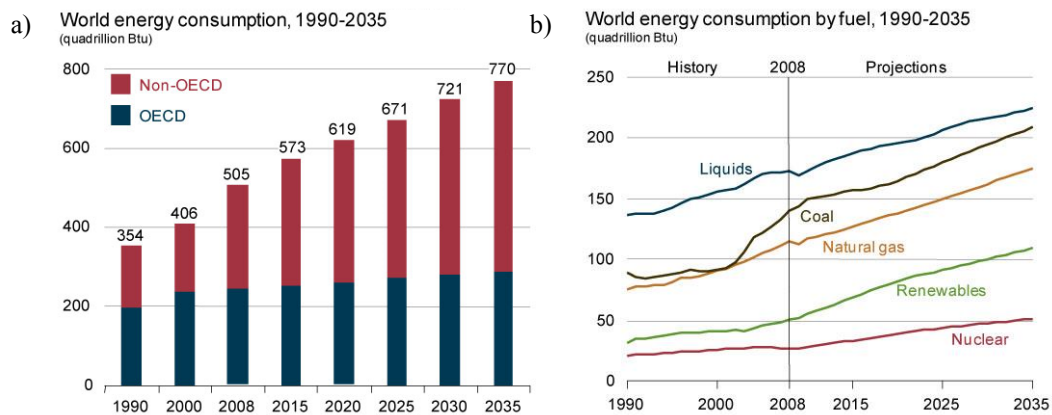


Figure 1.1. History and projection of the world's energy consumption (a) total consumption by year; (b) consumption by fuel [1]

In this context, fuel cells can be considered as a vital technology among the ongoing research in alternative energy. A fuel cell is a device that converts the chemical energy of a fuel directly to electricity. Sir William Grove was the first to demonstrate the fuel cell principle with the ‘gaseous voltaic battery’ in 1839 [2]. Subsequently, with the development of various electrolytes and electrodes, several types of fuel cells have emerged. In the 1960s, fuel cells were used by the U.S. space program to supply electricity to spacecraft. Until the 1990s, fuel cells did not attract much attention for terrestrial applications. Today, fuel cells are getting closer to commercialization as they constitute a viable alternative for various applications such as portable electronics, stationary power, and automotive propulsion.

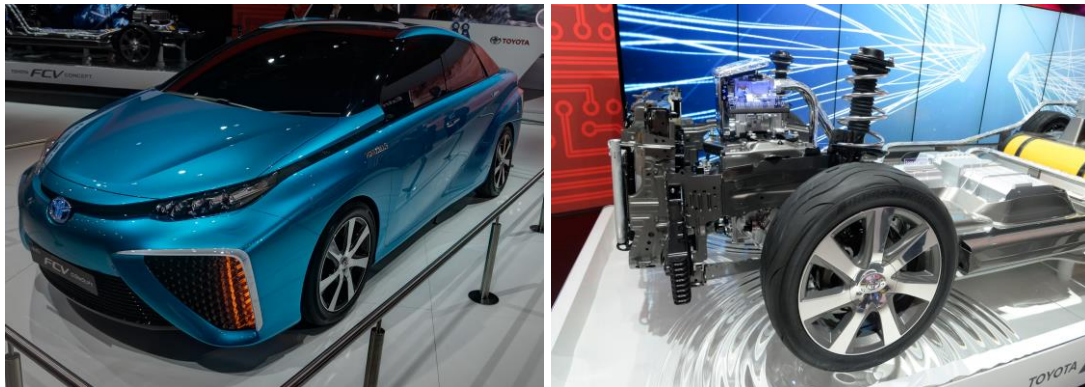


Figure 1.2. Fuel cell car by Toyota, 2014 FCV

The extreme reliance of automobiles on fossil fuels makes fuel cell technology even more critical for the automotive industry. Most automotive manufacturers have been developing proton exchange membrane (PEM) fuel cell powered vehicle prototypes. PEM fuel cells have a great potential for automotive applications for the following reasons. (1) Fuel cells are not heat engines, therefore, unlike internal combustion (IC) engines, their efficiency is not limited by the Carnot efficiency. (2)

The so-called zero-emission nature of fuel cells makes them superior to IC engines. In addition, since there are no moving parts, fuel cells are silent and mechanically durable with respect to IC engines. Recently, Toyota has announced that its fuel cell powered car (Fig. 1.2) will be available in the showroom by 2015. In this dissertation, we will be focusing on the PEM fuel cell which is briefly introduced in the next section.

1.2 Proton Exchange Membrane (PEM) Fuel Cell

The PEM fuel cell concept was first developed by General Electric in the early 1960s [3]. A sulfonated polymer was used as the electrolyte which is why it is also referred to as a polymer electrolyte membrane fuel cell. The term proton exchange membrane refers to the ion-exchange property of the electrolyte because it allows proton transfer while blocking the flow of electrons. Instead, the electrons are transported through an external circuit to produce electricity. The electrolyte membrane consists of a thin, permeable, solid sheet. Compared to liquid electrolyte cells, the solid polymer electrolyte provides many advantages such as low operating temperature and the ability to work in any orientation. PEM fuel cells generally operate between 50-100°C which allows quick startup and shutdown. The ability to work in any orientation and the quick startup property makes the PEM fuel cell very attractive for automotive applications. In addition, due to the use of hydrogen (H₂) as the fuel, PEM fuel cells do not release any pollutant as products of the electrochemical reactions within the cell.

1.2.1 Operating Principles

PEM fuel cell operation can be simply considered as the reverse of electrolysis. The goal is to produce electrical energy by combining hydrogen and oxygen. Similar to combustion, the overall chemical process in the PEM fuel cell is:



This overall reaction is a combination of two separate half-reactions taking place simultaneously at the anode and cathode. The process is illustrated in Fig. 1.3.

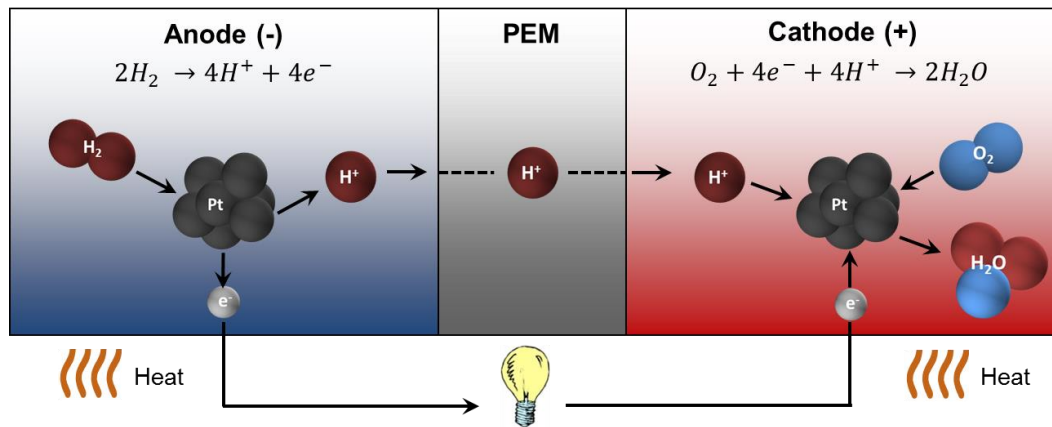


Figure 1.3. Anode-cathode reactions and PEM fuel cell operation

At the anode side, H₂ is supplied as the reactant which splits into protons and electrons at the active reaction sites in the anode CL. The protons migrate through the polymer electrolyte towards the cathode side, while the electrons are transferred to the cathode via an external circuit. At the cathode side, the supplied O₂ reacts with the incoming protons and electrons from the anode side to generate water. The net electrochemical reaction can be summarized as H₂ oxidation reaction (HOR) at the anode combined with the O₂ reduction reaction (ORR) at the cathode. The net process creates a

potential difference between the cathode and anode which generates electrical power. In addition, some heat is also produced due to various loss mechanisms.

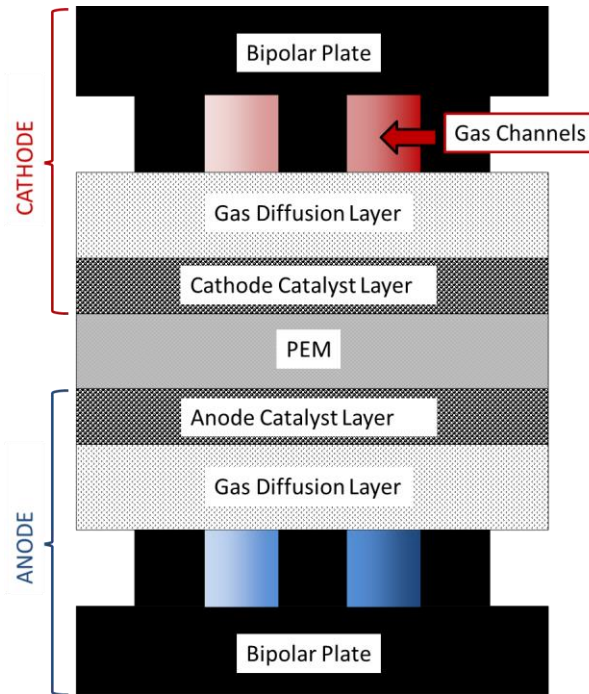


Figure 1.4. 2D schematic representation of the PEM fuel cell assembly

The amount of energy released by this process depends on the work potentials of the reactions. From a thermodynamic perspective, the maximum theoretical work potential is equal to the change in Gibbs free energy. The work potential can be converted to a voltage as follows:

$$E_0 = \frac{-\Delta G}{nF} \quad (1.2)$$

where E_0 is the cell voltage, ΔG is the change in the Gibbs free energy, n is the number of electrons transferred, and F is the Faraday constant. At standard conditions

(temperature and pressure), the theoretical voltage is calculated to be 1.229 V. The reversible voltage under non-standard conditions is governed by the Nernst equation as:

$$E_{rev} = E_0 - \frac{RT}{nF} \ln \left(\frac{a_{H_2O(g)}}{a_{H_2} a_{O_2}^{1/2}} \right) \quad (1.3)$$

where T is the absolute temperature, R is the gas constant, and a is the activity (partial pressure) of the reactants and products.

1.2.2 PEM Fuel Cell Components

In this section, brief information about the vital components of the PEM fuel cell is provided. The important components can be listed as the polymer electrolyte membrane, catalyst layers (CL), gas diffusion layers (GDL), and bipolar plates. There are two basic ways to assemble a PEM fuel cell: the catalyst-coated membrane (CCM) method, and the catalyst-coated GDL method. The PEM fuel cell assembly is depicted schematically in Fig. 1.4.

1.2.2.1 Polymer Electrolyte Membrane

The solid electrolyte can be considered among the most critical components of the PEM fuel cell. The electrolyte conducts protons from anode to cathode while blocking electron and gas transfer. The desired properties for the membrane are high proton conductivity, high resistance to electron flow, and low gas permeability. In addition, the membrane must have good mechanical, chemical and thermal stability for long term durability.

Nafion®, developed by DuPont, is the most commonly used membrane electrolyte that meets the desired features. Nafion® consists of a polymerized

tetrafluoroethylene (PTFE) backbone with sulfonic acid (SO_3H^+) side chains. The typical membrane thickness in PEM fuel cells is 25-50 μm . The proton conduction in Nafion® is initiated by the hydration of acid groups such that hydrated protons can move across the electrolyte. Therefore, being well-hydrated is a crucial issue for the proton conductivity whereas excessive hydration may cause cathode flooding due to accumulation of liquid water which will cover the pores in the GDL and block reactant access. Hence water management is an important research topic for PEM fuel cells.

1.2.2.2 Catalyst Layer

The catalyst layer (CL) is the most vital component of the PEM fuel cell as it accommodates all the electrochemical reactions. It is located between the electrolyte and the GDL with a thickness of about 10-30 μm . The CL consists of a heterogeneous mixture of catalyst particles, catalyst support, ionomer and gas pores as illustrated in Fig 1.5.

The catalyst support (typically carbon) is needed to adequately disperse the catalyst particles to maximize reaction surface area. Another function of the support is to provide a pathway for the conduction of electrons to and from the GDL. A small amount of ionomer is also added to the CL for ion transport. Finally, the gas pores are required to supply gaseous reactants to the active reaction sites and remove product water. Furthermore, three-phase contact between the catalyst/support, ionomer and gas is required for the reactions to occur. The desired features of the CL are high electrochemical surface area, high electrical and ionic conductivity, good access to reactant gases, and good chemical and mechanical stability.

The most commonly used catalyst for the PEM fuel cell is platinum (Pt). It meets all the requirements for a good catalyst except cost which is its biggest

drawback [4]. The Pt catalyst loading in previous years was as high as 2-4 mg/cm², whereas today it has been reduced to below 1 mg/cm². A second drawback with Pt is that it is susceptible to CO poisoning; hence the purity of the supplied H₂ has to be very high.

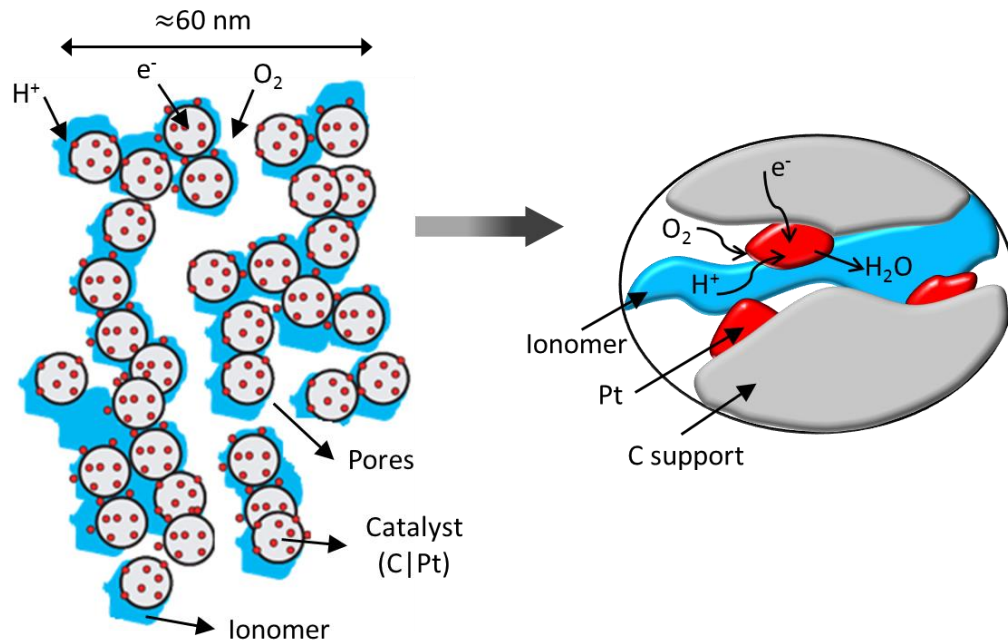


Figure 1.5. Schematic illustration of the cathode CL

Carbon black (C) is the commonly used catalyst support for the Pt particles as it exhibits good electrical and thermal conductivity, and low thermal expansion, while providing a large porosity for reactant and liquid water transport.

1.2.2.3 Gas Diffusion Layer (GDL)

The gas diffusion layer (GDL) is a porous structure located between the bipolar plate and the CL as shown in Figure 1.4 with a thickness of 100-300 μm. Generally the GDL is a carbon cloth or a carbon paper with a highly porous structure. The most

important functions of the GDL are the uniform distribution of reactant gases, electric current conduction and water evacuation from the cathode. In addition, good thermal conductivity is required for heat removal. PTFE is usually applied to the GDL as a wet-proofing agent. Sometimes an additional micro porous layer (MPL) is applied to facilitate water transport.

1.2.2.4 Bi-polar Plates

The bipolar plates are the outermost layers of the PEM fuel cell as shown in Figure 1.4. Their major functions are to distribute reactant via the gas channels, to remove heat and water from the cell, and to conduct electrons between the anode and cathode of adjacent cells. Their desired properties are high electrical and thermal conductivity, and corrosion resistance. Generally, the bipolar plates are made of metals or graphite and contribute about 45% of the total stack cost [5].

1.2.3 Voltage Losses and Polarization Curve

In practice, the cell potential is always below the theoretical voltage due to several loss mechanisms occurring within the fuel cell. The polarization curve characterizes the performance of the fuel cell by indicating the cell voltage as a function of the current density. A typical PEM fuel cell polarization curve is illustrated in Fig. 1.6 along with the four voltage loss mechanisms.

Although the membrane is supposed to be impermeable to electrons and reactant gases, some leakage of electrons and H₂ can occur through the membrane. This causes a drop in potential that is jointly referred to as internal current and fuel crossover loss. This loss causes a drop in the open circuit voltage (OCV) of the cell.

Second, activation losses are experienced due to kinetic resistance of electrode reactions. In PEM fuel cells, the majority of the activation loss is at the cathode because the anode reactions are many orders of magnitude faster [6]. The activation loss mainly depends on the type of catalyst, the catalyst loading, the operating temperature, and the reactant concentration. The activation loss is characterized by a steep fall in the cell voltage at low currents.

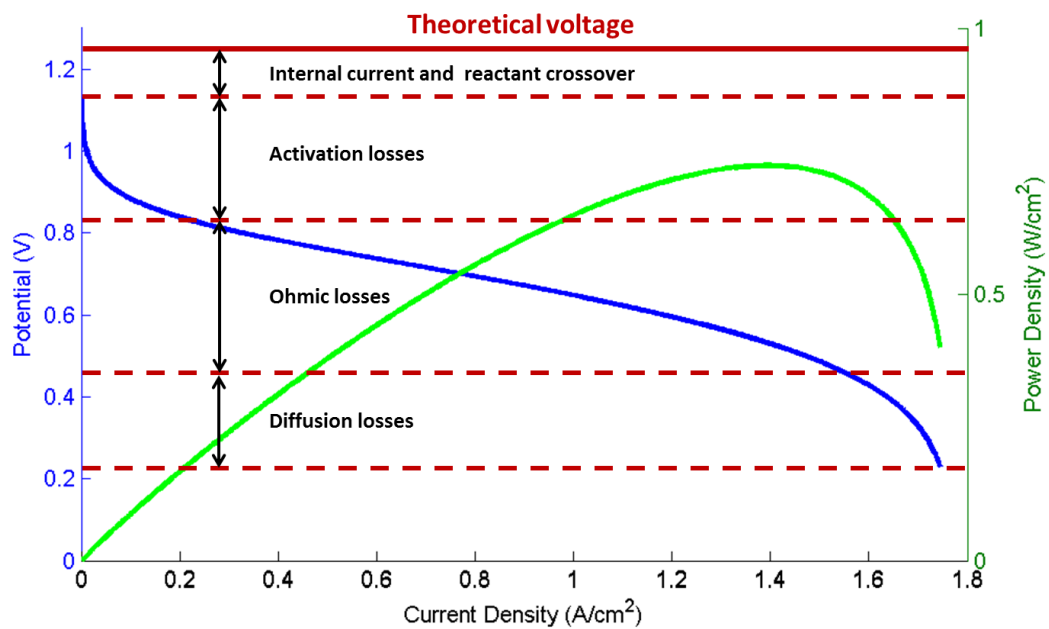


Figure 1.6. Typical polarization curve of a PEM fuel cell

Third, ohmic losses occur as a result of the electrical and ionic resistances of the materials used in the PEM fuel cell. Most of the ohmic loss is contributed by the ionic resistance. The ohmic loss is characterized by a gradual, almost linear drop in voltage across most of the operating current range.

Finally, at high current densities, the rate of diffusion of the reactants cannot keep pace with the increasing reaction rate (fuel starvation). Therefore, reactant

diffusion imposes a limit on the reaction rate and the current density. The diffusion losses are higher on the cathode side because of the lower diffusivity of O₂ compared to that of H₂. The diffusion losses are characterized by a steep drop in voltage at high currents.

1.3 Role of Modeling

PEM fuel cell design is a challenging task as it must account for numerous physical phenomena such as two-phase fluid flow, mass transport, charge transport, heat transfer and electrochemical reactions. Furthermore, all these physical processes are controlled by a large number of parameters that may have competing effects on the various physical processes. For instance, increasing the Pt loading can improve reaction kinetics, but at the cost of reduced porosity which hinders gas transport. Similarly, higher ionomer loading can improve proton transport but also at the cost of reduced porosity. Likewise, employing a wider gas channel may help to improve mass transport but it hinders current collection due to longer electron paths. Designing each fuel cell component can be a daunting task due to the complex interplay between the design variables. Conducting an experimental campaign within such a large design space can be prohibitively time-consuming and expensive. Therefore, numerical models serve as valuable alternatives to address critical design issues. Besides being fast and cheap, modeling may also help to understand the underlying physical phenomena which might be hard to explore experimentally. For instance, the spatial and temporal distribution of various quantities such as reaction rates, species concentration, overpotential, etc. which are almost impossible to monitor or measure experimentally, can be numerically calculated and visualized with high resolution. In

addition, reliable and accurate models may provide guidelines for innovative designs such as bio-inspired gas channels or functionally-graded fuel cell components.

On the other hand, PEM fuel cell modeling brings its own challenges; the overall system is a complex assembly of interacting physical components each having transport properties at different length-scales as illustrated in Fig. 1.7. Therefore, it requires multiscale modeling strategies which can properly reflect the effect of micro-level changes at the overall device level.

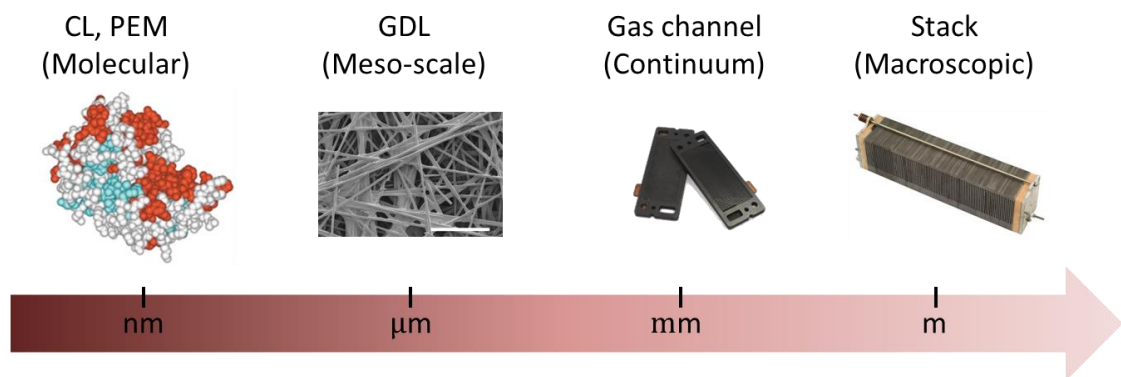


Figure 1.7. PEM fuel cell multiscale modeling chart

The study presented in this thesis focuses on developing CL models and optimizing its composition. Having introduced the PEM fuel cell components, their functions, and the importance of modeling, the next section will focus on previous work on PEM fuel cell modeling and specifically on CL modeling.

1.4 Previous Work

Modeling is a crucial tool for fuel cell design as it facilitates the intelligent evaluation of design ideas while saving money and time. It is possible to find a large number of models in the literature as modeling has received a lot of attention in the past two

decades. PEM fuel cell models range from zero-dimensional empirical models to full-scale 3D physical models.

Empirical models [7, 8] use correlations and algebraic equations to fit the polarization curves for the specifically tested cell. However, they cannot reveal details about the physical processes in the fuel cell. In addition, these models cannot be considered generic as they are only accurate for the specific fuel cell tested.

On the other hand, physical models can help to understand physical phenomenon that are hard to observe and evaluate experimentally. In addition, they are applicable to any fuel cell. Numerous types of physical models, which have evolved in complexity, are available in the literature. Physical models range from simple 1D [9, 10] to 2D channel configurations (along- or across-the-channel models) [11-13], and to 3D complex serpentine configurations [14, 15]. It is also possible to find various physical models depending on the assumptions made regarding water and heat management. For instance, models accounting for gas and liquid water transport are labeled as two-phase approaches [16-18]. Besides, many studies have focused on detailed modeling of specific components such as the membrane [9, 19-22], and the CL [23-68].

Among the PEM fuel cell components, the CL is the most significant because it accommodates all the electrochemical reactions as well as the highest energy losses. It is also a major cost-driver for the fuel cell due to the use of Pt as the catalyst. Furthermore, the complex porous structure of the CL accommodates various physical phenomena such as electrochemical reactions, charged species, heat, liquid water and reactant transport. Therefore, CL modeling is crucial for the overall fidelity of fuel cell

models. Next, we review the literature pertaining to CL modeling, followed by the numerical methods for optimal CL design.

1.4.1 Catalyst Layer Models

The high loading of expensive Pt catalyst is one of the major factors contributing to the high cost of fuel cells. The ultimate goal in CL research is to decrease the Pt loading or to replace Pt with an earth-abundant material. It is important to note that the overall performance of the fuel cell is not linearly proportional to the amount of Pt as the Pt/C is dispersed in a complex porous matrix within which it must interact effectively with ionomer and reactant gas (three-phase contact). Typically, better Pt utilization (as opposed to higher Pt loading) is required for improved performance. Therefore, proper design and optimization of the CL is a critical step for overall cost reduction and performance improvement. Many experimental studies [69-82] have been conducted to find a better CL design and improve performance. Besides these experimental efforts, quick and cost-effective numerical CL models have also played a vital role in improving CL design.

A good CL model should accurately predict the experimental polarization behavior as a function of CL composition. Furthermore, it must provide insight and understanding of the underlying physical phenomena, and suggest guidelines for the optimal CL design. CL modeling approaches vary as the functional and structural properties of the CL evolve from micro to macroscales. Broadly, CL models in the literature can be classified as micro and macro-scale approaches.

1.4.1.1 Microscale Models

Microscale models provide the most detailed understanding of the interactions between the transport phenomena and heterogeneous electrochemical reactions in the complex microporous CL structure. However, the micro-scale models are generally difficult to run and are very expensive in terms of computational power. Therefore, the literature contains only a limited number of micro-scale CL models.

Bultel et al. [23, 24] were the first to describe the catalyst nanoparticles discretely in a CL model. They solved the reactant conservation equations in a 2D axisymmetric CL section containing uniformly-distributed Pt particles within the electrolyte. They did not explicitly account for the existence of gas pores. Bultel et al. [23, 24] reported that it is necessary to model catalyst particles discretely in order to capture local diffusion losses in the presence of fast reaction kinetics. In another study, employing the same model in [23], Bultel et al. [25] investigated the effect of ion potential drop on fuel performance. Local potential drops were observed due to the presence of catalyst particles. Based on the discrete particle approach, Antoine et al. [26] studied the coupled effect of both charge and mass transport. They performed a parametric study to investigate the effect of particle size and location on polarization behavior. Similar to [23, 24] it is reported in [26] that the local diffusion effects can only be captured by modeling the particles discretely especially for fast reaction kinetics.

The preliminary studies of Bultel et al. [23-26] were followed by direct numerical simulation (DNS) studies focusing on the transport phenomenon in a reconstructed actual CL micro-structure. Wang et al. [27] developed a DNS model to investigate the cathode CL at pore scale within 2D and 3D domains. They assumed the CL to be a mixture of electrolyte/electronic phase and the gas phase. The effect of gas

pores on reactant and charge transport was investigated. It was reported that 3D realization of gas pores is necessary to accurately capture the effect of the porous structure. They extended this study in [28] to implement a random porous structure, and obtained an optimum pore structure in [29].

Siddique and Liu [30] developed a DNS model in which they reconstructed the CL by considering an agglomeration as it forms in a real fabrication process. Unlike Wang et al. [27-29], they considered the Pt, C, and ionomer as discrete phases along with the pores. The micro-level transport is realized by accounting for Knudsen diffusion and they investigated the effect of component volume fractions on CL performance. Based on their computational analysis, they reported an optimal agglomeration value.

Zhang et al. [31] constructed a small CL section that consisted of a randomly distributed catalyst phase and a mixture of ionomer-pore phase. They investigated the effect of ionomer-pore phase distribution on mass transport. It was concluded that a CL with high ionomer content on the membrane side and higher porosity on the GDL side is superior to the uniform case.

Hattori et al. [32] neglected the existence of discrete Pt particles by instead assuming a thin active Pt layer on the surface of a C sphere. They reconstructed the CL domain based on the normal distribution of C spheres which are covered by an ionomer film and investigated charge conservation without considering electrochemical reactions. They reported that the cell voltage increased as the ionomer film increases in thickness. Kim and Pitsch [33] employed the same assumption for C spheres and reconstructed a CL section based on a simulated annealing technique, and obtained effective transport properties for charge and mass transport.

Similar to [32, 33], Lange et al. [34] utilized C spheres to reconstruct the CL. Unlike Kim and Pitsch [33], they considered the electrochemical reactions along with the mass and charge transport. They averaged the random behavior of the CL architecture by running many cases and investigated the effect of domain size on effective properties. It is reported that C size is the crucial parameter that determines electrochemical reaction rates. In another study [35] they compared the effective properties obtained by using different reconstruction algorithms. It is reported that the reconstruction algorithm does not strongly influence the calculation of effective transport properties.

Besides the CL reconstruction studies, Yan and Wu [36] were the first to study the most basic microscopic structure of the CL which consists of an ideal spherical C support with ideal Pt particles dispersed on it, and the whole assembly surrounded by an ionomer film. They investigated mass transport within that structure and concluded that the Pt particle size, loading and ionomer volume play important roles in CL performance.

1.4.1.2 Macroscale Models

Macroscale CL modeling approaches are more popular and practical as they can be used along with the coupled transport phenomena for single-cell or stack-level simulations. The literature presents a few common approaches which can be classified as interface models [15, 37], homogeneous models [37-40], thin film models [41-44], and agglomerate models [45-68].

The simplest description of the CL is provided by the interface model in which an infinitesimally thin CL is considered between the membrane and the GDL. The structure of the CL is completely ignored. The influence of the catalytic activity is

introduced by source terms that are used as the boundary condition at the membrane/GDL interface. This simplification neglects all the ohmic and diffusion resistances in the CL. Harvey et al. [37] compared the agglomerate, homogenous and the interface models in their study and they reported overestimated current densities for the interface model. On the other hand, the computational convenience of the interface model cannot be ignored especially in 3D models. Therefore, the interface model is adequate if other effects are considered to be more crucial than the CL effects as in [15].

The homogeneous model represents the CL as a porous matrix consisting of a uniform mixture of Pt, carbon and ionomer. Gas phase reactants diffuse through the porous matrix to the reaction sites. Ions and electrons are assumed to diffuse through the ionomer and the carbon network, respectively. Effective medium theory is used to account for the charge and species transport in the porous medium. Although ohmic and diffusive transport resistances are taken into account, the homogeneous model cannot predict mass transport correctly because it only accounts for the diffusion of reactants in the gas pores by means of effective diffusivities (dissolution and transport in the ionomer or water are not considered). Therefore, it is unable to provide a limiting current density in most cases as observed in [37-40]. This issue was also pointed out by Rho et al. [38] in which they investigated mass transport at the PEM fuel cell cathode within a 1D domain that encompasses the GDL and the CL. It was reported that with the homogenous model, very low reactant diffusivity must be used to capture the rapid voltage drop in the diffusion loss region observed in experiments.

The thin film model is almost identical to the homogeneous model and employs the same type of CL structure. In contrast to the homogeneous model, the gas

pores are assumed to be flooded with liquid water. Therefore, unlike the homogenous model, the reactant must dissolve in liquid water to be transported in the pores. This model results in high diffusive resistances so a thin CL (i.e. thin film) must be assumed (such as 4 μm used in [44]) to obtain a match with experimental results. The thin film model is able to predict the limiting current density as in [41-44] unlike the homogenous model. For instance, Springer et al. [44] analyzed the gas transport limitations in the cathode using a 1D model. They employed the thin film approach to describe the CL and considered a CL thickness of only 4 μm which is very thin when compared to the typical CL thickness. However, they obtained a good match with the experimental polarization data including the diffusion loss region.

The agglomerate model is the most comprehensive approach among the CL models used in device-level simulations as it describes the CL using an agglomerate microstructure. Unlike the previously mentioned methods, only the agglomerate model represents the CL as a multiscale problem. Overall, the CL is assumed to consist of gas pores and aggregates of C|Pt particles that are covered by an ionomer film. The agglomerate approach attempts to model the C|Pt aggregates (shown schematically in Fig. 1.8a) that are typically seen in microscopic images of the CL. For simplicity, the aggregate microstructure, denoted as an agglomerate, is idealized as in Fig. 1.8b to resolve the complex CL activity. Here, the agglomerate core is assumed to consist of a homogenous mixture of Pt, C, and ionomer, and is surrounded by an ionomer film of specified thickness. In this model, reactant gases travel through the gas pores until they reach the ionomer film that covers the agglomerates. The gases then dissolve into the ionomer film and diffuse into the agglomerate core, while undergoing simultaneous reactions therein. Essentially, the mass transport and reaction processes

are solved within the agglomerate under a constant overpotential assumption, and the results are subsequently integrated with the macroscale simulation. Because it is possible to solve for the mass transport within the idealized agglomerate analytically, the proposed microstructure can be conveniently implemented in such a multiscale approach. More specifically, the analytical solution for the diffusion-reaction process within the agglomerate is used to calculate the volumetric current generation in the macroscopic domain.

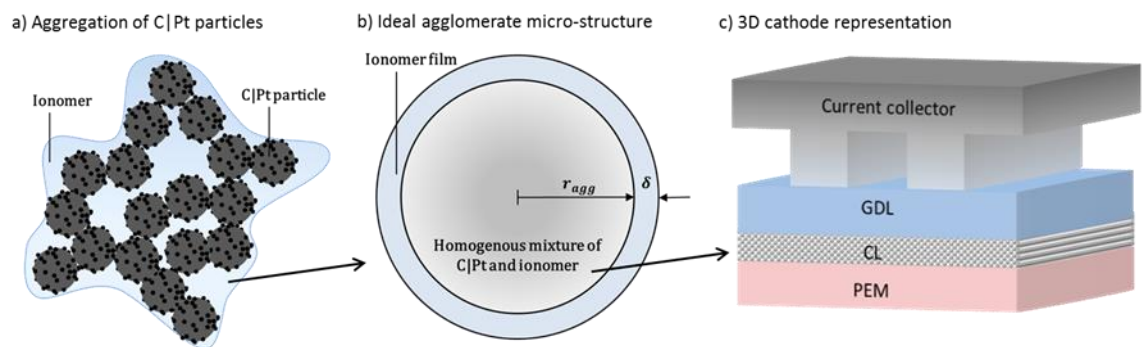


Figure 1.8. (a) Aggregation of C|Pt particles; (b) idealized representation of a C|Pt agglomerate; (c) 3D representation of PEM fuel cell cathode

Since the introduction of the agglomerate concept in the late 1980s [45, 46], numerous studies have been conducted with the agglomerate model to investigate the effect of CL properties on performance. The study of Broka and Ekdunge [47] is one of the first applications of the agglomerate model to the PEM fuel cell cathode CL. They assumed a spherical agglomerate structure on the basis of scanning electron microscope (SEM) images for their 1D model. They concluded that the agglomerate model is better than the homogeneous model at predicting the cell characteristics especially at high current densities.

Chan et al. [48] conducted a detailed parametric study to compare the homogenous and agglomerate CL modeling approaches by employing a 1D cathode model. In their study, it can be observed that the agglomerate model is superior at predicting polarization behavior in the mass transport limited regime. For the agglomerate model, it was reported that the parameters relating to reaction kinetics do not affect the limiting current density value. It can be inferred that the agglomerate model would predict the same limiting current for various catalyst loadings.

Jauen et al. [49] employed a 1D cathode model using the spherical agglomerate approach. Their predictions for performance under different operating conditions and for varying CL thickness matched with experimental data. In [50] they successfully predicted the experimentally-observed double Tafel slope and attributed that to local mass transport losses within the agglomerate. However, they did not present any results for varying CL composition.

Employing the spherical agglomerate approach in [47], Siegel et al. [51] presented a 2D along-the-channel PEM fuel cell model and studied the effect of CL composition. They obtained the agglomerate model parameters from microscopic analysis (TEM images) of a commercially available membrane electrode assembly (MEA). It was reported that the predicted performance is highly dependent on the geometrical properties of the agglomerates (which were obtained with TEM) and the CL volume fractions. It was concluded that controlling the agglomerate microstructure and void volume fraction may lead to performance improvements.

Wang et al. [52] studied water-filled and ionomer-filled spherical agglomerates to investigate the effect of O₂ diffusion and proton migration in different media. They compared the results from water-filled and ionomer-filled 1D spherical symmetric

agglomerate simulations. They obtained more homogenous reactions with the ionomer-filled agglomerate. On the other hand, water-filled agglomerates provided better ion transport resulting in high catalyst utilization.

Sun et al. [53] presented a 2D cathode model by employing a spherical agglomerate approach. First, they investigated the reaction distribution under the land and channel areas under a variable overpotential assumption. Then, they studied the effect of CL composition by varying the Pt and ionomer loading. In a similar manner to [48], it was reported that catalyst loading has no effect on cell performance at high current densities. They attributed this result to extremely low utilization of catalyst particles at high current densities.

Yin [54] presented a 1D cathode model using the spherical agglomerate approach to describe the CL. Yin proposed constitutive relations between the CL compositional variables by relating them to the agglomerate structural parameters. He employed relationships which caused the ionomer film thickness δ to decrease as the catalyst loading was increased. Unlike the previous studies, he accounted for negative δ to represent the case wherein the catalyst is not fully utilized due to a lack of ionomer. It was reported that the model captures the experimental trend of the polarization curve as a function of Pt and ionomer loading. Based on his parametric study, Yin obtained optimal values for the CL constituents. He also concluded that controlling the porosity was important for optimizing the CL.

Similar to [54], Secanell et al. [55] proposed relations between the CL composition and agglomerate structural parameters. They incorporated changes in the CL structure by varying the number of agglomerates per unit volume which concurrently changes the total surface area of the agglomerates with respect to the CL

volume. Thus, the agglomerate surface area was derived as a function of porosity and the number of agglomerates per unit volume. They then presented a framework for cathode optimization which is discussed in the next section.

Rao et al. [56] studied the dynamic behavior of a single spherical agglomerate. They investigated the dynamic response to step changes in boundary conditions (ion potential and O₂ concentration) and conducted a parametric study for the steady state case. In a similar manner to [48, 53], their steady-state model results gave identical limiting currents even though the catalyst loading was varied by a factor of 10.

Das et al. [57] developed a 3D multi-agglomerate model and employed three different arrangements in a group of agglomerates to investigate charge and reactant transport. They found that the agglomerate arrangements have a significant effect on reactant transport and on the performance. It was also reported that the lowest activation loss was incurred for the in-line arrangement.

Schwarz and Djilali [58] proposed a multiple film-covered agglomerate approach based on Baschuk and Li's [59] CL model. Baschuk and Li [59] accounted for transport limitations due to flooding by assuming a thin film of liquid water surrounding the thin film of ionomer. Schwarz and Djilali [58] extended their idea to a spherical agglomerate concept and employed it in a 3D multiphase PEM fuel cell model. They accounted for flooding by changing the thickness of the water film which is obtained by solving an additional differential equation for water saturation. They reported that cathode flooding has a severe effect on performance. They concluded that CL composition and structure must be designed to reduce ion and reactant transport resistances.

Kamarajugadda and Mazumder [60] presented a 2D PEM fuel cell model using the spherical agglomerate model for the cathode catalyst layer. Unlike the previous studies, they employed two effectiveness factors to account for the effect of ionic conductivity variation due to changes in the ionomer thickness. They conducted a parametric study by varying the CL composition and agglomerate parameters using the CL compositional relations proposed by [55]. They reported that catalyst loading needs to be at a moderate level to optimize performance.

While most of the agglomerate models in the literature employ a spherical geometry, it is also possible to assume alternate geometries for the shape of agglomerate. For example, Jain et al. [61] compared spherical, cylindrical and planar agglomerate geometries. They reported important differences between agglomerate geometries and the best performance was obtained with the spherically-shaped agglomerates.

Tabe et al. [62] presented a 1D cathode model with a three-phase boundary approach based on a simplified agglomerate concept. They investigated the effects of CL structural and compositional properties on performance. They suggested ways to optimize the CL design to improve performance. Similar to [48, 53, 56] they reported the same limiting current even when the catalyst loading was doubled.

Unlike previous studies, Yoon et al. [63] assumed the reaction order as 0.8 and considered the existence of platinum oxide in their 1D spherical agglomerate CL model. In addition to studying these assumptions, they also focused on the effect of low Pt loading. In order to investigate this issue, they conducted 2D simulations of a particle surface representing a quarter of an agglomerate. They divided the surface into several equivalent reactions zones and deactivated selected zones to mimic low

catalyst loading. Similar to [48, 53, 56, 62] they reported that reducing the catalyst loading produces no discernible change in performance beyond the kinetic effect. They reported significant mass transport limitations due to longer reactant diffusion pathways.

Most agglomerate models generally consider a single agglomerate diameter by assuming a uniform agglomerate size. Recently, Epting and Litster [64] examined the importance of agglomerate size distribution in the CL based on a nano-CT imaging of a typical CL. They concluded that the agglomerate size distribution significantly impacts the results obtained by the agglomerate approach.

The classic agglomerate approach assumes non-overlapped agglomerates that are perfectly covered by the ionomer film. In another recent study, Kamarajugadda and Mazumder [65] considered the case of two overlapped agglomerates with unequal radii. They developed a 3D model to solve the reaction-diffusion equation for the overlapped agglomerates as their generalized agglomerate model. They then coupled the generalized agglomerate model as a sub-grid-scale model in the 2D PEM fuel cell model. They concluded that while the agglomerate shape is unimportant for small agglomerates, the shape becomes a significant factor for larger agglomerates.

After carefully reviewing all the various agglomerate models, we recognized that the performance predictions for varying catalyst loading are worthy of further investigation. In particular, the results of [48, 53, 56, 62, 63] suggested that the classical agglomerate model is unable to realistically predict the effect of catalyst loading. All of these studies reported identical limiting currents despite wide variations in the catalyst loading. On the other hand, experimental results [69-71] indicate that Pt loading strongly influences fuel cell performance and the limiting

current density. Although the ongoing literature review indicates that a multiscale approach like the agglomerate model is best suited for the CL, it has inherent difficulty in predicting the effect of CL compositional variations such as catalyst loading. Therefore, a more sophisticated microscale formulation is required, along with a new procedure and supporting relations to couple the microscale solution to the macroscale to provide a better understanding of the CL.

1.4.2 Numerical Optimization and its Applications on CL Design

A large number of design variables, competing physical phenomena, and design objectives are common in many engineering problems. Coupling computational tools with numerical optimization algorithms facilitates the search for the optimal design for such problems. Numerical optimization techniques have many applications such as finding optimal shapes for airfoils [83], optimal topology for automotive parts, and MEMS systems [84].

Several types of formulation and solution algorithms are available in the literature for numerical optimization. These can be broadly classified into gradient-based and non-gradient-based methods. Gradient-based methods are also called local methods because they converge to a local minimum and the determination of the global minimum is not guaranteed. However, several methods (such as multi-start methods and ant-colony searches) can be employed to hunt for new minima with the goal of identifying the global minimum. The gradient-based methods require information about the gradient of the objective function, as well as constraints if it is a constrained optimization problem. Therefore, a sensitivity analysis must be performed to obtain derivatives of the objective function and constraints with respect to the design variables. On the other hand, the non-gradient-based methods only ask for the

objective function evaluation and do not need any gradient information to be supplied. The non-gradient-based methods are mostly stochastic-based. While these methods may find the global minimum, they require a large number of objective evaluations. Genetic algorithms, evolutionary algorithms, and simulated annealing algorithms are some commonly used non-gradient-based algorithms.

The application of numerical optimization methods in fuel cells is relatively rare in comparison to parametric studies in this area. The growing interest in fuel cell modeling has stimulated the use of numerical optimization methods in fuel cell research in the past decade. It is possible to find numerical optimization studies that have focused on gas channel [85- 89] and CL [55, 90-93] design.

In this dissertation the focus is on CL design, so the literature on numerical CL optimization is reviewed in detail. Song et al. [90] were one of the first to optimize the CL composition. They used a 1D macro-homogenous approach to describe the CL and considered the effect of liquid water saturation to model diffusion losses. They used a gradient-based method to optimize the Pt loading, Nafion loading, CL thickness, and porosity separately in order to maximize the current density at 0.6 V. In addition, they also performed a two-parameter optimization for various combinations of the design variables. In another pioneering study, Song et al. [91] optimized the Pt loading and Nafion content distributions in the through-thickness direction by employing the 1D model described in [90]. They divided the 1D CL into multiple sublayers and optimized the Pt and Nafion loading within each sublayer separately to obtain an optimum distribution that maximized the current density at 0.6 V. Next, they optimized both the Pt and NFP loadings together. Rao and Rengaswamy [92] focused on the optimization of a single agglomerate. They divided the agglomerate into

spherical shells and optimized the Pt|C weight ratio within each shell to either minimize the Pt loading, or maximize the agglomerate current.

Secanell et al. [55] optimized the Pt loading, Pt|C ratio, gas diffusion layer (GDL) porosity, and ionomer volume fraction within the agglomerate in order to maximize the current density under three different operating regimes (activation, ohmic, and diffusion loss). Their study represents the first multi-variable optimization study for the PEM fuel cell CL. In addition, they employed a sophisticated agglomerate model in which changes in the CL composition were incorporated by varying the number of agglomerates per unit volume which concurrently changes the effective agglomerate surface area. However, they modeled the effective surface area (which is an important parameter to determine diffusion losses) as an arbitrary function of the CL porosity by only considering two limiting cases. Employing the same model in [55], Jain et al. [93] performed a multizone optimization (similar to the sublayers in [91]) to obtain the optimal catalyst loading distribution in the through-thickness direction.

The preceding literature review shows that fuel cell optimization is quite challenging due to the large number of components and parameters that must be simultaneously optimized. It is therefore not surprising that such optimization studies have been infrequently attempted. For example, the literature contains only two studies focusing on 1D optimization of a functionally-graded fuel cell electrode. One of the goals of the current research is to address this gap in the literature.

1.5 Motivation, Objectives and Contributions

Fuel cells are beginning to play a prominent role as a sustainable and clean energy technology. Computational models are very useful in the design and optimization of

fuel cells because they can reduce dependence on costly and time-consuming experimental procedures. Especially for the CL, it is extremely challenging to investigate transport phenomena experimentally due to the complex microstructure and small scales involved. Accurate and complete models for the CL will also allow one to gain deeper insight into the physical phenomena within the CL.

Furthermore, future advances in microscale manufacturing techniques such as 3D printing will make it possible to tailor the microstructure and composition of the CL. Robust and reliable computational models will then be required to guide the design of the optimal CL structure and composition that delivers the best performance with high catalyst utilization (thereby lowering the cost). The preceding literature review indicates that while considerable process has been made in CL modeling and optimization, some important gaps remain to be filled. The overall goal of this study is to develop reliable and accurate CL models to properly capture the effects of varying CL composition on performance. The specific objectives of this research study are:

- Identify and investigate the limitations of the classical agglomerate approach which compromise the model's ability to capture the effects of CL composition on polarization behavior.
- Develop a novel multiscale modeling approach to overcome the limitations of the classical agglomerate model and accurately predict the influence of varying CL composition.
- Formulate physical relations to link the CL microstructure to the macroscale volume fractions of the various CL constituents and accordingly reorganize the agglomerate model equations to improve the predictions of the agglomerate model.

- Optimize the functionally-graded PEM fuel cell cathode CL composition for maximum performance.

The main contributions of this work belong to the area of CL modeling. Novel approaches have been proposed to improve the predictions of CL models. In addition, the spatial distribution of CL constituents has been optimized in both in-plane and through-thickness directions to improve performance. The following list details contributions that have been introduced for the first time in the literature:

- A modified agglomerate model which accounts for nanoscale discrete Pt particles within the agglomerate core instead of assuming a homogenous mixture.
- A modified agglomerate structure that accounts for the effect of random distributions of nanoscale Pt particles on catalyst utilization.
- A framework to integrate numerical results from the microscale CL simulation into a 3D cathode model.
- A physical model based on the sphere-packing approach to analytically quantify the reduction in the effective agglomerate surface area (a_{agg}) as the CL porosity decreases.
- An investigation of CL composition that is spatially-graded simultaneously in both the in-plane and through-thickness directions, and its optimization.

1.6 Thesis Overview

This dissertation is organized as follows. Chapter 1 presents the required background information for PEM fuel cell technology, and a comprehensive literature review of CL modeling and optimization approaches. In Chapter 2, the limitations and shortcomings of the classical agglomerate model are identified and investigated by

conducting micro and macroscale simulations. Chapter 3 introduces a modified agglomerate approach, which incorporates particle-level diffusion effects. Then a framework is presented to couple numerical results from the microscale CL simulation to a 3D cathode model. Next, in Chapter 4, a physical model is introduced based on the sphere-packing approach to determine the effective agglomerate surface area, which plays a key role in estimating diffusion losses in the CL. This idea is incorporated within a 2D cathode model to investigate the effect of CL composition on performance. In Chapter 5, functionally-graded compositions of the PEM fuel cell CL, are investigated and bidirectionally-graded CL composition distributions are optimized numerically. Finally, Chapter 6 presents a summary of the entire study with conclusions and suggestions for future work.

Chapter 2

INVESTIGATION OF THE SHORTCOMINGS OF THE CLASSICAL AGGLOMERATE APPROACH

The agglomerate approach provides the most detailed description of the CL among the macroscale modeling approaches. The agglomerate models provide a better match with experimental data in the mass transport regime as compared to the other macroscale models. However, the literature review in Chapter 1 reveals that the agglomerate model is unable to realistically predict the effect of catalyst loading on performance curves in the mass transport regime as evident in [48, 53, 56, 62, 63]. All of these studies reported identical limiting currents despite wide variations in the catalyst loading. On the other hand, experimental studies [69-71] indicate that Pt loading strongly influences cell performance and the limiting current density. The unphysical results in [48, 53, 56, 62, 63] suggest that the agglomerate model may have some inherent shortcomings in correctly predicting the effect of variations in catalyst loading.

The limitations of the agglomerate approach are investigated and discussed by conducting simulations from macro to nanoscales as illustrated in Fig. 2.1. First, the spherical agglomerate approach is employed to model a 2D PEM fuel cell cathode in order to discuss the suspected issue. Next, a single agglomerate model is constructed to explore in detail the reasons for these deficiencies. Finally, the basic CL structure consisting of carbon-supported Pt particles (C|Pt) and an ionomer binder is

investigated in order to highlight the effect of modeling discrete catalyst particles on model predictions.

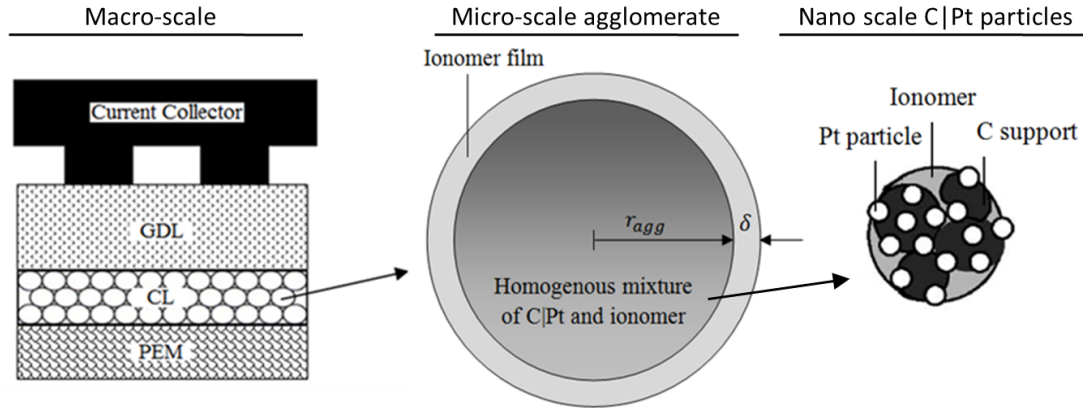


Figure 2.1. Multiscale agglomerate approach description of the CL

2.1 PEM Fuel Cell Cathode Model

2.1.1 Model Description

The 2D, steady-state cathode model accounts for the transport of chemical species, electrons, and ions in the GDL and the CL. The spherical agglomerate approach is used as an embedded model to describe the CL. For the sake of simplicity, the model assumes an isothermal, isobaric, and steady-state process. The highly-coupled equations that govern the electrochemical and transport phenomenon within the cell are solved with the finite element software COMSOL 4.2. The computational domain encompasses half of the channel and half of the land area as illustrated in Fig. 2.2. We employ the same domain and dimensions of Sun et al. [53] in our simulation as listed in Table 2.1.

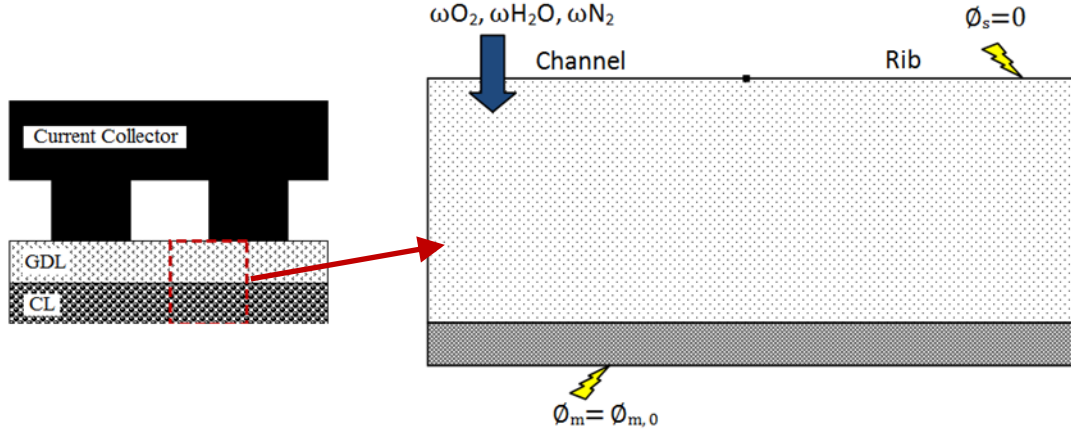


Figure 2.2. 2D computational domain with half-cell section view

The diffusion of oxygen, water vapor, and nitrogen in the cathode is described by using the Maxwell-Stefan equations after neglecting the convective terms.

$$\nabla \cdot \left[-\rho \omega_j \sum_k D_{jk}^{eff} \nabla \frac{\omega_k}{M_k} M_n \right] = R_j \quad (2.1)$$

Eq. (2.1) is solved for the mass fraction (ω_j) of each chemical species with R_j representing the source term. The density of the mixture is calculated using the ideal gas law as follows.

$$\rho = \frac{M_n P}{RT} \quad \text{where} \quad M_n = \left(\sum_j \frac{\omega_j}{M_j} \right)^{-1} \quad (2.2)$$

The Bruggeman approximation is commonly used to calculate the effective properties of isotropic porous structures. Here, we use this approximation to calculate the effective diffusivities.

$$D_{jk}^{eff} = D_{jk} \epsilon_i^{1.5} \quad (2.3)$$

Here, ϵ represents the volume fraction of the relevant phase. Charge transport by the electron and ion phases is governed by:

$$\nabla \cdot (\sigma_m^{eff} \nabla \phi_m) = \nabla \cdot i \quad (2.4)$$

$$\nabla \cdot (\sigma_s^{eff} \nabla \phi_s) = -\nabla \cdot i \quad (2.5)$$

where σ_m^{eff} and σ_s^{eff} are the effective ion and electron conductivities, ϕ_m and ϕ_s are ionic and electronic potentials, and $\nabla \cdot i$ is the volumetric current density. The Bruggeman approximation is again used to calculate the effective conductivities.

$$\sigma_j^{eff} = \sigma_j \epsilon_i^{1.5} \quad (2.6)$$

We assume that the water content in the cathode does not vary, hence the ionic and electrical conductivities are assumed to be constant.

The effects of the electrochemical reaction on charge and reactant transport are described by the source terms in the governing equations. The O_2 and H_2O source terms (R_{O_2} and R_{H_2O}) are calculated from Faraday's law.

$$R_{O_2} = -\frac{\nabla \cdot i}{4F} \quad (2.7)$$

$$R_{H_2O} = \frac{\nabla \cdot i}{2F} \quad (2.8)$$

The volumetric current density directly quantifies the rate of the electrochemical reaction occurring within the catalyst layer. We employ the spherical agglomerate model to describe the relevant electrochemical phenomena. Briefly, the reactants are first transported through the gas pores of the CL until they arrive at the electrolyte film that covers the agglomerate. The reactant then dissolves in the electrolyte film in order to reach the active reaction sites. Henry's law is used to calculate the dissolved oxygen concentration at the electrolyte film-gas pore interface.

$$C_0 = \frac{P_{O_2}}{H} \quad (2.9)$$

Upon dissolution, the reactant diffuses through the thickness of the film (δ) until it reaches the film-agglomerate interface. No reaction occurs within the thin film; therefore the dissolved flux for the steady-state diffusion process can be calculated by applying the Fick's law.

$$N_{O_2} = D \frac{C_0 - C_s}{\delta} \quad (2.10)$$

Earlier studies [10-13, 30] employed Eq. (2.10) directly, whereas recent studies [5, 19, 20, 22, 23, 26, 27] accounted for the situation where the electrolyte film thickness is not negligible in comparison with the agglomerate radius (r_{agg}). This latter situation is considered in our study and the dissolved reactant flux is calculated as follows:

$$N_{O_2} = D \frac{r_{agg}}{(r_{agg} + \delta)} \frac{C_0 - C_s}{\delta} \quad (2.11)$$

After diffusing through the electrolyte film, the reactant finally arrives at the agglomerate's internal structure which represents the reaction zone. The electrochemical process occurring within the spherical agglomerate structure is based on the spherical porous catalyst pellet model which is governed by the following diffusion-reaction equation [94]:

$$\frac{d}{dr} \left(-r^2 D_{eff} \frac{dC}{dr} \right) = r^2 k_c C \quad (2.12)$$

where k_c is the reaction rate constant.

The reaction rate inside the spherical agglomerate is calculated using an effectiveness factor [94]. Briefly, the effectiveness factor is defined as the ratio between the actual reaction rate and the expected reaction rate if all the catalyst

particles inside the agglomerate are subjected to the surface concentration of the reactant at the wall of the agglomerate.

$$E_r = \frac{\text{actual reaction rate}}{\text{reaction rate if all catalyst particles are subjected to } C_s} = \frac{R_a}{R_s} \quad (2.13)$$

The effectiveness factor is a dimensionless number that arises from a non-dimensionalization of the reaction-diffusion equation. Although the steps are omitted here, it is important to note that the effectiveness factor is obtained by assuming that the actual reaction rate is the rate when all of the reactant that enters the pellet is consumed. Then, from first-order reaction kinetics, the effectiveness factor for a spherical porous pellet is given by [94]:

$$E_r = \frac{3}{Th^2} (Th \coth(Th) - 1) \quad (2.14)$$

where ψ is the dimensionless Thiele modulus defined as the ratio between the surface reaction rate and the diffusion rate through the catalyst pellet:

$$Th = r_{agg} \sqrt{\frac{k_c}{D_{eff}}} \quad (2.15)$$

Similar to the other effective properties, the effective diffusivity D_{eff} can be calculated in terms of the ionomer volume fraction in the agglomerate by using the Bruggeman relation:

$$D_{eff} = D \epsilon_{agg}^{1.5} \quad (2.16)$$

The reaction rate if all the catalyst particles are subjected to the reactant concentration at the surface of the agglomerate can be expressed as:

$$R_s = k_c C_s \quad (2.17)$$

Then, as can be clearly seen from Eq. (2.13), multiplying the reaction rate for the surface concentration (R_s) by the effectiveness factor gives the actual reaction rate per unit volume (R_a) which is required to calculate the volumetric current density.

$$R_{O_2} = R_a = E_r R_s = E_r k_c C_s \quad (2.18)$$

On the other hand, as assumed in the calculation of the effectiveness factor, all of the reactant entering the spherical agglomerate is depleted. Therefore, the reaction rate can also be expressed in terms of the flux entering the spherical pellet.

$$R_{O_2} = a_{agg} N_{O_2} \quad (2.19)$$

Here a_{agg} is the effective agglomerate surface area. As previously stated, the concentration at the gas pore-ionomer film interface is given by Henry's law. Then the agglomerate surface concentration can be expressed in terms of the film surface concentration by equating Eq. (2.18) and Eq. (2.19) where the flux term is given by Eq. (11). Using the expression obtained for the agglomerate surface concentration, the reaction rate can be written as:

$$R_{O_2} = \frac{\nabla \cdot i}{4F} = C_0 \left(\frac{1}{E_r k_c} + \frac{(r_{agg} + \delta)\delta}{a_{agg} r_{agg} D} \right)^{-1} \quad (2.20)$$

Finally, the volumetric current density based on the spherical agglomerate approach is expressed as:

$$\nabla \cdot i = 4F C_0 \left(\frac{1}{E_r k_c} + \frac{(r_{agg} + \delta)\delta}{a_{agg} r_{agg} D} \right)^{-1} \quad (2.21)$$

For fuel cell reaction kinetics, the reaction rate constant (k_c) can be expressed in terms of a Butler-Volmer type expression:

$$k_c = \frac{\alpha_{Pt} i_0^{ref}}{4F C_{O_2,ref}} \left[\exp\left(-\frac{\alpha_c F}{RT} \eta\right) - \exp\left(\frac{(1-\alpha_c)F}{RT} \eta\right) \right] \quad (2.22)$$

In this particular spherical agglomerate model, the variation of overpotential in the agglomerate is neglected. The local overpotential can be simply expressed as the difference between the electronic and ionic potentials.

$$\eta = \phi_s - \phi_m \quad (2.23)$$

The total reaction area per unit volume of catalyst layer is expressed as [95]:

$$a_{Pt} = A_0 \frac{m_{Pt}}{t_{CL}} \quad (2.24)$$

where A_0 is the catalyst surface area per unit mass, m_{Pt} is the catalyst loading (g/cm^2) and t_{CL} is the thickness of the catalyst layer. Secanell et al. [95] fit a curve to the data provided by ETEK [32] in order to determine the value of A_0 :

$$A_0 = 2.2779 \times 10^6 (Pt|C)^3 - 1.5857 \times 10^6 (Pt|C)^2 - 2.0153 \times 10^6 (Pt|C) + 1.5950 \times 10^6 \quad (2.25)$$

where A_0 is specified as cm^2/g and $Pt|C$ is the weight ratio of Pt to C. Additional details are available in [95].

The boundary conditions employed to solve the above equations are described next. The inlet mass fractions are specified at the channel region (left half of the top edge in Fig. 2.2). The remaining boundaries are specified as no-flux boundaries for the Maxwell-Stefan equation. For the electron conservation equation, the potential is set to zero at the rib region (right half of the top edge in Fig. 2.2) and the remaining outer boundaries are defined as no-flux. For the ionic charge conservation equation, the ionic potential is set to $\phi_{m,0}$ at the membrane/CL interface and all the other outer boundaries are defined as no-flux.

The simulation results provided in the next section are based on the parameter values given in Table 2.1.

Table 2.1. Parameters used in 2D cathode model simulations with COMSOL

Temperature	T	353 [K]	[55]
Pressure	P	1.5 [atm]	[55]
GDL thickness	t_{gdl}	250[μm]	[53]
Half channel length	x_c	0.5 [mm]	[53]
Half land length	x_l	0.5 [mm]	[53]
Inlet mass fractions	ω_{O_2}	0.1773	[55]
	ω_{H_2O}	0.1557	[55]
	ω_{N_2}	0.667	[55]
Electron conductivity	σ_s	100 [S/m]	[55]
Ion conductivity	σ_m	0.0263 [S/cm]	[55]
Diffusivities	D_{O_2,N_2}	1.86e-5 [m ² /s]	[53]
	D_{H_2O,N_2}	2.58e-5 [m ² /s]	[53]
	D_{O_2,H_2O}	2.47e-5 [m ² /s]	[53]
Diffusivity of O ₂ in Nafion	D	8.45e-10 [m ² /s]	[53]
Henry's constant	H	0.3125 [atm m ³ /mol]	[53]
Ref. concentration	$C_{O_2,ref}$	0.85 [mol/m ³]	[55]
Ref. exchange current density	$i_{0,ref}$	1.5e-6 [A/cm ²]	[55]
Charge transfer coeff.	α_c	0.61	[55]
Porosities	ϵ_{gdl}	0.4	[53]
	ϵ_v	0.1	[53]
Nafion volume fraction in CL	ϵ_N	0.5	[53]
Nafion volume fraction in agg.	ϵ_{agg}	0.5	[53]
Pt loading	m_{Pt}	0.01 [mg/cm ²]	[53]
Pt/C ratio	$Pt C$	0.28	[55]
Ionomer film thickness	δ	80e-9 [m]	[53]
Agg. Radius	r_{agg}	1e-6 [m]	[53]
Agg. specific surface area	a_{agg}	3.6e5 [m ² /m ³]	[53]

2.1.2 Results and Discussion

As stated previously, nearly identical performances and limiting current densities were obtained in [48, 53, 56, 62] despite large variations in the Pt loading. Hence, we

created a 2D cathode model in COMSOL in order to investigate the role of various parameters on the performance and limiting current density.

First, the cathode model is employed to simulate the effect of Pt loading on the cathode polarization curve and reproduce the unphysical results observed in the literature, as shown in Fig. 2.3.

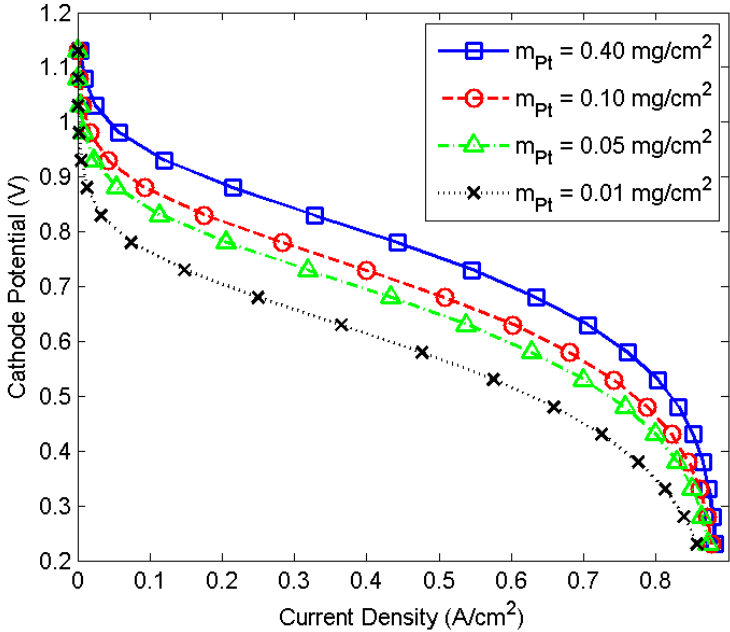


Figure 2.3. Cathode polarization curve for various Pt loadings

The curves in Fig. 2.3 closely reflect the results reported in the previous spherical agglomerate model studies [48, 53, 56, 62]. In addition, Fig. 2.3 indicates that even a 40-fold decrease in the Pt loading does not affect the cathode performance significantly and the same limiting current is obtained for all cases. Although Fig. 2.3 shows that higher Pt loadings reduce losses in the activation region, the remaining portions of the polarization curves are nearly identical to each other. Clearly, this result contradicts experimental observations.

In order to resolve this issue, we investigated the role of parameters used in the embedded spherical agglomerate model. The final product of the embedded agglomerate model is the volumetric current density given by Eq. 2.21. It includes the so-called reaction $\left(\frac{1}{E_r k_c}\right)$ and diffusion $\left(\frac{(r_{agg} + \delta)\delta}{a_{agg} r_{agg} D}\right)$ resistance terms. It is apparent from Eq. 2.21 that as the effectiveness factor goes to zero, the influence of the k_c term is diminished and the reaction becomes diffusion-dominated. While this seems to explain the insensitivity to Pt loading in the diffusion-limited region, it should be noted that the effectiveness factor was kept constant ($E_r = 1$) in [53], and they still reported the unphysical, Pt loading-independent results that we discuss. Therefore, it is evident that even if the effectiveness factor is held constant, the diffusive resistance has a dominating effect on the reaction characteristics and the limiting current. These observations lead us to believe that the lack of influence of Pt loading on the limiting current is related to the way that the diffusion-limited region is modeled.

Turning to the diffusion resistance term in Eq. (2.21), the effect of agglomerate surface area (a_{agg}) and ionomer film thickness (δ) on performance is studied next, and the results are shown in Figs. 2.4 and 2.5, respectively.

Not surprisingly, a_{agg} and δ have opposite effects on performance as suggested by Eq. 2.21. In addition, Figs. 2.4 and 2.5 show identical activation losses for all the cases examined. Based on the results in Figs. 2.3, 2.4, and 2.5, it is apparent that the diffusion resistance parameters have no effect on the activation region, whereas the reaction rate constant (which varies with Pt loading) has no effect on the diffusion loss region. These observations suggest a way to resolve the issue by correlating the Pt loading to the agglomerate's structural parameters such that it regulates the amount of reactant entering into the agglomerate. Such an approach

would superpose the effects of reaction and diffusion resistances in Eq. (2.21) as the Pt loading is varied.

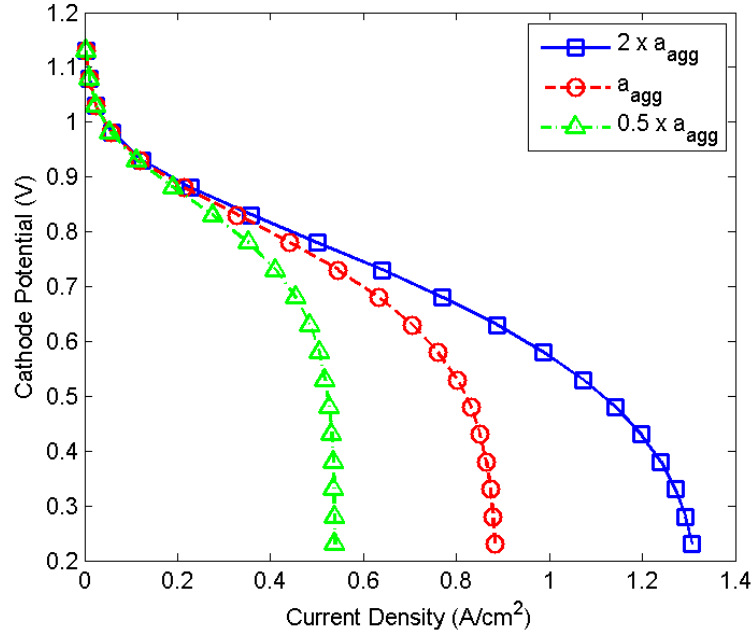


Figure 2.4. Influence of effective agglomerate surface area on cathode performance ($m_{Pt} = 0.4 \text{ mg/cm}^2$)

In this context, it is possible to find several relations between CL and agglomerate parameters. [54, 55] proposed relations to link the microstructural agglomerate parameters to macroscale volume fractions of the various CL components. Yin [54] employed relationships which caused the ionomer film thickness δ to decrease as $Pt|C$ was increased while maintaining a constant CL porosity ϵ_v , agglomerate radius r_{agg} , and ionomer volume fraction ϵ_{agg} . [55] incorporated changes in the CL structure by varying the number of agglomerates per unit volume which concurrently changes the total specific surface area of the agglomerates with respect to the CL volume. It can be observed in [54] that the model can capture effect of catalyst loading in mass transport regime.

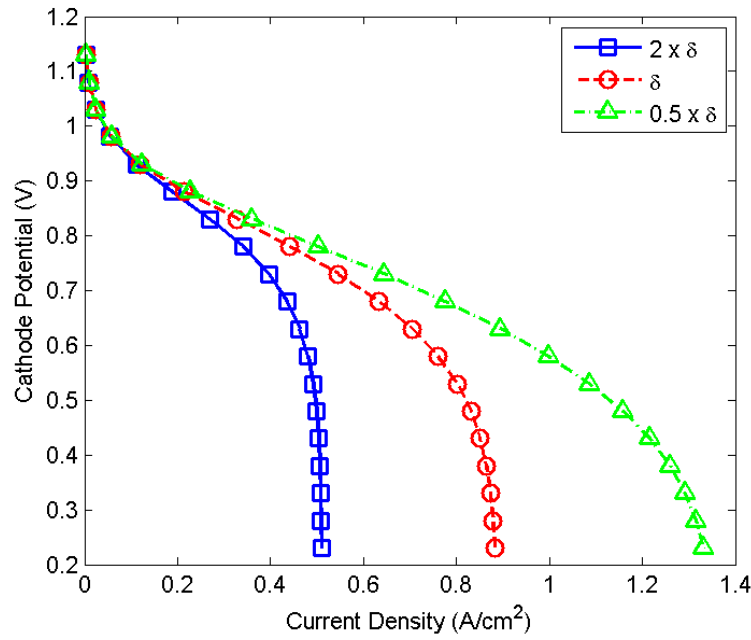


Figure 2.5. Influence of ionomer film thickness on cathode performance ($m_{Pt} = 0.4 \text{ mg/cm}^2$)

The foregoing discussion suggests that without the help of physical relations between agglomerate and CL parameters, the agglomerate model is limited in its ability to predict the effect of variation in reaction surface area on performance. However, it should also be noted that although the agglomerate structure is modeled on the basis of microscope images, it is still an imaginary structure. Such artifacts make it difficult to establish the proper relations between complex CL properties and the agglomerate structure. In the next section, the reasons for the unphysical results discussed so far are investigated with the help of the single spherical agglomerate model that circumvents the need to deal with the complex CL structural properties.

2.2 Single Agglomerate Model

2.2.1 Model Description

The single spherical agglomerate model is solved numerically to investigate the effect of Pt loading without the need for complex relations between structural properties.

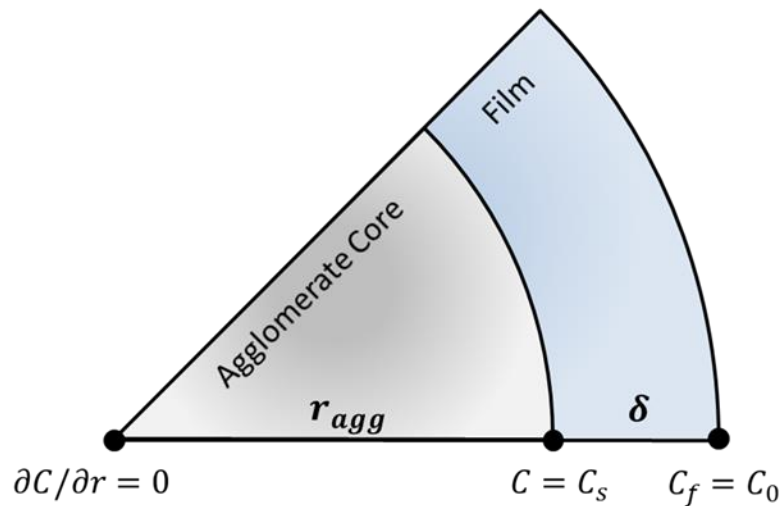


Figure 2.6. Spherically-symmetric, 1D computational domain and boundary conditions for the single agglomerate model

A spherically-symmetric, 1D, single agglomerate model is constructed as shown in Fig. 2.6. The computational domain consists of a spherical structure of radius r_{agg} , containing carbon-supported Pt catalyst particles within a matrix of ionomer, surrounded by an ionomer film of thickness δ . Since the agglomerate dimensions are so small, the local overpotential in the agglomerate is assumed to be constant for simplicity.

Transport in the ionomer film occurs purely by diffusion, whereas the electrochemical process within the agglomerate is governed by the reaction-diffusion equation:

$$\frac{D}{r} \frac{\partial}{\partial r} \left(r^2 \frac{\partial C_f}{\partial r} \right) = 0 \quad (2.26)$$

$$\frac{D_{eff}}{r} \frac{\partial}{\partial r} \left(r^2 \frac{\partial C}{\partial r} \right) = R_{orr} \quad (2.27)$$

where the reaction source term (R_{orr}) is given in terms of the concentration-dependent Butler-Volmer expression [56]:

$$R_{orr} = \frac{a_a}{4F} i_0 \left[\frac{C}{C_0} \exp\left(-\frac{\alpha_c F}{RT} \eta\right) - \exp\left(\frac{(1 - \alpha_c) F}{RT} \eta\right) \right] \quad (2.28)$$

where C_0 is the concentration at the surface of the ionomer film ($r_{agg} + \delta$). The active surface area of Pt per unit volume of agglomerate (a_a) is given by [56]:

$$a_a = \frac{m_{Pt} a}{(1 - \epsilon_v) t_{cl}} \quad (2.29)$$

where a is the specific surface area of Pt.

The agglomerate current is calculated in a similar way to the actual reaction rate using the effectiveness factor approach. One can refer to [56] and [94] for more information. Assuming all of the reactant diffusing into the agglomerate is consumed, and substituting the reaction rate in Eq. (2.7), the following expression can be obtained for the agglomerate current.

$$I_a = 16F\pi r_{agg}^2 D_{O_2} \left. \frac{dC}{dr} \right|_{r=r_{agg}} \quad (2.30)$$

It should be noted that the effective agglomerate surface area in Eq. (2.30) is equal to the surface area of a sphere of radius r_{agg} .

Equations (26-29) are solved in a coupled manner with COMSOL 4.2. For boundary conditions, the surface concentration is specified at $r = r_{agg} + \delta$ and symmetry is imposed at $r = 0$. In addition, the coupling between Eqs. (2.26) and (2.27) is established by applying mass continuity at $r = r_{agg}$. The parameters used in the single agglomerate model are obtained from Rao and Rengaswamy [56] and are listed in Table 2.2.

Table 2.2. Parameters used in single spherical agglomerate model simulations [56]

Temperature	T_{agg}	353.15[K]
Nafion volume fraction in agglomerate	ϵ_{agg}	0.4
CL porosity	ϵ_v	0.4
Effective specific area of Pt	a	1000[cm ² /mg]
Pt loading	m_{Pt}	0.4[mg/cm ²]
CL thickness	t_{cl}	30e-6[m]
Diffusivity of O ₂ in Nafion	D_a	3.1e-3*exp(-2768[K]/ T _{agg})[cm ² /s]
Diffusivity of O ₂ in agglomerate	$D_{a,eff}$	$D_a * \epsilon_{agg}^{1.5}$
Ionomer film surface concentration	C_0	2.478 [mol/m ³]
Charge transfer constant	α_c	0.5
Exchange current density	i_0	6e-8[A/cm ²]
Agglomerate radius	r_{agg}	1e-4[cm]
Ionomer film thickness	δ_{agg}	1e-5[cm]

2.2.2 Results and Discussion

Utilizing the single spherical agglomerate model, we first simulate the effect of Pt loading on current-potential curves in order to show that the problem originates from the ideal agglomerate microstructure assumption. Figure 2.7 shows that the single agglomerate approach also provides the same unphysical results as in previous section. As shown in Fig. 2.7, the case with higher Pt loading (higher reaction surface area) experiences smaller activation losses as expected. On the other hand, the performance

curves show almost identical trends for the remainder of the current range. It is reasonable to expect the same behavior (slope) in the ohmic region due to the constant overpotential assumption. However, it is not physical that the same limiting current is observed irrespective of Pt loading at high currents.

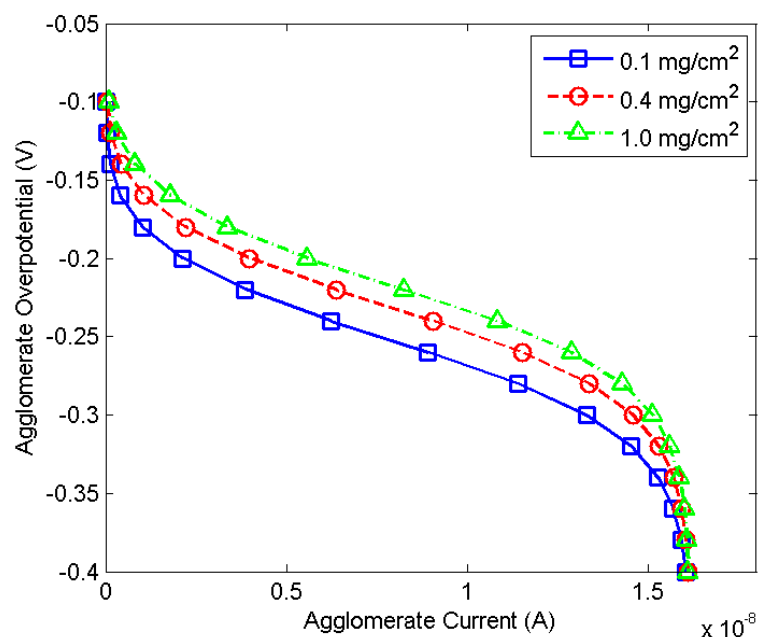


Figure 2.7. Effect of Pt loading on the agglomerate's characteristic curve

In order to clarify the issue, the normalized concentration distribution within the ionomer film is plotted against the radial position in the agglomerate for different Pt loadings, for $\eta=0.16$ V and 0.40 V in Figs. 2.8 and 2.9, respectively.

The slope of the normalized concentration profile is proportional to the reactant flux into the agglomerate. Comparing Figs. 2.8 and 2.9, one can see that the slopes at the higher discharge rate of 0.40V are independent of Pt loading, whereas at the lower discharge rate of 0.16V in Fig. 2.8, the slopes are distinctly different and increase with Pt loading. This result corroborates our earlier statement that the

agglomerate model allows us to distinguish the effect of catalyst loading in the activation region but not in the diffusion-limited region. In Fig. 2.9, it is important to realize that for all the cases, the reactant concentration approaches zero with the same slope at the agglomerate wall. According to Eq. (2.11) the reactant flux approaches an upper bound as C_s approaches zero for constant D , r_{agg} , δ , and C_0 . Therefore, the effect of Pt loading on reaction rate cannot be discerned in the diffusion-limited region because C_s approaches zero at high overpotentials, and all the cases converge to the limiting flux and limit the reaction rate. In the case of a more sluggish reaction (with very low exchange current density), C_s would not go to zero, and the diffusion-limited region in the polarization curve would be absent.

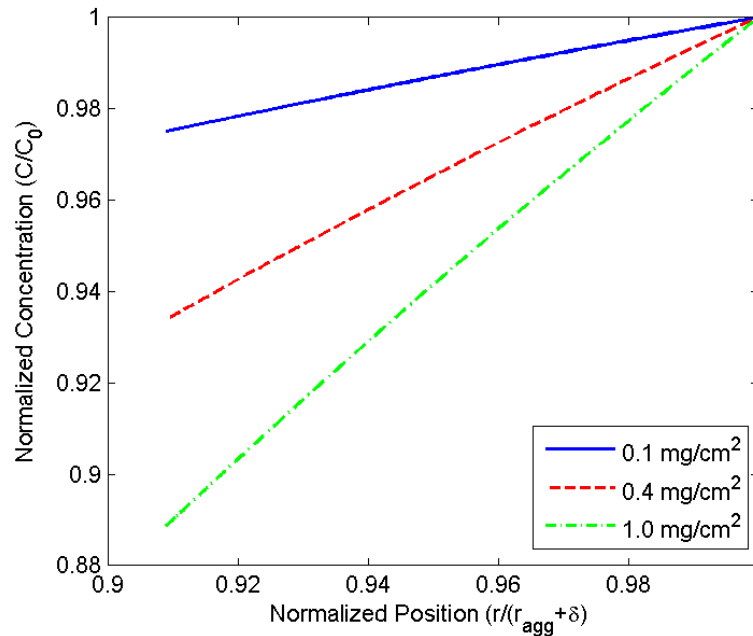


Figure 2.8. Oxygen concentration in the ionomer film for various Pt loadings at $\eta=0.16$ V

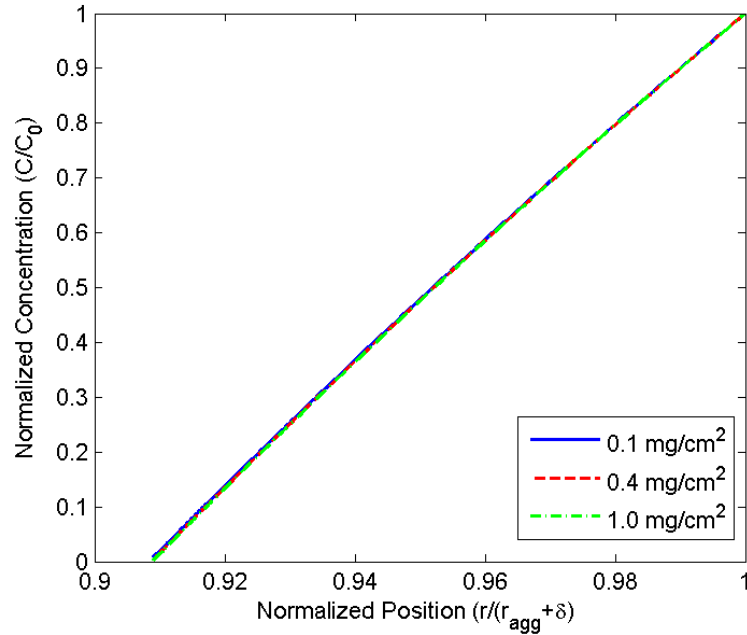


Figure 2.9. Oxygen concentration in the ionomer film for various Pt loadings at $\eta=0.40V$

Furthermore, the ionomer film is responsible for the limiting reaction rate as evident from Fig. 2.10 which illustrates the case without the ionomer film. Figure 2.10 also indicates that the performance curves for different Pt loadings can be easily distinguished in the absence of the ionomer film. Hence, it can be inferred that the ionomer film is the critical component that determines the diffusion process in the classical agglomerate approach.

It is also necessary to mention that C_s depends on the ionomer film diffusion resistance and the concentration gradient in the agglomerate which is determined by the reaction source term R_{orr} in Eq. (2.29). In addition, especially for high reaction rates (high overpotentials), R_{orr} is mostly dominated by the exponential terms in comparison to multiplicative factors. Therefore, the limiting flux is weakly dependent on multiplicative factors in R_{orr} (such as the reaction surface area), whereas it

depends strongly on the parameters that change the diffusion resistance in the ionomer film. Consequently, the agglomerate approach produces identical limiting currents even though the catalyst loading is varied ten-fold.

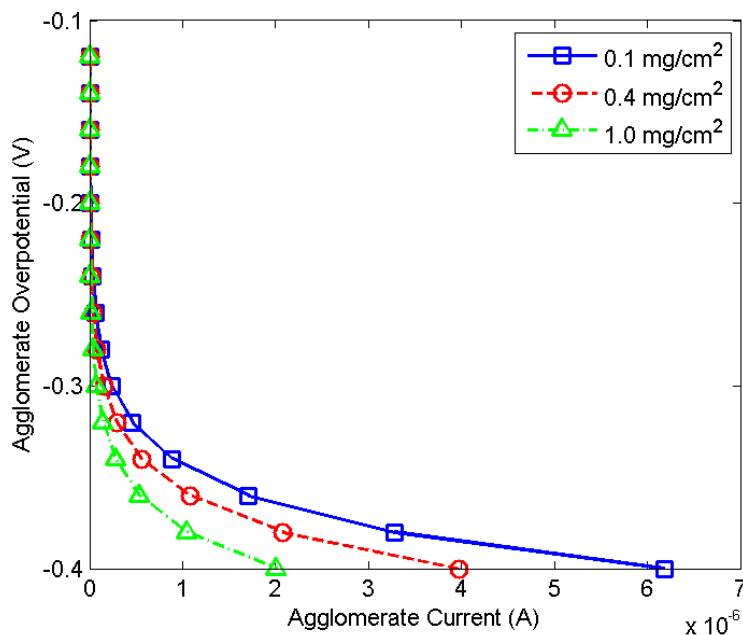


Figure 2.10. Effect of Pt loading on the agglomerate's characteristic curve when the ionomer film is removed in the single spherical agglomerate model

Based on these findings, we may conclude that the agglomerate approach models the diffusion limitations only within the ionomer film, which imposes the same reaction limit nearly independent of Pt loading inside the agglomerate. Consequently, the desired effect of Pt loading can be observed with the agglomerate model only if the Pt loading is related to the agglomerate parameters that change the diffusion resistance in ionomer film or agglomerate surface area, as concluded in the previous section. If one could construct and test the proposed agglomerate structures experimentally, we would find that the diffusion-limited region was affected by the Pt loading due to particle-level limitations which are neglected in agglomerate model. In

order to gain insight into these particle-level interactions, modeling the effect of discrete Pt particles is investigated next.

2.3 Modeling the Effect of Discrete Catalyst Particles

As mentioned in the previous chapter, [23-25, 36] were the first to study the effect of discretely-modeled catalyst particles. In a similar manner, Yan et al. [36] considered the discrete configuration of Pt particles and proposed a microscopic model to investigate a single catalyst particle consisting of carbon-supported Pt nanoparticles with an ionomer binder. They modeled the single catalyst particle in conjunction with the constitutive relations provided by the agglomerate approach.

In this section, we reinterpreted the catalyst particle model of Yan et al. [36] by considering the reaction-diffusion phenomena based solely on the geometric parameters of the particles (no constitutive relations are used). The main goal is to investigate the effects of modeling discrete Pt particles on the carbon support by comparing the cell performance results with the case in which the Pt is assumed to be distributed uniformly over the carbon support as a thin layer. Figure 2.11 shows the schematic representation for the two approaches.

2.3.1 Model Description

The transport process in the CL starts with the diffusion of reactant gases into the pores. In the absence of flooding by liquid water, the reactant dissolves in the ionomer and is transported towards the active reaction sites where the three-phase contact (ionomer, Pt and C) is present. Finally, the electrochemical reactions at the reaction sites generate voltages that drive the electronic and ionic current flows.

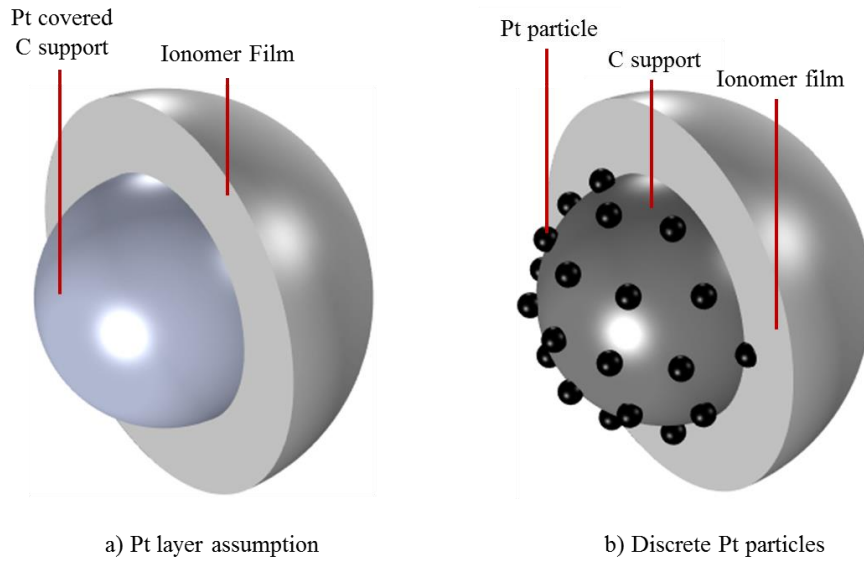


Figure 2.11. Computational domains for the two agglomerate constructions

This study focuses on the active reaction sites without explicitly accounting for the presence of pores. For the C|Pt particles in Fig. 2.11, the transport phenomena can be reduced to diffusion and reaction of the reactants, and current conduction. For simplicity, the local overpotential is considered constant because the potential drop is expected to be negligible in such a nanoscale domain. Even at the CL level [95], the overpotential varies less than 0.01 %. With the constant overpotential assumption, the current density solely becomes a function of reactant concentration. We also assume isothermal conditions for the CL transport processes. Based on these assumptions, the transport process can be described by the following diffusion equation:

$$\nabla \cdot (D \nabla C_{O_2}) = 0 \quad (31)$$

where D is the diffusivity of O_2 in the ionomer which is calculated from the following equation [56]:

$$D = 3.1 \times 10^{-3} \exp\left(-\frac{2768}{T}\right) \quad [cm^2/s] \quad (32)$$

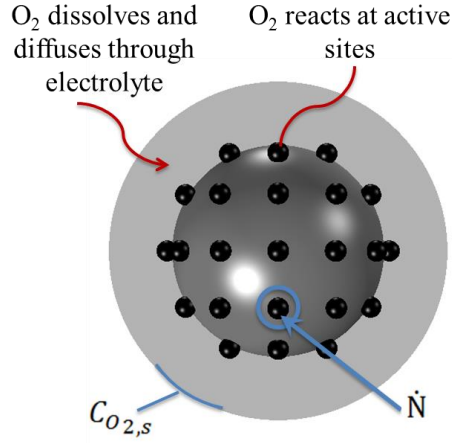


Figure 2.12. Physical process and boundary conditions for the discrete particle model

It is important to note that the two models are only different in the way that the electrochemical process is described. For the uniformly Pt-covered C sphere case, the chemical process is described by the reactions on the C surface uniformly. On the other hand, for the discrete particle approach the reactions are only defined on the surfaces of the discrete Pt particles as in Fig. 2.12. In the numerical model, the electrochemistry is interpreted by a boundary condition on the active surfaces (are described above for each approach) that describes the reactant consumption flux as:

$$\dot{N} = \frac{dC_{O_2}}{d\vec{n}} = \frac{i}{4F} \quad (33)$$

where the generated current density (i) is given by the Butler-Volmer equation as:

$$i = i_0 \left[\frac{C_{O_2}}{C_{O_{2,s}}} \exp\left(-\frac{\alpha_c F}{RT} \eta\right) - \exp\left(\frac{(1 - \alpha_c) F}{RT} \eta\right) \right] \quad (34)$$

where i_0 is the exchange current density, $C_{O_2,s}$ is the O_2 concentration at the outer wall of ionomer film, η is the constant local overpotential, and α_c is the cathodic charge transfer coefficient. $C_{O_2,s}$ is defined as a Dirichlet boundary condition at the outer surface of the ionomer film. Assuming a constant operating pressure P_{O_2} , the reactant surface concentration can be calculated using Henry's constant H [56] as:

$$C_{O_2,s} = \frac{P_{O_2}}{H} \quad (35)$$

The current density is calculated based on the approach presented in [56] as:

$$I = FD \left(\vec{n}_x \frac{dC_{O_2}}{dx} + \vec{n}_y \frac{dC_{O_2}}{dy} + \vec{n}_z \frac{dC_{O_2}}{dz} \right)_{@r=r_c+\delta} \quad (36)$$

where r_c is the radius of the C sphere, and δ is the thickness of the ionomer film. The parameters and operating conditions utilized in the simulations are listed in Table 2.3.

Table 2.3. Parameters used for simulating the baseline case

Temperature	T	353.15[K]
Oxygen pressure	P_{O_2}	1.5 [atm]
Henry's constant	H	0.3125 [atm m ³ /mol]
Pt particle radius	r_{Pt}	2 [nm]
C support radius	r_c	20 [nm]
Ionomer film thickness	δ	12 [nm]
Charge transfer constant	α_c	0.5
Exchange current density	i_0	6e-8[A/cm ²]

The diffusion equation coupled with a nonlinear flux term at the active boundaries is solved with COMSOL 4.3 by using a stationary parametric solver. A sweep study is conducted in order to plot the performance curves. It is important to note that the high reaction rates on the active boundaries can cause the solver to return

negative concentration values which are not physical; this problem can be solved by increasing the mesh density near the active boundaries. Another way is to apply a logarithmic transformation to the governing equation in order to ensure stability of the diffusion equation.

2.3.2 Model Verification

In order to verify our numerical solutions, we compared our results with the analytical solution for the uniform Pt layer case. Because the uniform Pt layer case can be treated as a spherically-symmetric problem, it is possible to solve it analytically in 1D. The problem description and solution in the 1D spherically-symmetric domain is provided in Fig. 2.13. Figure 2.14 shows a good agreement between the results of the 3D COMSOL solution for the uniform Pt layer case and its 1D analytical counterpart.

$$\frac{d}{dr} \left(r^2 \frac{dC_{O_2}}{dr} \right) = 0$$

$$-D \frac{dC_{O_2}}{dr} \Big|_{r=r_i} = \dot{N}$$

$$C_{O_2} \Big|_{r=r_o} = C_{O_{2,s}}$$

Solution: $C_{O_2}(r) = -\frac{3.96}{r} + 19.8$

Figure 2.13. Physical process and boundary conditions for the Pt layer assumption

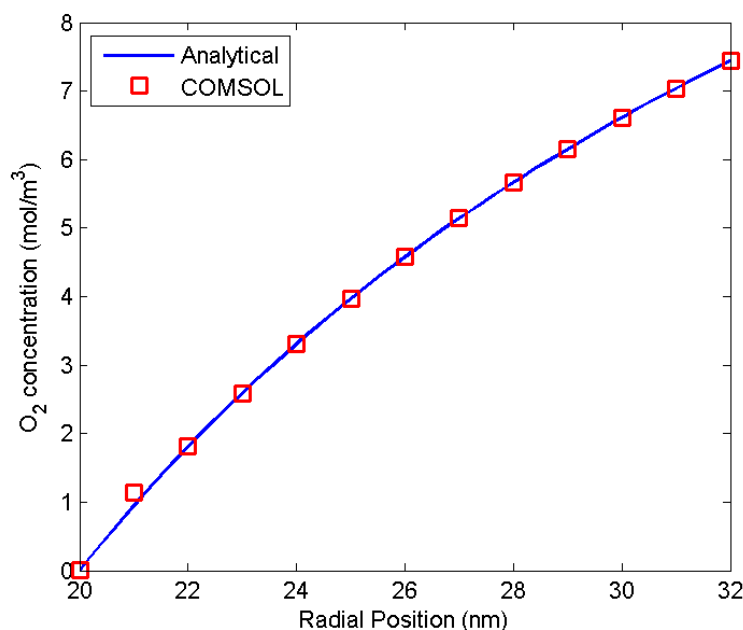


Figure 2.14. Comparison of 1D spherical symmetric analytical solution and 3D COMSOL model for uniform Pt layer assumption

2.3.3 Results and Discussion

The performance curves for the approaches in Fig. 2.11 are presented in Fig. 2.15. It is important to note that the surface area of the uniform Pt layer is equal to the total active area of the Pt particles in the discrete particle case. Figure 2.15 indicates that the performance plots are in agreement in the activation and ohmic regions at low and intermediate current densities, respectively. However, the discrete particle approach predicts an earlier entry into the diffusion-limited region at high current densities. Hence, the discrete modeling of particles resulted in increased diffusion losses. It may be inferred that the Pt-particle interactions impose an additional diffusion loss whereas the diffusion loss for the uniform Pt-coverage case arises solely from the ionomer film coating the C|Pt particle. In other words, the ability to capture the effect of local mass

diffusion losses results in increased diffusion losses with respect to the uniform catalyst layer assumption.

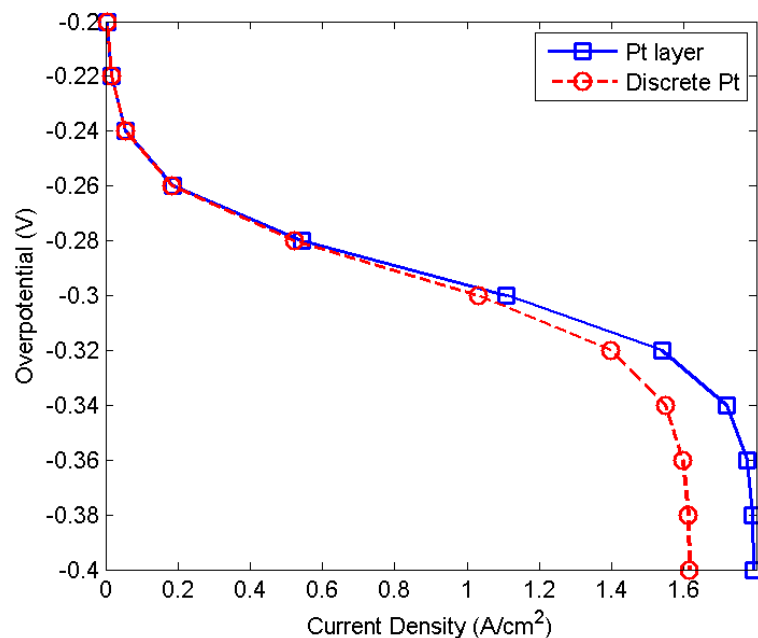


Figure 2.15. Comparison of performance obtained with the uniform Pt layer and discrete Pt particle approaches

Next, we investigate the variation in the Pt loading which changes the reaction surface area. In order to increase the Pt loading for the discrete particle approach, one can increase the Pt-particle size, or the number of particles. Here, we chose to increase the particle size so as to preserve the particle distribution; hence, the total active surface area varies as the square of Pt-particle radius. For the uniform coverage assumption, we modified the active area by employing a multiplicative factor that is equivalent to increasing Pt utilization.

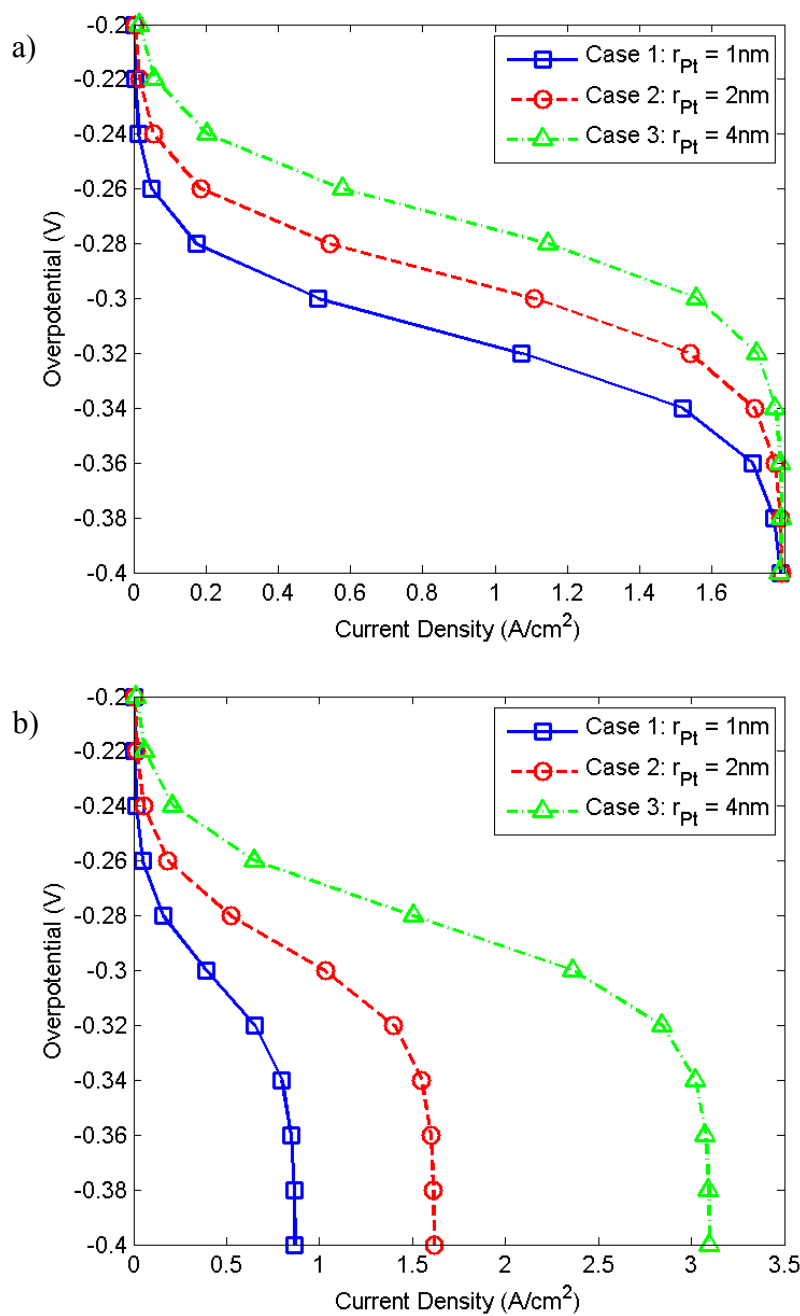


Figure 2.16. Effect of catalyst loading on performance obtained with (a) the uniform Pt layer approach, and (b) the discrete Pt particle approach

Figure 2.16a indicates that for the uniform coverage case, the variation in reaction surface area produces expected changes in the activation region of the polarization plot. However, all three curves indicate the same limiting current in the diffusion-limited region. On the other hand, the discrete particle approach indicates that the performance depends strongly on reaction area in both the activation and diffusion-limited regions as seen in Fig. 2.16b. Consistent with the results from Fig. 2.15, comparison between Figs. 2.16a and 2.16b suggests that capturing the local mass diffusion losses and particle interactions are important in the diffusion-limited region, whereas the diffusion losses are dominated by the ionomer film in the uniform coverage case.

This comparison reveals the importance of modeling the Pt as discrete particles. This conclusion leads us to examine the effect of variations in the parameters related to the discrete Pt particles. Therefore, we conducted a parametric study to understand the effect of particle size while maintaining a constant weight ratio between Pt, C, and ionomer; particle number; particle distribution; and ionomer film thickness on fuel cell performance.

Results from experiments have shown that smaller Pt particles with the same CL composition give better performance due to an increase in the reaction surface area. In order to simulate this case, we need to keep the volume fraction of Pt, C, and ionomer constant. Accordingly, we changed the C sphere size and ionomer film thickness with the Pt-particle radius. We could have achieved the same effect by increasing the number of Pt particles for the same weight ratio, but the preferred way is computationally more efficient.

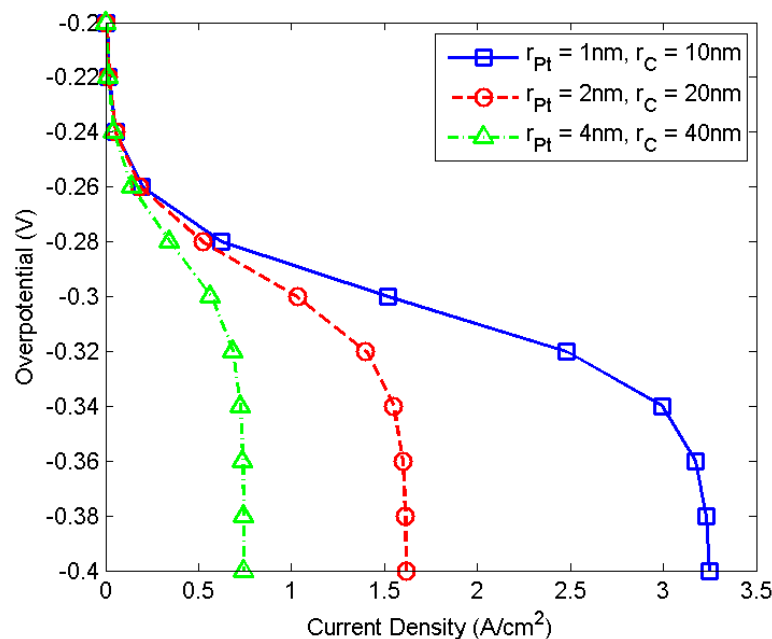


Figure 2.17. The effect of catalyst particle size on performance using the discrete particle approach

Figure 2.17 shows the influence of C|Pt particle size on performance. In Fig. 2.16b we showed that the performance increases with the increasing Pt-particle size due to increased surface area. However, in Fig. 2.17 we maintained a constant weight and volume fraction while decreasing the Pt-particle size. Figure 2.17 clearly indicates that performance improves as the catalyst particles become smaller.

As previously stated the Pt loading can also be increased by increasing the number of particles. The effect of increasing the number of Pt particles on the reaction concentration contours, and the performance plot are illustrated in Figs. 2.18 and 2.19 respectively.

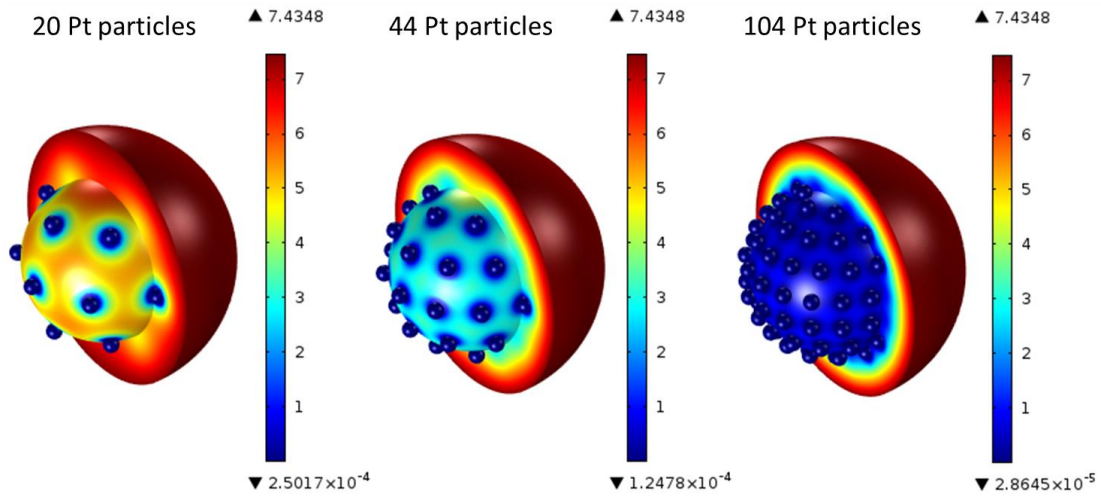


Figure 2.18. Concentration contours of reactant in mol/m^3 obtained for $\eta = -0.4 \text{ V}$, $r_C = 20 \text{ nm}$, and $r_{Pt} = 2 \text{ nm}$

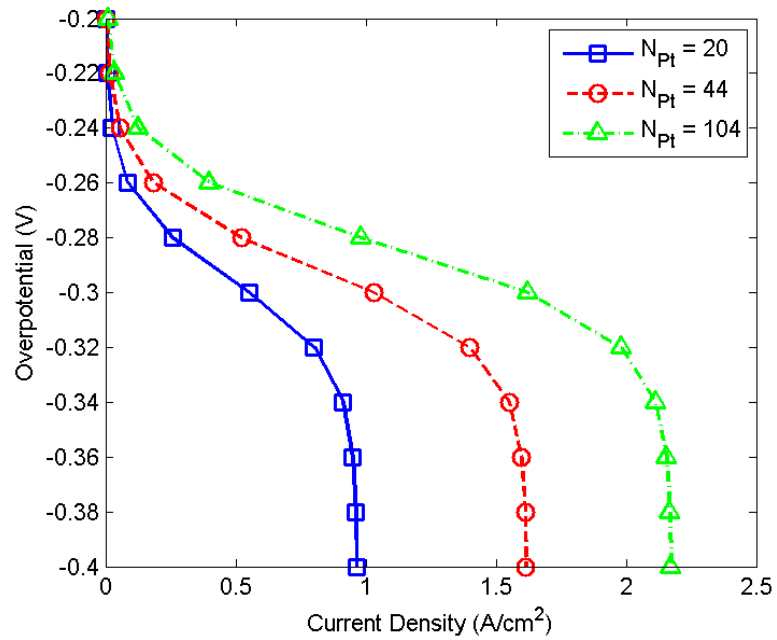


Figure 2.19. The effect of number of Pt particles on performance

Figure 2.18 shows that the reactant consumption increases with the number of catalyst particles. Reactant consumption grows as surface area increases, and the

performance improves for the same reason. As expected, Fig. 2.19 shows that the best performance is obtained with the highest number of Pt particles.

For all the previously examined cases, the particles are uniformly distributed over the surface of the C sphere. The effect of inter-particle distance and non-uniform particle distribution on performance can be investigated by employing randomly distributed Pt particles. The effect of particle distribution on concentration contours and performance are shown in Figs. 20 and 21, respectively.

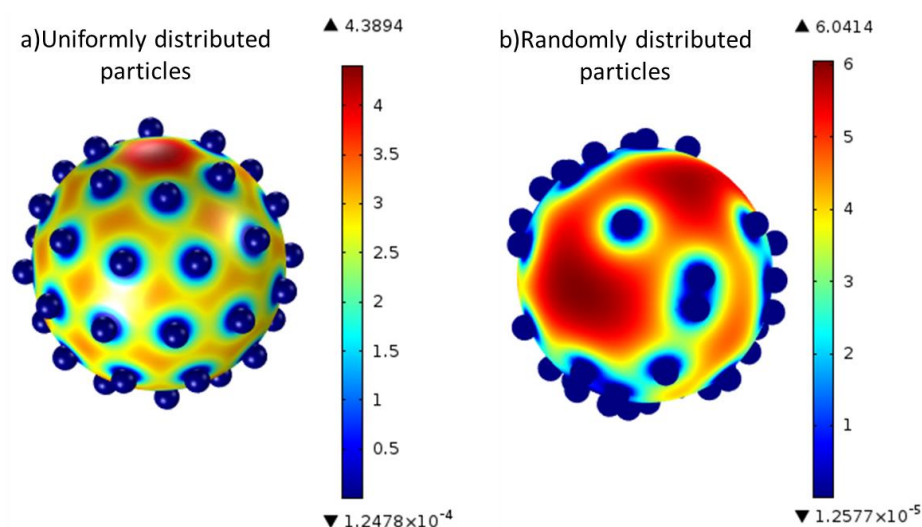


Figure 2.20. The effect of Pt particle distribution on concentration contours in mol/m³ for $\eta = -0.4$ V, $r_C = 20$ nm, and $r_{Pt} = 12$ nm

Figure 2.20 illustrates that the minimum concentration obtained with the random distribution is about 10 times lower than the one obtained with the uniform distribution because several particles are very closely clustered in the former case. Similarly, the highest concentration in the random distribution case is higher than the one in the equi-spaced case due to the presence of large dead zones as shown in Fig. 20b. These large dead zones would cause lower overall performance for the random distribution case as verified in Fig. 2.21.

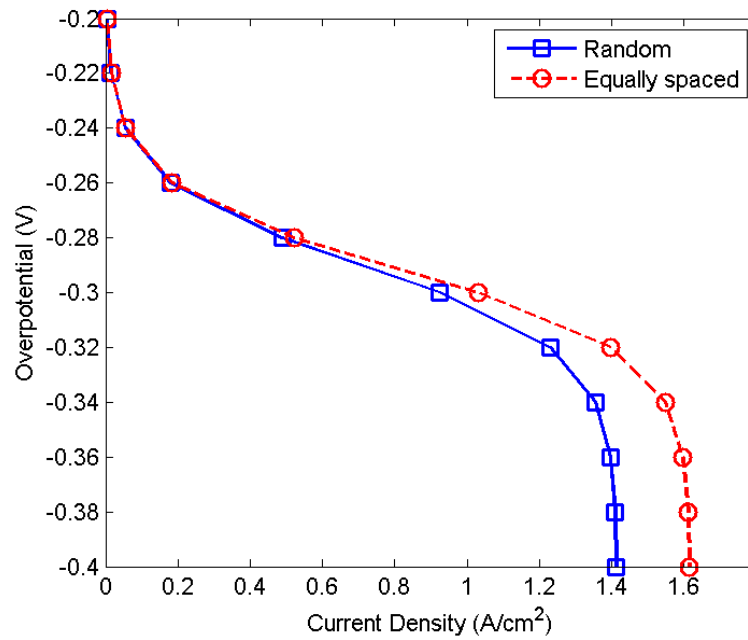


Figure 2.21. The effect of Pt particle distribution on performance

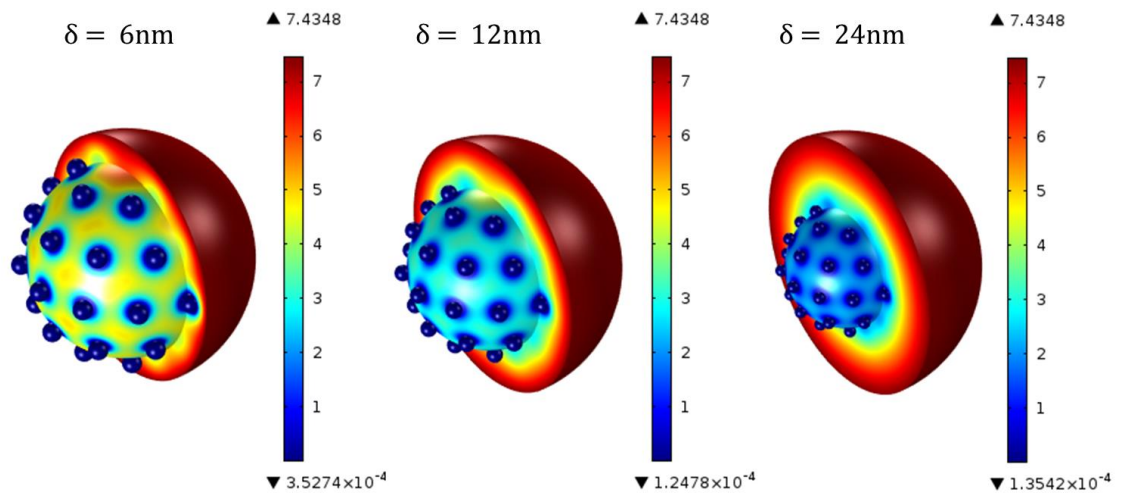


Figure 2.22. The effect of ionomer film thickness on performance

The influence of ionomer film thickness on the reactant concentration contours and the performance obtained by the discrete particle approach are shown in Figs. 2.22 and 2.23, respectively. The concentration contours in Fig. 2.22 verifies that a thicker

ionomer film leads to greater reactant depletion on the C-support surface due to the film's higher diffusion resistance. This result is confirmed by the performance plots in Fig. 2.23 where a thicker ionomer film forces an earlier entry into the diffusion-limited region, and a smaller limiting current.

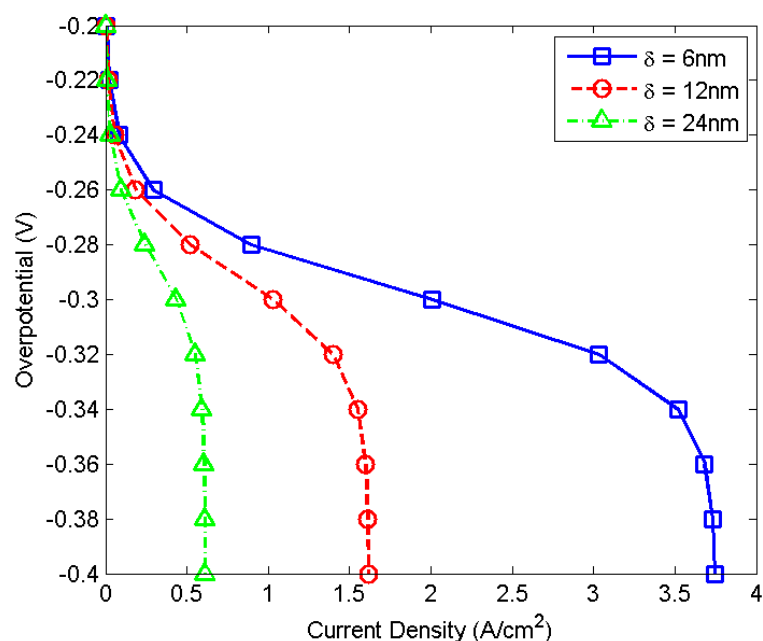


Figure 2.23. The effect of ionomer film thickness on performance

2.4 Summary

In Chapter 2 the shortcomings of the well-known spherical agglomerate model are investigated. A 2D cathode model with an embedded spherical agglomerate model was formulated to explore its predictions as the Pt loading is varied. Then a single spherical agglomerate model was employed to investigate the intrinsic characteristics of the model in order to identify the reasons for unphysical predictions as the catalyst loading is varied. Finally the effect of modeling the catalyst as discrete particles is investigated with a single C|Pt particle model.

With the 2D cathode model it was conclusively shown that if the variation in catalyst loading is not related to the agglomerate parameters that are responsible for the amount of reactant entering the agglomerate, the embedded agglomerate model cannot accurately capture the response in the diffusion-limited region. The single agglomerate model revealed that the agglomerate approach is incapable of capturing the effect of catalyst loading due to the existence of the ionomer film. The single C|Pt particle model revealed that the diffusion losses can be properly captured by accounting for discrete Pt particles which help to predict the local diffusion losses.

In conclusion, there are two ways to improve the predictions of the agglomerate model: (i) by accounting for local diffusion losses by modeling discrete catalyst particles, and (ii) by deriving relations to link the microstructure to macroscale volume fractions.

Next, we present a modified agglomerate approach in Chapter 3 that incorporates the diffusion and electrochemical reactions at the particle level. Then in Chapter 4 the classical agglomerate model is further improved using the sphere-packing approach to model the reduction in agglomerate surface area as the porosity is reduced.

Chapter 3

MODIFIED AGGLOMERATE MODEL WITH DISCRETE CATALYST PARTICLES

The results of Chapter 2 confirmed our observation, based on a review of the agglomerate model literature, that the spherical agglomerate approach is incapable of capturing the effect of catalyst loading on polarization behavior in the mass transport regime. The limitation was attributed to the high diffusion resistance of the ionomer film coupled with the highly reactive agglomerate core. We then showed with our C|Pt model that modeling local diffusion losses by accounting for discrete catalyst particles on the surface of the agglomerate can provide more realistic results.

In this chapter, we first introduce a modified agglomerate approach by representing the catalyst phase as discrete particles distributed throughout the agglomerate core. Next, we present a framework to integrate the modified agglomerate approach within a 3D cathode model.

3.1 Modified Agglomerate Model

A modified agglomerate approach is proposed to overcome the shortcoming of the agglomerate model by representing the catalyst phase as discrete particles distributed throughout the agglomerate core. The modified approach incorporates local mass diffusion effects and electrochemical reactions at the catalyst particle level. In addition, it facilitates an investigation of the effects of random Pt particle distributions.

In this section, the results from our particle-based spherical agglomerate model are compared with the classical spherical agglomerate model. Utilizing the modified

approach, the effect of Pt loading on the agglomerate characteristic curves is examined by varying the size, number, and distribution of the particles. Then, the effect of the discrete particle distribution on Pt utilization is discussed.

3.1.1 Classical Agglomerate Model Description with 2D Cylindrical Approach

The classical approach defines the agglomerate core as a homogeneous mixture of carbon-supported catalyst particles and the electrolyte as shown in Fig. 3.1. A spherically-symmetric 1D representation would suffice to investigate the classical spherical agglomerate configuration. However, for reasons explained later, we have employed a 2D cylindrical treatment in our mathematical analysis.

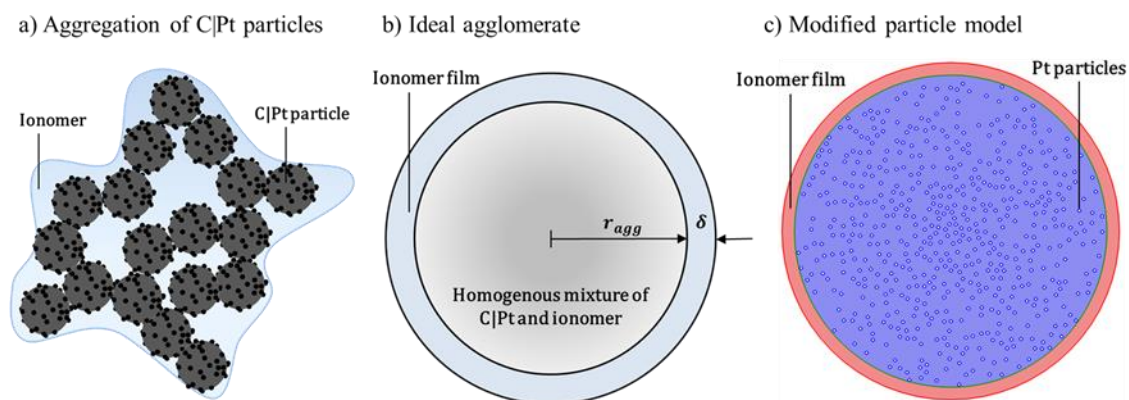


Figure 3.1. Representation of (a) catalyst agglomeration; (b) the homogenous mixture assumption; (c) randomly-located discrete Pt particles

Upon approaching the agglomerate, the reactant dissolves in the ionomer film and diffuses into the agglomerate. Within the ionomer film, the reactant transport is purely diffusive without any reaction. Immediately after reaching the surface of the agglomerate core ($r = r_{agg}$), according to the homogenous mixture assumption, the reactant diffuses into the agglomerate core while simultaneously undergoing reaction. In addition to the homogenous mixture assumption, the process is assumed to be

isothermal due to the low heat generation-to-conduction ratio [95]. A constant local overpotential is also assumed based on the results of [94] which show that the overpotential varies less than 0.01%. With these assumptions, the transport in the ionomer film and in the agglomerate core is described by Eqs. (3.1) and (3.2), respectively.

$$\nabla \cdot (D\nabla C) = 0 \quad (3.1)$$

$$\nabla \cdot (D_{eff}\nabla C) = R_{orr} \quad (3.2)$$

The effective diffusivity (D_{eff}) in the agglomerate core is calculated by employing the Bruggeman relation:

$$D_{eff} = D\epsilon_{agg}^{1.5} \quad (3.3)$$

where ϵ_{agg} is the porosity of the spherical agglomerate core. Diffusivity of oxygen (D) in the ionomer is calculated using [18]:

$$D = 3.1 \times 10^{-3} \exp\left(-\frac{2768}{T}\right) \quad [\text{cm}^2/\text{s}] \quad (3.4)$$

The reaction source (R_{orr}) term is given by Faraday's law as:

$$R_{orr} = a_a \frac{i}{4F} \quad (3.5)$$

where i is the local current density, F is the Faraday constant, and a_a is the active surface area of Pt per unit volume of agglomerate which is calculated as:

$$a_a = \frac{m_{Pt}a}{(1 - \epsilon_v)t_{cl}} \quad (3.6)$$

where a is the specific surface area of Pt, t_{cl} is the thickness of the CL, and ϵ_v is the porosity of the CL.

Generally, the current density (i) resulting from the electrochemical reactions in fuel cells is expressed by the concentration-dependent Butler-Volmer expression:

$$i = i_0 \left[\frac{C_{ox}}{C_{ox}^0} \exp\left(-\frac{\alpha_a n_e F}{RT} \eta\right) - \frac{C_{red}}{C_{red}^0} \exp\left(\frac{\alpha_c n_e F}{RT} \eta\right) \right] \quad (3.7)$$

where n_e is the number of electrons transferred during the ORR's rate-determining step. It should be noted that n_e is not necessarily equal to the total number of electrons transferred during the ORR as was assumed in [56]. In the literature, two Tafel slopes are reported corresponding to $n_e = 1$ and 2 for high and low current regimes, respectively [97]. In this study, we consider only the ORR and assume $n_e = 2$. Neglecting mass transport effects for the backward reaction as in [56], the local current density is calculated as:

$$i = i_0 \left[\frac{C}{C_0} \exp\left(-\frac{\alpha_c 2F}{RT} \eta\right) - \exp\left(\frac{(1 - \alpha_c) 2F}{RT} \eta\right) \right] \quad (3.8)$$

Equations (3.1) and (3.2) are solved in a coupled manner using COMSOL 4.2. For the boundary conditions, surface concentration is defined at the ionomer film surface ($r = r_{agg} + \delta$) where (δ) is the ionomer film thickness. Assuming constant oxygen pressure in the cathode, the dissolved reactant concentration is assigned as the boundary condition at the ionomer film surface and is calculated from Henry's law:

$$C_0 = \frac{P_{O_2}}{H} \quad (3.9)$$

In addition, Eqs. (3.1) and (3.2) are coupled by enforcing flux continuity at $r = r_{agg}$.

The agglomerate current density is calculated based on the approach presented in [56, 94]. Briefly, it is assumed that all of the reactant diffusing into the agglomerate is consumed, and then the agglomerate current is given as:

$$I_a = 4FD \left(\vec{n}_x \frac{dC_{O_2}}{dx} + \vec{n}_y \frac{dC_{O_2}}{dy} \right) \Big|_{x^2+y^2=r_{agg}^2} \quad (3.10)$$

Simulations were conducted with the input parameters listed in Table 3.1.

Table 3.1. Parameters used in simulations [56]

Temperature	T	353.15 [K]
Oxygen pressure	P_{O_2}	1.5 [atm]
Nafion volume fraction in agglomerate	ϵ_{agg}	0.4
CL porosity	ϵ_v	0.4
Pt loading	m_{Pt}	0.4 [mg/cm ²]
CL thickness	t_{cl}	30e-6 [m]
Henry's constant	H	0.3125 [atm m ³ /mol]
Charge transfer constant	α_c	0.5
Exchange current density	i_0	6e-8 [A/cm ²]
Agglomerate radius	r_{agg}	1e-4 [cm]
Ionomer film thickness	δ_{agg}	1e-5 [cm]

As stated earlier, the classical spherical agglomerate model depicted in Fig. 3.1 can be solved in 1D by enforcing spherical symmetry, whereas the modified agglomerate model containing discrete particles would require a full 3D treatment. For the sake of computational efficiency, we instead chose to conduct a 2D simulation for the particle approach. For consistency, we employed the same 2D treatment for the classical agglomerate case as well. Hence, the geometry shown in Fig. 3.1 represents a cylinder rather than a sphere. Figure 3.2 confirms that our 2D approach provides results that are almost identical to the 1D spherically-symmetric model. Therefore, the 2D cylindrical configuration is a very good approximation to the spherically-symmetric agglomerate model.

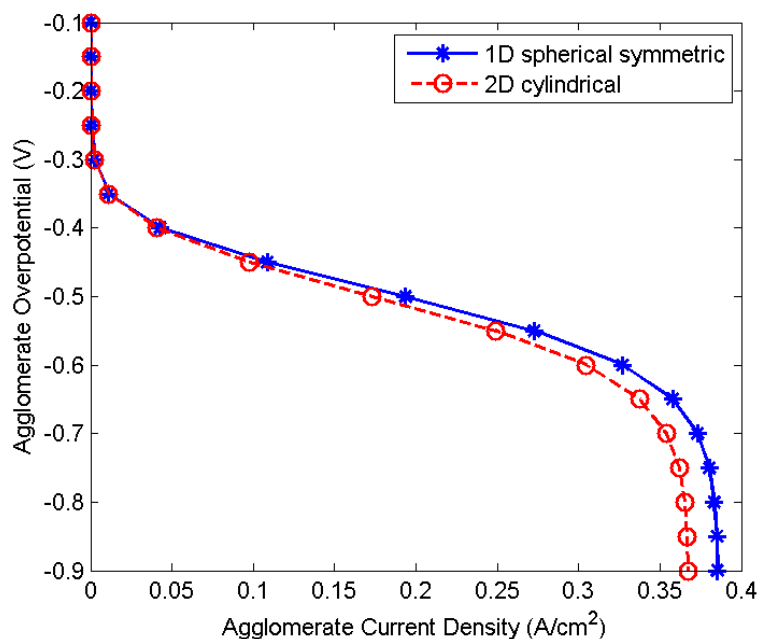


Figure 3.2. Comparison between 2D (cylindrical) and 1D (spherically-symmetric) classical agglomerate models

3.1.2 Particle Agglomerate Model Description

The particle approach proposed in this work employs discrete Pt particles embedded throughout the spherical agglomerate structure. Instead of assuming a homogenous mixture as in the classical approach, the modified agglomerate is assumed to consist of the electrolyte containing randomly distributed Pt particles. Particle parameters that can be easily varied include the particle size, number density, and spatial distribution. We do not account for the existence of carbon particles within the agglomerate because electrical conduction is not considered due to the constant agglomerate overpotential assumption in classical agglomerate models. The Pt particles are modeled as circles with diameters ranging from 5-20 nm as shown in Fig. 3.1 with $r_{agg} = 1 \mu\text{m}$. The particles are placed randomly within the agglomerate without

overlap. As stated earlier, the spherical agglomerate in Fig. 3.1 is approximated as a 2D cylindrical configuration in the following analysis and simulations.

The electrochemical process in the particle approach consists of reactions occurring on the surface of the Pt particles. Therefore, a Neumann boundary condition is applied to describe the flux of reactant consumed at the Pt particle surface. Using Faraday's law, the boundary condition at the surface of the Pt particles is given as:

$$\dot{n} = \frac{i}{4F} \quad (3.11)$$

where the current density (i) is given by Eq. 3.8 as in the classical approach.

To calculate the number of Pt particles, first the area of catalyst per unit volume of agglomerate (a_a), and the specific area of the catalyst (a) are calculated using Eqs. (3.12) and (3.13), respectively.

$$a_a = \frac{N_{Pt} 2\pi r_{Pt} l}{\pi r_{agg}^2 l} \quad (3.12)$$

$$a = \frac{2\pi r_{Pt} l}{\pi r_{Pt}^2 \rho_{Pt} l} \quad (3.13)$$

Here N_{Pt} is the number of particles, and l is the nominal thickness of the 2D domain. Substituting Eqs. (3.12) and (3.13) into Eq. (3.6) and rearranging gives:

$$N_{Pt} = m_{Pt} \frac{r_{agg}^2}{r_{Pt}^2 t_{cl} \rho_{Pt} (1 - \varepsilon_{cl})} \quad (3.14)$$

It is important to note that the same value for specific area of catalyst (a) calculated in Eq. 3.13 is used in the classical model as well. Finally, the agglomerate current density for the particle model is calculated as in the classical model using Eq. 3.10.

3.1.3 Results and Discussion

Simulations are conducted with the modified particle agglomerate model to investigate whether a distribution of discrete Pt particles within the spherical agglomerate can help to improve the response of the agglomerate approach in the diffusion-limited region.

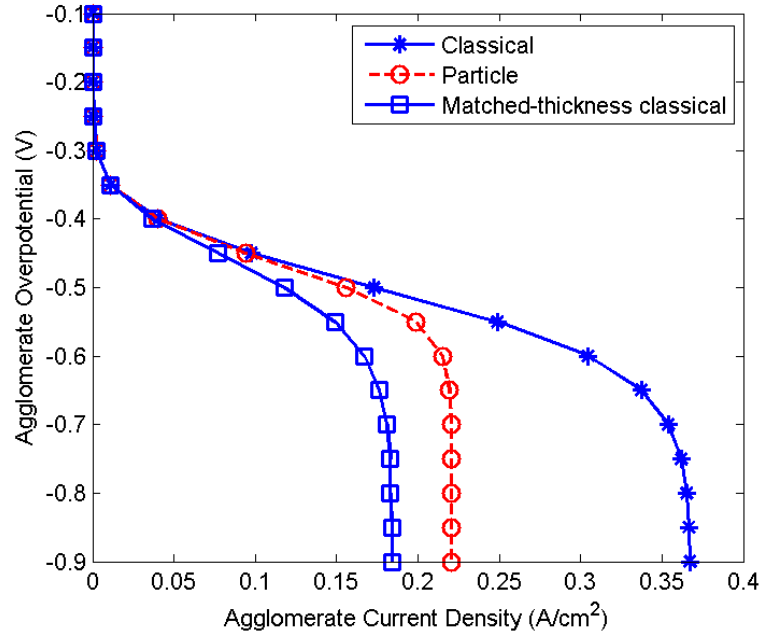


Figure 3.3. Polarization curves for the particle, classical, and matched-thickness classical approaches ($m_{Pt} = 0.4$ [mg/cm²])

The polarization curves presented in Fig. 3.3 indicate that the classical and particle approaches provide nearly identical results in the activation and ohmic regions. In contrast, the curves differ significantly in the diffusion region. The particle model predicts diffusion losses at much lower current densities than the classical model indicating that higher diffusion losses are experienced due to the presence of discrete particles.

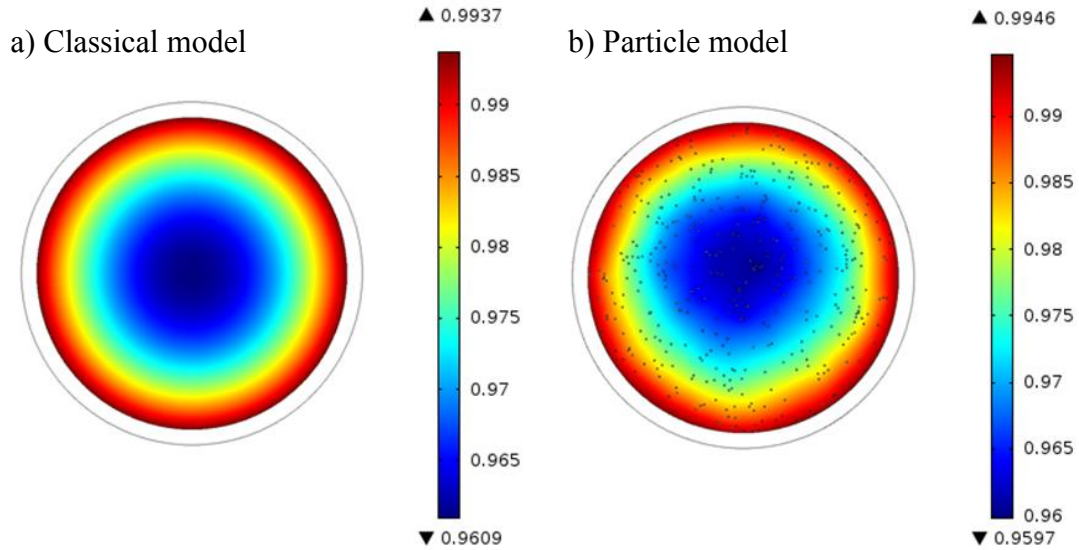


Figure 3.4. Normalized concentration (C_{O_2}/C_0) contours for $\eta = 0.3 V$

In the classical approach the reactant reacts immediately upon entering the agglomerate core, whereas in the discrete particle approach the reactant has to diffuse into the agglomerate core until it reaches the outermost catalyst particles which are the first to participate in the reaction. In order to enable a fair comparison between the classical and modified approaches, it is helpful to calculate the actual film thickness in the discrete particle case by noting the radial locations of the outermost catalyst particles and employ it as the ionomer film thickness in the classical model. The result from the classical approach with matched film thickness is also shown in Fig. 3.3; it is seen that this result is now much closer to the discrete particle result even in the diffusion-limited region. Despite the improved agreement in this instance, it is not possible to fully characterize the effect of the discrete particle distribution only by matching the film thickness in the classical approach. We will show subsequently that the discrete particle approach reveals the importance of diffusion inside the agglomerate core by accounting for particle-level diffusion effects and the particle

distribution, whereas diffusion losses in the classical model arise purely from the ionomer film. Therefore, it is necessary to model the individual catalyst particles to capture the local mass diffusion effects inside the agglomerate.

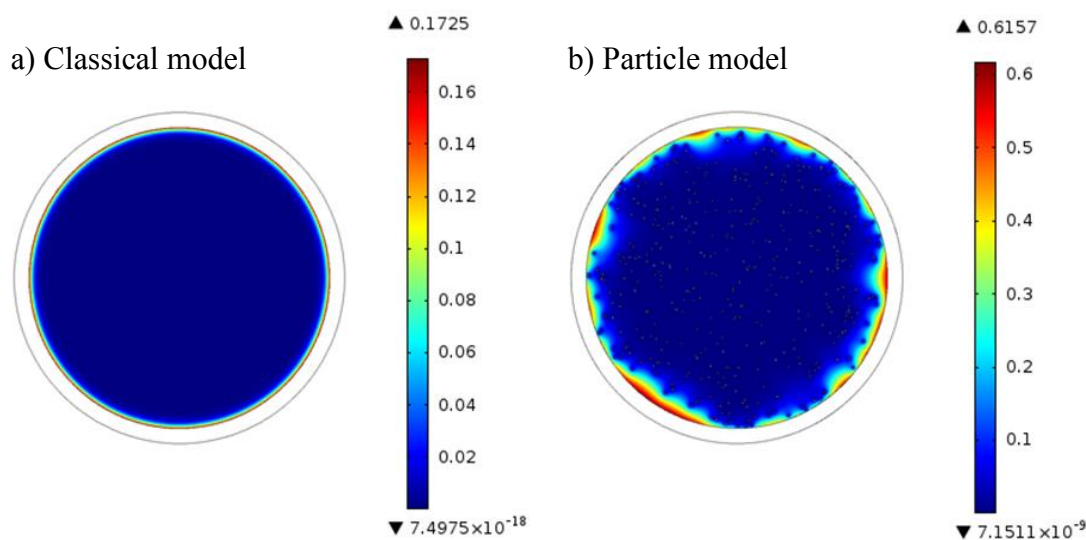


Figure 3.5. Normalized concentration (C_{O_2}/C_0) contours for $\eta = 0.6$ V

Oxygen concentration contours for the two modeling approaches are shown in Figs. 3.4 and 3.5 for low and high discharge levels, respectively. Figure 3.4 shows that both models behave similarly at low discharge levels, whereas for high current densities, the concentration contours are quite different as can be seen in Fig. 3.5. The agglomerate wall concentration (C_s) in Fig. 3.5a for the classical model is less than half of that in Fig. 3.5b for the particle model, indicating that the concentration gradient across the ionomer film, and therefore the diffusive flux into the agglomerate, is higher for the classical model. This difference arises from the presence of discrete Pt particles which is neglected in the classical approach. For the discrete particle case, the reactant must diffuse to the individual active sites to be reacted, whereas it is reacted more readily under the homogenous mixture assumption. Consequently, the ionomer

film in the discrete particle case experiences a smaller concentration gradient, and hence a smaller diffusion loss. On the other hand, a higher diffusion loss is predicted within the agglomerate core due to the particle-level effects as is evident in Figs. 3.3 and 3.5.

The increased significance of diffusion within the agglomerate core due to particle-level effects is investigated next. Accordingly, polarization curves are plotted for three values of reactant diffusivity within the agglomerate core for the classical and particle models in Figs. 3.6a and 3.6b, respectively. Note that the reactant diffusivity within the ionomer film is fixed at the baseline value for these simulations. The polarization curves for the classical model in Fig. 3.6a do not exhibit a significant effect of the diffusivity inside the agglomerate. On the other hand, Fig. 3.6b shows that the performance predicted by the particle approach is strongly dependent on the reactant diffusivity. Comparing Figs. 3.6a and 3.6b indicates that representing the Pt catalyst in the form of discrete particles greatly increases the influence of diffusion inside the agglomerate core due to particle-level effects. Consequently, it leads to the conclusion that particle-level diffusion plays an important role on the rate of the reaction.

High performance at low catalyst loading is highly desirable for the commercialization of PEM fuel cells. A major goal of this study is to examine the effect of catalyst loading with the particle agglomerate model. The catalyst loading is varied by changing the number of Pt particles in the particle approach. The effect of Pt loading as predicted by the classical and particle approaches is presented in Figs. 3.7a and 3.7b, respectively.

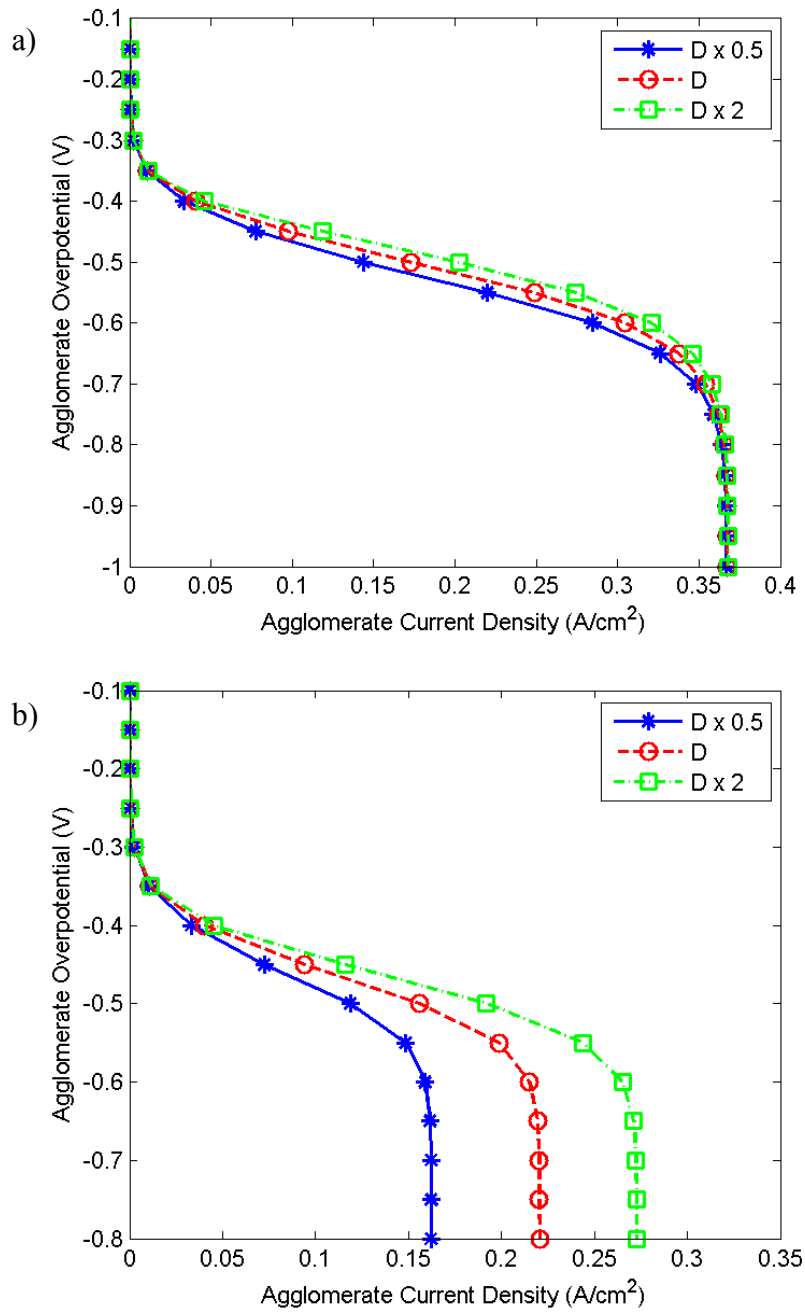


Figure 3.6. Polarization curves for various diffusivities inside the agglomerate core for (a) the classical model, and (b) the particle model

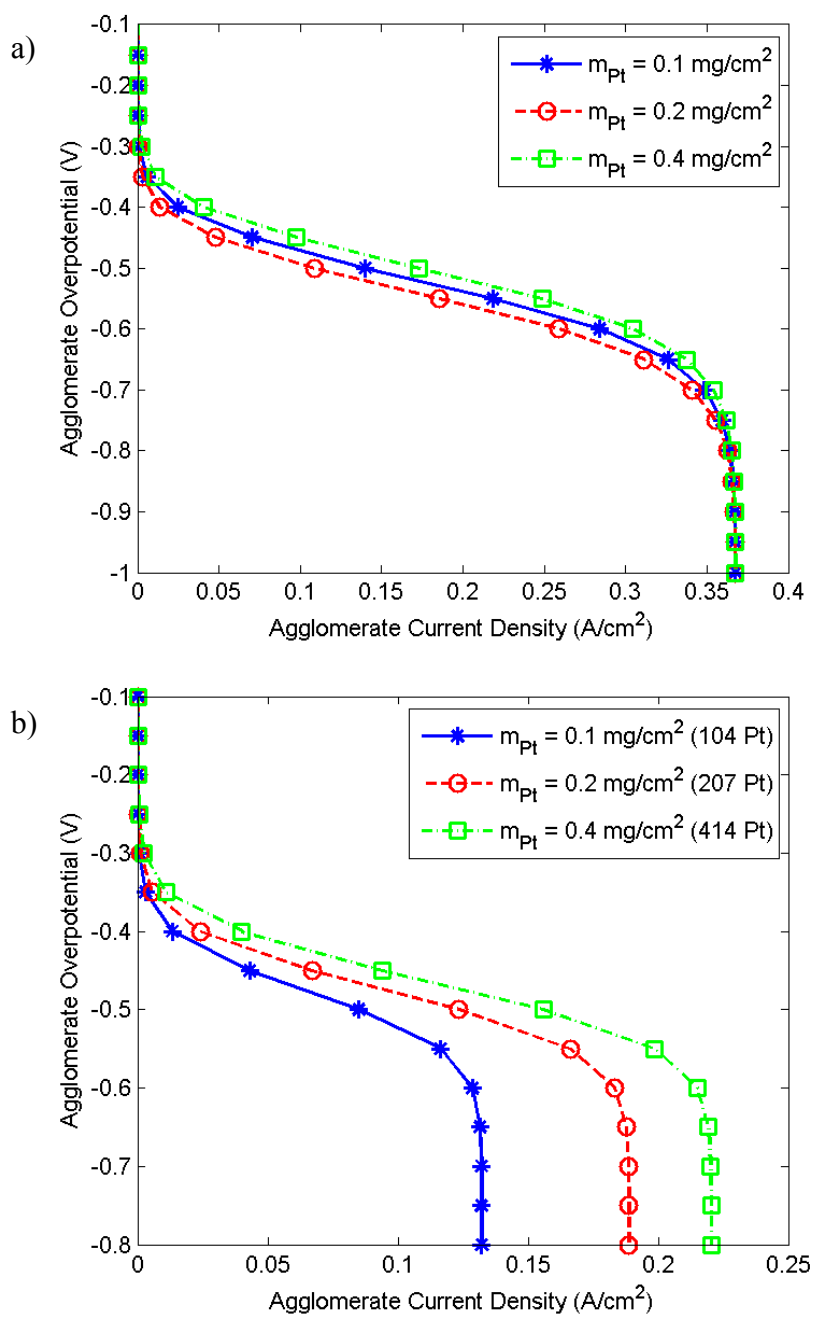


Figure 3.7. Polarization curves for various Pt loadings in mg/cm^2 for (a) the classical model, and (b) the particle model

For a given specific catalyst area, Pt loading directly correlates to the number of active reaction sites. Therefore, one would expect to see a noticeable change in the reaction rate as the Pt loading is varied. However, Fig. 3.7a reveals that, except for the activation region, the Pt loading has almost no effect on the polarization curves in the classical approach. On the other hand, Fig. 3.7b for the particle model shows that the performance is strongly dependent on Pt loading. The inability of the classical model to produce realistic results in the diffusion loss region is attributed to the diffusion limit imposed by the ionomer film that covers the agglomerate. Although the ionomer film exists in the particle model as well, this approach is successful in predicting the effect of Pt loading on performance by accounting for the local particle-level diffusion effects. As previously explained with Figs. 3.6a and 3.6b, the particle-level diffusion limitations influence the reaction-diffusion process inside agglomerate core, due to which the particle model is able to accurately reflect the effect of Pt loading on performance. In contrast, the homogenous mixture assumption results in a highly reactive agglomerate wherein the rate-limiting step for the reaction is imposed by the diffusion loss due to the ionomer film. As a result, except for the expected kinetic variation in the activation loss region, the classical agglomerate model does not display sensitivity to catalyst loading.

In Fig. 3.7a, an increase in the number of particles within the agglomerate was correlated to an increase in reaction surface area. Another way to increase the reaction surface area is to increase the Pt particle diameter while keeping the identical particle distribution as investigated in Fig. 9. In this case, the local diffusion effects due to variations in particle location are eliminated. Therefore, the

results obtained are purely due to the influence of increased reaction surface area on the polarization curve.

Figure 3.8 shows the expected result that larger particles produce better performance due to increased surface area. As this is a 2D simulation, doubling the particle diameter provides the same increase in surface area as doubling the number of particles. However, it should be noted that the performance increase seen in Fig. 3.8 is less than in Fig. 3.7b. Figure 3.5b has already shown that at high current densities the catalyst particles located at the periphery of the agglomerate contribute more to the reaction, whereas particles placed in the interior do not participate as effectively. Consequently, the unequal improvements in performance in Figs. 3.7b and 3.8 highlight the role of particle distribution on the catalyst utilization rate and performance.

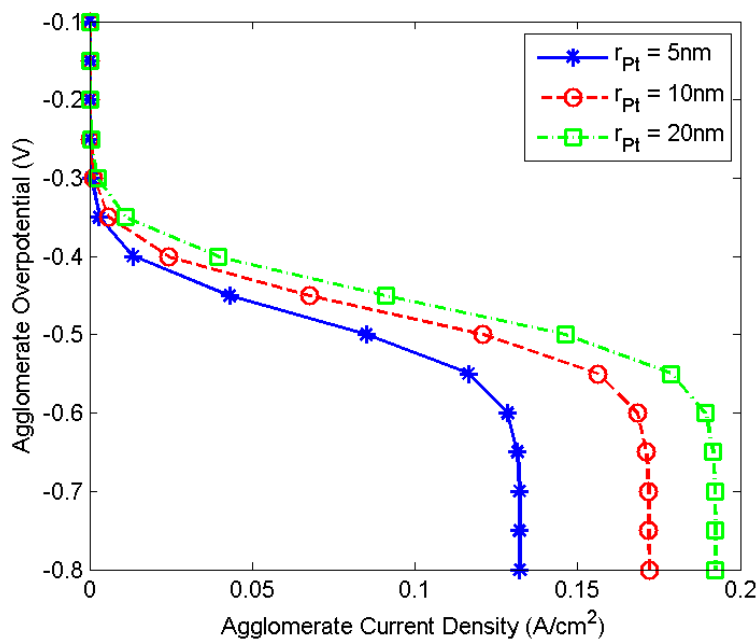


Figure 3.8. Polarization curves with the particle model showing the influence of particle size on performance

Based on the preceding observations, we attempt to improve Pt utilization by concentrating the Pt particles towards the periphery of the agglomerate. Figure 3.9 shows three situations where the same 104 particles are restricted to an annular region at the periphery ($r_{in} < r < r_{agg}$) with $r_{in}/r_{agg} = 0.5, 0.75,$ and 1.0 . The polarization curves for these three situations are shown in Fig. 3.10 along with the homogeneously-distributed case.

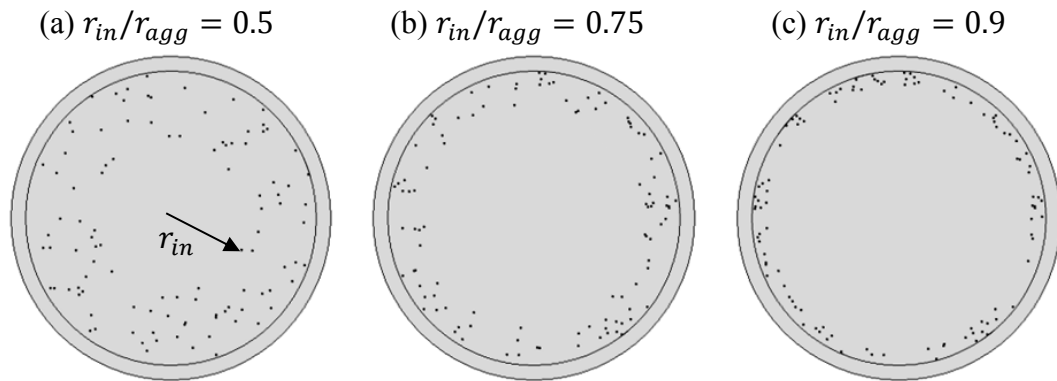


Figure 3.9. Distribution of 104 Pt particles with a higher concentration towards the periphery; r_{agg} is the agglomerate radius, and all particles are located outside the circle with radius = r_{in} .

Figure 3.10 confirms that the performance improves as the particles are concentrated towards the periphery of the agglomerate. Concentrating the particles towards the periphery reduces the diffusion loss and increases the reaction rate. Therefore, the results in Fig. 3.10 identify an important parameter for performance improvement. Because particles in the interior cannot participate in the reaction due to diffusion limitations, Pt utilization can be greatly improved by employing such non-uniform particle distributions.

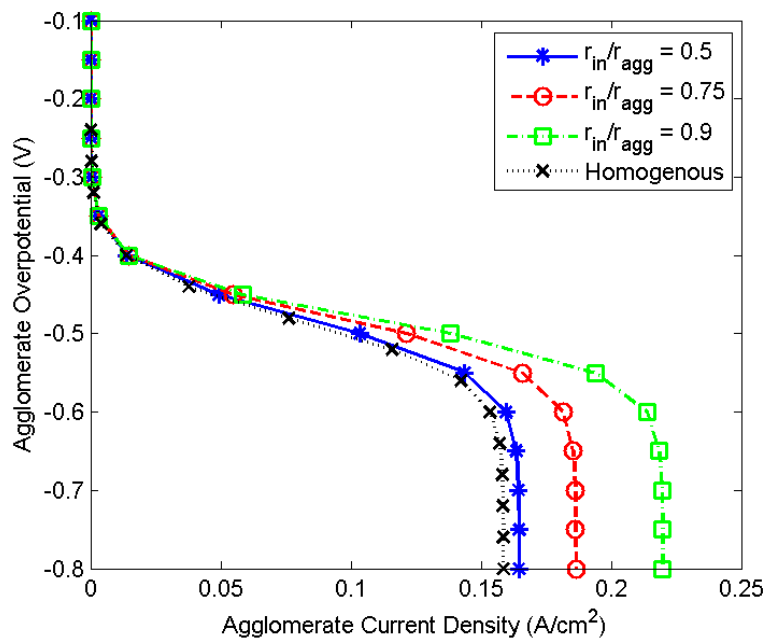


Figure 3.10. Effect of particle concentration towards the agglomerate periphery on the polarization curve

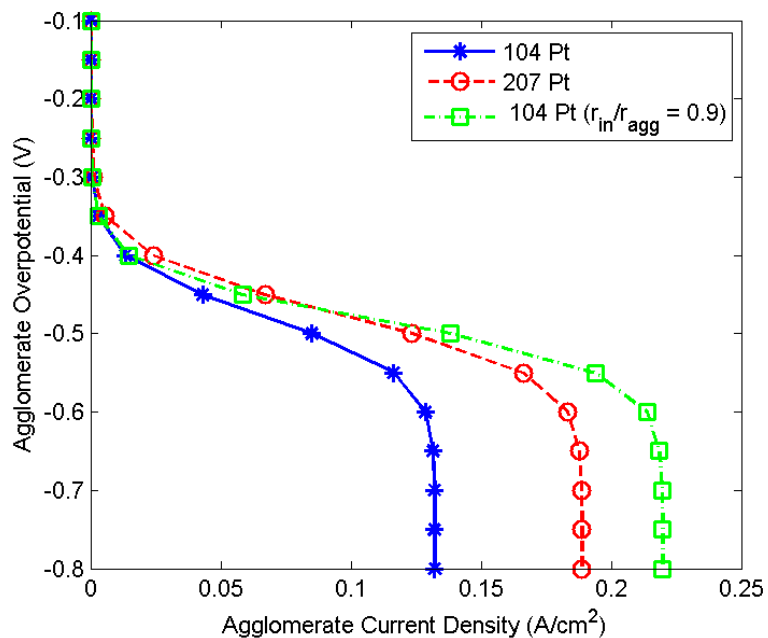


Figure 3.11. Polarization curves for uniform distributions of 104 and 207 Pt particles, and one non-uniform distribution of 104 particles with $r_{in}/r_{agg} = 0.9$.

Next, we use the particle agglomerate model to assess Pt utilization. Three cases are studied in Fig. 3.11: two uniform distributions of 104 and 207 Pt particles, and one non-uniform distribution of 104 particles with $r_{in}/r_{agg} = 0.9$. Figure 3.11 shows that the case with higher loading experiences a lower activation loss as expected. However, in the diffusion-dominated region, the non-uniform case with 104 particles outperforms even the case of 207 uniformly-distributed particles. This result confirms our hypothesis that Pt utilization is highly dependent on particle distribution within the agglomerate.

3.2 3D Cathode Model using a Modified Agglomerate Approach

In the classical approach, the microscale model is coupled to the macroscale model via an analytical expression for volumetric current density ($\nabla \cdot i$) which quantifies the rate of the electrochemical reaction occurring within the CL. However, unlike the classical agglomerate approach, the modified particle approach does not lend itself to an analytical solution which is easily coupled to the macroscale model. Therefore, the coupling method used in [53] has to be modified in order to interface with the numerical results from the discrete particle approach.

Accordingly, in this section a framework is presented to couple the numerical solution obtained from the 2D microscale model with the 3D cathode model. Simply, the numerical solution is expressed as a function of macroscale model variables and then incorporated within 3D cathode model. In addition, we compare the predictions of the macro-homogenous, classical, and modified agglomerate approaches by plotting their polarization curves and current density distributions. Finally, we investigate the sensitivity of the different agglomerate models to Pt loading.

3.2.1 Cathode Model Description

We have implemented a 3D, single channel, isothermal, steady-state cathode model that accounts for the conservation of mass, momentum, chemical species, electrons, and ions. The CL is modeled by the macro-homogenous, classical, and modified agglomerate approaches which will be explained in the subsequent sections. Symmetry in the single channel is exploited to reduce the computational domain such that it encompasses half of the channel and half of the land area as illustrated in Fig. 3.12. The domain dimensions are listed in Table 3.2. The highly-coupled equations that govern the electrochemical and transport phenomena within the cell are solved with the finite element software COMSOL 4.2.

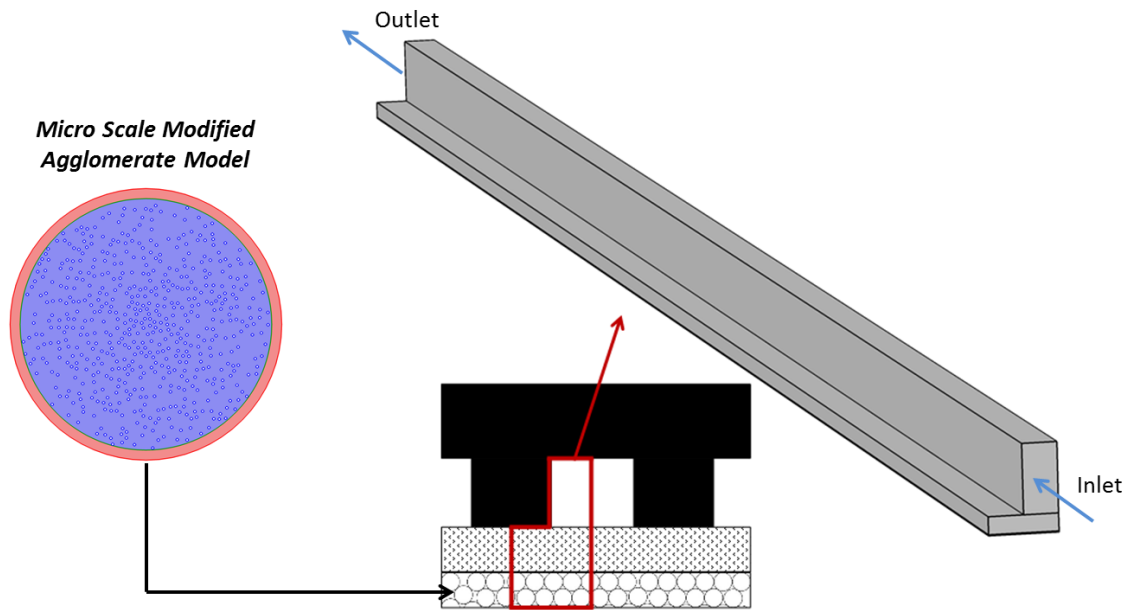


Figure 3.12. Computational domain for the 3D cathode model

Assuming laminar, incompressible flow, mass and momentum conservation in the gas channel are governed by the following equations:

$$\nabla \cdot \mathbf{u} = 0 \quad (3.15)$$

$$\rho(\mathbf{u} \cdot \nabla) \mathbf{u} = -\nabla p + \nabla \cdot \mu(\nabla \mathbf{u} + (\nabla \mathbf{u})^T) \quad (3.16)$$

where \mathbf{u} is the velocity field, p is pressure, ρ is density and μ is dynamic viscosity. In the porous domains (GDL and CL) the flow is described by the Brinkman equation which extends Darcy's law to account for the momentum balance.

$$\rho \nabla \cdot \mathbf{u} = Q \quad (3.17)$$

$$\begin{aligned} \frac{\rho}{\epsilon_v} \left((\mathbf{u} \cdot \nabla) \frac{\mathbf{u}}{\epsilon_v} \right) = & -\nabla p + \nabla \cdot \frac{\mu}{\epsilon_v} (\nabla \mathbf{u} + (\nabla \mathbf{u})^T) \\ & - \nabla \cdot \frac{2\mu}{3\epsilon_v} (\nabla \cdot \mathbf{u}) - \left(\frac{\mu}{k} + Q \right) \mathbf{u} \end{aligned} \quad (3.18)$$

where Q is the mass source term which is calculated from the reactions in the CL, ϵ_v is the porosity, and k is the permeability of the GDL.

The diffusion of oxygen, water vapor, and nitrogen in the cathode is described by using the Maxwell-Stefan equations including the effect of convection.

$$\nabla \cdot \left[-\rho \omega_j \sum_k D_{jk}^{eff} \nabla \frac{\omega_k}{M_k} M_n \right] + \rho(\mathbf{u} \cdot \nabla) \omega_j = R_j \quad (3.19)$$

Eq. (3.19) solves for the mass fraction (ω_j) of each chemical species with R_j representing the source term due to electrochemical reactions in the CL. The diffusion coefficients for different operating conditions can be calculated based on the reference values of binary diffusivities [98]

$$D_{ij} = D_{ij}^{ref} \left(\frac{p_{ref}}{p} \right) \left(\frac{T}{T_{ref}} \right)^{1.75} \quad (3.20)$$

where the reference pressure (p_{ref}) is 1 atm, the reference temperature (T_{ref}) is 298 K, and the reference diffusivities D_{ij}^{ref} used are listed in Table 3.3.

Table 3.2. Geometric parameters for the single channel computational domain

Channel length	L_{ch}	50[mm]
Channel height	h_{ch}	1[mm]
Channel width	w_{ch}	1[mm]
Land width	w_l	1[mm]
GDL thickness	t_{GDL}	250[μm]
CL thickness	t_{CL}	15[μm]

The density of the mixture, which is also used in the mass and momentum conservation equations, is calculated using the ideal gas law as follows.

$$\rho = \frac{M_n P}{RT} \quad \text{where } M_n = \left(\sum_j \frac{\omega_j}{M_j} \right)^{-1} \quad (3.21)$$

The Bruggeman approximation is commonly used to calculate the effective properties of isotropic porous structures. Here, we use this approximation to calculate the effective diffusivities:

$$D_{jk}^{eff} = D_{jk} \epsilon_{v_i}^{1.5} \quad (3.22)$$

where ϵ_i represents the porosity of the corresponding domain. Charge transport by the electron and ion phases is governed by the following equations:

$$\nabla \cdot (\sigma_m^{eff} \nabla \phi_m) = \nabla \cdot i \quad (3.23)$$

$$\nabla \cdot (\sigma_s^{eff} \nabla \phi_s) = -\nabla \cdot i \quad (3.24)$$

where σ_m^{eff} and σ_s^{eff} are the effective ion and electron conductivities, ϕ_m and ϕ_s are ionic and electronic potentials, and $\nabla \cdot i$ is the volumetric current density. The Bruggeman approximation is again used to calculate the effective conductivities:

$$\sigma_j^{eff} = \sigma_j \epsilon_i^{1.5} \quad (3.25)$$

Table 3.3. Binary diffusivities at 1 atm and 298 K [98]

$D_{O_2N_2}^{ref}$	$2.07 \times 10^{-5} [m^2/s]$
$D_{O_2H_2O}^{ref}$	$2.64 \times 10^{-5} [m^2/s]$
$D_{N_2H_2O}^{ref}$	$2.64 \times 10^{-5} [m^2/s]$

The ionic conductivity (σ_m) is dependent on the local water content and temperature. In order to determine the local ionic conductivity we used the empirical relation reported by Springer et al. [9] for Nafion™:

$$\sigma_m = 100(5.139 \times 10^{-3} \lambda - 3.26 \times 10^{-3}) \exp \left[1268 \left(\frac{1}{303} - \frac{1}{T} \right) \right] \quad (3.26)$$

where λ is the local water content which is expressed as a function of local relative humidity as [53]:

$$\lambda = 0.3 + 10.8 \phi_{RH} - 16 \phi_{RH}^2 + 14.1 \phi_{RH}^3 \quad (3.27)$$

where ϕ_{RH} is the local relative humidity.

The effects of the electrochemical reaction on charge and reactant transport are described by the source terms in the governing equations. The O_2 and H_2O source terms in the CL domain (R_{O_2} and R_{H_2O}) are calculated from Faraday's law:

$$R_{O_2} = -\frac{\nabla \cdot i}{4F} \quad (3.28)$$

$$R_{H_2O} = \frac{(\alpha_{OD} + 1) \nabla \cdot i}{2F} \quad (3.29)$$

where α_{OD} is the osmotic drag coefficient which can be written as a function of the nominal cathode overpotential (η_{NCO}) as [53]:

$$\alpha_{OD} = \begin{cases} 1.0 & \eta_{NCO} < 0.25 \\ 46\eta_{NCO}^2 - 31.52\eta_{NCO} + 5.7 & 0.25 \leq \eta_{NCO} \leq 0.35 \\ 0.3 & \eta_{NCO} > 0.35 \end{cases} \quad (3.30)$$

The nominal cathode overpotential (η_{NCO}) can be defined as the measure of total losses (including activation and ohmic losses) in the cathode. It can be expressed as [53]:

$$\eta_{NCO} = \phi_s|_{\text{Current Collector}} - \phi_m|_{\text{Membrane-CL Interface}} \quad (3.31)$$

where the electron potential at the current collector and ion potential at the membrane-CL interface are the boundary conditions for the charge conservation equations. All the boundary conditions are clarified later. Neglecting the losses in anode and membrane, the cathode potential can be expressed as [53]:

$$V_c = E_{th} - \eta_{NCO} \quad (3.32)$$

$$E_{th} = 1.229 - 8.456 \times 10^{-4}(T - 295.15) + 4.31 \times 10^{-5}T \left[\ln(P_{H_2}) - \frac{1}{2} \ln(P_{O_2}) \right] \quad (3.33)$$

3.2.1.1 Spherical Agglomerate Model

Catalyst layer modeling techniques are required to obtain an expression for the volumetric current density ($\nabla \cdot i$) which quantifies the rate of the electrochemical reaction occurring within the CL. As stated earlier, the spherical agglomerate approach is the most comprehensive description of the CL as it accounts for reaction-diffusion phenomena inside the imaginary microstructures called agglomerates. It is a multi-scale approach that ranges from the agglomerate at the microscale to the entire CL at the macroscale.

The mass balance of O_2 in the CL can be written in terms of the agglomerate flux or total reaction rate in the CL as [19]:

$$\nabla \cdot N_{O_2} + a_{agg} N_{O_2}^{agg} = 0 \quad (3.34)$$

$$\nabla \cdot N_{O_2} + R_{O_2}^{total} = 0 \quad (3.35)$$

where a_{agg} is the ratio of total agglomerate surface area to CL volume, $N_{O_2}^{agg}$ is the O_2 flux at the surface of a single agglomerate, and $R_{O_2}^{total}$ is the total reaction rate in CL. Sun et al. [53] tied the microscale agglomerate to the macroscale CL by noting the equality between Eqs. (3.34) and (3.35) and obtained an expression for $\nabla \cdot i$. Kamarajugadda and Mazumder [65] used only Eq. (3.35) to integrate their 3D numerical agglomerate into a 2D device-scale simulation. In this study, we use Eq. (3.34) to derive the volumetric current density because; the goal is to develop a procedure that can be used either for the 2D numerical results of the modified agglomerate model.

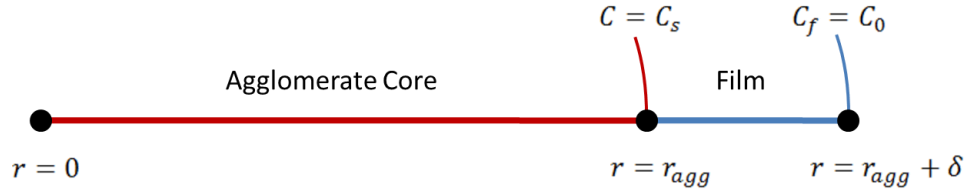


Figure 3.13. 1D spherical agglomerate domain and boundary conditions

The classical agglomerate problem can be summarized as a reaction-diffusion process in the homogenous agglomerate core following the pure diffusion of reactant through the ionomer film. For simplicity, the problem is solved in a 1D spherically-symmetric domain as in Fig. 3.13. The goal is to calculate the reaction rate per unit volume by obtaining the analytical solution of Eqs. (3.36) and (3.37):

$$\frac{D_{eff}}{r^2} \frac{d}{dr} \left(r^2 \frac{dC}{dr} \right) = k_c C \quad \text{in agglomerate core} \quad (3.36)$$

$$\frac{D}{r^2} \frac{d}{dr} \left(r^2 \frac{dC_f}{dr} \right) = 0 \quad \text{in ionomer film} \quad (3.37)$$

where D is the diffusivity of O_2 in the ionomer film which is curve-fitted in [53] using the experimental data of [99] as:

$$D = 0.0438 \exp\left(\frac{-25 \text{ kJ/mol}}{RT}\right) \quad \text{cm}^2/\text{s} \quad (3.38)$$

D_{eff} is the effective diffusivity of O_2 in the agglomerate core which is calculated from the Bruggeman correlation, and k_c is the reaction rate constant given by the Butler-Volmer type expression as:

$$k_c = \frac{a_{Pt}}{4F} \frac{i_0^{ref}}{C_{O_2,ref}} \left[\exp\left(-\frac{\alpha_c F}{RT} \eta\right) - \exp\left(\frac{(1 - \alpha_c) F}{RT} \eta\right) \right] \quad (3.39)$$

where a_{Pt} is the total reaction area per unit volume of agglomerate, i_0^{ref} is the reference exchange current density, $C_{O_2,ref}$ is the standard reference O_2 concentration, α_c is the charge transfer coefficient, and η is the local over-potential in the CL domain. The total reaction area per unit volume of the agglomerate is expressed as:

$$a_{Pt} = A_0 \frac{m_{Pt}}{t_{CL}(1 - \varepsilon_{CL})} \quad (3.40)$$

where A_0 is the catalyst surface area per unit mass, m_{Pt} is the catalyst loading (kg/m^2), and t_{CL} is the thickness of the catalyst layer.

Parthasarathy et al. [99-100] reported two Tafel slopes corresponding to high and low current regimes. In order to account for the variation in Tafel slope, we used two distinct values for the exchange current density (i_0^{ref}), and the charge transfer coefficient (α_c) as given in Table 3.4.

It is important to note that the overpotential within the agglomerate (η_{agg}) is assumed to be constant due to the agglomerate's small size. On the other hand, the macroscale overpotential (η) is a variable governed by the charge transport equations. Selecting the oxygen electrode as the reference electrode with zero potential, the local overpotential in the CL domain can be expressed simply as the difference between the electronic and ionic potentials.

$$\eta = \Phi_s - \Phi_m \quad (3.41)$$

Table 3.4. Parameters used in PEM fuel cell cathode model simulations

Pressure	P	151987.5 Pa
Temperature	T	353 K
Relative humidity	RH	0.5
Stoichiometry	λ_{ST}	2
O ₂ mass fraction	y_{O_2}	0.209
H ₂ O mass fraction	y_{H_2O}	0.102
GDL porosity	ϵ_{GDL}	0.4
CL porosity	ϵ_v	0.1
Ionomer vol. fraction in agglomerate	ϵ_{agg}	0.5
GDL permeability	k_{GDL}	$1.45e - 11 \text{ m}^2$
CL permeability	k_{CL}	$1.45e - 11 \text{ m}^2$
Platinum loading	m_{Pt}	$4e - 3 \text{ kg/m}^2$
Platinum particle radius	r_{Pt}	$5e - 9 \text{ m}$
Agglomerate radius	r_{agg}	$1e - 6 \text{ m}$
Effective agglomerate area	a_{agg}	$3.6e5 \text{ m}^2/\text{m}^3$
Ionomer film thickness	δ	$80e - 9 \text{ m}$
Reference O ₂ concentration	$C_{O_2,ref}$	0.85 mol/m^3
Henry's constant	H	$31663 \text{ Pa m}^3/\text{mol}$
Reference exchange current density	$i_{0,ref}$	$3.86e - 4 \text{ A/m}^2$ for $V_c \geq 0.8 \text{ V}$ $1.46e - 2 \text{ A/m}^2$ for $V_c \leq 0.8 \text{ V}$
Cathodic transfer coefficient	α_c	1 for $V_c \geq 0.8 \text{ V}$ 0.617 for $V_c \leq 0.8 \text{ V}$
Electron conductivity	σ_s	100 S/m

Using the solution procedure outlined in [94] the O_2 concentration within the agglomerate core and the ionomer film (solutions for Eqs. 3.36 and 3.37) are given by:

$$C(r) = C_s \frac{\sinh\left(Th \frac{r}{r_{agg}}\right)}{\frac{r}{r_{agg}} \sinh(Th)} \quad \text{in the agglomerate core} \quad (3.42)$$

$$C_f(r) = \frac{\left(-D_{eff} \frac{dC}{dr}\right) r_{agg}^2}{D} \left(\frac{1}{r} - \frac{1}{r_{agg} + \delta}\right) + C_0 \quad \text{in the ionomer film} \quad (3.43)$$

where Th is the dimensionless Thiele modulus defined as the ratio of the surface reaction rate and the diffusion rate through the catalyst pellet:

$$Th = r_{agg} \sqrt{\frac{k_c}{D_{eff}}} \quad (3.44)$$

Referring back to Eq. 3.34 and Fig. 3.13, the reactant flux on the agglomerate core surface can be written in terms of reactant concentrations using Fick's law for the 1D spherically-symmetric domain as:

$$N_{O_2}^{agg} = D \frac{r_{agg} + \delta}{r_{agg}} \left(\frac{C_0 - C_s}{\delta}\right) \quad (3.45)$$

where C_s can be expressed in terms of C_0 using Eqs. (3.42) and (3.43) as:

$$C_s = \frac{C_0}{1 + \frac{D_{eff}}{D} \left(\frac{\delta}{r_{agg} + \delta}\right) (Th \coth(Th) - 1)} \quad (3.46)$$

Similar to the overpotential, C_0 is assumed constant for a given agglomerate, whereas it varies across agglomerates within the macroscale CL domain. Within the macroscale domain, C_0 can be found by Henry's law as:

$$C_0 = \frac{P_{O_2}}{H} \quad (3.47)$$

where P_{O_2} is the partial pressure of O_2 , and H is Henry's constant. Finally, using Faraday's law and Eq. (3.34), the volumetric current density is obtained as follows:

$$\nabla \cdot i = -4F \nabla \cdot N_{O_2} = 4F a_{agg} N_{O_2}^{agg} \quad (3.48)$$

$$\nabla \cdot i = 4F a_{agg} \frac{P_{O_2}}{H} \left(\frac{\frac{D_{eff}}{r_{agg}} (Th \coth(Th) - 1)}{1 + \frac{D_{eff}}{D} \left(\frac{\delta}{r_{agg} + \delta} \right) (Th \coth(Th) - 1)} \right) \quad (3.49)$$

Equation (3.49) includes two macroscale variables, P_{O_2} and η (embedded in the Th term), which are related to the microscale parameters C_0 and η_{agg} . All the remaining parameters are constants relating to the material and geometric properties of the microstructure. So Eq. (3.49) gives the current generation per unit volume of the CL in terms of reactant concentration and overpotential by representing the effect of CL microscale agglomerate structure (without solving the microscale problem).

3.2.1.2 Modified Agglomerate Model

In the modified approach, the reaction-diffusion problem needs to be solved numerically, whereas the classical model has an analytical solution. Therefore, the micro to macroscale coupling procedure here is based on a numerical solution.

Equation (3.49) can now be applied to accept numerical results from the modified microscale model. The goal is to couple the modified model in a way that eliminates the need to numerically solve for the microscale model at every grid point. Equation (3.48) indicates that we need to solve for $N_{O_2}^{agg}$ at the microscale in order to obtain the local value of the current generation per unit volume of the CL. Furthermore, Eq. (3.49) indicates that $N_{O_2}^{agg}$ can be expressed as a function of microscale parameters C_0 and η_{agg} , which can be written in terms of macroscale

parameters P_{O_2} and η . So we simulated the modified microscale model for various values of C_0 and found that $N_{O_2}^{agg}$ varies linearly with C_0 , and also with the macroscale parameter P_{O_2} . We conducted the simulations for agglomerate overpotentials η_{agg} between 0 and 1 V and obtained a curve (called the agglomerate characteristic curve) for $N_{O_2}^{agg}$ vs. η_{agg} . Next, we fitted a polynomial to this characteristic curve and expressed it in terms of C_0 . Finally, the volumetric current density of the CL was obtained as:

$$\nabla \cdot i = 4F a_{agg} \frac{P_{O_2}}{H C_{0,ref}^{agg}} f(\eta) \quad (3.50)$$

where $C_{0,ref}^{agg} = 8 \text{ mol}/\text{m}^3$ is the reference C_0 value, and $f(\eta)$ is the polynomial fit to the $N_{O_2}^{agg}$ vs. η_{agg} characteristic curve.

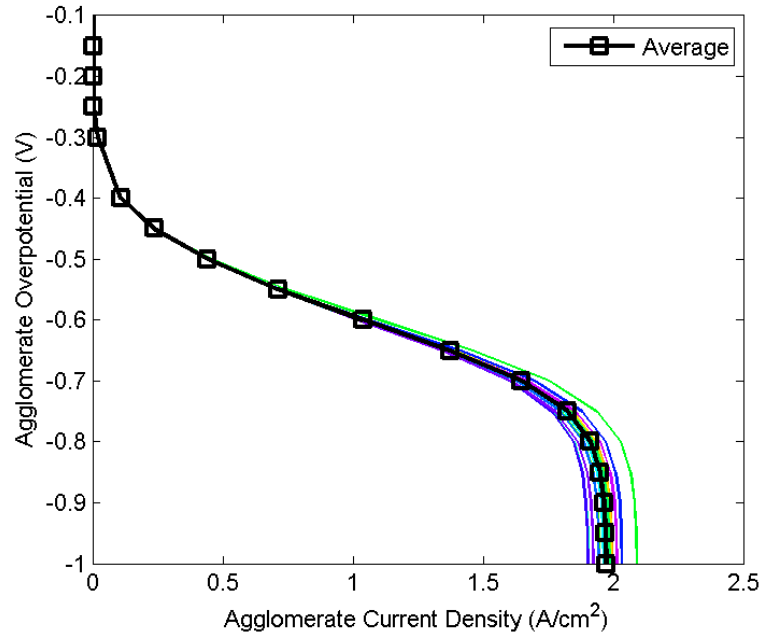


Figure 3.14. Agglomerate polarization curves from the modified approach for 20 different random particle distributions ($m_{pt} = 0.4 \text{ mg}/\text{cm}^2$)

It is important to note that the characteristic curves for the modified agglomerate model vary in the diffusion-limited region, as shown in Fig. 3.14, depending on the specific distribution of catalyst particles in the agglomerate core. This is because variations in the randomly-generated distributions result in differences in diffusion at the particle level, leading to different limiting currents as explained in the previous section. Hence it is necessary to average the results across an adequate number of samples with random distributions. We investigated samples containing 10, 20 and 30 random distributions of catalyst particles and obtained standard deviations of their limiting current densities as 0.048, 0.044, and 0.0441 A/cm^2 , respectively. It was decided that a sample size of 20 was adequate to obtain a reliable average of the diffusion-loss behavior of agglomerates as shown in Fig. 3.14.

We assessed the accuracy of the modified agglomerate model as shown in Fig. 3.15. First, we validated our COMSOL code by comparing our numerically obtained polarization curve for the 1D spherically-symmetric agglomerate model with its analytical solution. As Fig. 3.15 indicates, the comparison is perfect. Next, we investigated the loss in accuracy incurred by using a 2D cylindrical agglomerate approximation in place of a spherically symmetric one. As previously mentioned, the 2D formulation is preferred as it is computationally more efficient. Figure 3.15 shows that the polarization curve from the 2D simulation differs from the analytical solution in the diffusion loss region, but the difference is acceptably small. Next, we plot the polarization curve obtained with the discrete particle model. It is immediately apparent that our modified particle approach predicts much higher diffusion losses compared to the classical approach. This is because the outermost particles in a random distribution may be situated some distance away from the ionomer film (see Fig. 3.1) leading to a

higher effective film thickness, and hence higher diffusion losses. Accordingly, when we reduced the thickness of the ionomer film in the discrete particle model, we found that it was possible to match the limiting current predicted by the classical model. Such a tuning process is employed by many other modeling studies which adjust agglomerate structural parameters to match experimental results.

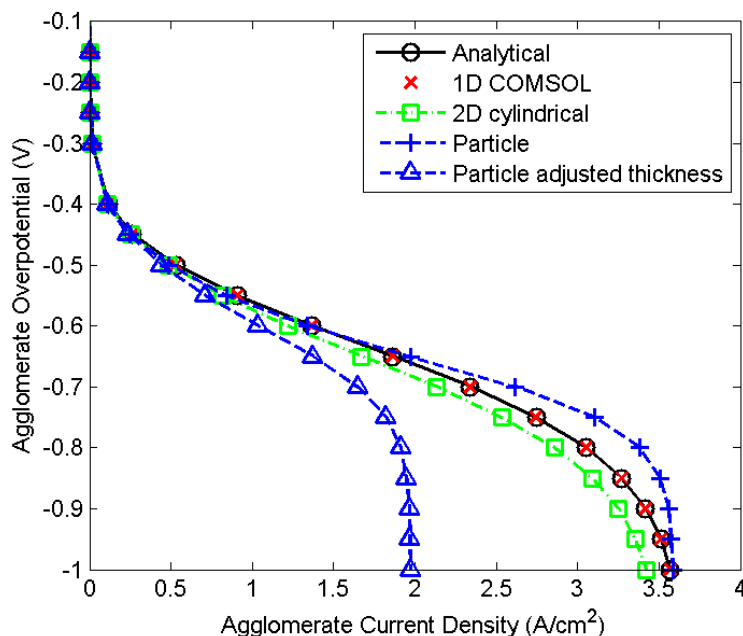


Figure 3.15. Agglomerate polarization curves for various microscale models

3.2.1.3 Macro-homogenous Model

In order to show the importance of multiscale modeling, we will also compare the agglomerate model results with the macro-homogenous model. The macro-homogenous model does not consider a microscale structure for the CL; instead, the CL is represented using an effective medium theory for which it is only necessary to calculate the effective diffusion properties for charge and species transport. The volumetric current density is then calculated from the Butler-Volmer equation. The

area term a_{scale} is used as a fitting parameter as in [37] to match results with the agglomerate models.

$$\nabla \cdot i = a_{scale} i_0^{ref} \frac{C_{O_2}}{C_{O_2,ref}} \left[\exp\left(-\frac{\alpha_c F}{RT} \eta\right) - \exp\left(\frac{(1 - \alpha_c) F}{RT} \eta\right) \right] \quad (3.51)$$

3.2.1.4 Boundary Conditions and Model Parameters

The model parameters and operating conditions for our simulations are provided in Table 3.4. For the conservation of mass and momentum, a laminar inflow boundary condition was used with a specified inlet velocity, and an outlet pressure was specified as the outflow boundary condition. The air inlet velocity is calculated from the operating conditions listed in Table 3.4. The mass fractions at the air inlet are also calculated from the given operating conditions and used to specify the inlet boundary conditions for the Maxwell-Stefan equations. For the diffusion of electrons, we set $\eta = 0$ along the surface of the current collector rib, and zero flux at the membrane/CL interface. For ionic charge transport, the ion potential at the current collector is set to zero, whereas the ion potential at the membrane/CL interface is set to η_{NCO} . Symmetry boundary conditions are applied as appropriate in the transverse ($x - z$) plane (see Fig. 3.12) for each governing equation.

3.2.2 Results and Discussion

First, we focus on the general trends obtained with the 3D single channel cathode model using the modified agglomerate approach (with adjusted film thickness). The goal is to confirm that the coupling works properly. Subsequently, we will compare our 3D cathode model results coupled using the modified agglomerate model approach

with the 3D cathode model coupled to the classical agglomerate model and the macro-homogenous model.

Mass fraction contours of O_2 and H_2O (vapor) are presented for the diffusion-loss regime in Figs. 3.16a and 3.16b, respectively. As expected, O_2 is being depleted as it passes through the channel. In addition, the O_2 concentration is always higher under the channel than under the land, which implies a higher reaction rate under the channel. Again as expected, the product water vapor concentration increases towards the outlet of the channel.

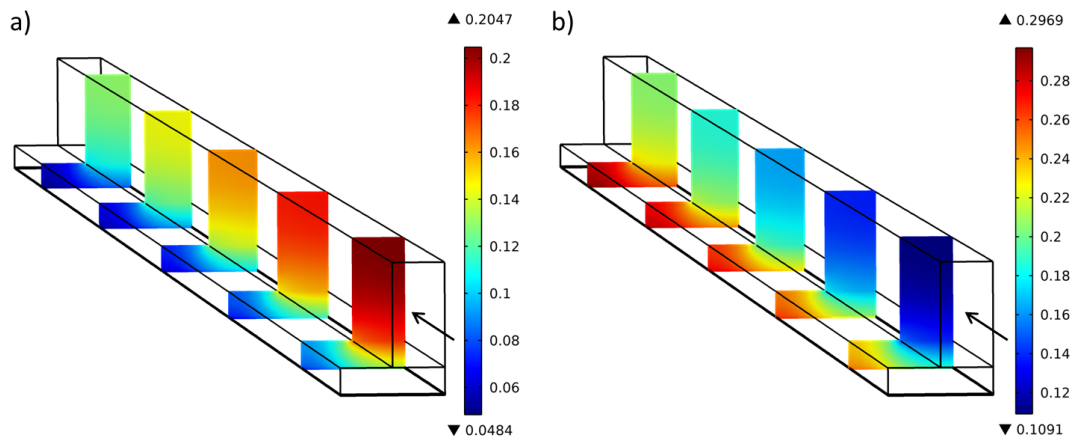


Figure 3.16. Mass fraction distribution in the cathode at $V_c = 0.2 V$ (a) O_2 , and (b) H_2O . The cross-section includes the channel, the GDL, and the CL

Figure 3.17 shows the overpotential distribution through the CL thickness under three different operating regimes. Consistent with the results in [53], the overpotential distributions in Fig. 3.17 are seen to be nonuniform. As in [53], the overpotential is always higher under the land because of shorter electron paths that reduce ohmic losses. The difference in overpotential between the land and channel regions increases with reaction rate because the ohmic losses become more noticeable

at higher current densities. It is also important to note that reaction rate, and so the current density distribution, is an exponential function of overpotential. Therefore, even the small variations shown in Fig. 3.17 can significantly affect the current density distribution.

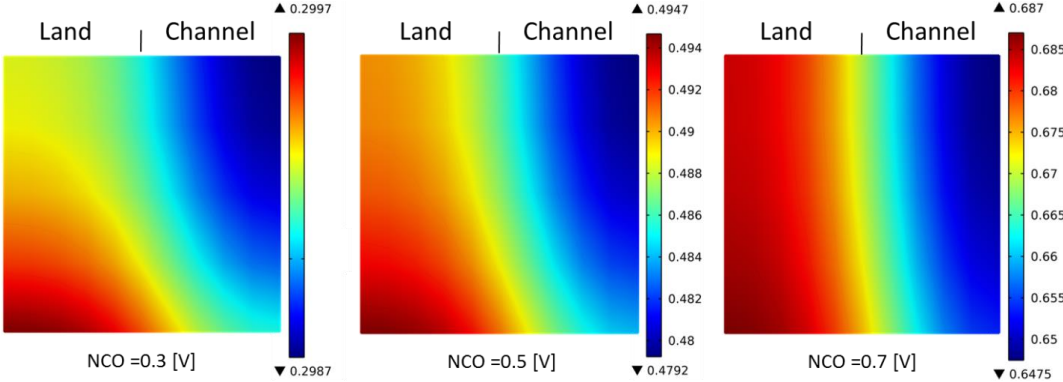


Figure 3.17. Cathode overpotential (φ) distribution across the CL thickness from the modified agglomerate approach along the transverse ($x - z$) plane at $y = 0.95L_{ch}$. The bottom boundary of the plot corresponds to the CL/membrane interface.

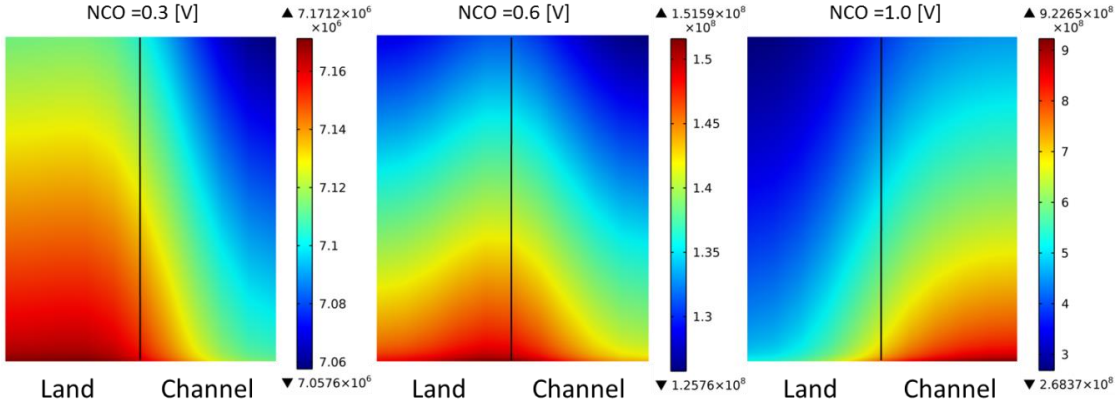


Figure 3.18. Volumetric current density along the membrane/CL interface ($x - y$ plane) [A/m^3]

Volumetric current density is plotted along the longitudinal ($x - y$) plane occupied by the membrane/CL interface in Fig. 3.18 for three different operating

regimes. At low current densities ($NCO = 0.3 V$), the reaction rate is slow enough that O_2 diffusion is not the limiting factor. Therefore, the reaction rate is maximized under the land due to reduced ohmic losses as shown in Fig. 3.18. On the other hand, at high current densities ($NCO = 1.0 V$), mass transport losses begin to dominate and hence the highest reaction rates occur under the channel region. Finally, at intermediate current densities ($NCO = 0.6 V$), Fig. 3.18 indicates that the reaction zone straddles the junction between the land and channel owing to roughly equal contributions from ohmic and mass transport losses; in fact, the reaction rate is maximized at the corner of the land. In addition, Fig. 3.18 also shows the effect of mass transport loss along the channel. In all cases, the reaction rate decreases away from the inlet, and the longitudinal gradient increases with η_{NCO} .

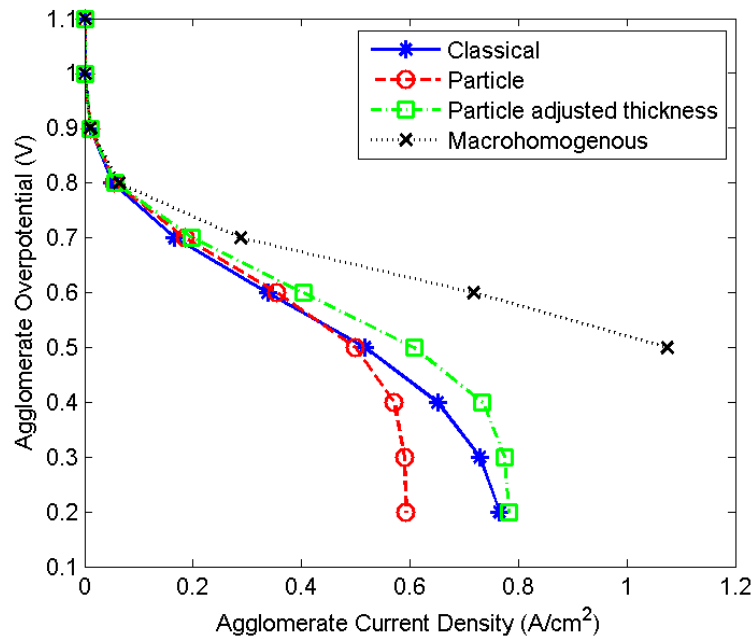


Figure 3.19. Comparison of polarization curves for the 3D cathode obtained with different CL modeling approaches

Results presented thus far show that the coupled modified agglomerate approach is successful at providing the expected results for the 3D PEM fuel cell cathode. Figure 3.19 presents polarization curves predicted by the classical spherical agglomerate model, the particle model with and without matched ionomer film thickness, and the macro-homogenous model. It is seen that the macro-homogenous model cannot produce realistic predictions in the mass transport limited region due to an absence of microscale structure that could account for the dissolution and diffusion of reactant in the ionomer. On the other hand, the classical agglomerate model is able to capture the sharp drop-off in current density in the mass transport limited region as seen in Fig. 3.19. It should be noted that the ionomer film is the only diffusion-loss mechanism for the classical agglomerate which neglects the significance of diffusion inside the agglomerate core. On the other hand, the modified particle approach correctly accounts for the significance of diffusion inside the agglomerate core by considering a discrete distribution of particles. Therefore, the particle approach predicts an earlier and sharper drop-off of voltage in the mass transport limited region than the classical approach. However, Fig. 3.19 shows that when the ionomer film thickness is adjusted in the modified model to match that of the classical model, the overall performances are comparable. Hence, for the comparison purposes, it is appropriate to match the film thickness.

Next we compare the predictions of current density distribution by the three models along a transverse line on the membrane/CL interface close to the outlet. We investigated the ohmic and mass transport loss regions in Figs. 3.20 and 3.21, respectively. Figure 3.20 indicates that for the ohmic region, all models predict the highest current density close to the corner of the land. It is also seen that the classical

and the modified agglomerate model predictions are close to each other throughout. However, while the agglomerate models show a higher current density under the channel, the macro-homogenous model predicts a higher current density under the land. For the mass transport region in Fig. 3.21, the modified agglomerate model behaves identically with the classical approach. While the agglomerate model predicts the highest current densities under the channel due to mass transport limitations, the macro-homogenous approach continues to predict the highest current density close to the corner. As mentioned earlier, the predictions of the macro-homogenous approach in Figs. 3.20 and 3.21 are not realistic because it does not account for the dissolution and diffusion of reactant in the ionomer.

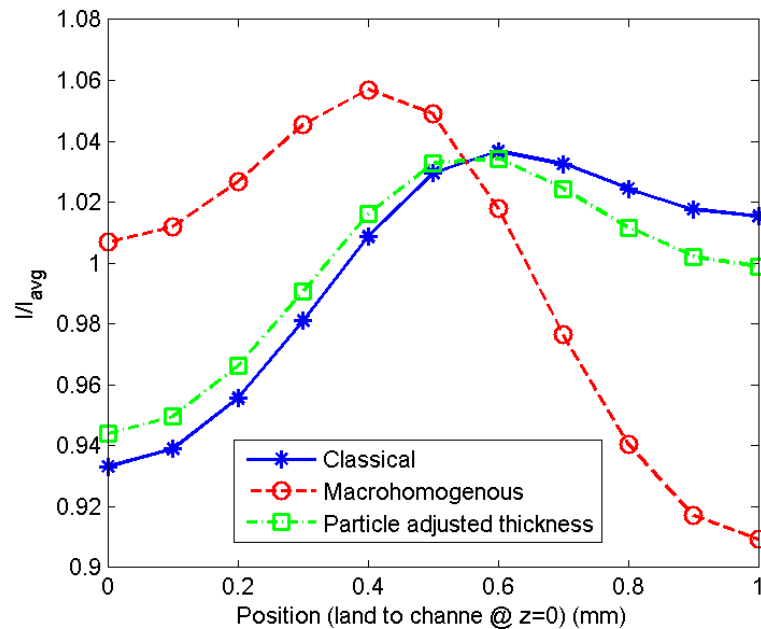


Figure 3.20. Comparison of current density distribution from different CL modeling approaches along a line at the membrane/CL interface at $y = 0.98L_{ch}$ and $I_{avg} = 0.4 A/cm^2$

Finally, we investigated the effects of Pt loading on the polarization curve. Figures 13 and 14 show the effect of Pt loading on polarization curves as predicted by the classical and modified agglomerate models, respectively. Although the trends are similar for both models in the activation and ohmic loss regions, the predictions diverge in the mass transport region. The classical agglomerate model predicts nearly identical limiting currents as in [53] despite a fourfold increase in Pt loading as seen in Fig. 3.22. This is because diffusion losses in the classical agglomerate model are dominated by the ionomer film which imposes the same limiting current irrespective of Pt loading inside the core. On the other hand, experimental results in [69-71] show that Pt loading affects the performance and the limiting current. The modified approach correctly accounts for the significance of diffusion inside the agglomerate core by modeling the particle-level effects. Therefore, the particle model is sensitive to Pt loading in the mass transport loss region as shown in Fig. 3.23.

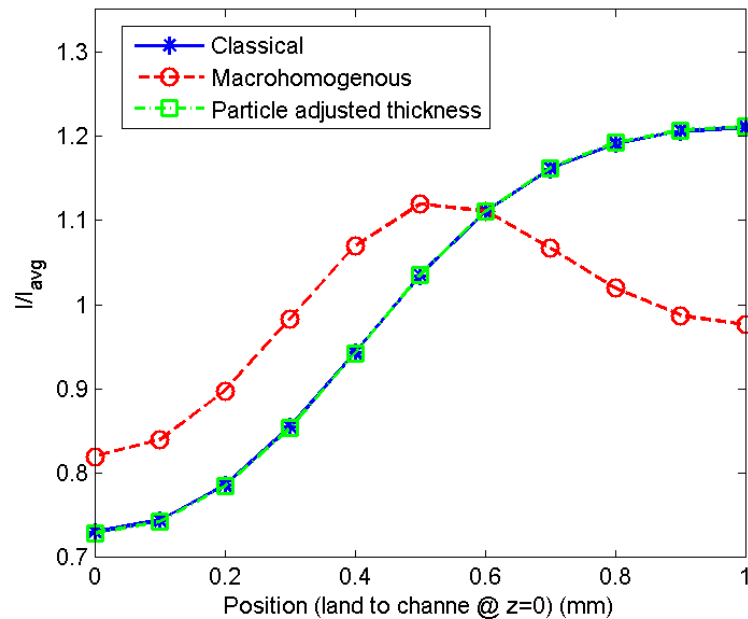


Figure 3.21. Comparison of current density distribution from different CL modeling approaches along a line at the membrane/CL interface at $y = 0.98L_{ch}$ and $I_{avg} = 0.77 \text{ A/cm}^2$

As previously mentioned in Chapter 2, it is possible to obtain different limiting currents even with the classical agglomerate model by setting relations between the agglomerate and CL structural parameters. For instance, Refs. [55, 60, 68] incorporated changes in the CL structure by varying the number of agglomerates per unit volume which concurrently changes the total effective agglomerate surface area (a_{agg}). However, none of these is equivalent to incorporating the effect of particle-level diffusion losses in the microscale model.

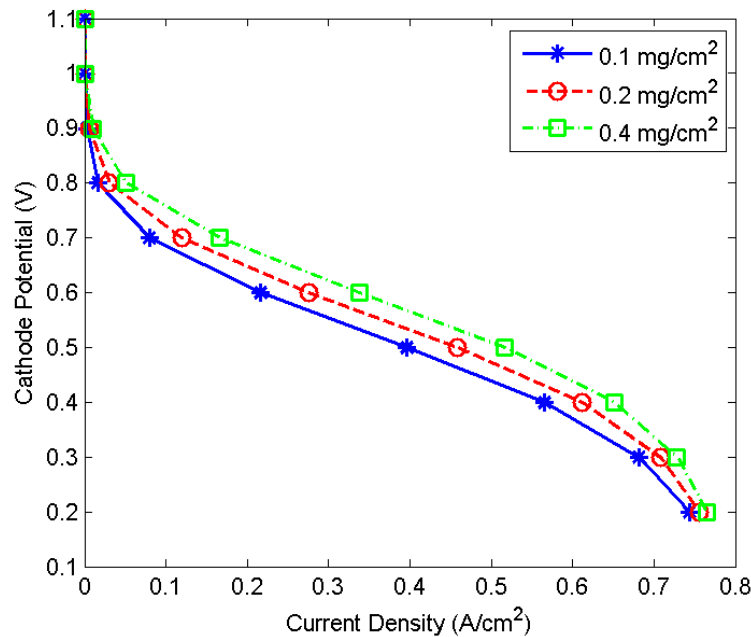


Figure 3.22. Polarization curves for various Pt loadings (mPt) in mg/cm^2 predicted by the classical agglomerate model

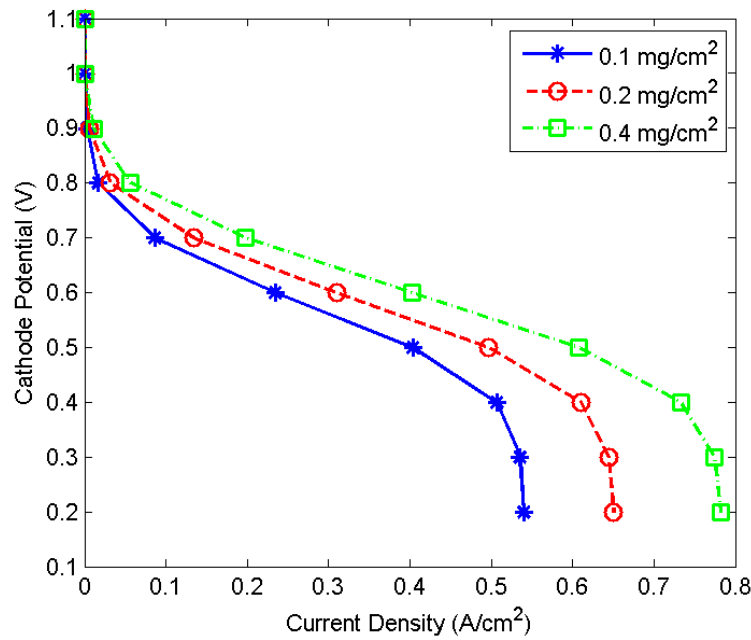


Figure 3.23. Polarization curves for various Pt loadings (mPt) in mg/cm^2 predicted by the modified agglomerate model

3.3 Summary

In this chapter, a modified particle agglomerate model was developed which employs discrete catalyst particles distributed throughout the agglomerate core to investigate particle-level diffusion effects which are neglected due to the homogenous mixture assumption of classical model. Next, the microscale-to-macroscale coupling procedure employed in the classical agglomerate approach in [53] was modified to permit the use of numerical results from microscale model. Then the modified agglomerate approach was employed to build a 3D model for the PEM fuel cell cathode.

In comparison to the discrete particle approach, it was shown that the classical homogenous mixture assumption results in a highly reactive agglomerate core wherein the diffusion resistance imposed by the ionomer film determines the overall rate of the reaction. Therefore, the classical agglomerate model becomes insensitive to Pt loading

except for a small effect in the activation loss region. In contrast, the discrete particle approach recognizes the importance of the diffusion-reaction process inside the agglomerate core by accounting for particle-level diffusion effects and the effect of catalyst distribution, and can provide realistic estimates for catalyst utilization within the agglomerate core. Consequently, in contrast to the classical model, the modified particle approach is sensitive to catalyst loading and distribution in both the activation and diffusion-loss regimes. It was also shown that Pt utilization could be greatly improved by concentrating the catalyst particles in a narrow annular band at the periphery of the agglomerate.

The novel 3D cathode model was found to produce expected results for species concentration, overpotential, and reaction rate distributions in the cathode. By comparing the predictions of the modified model with the classical and macro-homogeneous models, it was shown that the modified approach provided results that matched with the classical approach under all operating regimes. However, the macro-homogenous model, which ignores the importance of microscale effects, fails to successfully predict mass transport losses. In addition, the modified approach was shown to be superior to the classical approach in predicting the effect of Pt loading inside the agglomerate core.

Next, in Chapter 4, we present an improvement to the classical agglomerate model using the sphere-packing approach to accurately model the agglomerate surface area as a function of CL porosity.

Chapter 4

IMPROVED AGGLOMERATE MODEL WITH ACCURATE SURFACE AREA CALCULATION BASED ON SPHERE PACKING APPROACH

A key requirement for CL models is that they should be able to capture the effects of CL composition variations. In Chapter 2 it was shown that the classical agglomerate model is unable to properly predict the effects compositional variation on polarization behavior in mass transport regime. In Chapter 3, we addressed this issue by replacing the homogenous mixture within the agglomerate core with discrete catalyst particles. However, this approach is relatively expensive as the microscale model has to be solved numerically.

Instead of modifying the microstructure, another way to obtain the desired compositional effects is to set relations between the agglomerate and macroscale volume fractions as reported in Chapter 2. A good starting point is the relations proposed in [54, 55]. Yin [54] employed relationships which caused the ionomer film thickness δ to decrease as $Pt|C$ was increased while maintaining a constant CL porosity ϵ_v , agglomerate radius r_{agg} , and ionomer volume fraction ϵ_{agg} . In Yin's study [54], δ can approach zero such that the agglomerate model behaves like the macro-homogenous model, so it fails to predict the limiting current in such cases. Moreover, contrary to Yin's [54] assumption, it is reported that the ionomer fills the pores between agglomerates (the secondary pores) first [101], implying that $\delta \neq 0$. Secanell et al. [55] incorporated changes in the CL structure by varying the number of agglomerates per unit volume which concurrently changes the total specific surface

area of the agglomerates with respect to the CL volume. We will denote this quantity henceforth as a_{agg} , the effective surface area. Secanell et al. used constant agglomerate parameters and a constant CL thickness while varying the number of agglomerates to relate the CL volume fractions with the agglomerate parameters. They then proposed an expression for the effective surface area as a function of porosity and the number of agglomerates per unit volume. Here it is important to note that they modeled the reduction of the effective surface area as an arbitrary function of the CL porosity by only considering two limiting cases of CL porosity.

The main goal of this study is to build a physical model to analytically quantify the reduction in the effective surface area (a_{agg}) as the CL porosity decreases. We have adapted the sphere-packing approach used by Taylor et al. [102] who studied the effect of bio-film growth over rigid particles on porosity and specific surface area. We have developed a new method to obtain the effective surface area for two different sphere-packing schemes as a function of CL porosity which is calculated using model inputs. Unlike [55], ionomer weight fraction is used as an input, and the ionomer volume fraction inside the agglomerate is calculated based on the number of agglomerates per unit volume. Furthermore, we have reformulated the agglomerate model equations to correctly account for the reduction of the effective surface area in the case of overlapping agglomerates. Next, we implemented the agglomerate approach in a 2D cathode domain to simulate the effect of ionomer weight fraction and Pt loading on performance. The influence of our effective surface area calculation method on the effect of Pt loading, ionomer weight fraction, and $Pt|C$ ratio on performance was studied for both sphere-packing schemes and compared with the

method in [55]. Finally, we conducted a parametric sweep study to define optimum CL composition.

4.1 Model Description

4.1.1 Cathode Model

The 2D, steady-state cathode model accounts for the transport of chemical species, electrons, and ions in the GDL and the CL. The spherical agglomerate approach is used as an embedded model to describe the CL activity. For simplicity, the model assumes an isothermal, isobaric, and steady-state process. The computational domain encompasses half of the channel and half of the land area as illustrated in Fig. 4.1 and the associated geometric parameters are listed in Table 4.1.

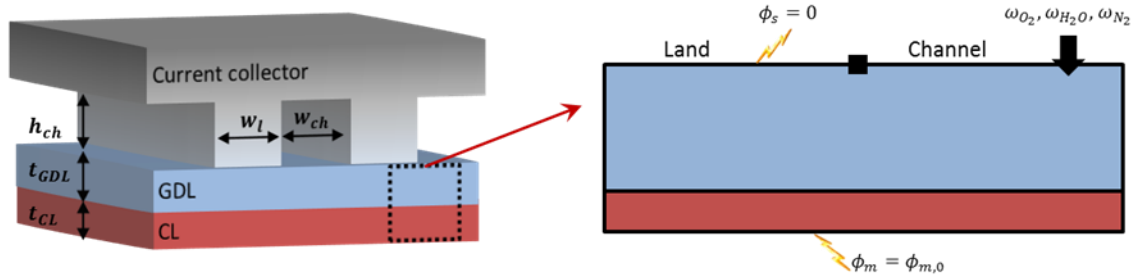


Figure 4.1. 2D computational domain with 3D representation of cathode

Table 4.1. Geometric parameters for the single channel computational domain

Channel height	h_{ch}	1 mm
Channel width	w_{ch}	1 mm
Land width	w_l	1 mm
GDL thickness	t_{GDL}	250 μm
CL thickness	t_{CL}	14 μm

The diffusion of oxygen, water vapor, and nitrogen in the cathode is described by the Maxwell-Stefan equations after neglecting the convective terms:

$$\nabla \cdot \left[-\rho \omega_j \sum_k D_{jk}^{eff} \nabla \frac{\omega_k}{M_k} M_n \right] = R_j \quad (4.1)$$

Eq. (4.1) is solved for the mass fraction (ω_j) of each chemical species where R_j is the source term calculated from the electrochemical reactions, and mixture density ρ is calculated using the ideal gas law.

Charge transport by the electron and ion phases is governed by:

$$\nabla \cdot (\sigma_m^{eff} \nabla \phi_m) = I_v^{CL} \quad (4.2)$$

$$\nabla \cdot (\sigma_s^{eff} \nabla \phi_s) = -I_v^{CL} \quad (4.3)$$

where σ_m^{eff} and σ_s^{eff} are the effective ionic and electronic conductivities, ϕ_m and ϕ_s are ionic and electronic potentials, and I_v^{CL} is the volumetric current density. For both charge and mass transport the effective properties are calculated using the Bruggeman approximation:

$$P_i^{eff} = P_i \epsilon_i^{1.5} \quad (4.4)$$

where P is the property and ϵ_i is the volume fraction of the i^{th} phase in the porous medium. The local ionic conductivity (σ_m) is determined by using the empirical relation reported by Springer et al. [9] for Nafion:

$$\sigma_m = (0.5139\lambda - 0.326) \exp \left[1268 \left(\frac{1}{303} - \frac{1}{T} \right) \right] \quad (4.5)$$

where T is the operating temperature in K, and λ is the local water content which is expressed as a function of the local relative humidity ϕ_{RH} as [53]:

$$\lambda = 0.3 + 10.8\phi_{RH} - 16\phi_{RH}^2 + 14.1\phi_{RH}^3 \quad (4.6)$$

The source terms in Eq. (4.1) are only non-zero in the CL domain. The O₂ and H₂O source terms (R_{O_2} and R_{H_2O}) are calculated from the volumetric current generation using Faraday's law:

$$R_{O_2} = -\frac{I_v^{CL}}{4F} \quad (4.7)$$

$$R_{H_2O} = \frac{(\alpha_{OD} + 1)I_v^{CL}}{2F} \quad (4.8)$$

where α_{OD} is the electroosmotic drag coefficient which can be expressed as [53]:

$$\alpha_{OD} = \begin{cases} 1.0 & \eta_{NCO} < 0.25 [V] \\ 46\eta_{NCO}^2 - 31.52\eta_{NCO} + 5.7 & 0.25 [V] \leq \eta_{NCO} \leq 0.35[V] \\ 0.3 & \eta_{NCO} > 0.35 [V] \end{cases} \quad (4.9)$$

The nominal cathode overpotential (η_{NCO}) is defined as the measure of total losses (including activation and ohmic losses) in the cathode by [53]:

$$\eta_{NCO} = \Phi_s|_{\text{Current Collector}} - \Phi_m|_{\text{Membrane-CL Interface}} \quad (4.10)$$

where the electron potential at the current collector and the ion potential at the membrane-CL interface are the boundary conditions for the charge conservation equations.

The spherical agglomerate model is used to describe the relevant electrochemical phenomena in the CL. At the microscale, the reaction rate (which is directly proportional to the current generation) can be calculated in two ways: (1) using the reactant flux at the agglomerate surface, or (2) using the effectiveness factor approach [94]. Therefore, the following equation can be written for the current generation in a single agglomerate:

$$\begin{aligned}
I_v^{agg} &= -4FD \frac{(C_0 - C_s)}{\delta} \left(\frac{r_{agg}}{r_{agg} + \delta} \right) A_{agg} \\
&= -4FE_r k_c C_s \left(\frac{r_{agg}}{r_{agg} + \delta} \right)^3
\end{aligned} \tag{4.11}$$

where r_{agg} is the agglomerate radius, δ is the ionomer film thickness, A_{agg} is the specific surface area of an agglomerate (ratio of agglomerate outer surface area to its volume), D is the diffusivity of oxygen in ionomer, C_0 is the oxygen concentration on the ionomer film surface, C_s is the oxygen concentration on the agglomerate core surface, k_c is the reaction rate coefficient, and E_r is the effectiveness factor. The effectiveness factor is defined as the ratio of the actual reaction rate to the expected reaction rate if all the catalyst particles inside the agglomerate are subjected to the surface concentration of the reactant at the wall of the agglomerate [94].

Knowing the current generation for a single agglomerate, the volumetric current for the entire CL can be easily obtained. For the flux approach, the effective surface area (a_{agg}) must be defined as the ratio of the total surface area of all agglomerates to the CL volume. Then, by multiplying the left hand side of Eq. 4.11 by a_{agg}/A_{agg} , the current generation per unit volume of the CL can be written in terms of the flux at the agglomerate surface as in left hand side of Eq. 4.12. Similarly, by considering the ratio of the total volume of all agglomerates in the CL to that of a single agglomerate, the current generation per unit CL volume can be written as:

$$\begin{aligned}
I_v^{CL} &= - \left(\frac{a_{agg}}{A_{agg}} \right) 4FD \frac{(C_0 - C_s)}{\delta} \left(\frac{r_{agg}}{r_{agg} + \delta} \right) A_{agg} \\
&= -(1 - \epsilon_v) 4FE_r k_c C_s \left(\frac{r_{agg}}{r_{agg} + \delta} \right)^3
\end{aligned} \tag{4.12}$$

where ϵ_v is the catalyst layer porosity. Here, it should be noted that without the correction term $\left(\frac{r_{agg}}{r_{agg} + \delta} \right)^3$, the right hand side of Eq. (4.11) gives the reaction rate per

unit volume of agglomerate core rather than per unit volume of the entire agglomerate (core plus ionomer film). This correction was not taken into account in [53, 55].

More crucially, since $\left(\frac{a_{agg}}{A_{agg}}\right) = (1 - \epsilon_v)$ only for non-overlapping agglomerates, Eq. (4.12) is only valid for the case of non-overlapping agglomerates. For overlapping agglomerates, the effectiveness factor must be derived for each overlapping geometry, i.e. a_{agg} must be computed accurately. The major contribution of this chapter is to correctly estimate a_{agg} using a sphere-packing approach, and highlight differences with previous approaches such as [55].

For the overlapping case, the effectiveness factor derived for a single agglomerate is no longer valid. In contrast, the flux approach is more suitable because it can account for the surface area reduction due to overlapping agglomerates. Assuming that C_s does not change between a single agglomerate and overlapping ones, Eqs. (4.13) - (4.15) can be used to calculate the volumetric current generation in the CL:

$$I_v^{CL} = -4FD \frac{(C_0 - C_s)}{\delta} \left(\frac{r_{agg}}{r_{agg} + \delta} \right) a_{agg} \quad (4.13)$$

$$C_s = \frac{C_0}{1 + \frac{D_{agg}}{D} \left(\frac{\delta}{r_{agg} + \delta} \right) (\coth(Th) Th - 1)} \quad (4.14)$$

$$C_0 = \frac{P_{O_2}}{H} \quad (4.15)$$

Th is the dimensionless Thiele modulus defined as the ratio of the surface reaction rate to the diffusion rate through the catalyst pellet [94]:

$$Th = r_{agg} \sqrt{\frac{k_c}{D_{eff}}} \quad (4.16)$$

D_{eff} is the effective diffusivity of oxygen inside the agglomerate and is calculated using Bruggeman approximation. The reaction rate coefficient depends on the fuel cell reaction kinetics according to [55]:

$$k_c = \frac{a_{Pt}}{4F(1 - \epsilon_v)} \frac{i_0^{ref}}{C_{O_2,ref}} \exp\left(-\frac{\alpha_c F}{RT} (\Phi_s - \Phi_m)\right) \quad (4.17)$$

where i_0^{ref} is the reference exchange current density, $C_{O_2,ref}$ is the reference oxygen concentration, α_c is the cathode charge transfer coefficient, and a_{Pt} is the total reaction area per unit volume of the agglomerate which is expressed as:

$$a_{Pt} = A_0 \frac{m_{Pt}}{t_{CL}} \quad (4.18)$$

where m_{Pt} is the catalyst loading (kg/m^2), t_{CL} is the catalyst layer thickness, and A_0 is the catalyst surface area per unit mass. The following correlation for A_0 was developed by [15] as a function of Pt|C ratio based on the experimental data of [103]:

$$A_0 = 2.2779 \times 10^6 (Pt|C)^3 - 1.5857 \times 10^6 (Pt|C)^2 - 2.0153 \times 10^6 (Pt|C) + 1.5950 \times 10^6 \quad \text{cm}^2/\text{g} \quad (4.19)$$

Table 4.2 lists all the parameter values employed in the current simulations. The literature indicates two Tafel slopes corresponding to high and low current regimes [99-100]. Accordingly, we used two distinct values for i_0^{ref} and α_c as listed in Table 4.2. In addition to the various material property values and operating conditions, Table 4.2 also gives the agglomerate dimensions selected for this study.

All agglomerate models require the use of tuning parameters to match experimental data; in our case, we tuned the exchange current density and the agglomerate dimensions to fit the experimental polarization data of [71] as shown subsequently in validation section. The literature reports a wide range of values for the

agglomerate dimensions. For example, one of the pioneering agglomerate modelling studies employed an agglomerate radius ranging from 1-5 μm based on their SEM images [47]. On the other hand, a recent experimental study [104] suggests that the carbon particles form agglomerates of about 100-120 nm . In particular, modeling studies employ a wider range of agglomerate radius of between 0.5-5 μm compared to experimental observations such as [104]. This discrepancy can be understood by noting that the agglomerate model does not attempt to represent the actual physical microstructure of the CL. Rather, the agglomerate dimensions employed in models are selected to represent the mean path that dissolved oxygen must travel before reaching the reaction sites and thereby accurately model the various transport losses in the CL [105]. Consequently, the agglomerate sizes used in models are larger than those observed in SEM or TEM images. In our study, we set $r_{agg} = 3 \mu m$ and $\delta = 145 nm$ as listed in Table 4.2.

Neglecting the losses in the anode and the membrane, the polarization curves are plotted as a function of the cathode potential which is given as [53]:

$$V_c = E_{th} - \eta_{NCO} \quad (4.20)$$

$$E_{th} = 1.229 - 8.456 \times 10^{-4}(T - 295.15) \quad (4.21)$$

$$+ 4.31 \times 10^{-5}T \left[\ln(P_{H_2}) - \frac{1}{2} \ln(P_{O_2}) \right]$$

Referring to Fig. 4.1, the boundary conditions employed to solve the above equations are as follows. The inlet mass fractions are specified at the channel region (left half of the top edge in Fig. 4.1). The remaining boundaries are specified as no-flux boundaries for the Maxwell-Stefan equation. For the electron conservation equation, the potential is set to zero at the rib region (right half of the top edge in Fig. 4.1) and the remaining outer boundaries are defined as no-flux. For the ionic charge

conservation equation, the ionic potential is set to $\phi_{m,0}$ at the membrane/CL interface and all the other outer boundaries are defined as no-flux.

Table 4.2. Parameter values used in the cathode simulation for the baseline case

Pressure	P	2.04 atm (30 psi)	[71]
Temperature	T	353 K	[71]
Relative humidity	RH	1.0	[71]
O ₂ mass fraction	y_{O_2}	0.197	[71]
H ₂ O mass fraction	y_{H_2O}	0.155	[71]
GDL porosity	ε_{GDL}	0.5	[53]
Platinum loading	m_{Pt}	0.00325 kg m ⁻²	[71]
Pt to C weight ratio	Pt C	0.2	[71]
Ionomer weight fraction	NFP	0.33	[71]
Agglomerate radius	r_{agg}	3E – 6 m	
Ionomer film thickness	δ	145E – 9 m	
Reference O ₂ concentration	$C_{O_2,ref}$	0.85 mol m ⁻³	[53]
Henry's constant	H	31663 Pa m ³ mol ⁻¹	[53]
Reference exchange current density	$i_{0,ref}$	6.72E – 5 A m ⁻² for $V_c \geq 0.8 V$ 0.8 V 6.20E – 3 A m ⁻² for $V_c \leq 0.8 V$	
Cathode charge transfer coefficient	α_c	1 for $V_c \geq 0.8 V$ 0.61 for $V_c \leq 0.8 V$	[53] [53]
Electron conductivity	σ_s	100 S m ⁻¹	[53]
Diffusivity of O ₂ in ionomer	D	8.75E – 10 m ² s ⁻¹	[53]
Diffusivities	D_{O_2,N_2}	1.86E – 5 m ² s ⁻¹	[53]
	D_{H_2O,N_2}	2.58E – 5 m ² s ⁻¹	[53]
	D_{O_2,H_2O}	2.47E – 5 m ² s ⁻¹	[53]

4.1.2 Physical Model for Effective Specific Surface Area

The goal of this study is to geometrically quantify the variation of the effective surface area for varying volume fractions of the CL. Previously, Secanell et al. [55] suggested

the following expression for effective surface area by considering the limiting case of zero porosity:

$$a_{agg} = 4\pi n(r_{agg} + \delta)^2 \epsilon_v \quad (4.22)$$

where n is the number of agglomerates per unit volume of the CL. However, [55] did not present any physical or geometrical evidence for this expression. Now, n can be expressed as a function of CL porosity and agglomerate dimensions as:

$$n = \frac{1 - \epsilon_v}{\frac{4\pi}{3}(r_{agg} + \delta)^3} \quad (4.23)$$

Substituting Eq. (4.23) back in to Eq. (4.22), it is seen that the effective surface area as modeled by [55] becomes a quadratic function of the catalyst layer porosity because the agglomerate dimensions are assumed to be constant:

$$a_{agg} = \epsilon_v(1 - \epsilon_v) \left(\frac{3}{r_{agg} + \delta} \right) \quad (4.24)$$

Equation 4.24 indicates that a_{agg} is maximized when $\epsilon_v = 0.5$, and $a_{agg} \rightarrow 0$ as $\epsilon_v \rightarrow 0, 1$. Apparently, this quadratic dependence of effective surface area on CL porosity was modeled without considering the actual geometrical aspects of how the agglomerates begin to overlap as the CL porosity is decreased, and its consequent effect on agglomerate surface area. Therefore, while Secanell et al.'s expression for a_{agg} [55] is correct for the two limiting cases of $\epsilon_v = 0$ and 1, there is no physical basis for this expression for $0 < \epsilon_v < 1$.

Modeling a_{agg} accurately is of critical importance as it directly affects the agglomerate model predictions for the diffusion loss region. Therefore, a more physically realistic approach based on the geometry of overlapping agglomerates is required to determine how exactly a_{agg} varies with ϵ_v . This paper describes such an

approach based on the work of Taylor et al. [102] who were interested in the effect of biofilm growth on the permeability of porous media. They represented the porous medium as regularly-packed rigid spheres with a uniform film growing on the surface of each spherical particle, and derived expressions for the porosity and specific surface area as a function of film thickness for various sphere-packing arrangements.

By adapting the sphere-packing idea presented in [102], we developed a new, more accurate method to calculate the effective agglomerate surface area for the classical spherical agglomerate approach. Unlike [102] which determines the porosity as only a function of film thickness, our porosity calculation incorporates the entire input dataset provided for the CL composition.

The catalyst ink composition is specified in terms of the weight fractions of its various components which, consistent with experimental studies, are expressed in terms of the Pt loading. In addition, it should be noted that the CL thickness (t_{CL}) is assumed to be constant as in [55]. Then the volume fractions of Pt (ϵ_{Pt}), C (ϵ_C), ionomer (ϵ_N), ionomer in the agglomerate (ϵ_{agg}), and CL porosity (ϵ_v) are calculated as:

$$\epsilon_{Pt} = \frac{m_{Pt}}{t_{CL}\rho_{Pt}} \quad (4.25)$$

$$\epsilon_C = \frac{m_{Pt}(1 - Pt|C)}{Pt|C t_{CL}\rho_C} \quad (4.26)$$

$$\epsilon_N = \frac{m_{Pt}(NFP)}{Pt|C(1 - NFP)t_{CL}\rho_N} \quad (4.27)$$

$$\epsilon_{agg} = 1 - \left(\frac{\epsilon_{Pt} + \epsilon_C}{\frac{4\pi}{3} n\pi r_{agg}^3} \right) \quad (4.28)$$

$$\epsilon_v = 1 - \epsilon_{Pt} - \epsilon_C - \epsilon_N \quad (4.29)$$

where $Pt|C$ and NFP are the Pt and ionomer mass fractions, respectively, in the catalyst powder and the ink.

In our model we derive expressions for the reduction in CL porosity and agglomerate surface area due to agglomerate overlap, as opposed to particle-film growth as in [55]. The agglomerate and the ionomer film are assumed to form a spherical particle with radius $R = (r_{agg} + \delta)$ which is allowed to overlap with others as shown in Fig. 4.2. For zero overlap, the effective surface area is obtained trivially as:

$$a_{agg} = 4\pi n(r_{agg} + \delta)^2 \quad \text{for } \epsilon_v \geq \epsilon_{v,cr} \quad (4.30)$$

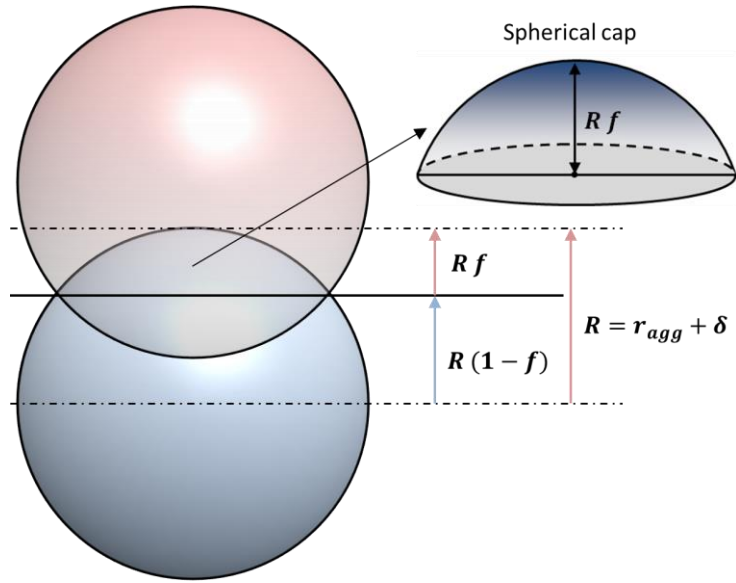


Figure 4.2. Geometry of overlapping agglomerates and the spherical cap

The porosity value when all the spheres are just touching each other is defined as the critical porosity ($\epsilon_{v,cr}$) which is specific to each packing scheme. The agglomerates are considered to overlap if $\epsilon_v < \epsilon_{v,cr}$. There are four possible arrangements for regularly packed spheres of uniform size: cubic, orthorhombic,

tetragonal and rhombohedral, which are named after the shape of the unit cell [106]. For the cubic and orthorhombic packing schemes, the agglomerates start overlapping at porosities of 48% and 40%, respectively, implying that the available surface area, and hence performance, would begin to decline below these porosity values. The corresponding porosities for the tetragonal and rhombohedral schemes are 30% and 26%, respectively. Typical CL porosities are generally less than 50%. Therefore, we preferred to use the tetragonal and rhombohedral schemes (illustrated in Fig. 4.3) in our study as they provide a higher packing density than the cubic and orthorhombic schemes. Properties for the employed packing schemes are listed in Table 4.3. The packing factor (α_m) in Table 4.3 is a dimensionless number that characterizes the packing scheme and is equal to $V_{uc}/(D_p(1-f))^3$, where V_{uc} is the volume of the unit cell, and D_p is the particle diameter.

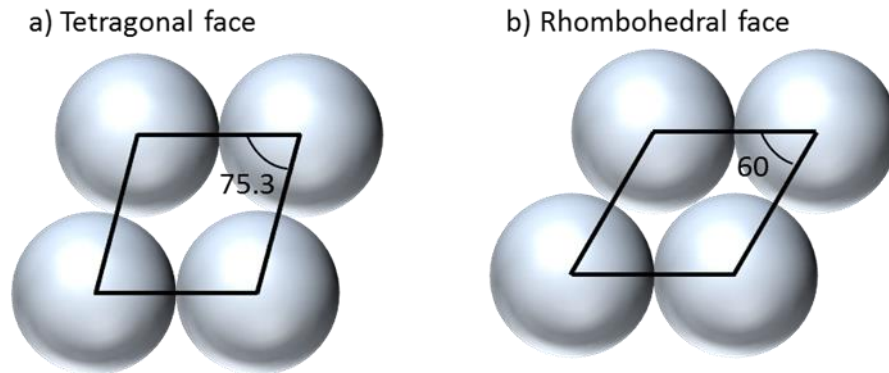


Figure 4.3. Unit cell representation for (a) tetragonal, and (b) rhombohedral packing schemes

For $\epsilon_v < \epsilon_{v,cr}$, the overlapping ratio (f) defines the extent of overlap between particles. It is apparent that increasing f results in decreased void fraction and specific surface area (surface area of spheres/unit cell volume). The variation of porosity and the specific surface area with f depends greatly on the packing scheme as each

packing arrangement is characterized by a unique number of contact points between neighboring particles as listed in Table 4.3.

Table 4.3. Characteristic properties of packing options used in this study

	Number of contact points (m)	Critical porosity ($\epsilon_{v,cr}$)	Packing factor (α_m)	Critical overlapping porosity ($\epsilon_{v,o}$)
Tetragonal- sphenoidal	10	0.3019	0.75	0.0634
Rhombohedral	12	0.2595	$1/\sqrt{2}$	0.0359

By representing the CL as a bed of regularly-packed spheres, the CL porosity given by Eq. (4.29) is linked to the void volume fraction of the unit cell. The unit cell's void volume fraction is in turn obtained as a function of the overlapping ratio for the given packing scheme. The unit cell volume for a given packing option is calculated using the packing factor given in Table 4.3, and the void volume is obtained by subtracting the spherical particle volume from the unit cell volume after accounting for the volume lost in the overlapping regions. The total volume loss due to overlapping regions can be expressed in terms of the spherical cap volume and the number of contact points. The total volume occupied by overlapping agglomerates in the unit cell is obtained as:

$$V_s = \frac{\pi}{6} D_p^3 - \frac{\pi}{24} m D_p^3 f^2 (3 - f) \quad (4.31)$$

where the first term is the volume of spherical particles in the unit cell without accounting for overlapping, and the second term is the total overlapped volume due to the particle's contact with m neighboring particles. Noting that the unit cell volume

depends on the overlapping ratio, the CL porosity is obtained from the void volume fraction of the unit cell as:

$$\epsilon_v = 1 - \frac{\pi}{6\alpha_m(1-f)^3} \left[1 - \frac{mf^2(3-f)}{4} \right] \quad (4.32)$$

As the CL porosity can be determined from Eq. (4.29), the goal here is to determine the amount of overlap between the agglomerates for a given CL composition. Equation 4.32 can be rearranged to yield a third order polynomial for f :

$$\begin{aligned} & \left(\frac{m\pi}{24(1-\epsilon_v)\alpha_m} + 1 \right) f^3 - 3 \left(\frac{m\pi}{24(1-\epsilon_v)\alpha_m} + 1 \right) f^2 + 3f \\ & + \left(\frac{\pi}{6(1-\epsilon_v)\alpha_m} - 1 \right) = 0 \end{aligned} \quad (4.33)$$

Only the smallest root of Eq. (4.33) satisfies the constraint that $0 < f < 1$ while also behaving in a physically realistic manner, and so it represents the desired overlapping ratio. Knowing f , the effective surface area a_{agg} can be derived in a similar manner to Eq. (4.32). Accounting for the surface area lost due to overlapping particles, the effective surface area is calculated as:

$$a_{agg} = \frac{\pi}{\alpha_m D_p (1-f)^2} \left[1 - \frac{mf}{2} \right] \quad \text{for } \epsilon_{v,o} \leq \epsilon_v < \epsilon_{v,cr} \quad (4.34)$$

It should be noted that Eqs. (4.32) - (4.34) cannot be applied when the CL porosity drops below a limiting value denoted by $\epsilon_{v,o}$. For $\epsilon_v < \epsilon_{v,o}$, the amount of overlap increases to such an extent that spherical caps from neighboring spheres themselves begin to overlap with each other as illustrated in Fig. 4.4b. In this case, Eq. (4.32) underestimates the porosity as it does not account for the overlap of the spherical caps with each other, and Eqs. (4.32) - (4.34) become invalid. A similar situation was examined by [106, 107] for Taylor's problem. Adapting their approach, we

determined the limiting overlapping porosity $\epsilon_{v,o}$ for each packing option as listed in Table 4.3.

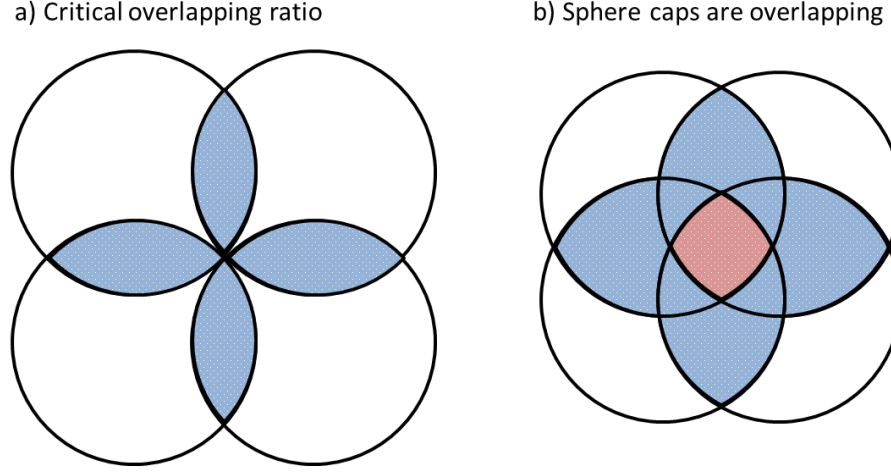


Figure 4.4. Representation of (a) the critical overlapping ratio, and (b) overlapping spherical caps

The values of $\epsilon_{v,o}$ are 6% for the tetragonal-sphenoidal arrangement, and 3% for the rhombohedral arrangement. These porosity values are much too small to be meaningful in the context of a PEM fuel cell CL, and hence it is not worthwhile to solve the relevant higher-order equations for this low-porosity range as in [106, 107]. It is readily apparent that $a_{agg} = 0$ when $\epsilon_v = 0$, and Eqs. (4.32) - (4.34) allow us to compute a_{agg} for small values of ϵ_v down to $\epsilon_{v,o}$. Hence, for our purposes, it is sufficient to bridge the gap for a_{agg} in the small range $0 < \epsilon_v < \epsilon_{v,o}$ by a simple curve fit. A parabolic fit was selected and its coefficients were obtained by matching the known values of a_{agg} at $\epsilon_v = 0$ and $\epsilon_{v,o}$, and the slope of a_{agg} at $\epsilon_{v,o}$:

$$\begin{aligned}
 a_{agg} &= f(\epsilon_v) \\
 &= \left(\frac{f'(\epsilon_{v,o})\epsilon_{v,o} - f(\epsilon_{v,o})}{\epsilon_{v,o}^2} \right) \epsilon_v^2 \\
 &+ \left(\frac{2f(\epsilon_{v,o}) - f'(\epsilon_{v,o})\epsilon_{v,o}}{\epsilon_{v,o}} \right) \epsilon_v \quad \text{for } \epsilon_v < \epsilon_{v,o}
 \end{aligned} \tag{4.35}$$

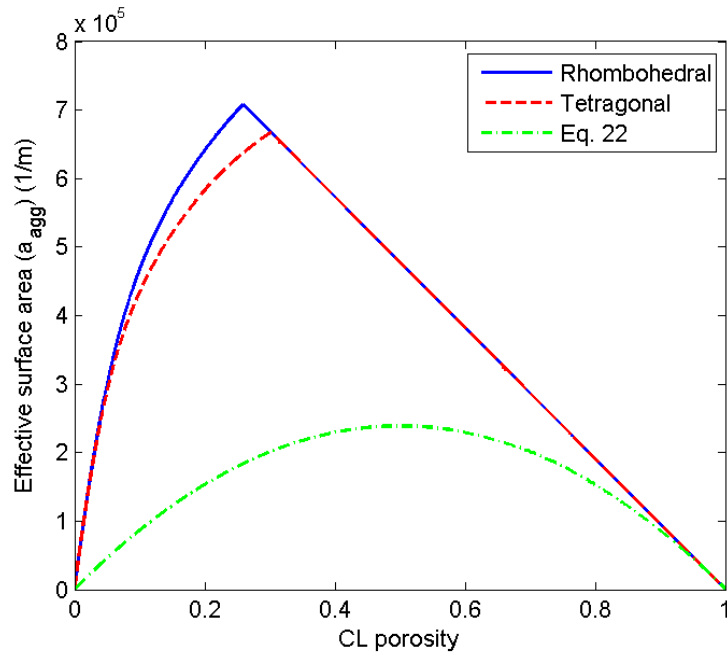


Figure 4.5. Effective surface area as a function of porosity for the two packing schemes considered here, and the expression provided by [55]

In summary, the variation of effective surface area with respect to CL composition is fully described by Eqs. (4.30), (4.34), and (4.35). The variation of effective surface area is plotted against CL porosity in Fig. 4.5 for the two packing schemes studied here. For each packing scheme, the specific surface area varies linearly with CL porosity for large values of porosity at which the agglomerates do not overlap. The linear behavior is simply due to the number of agglomerates per unit CL volume increasing linearly with the decreasing porosity. The effective surface area reaches its maximum value at the critical porosity value ($\epsilon_{v,cr}$) when overlap just begins for each packing scheme. Then, due to overlapping agglomerates the effective surface area decreases for $\epsilon_{v,o} < \epsilon_v < \epsilon_{v,cr}$ according to Eq. (4.34). Finally, for $\epsilon_v < \epsilon_{v,o}$, the approximate curve-fit of Eq. (4.35) is applied. Figure 6 also shows the variation of a_{agg} vs. ϵ_v as modeled by Eq. (4.22) [55]. Although Eq. (4.22) is correct

at the two limits of the porosity range as stated earlier, the surface area is arbitrarily maximized at 50% porosity and it seriously underpredicts a_{agg} for all other values of ϵ_v compared to the sphere-packing approach presented here.

4.2 Validation

The accuracy of our numerical model is validated by comparing its predictions against experimental data. As stated earlier, only the exchange current density and agglomerate dimensions are tuned to match the experimental results of [71]. Utilizing the identical operating conditions and CL architecture of [71] the model (with rhombohedral sphere packing) is shown to accurately reproduce the polarization curve of [71] in the activation, ohmic, and mass transport regimes as shown in Fig. 4.6.

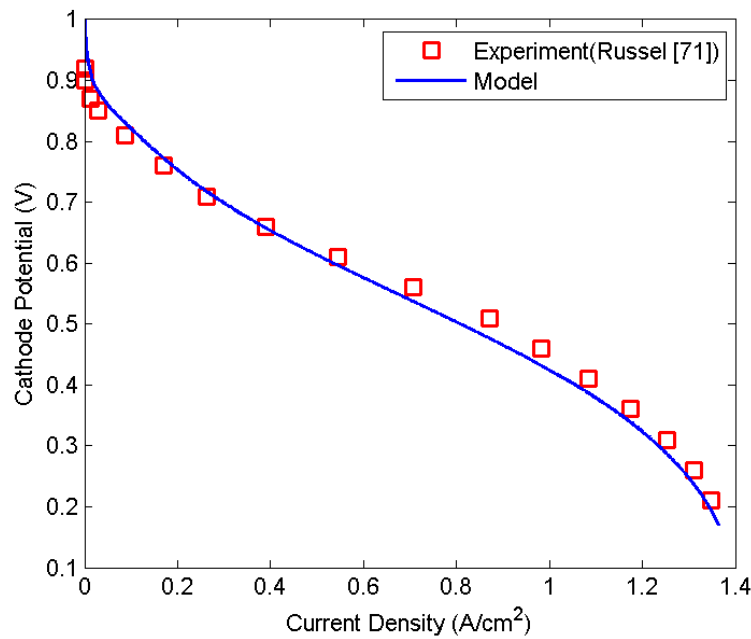


Figure 4.6. Validation of the numerical model (with rhombohedral sphere packing) against the experimental data of [71]

Additional validation is obtained by comparing the model's predictions (with rhombohedral sphere packing) against experimental data when the CL composition is varied. The effect of Nafion percentage (NFP) on current density at a constant operating voltage as predicted by the model is shown in Fig. 4.7 along with the experimental data of [69]. As shown in Fig. 4.7, the agreement is excellent. The current density is seen to increase with NFP up to about 30%, beyond which the decreasing porosity results in a loss of surface area which causes the current density to drop. Figure 4.7 also shows the calculated porosity value which decreases from 40% to 5% with increasing NFP.

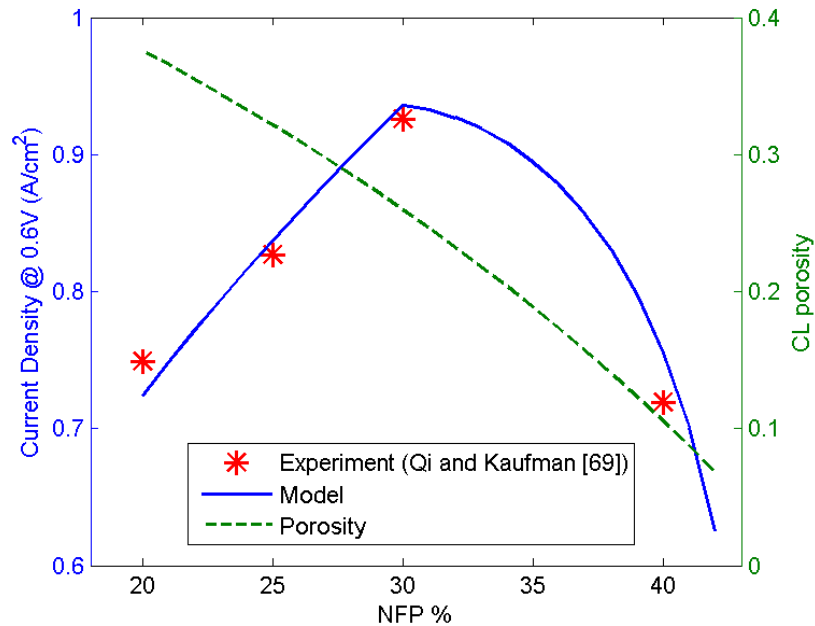


Figure 4.7. Validation of the numerical model (using rhombohedral sphere packing) against the experimental data of [69] for $t_{cl} = 13 \mu m$ and $i_0 = 0.084 A/m^2$

Further validation (with rhombohedral sphere packing) is obtained by examining the current density distribution along the membrane/CL interface for three different operating regimes. Figure 4.8 shows that the current density is maximized under the land for the activation region loss ($V_c = 0.87$ V), at the corner of the land for the ohmic loss region ($V_c = 0.57$ V), and under the channel for the diffusion loss region ($V_c = 0.27$ V). This overall trend is in agreement with the results in [37, 53].

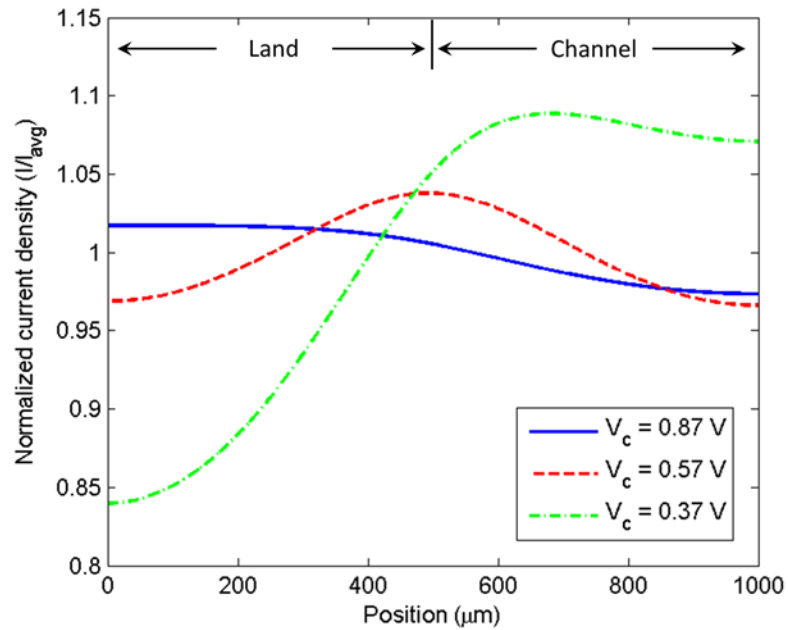


Figure 4.8. Current density distribution along the membrane/CL interface for three values of cathode potential, V_c (using rhombohedral sphere packing)

4.3 Results and Discussion

In the previous sections, we have described and validated a new method to calculate the effective agglomerate surface area which plays a critical role in determining the diffusion resistance in the agglomerate model. Next, we present results from simulations to optimize the CL composition using this new approach to calculate the effective surface area.

The ultimate goal in CL optimization is to achieve high performance at low catalyst loading. For this purpose, one must be able to accurately capture the effect of catalyst loading in numerical models. Hence, we begin by evaluating the performance of our model incorporating the new effective surface area calculation method as the catalyst loading is varied. Figure 4.9 presents the polarization curves for the different effective surface area calculation methods (the two packing schemes discussed here and Eq. (4.22)) as the Pt loading is varied from 0.2 to 0.4 mg/cm² for a fixed Pt|C weight ratio of 20%. Figure 4.9 indicates that the polarization curve is very sensitive to the effective surface area. The polarization curves in Figs. 4.9b and 4.9c obtained with our sphere-packing approach are very similar, except that the rhombohedral scheme predicts higher performances for 0.35 mg/cm² Pt loading. In both Figs. 4.9b and 4.9c, performance improves substantially as the Pt loading is increased from 0.2 to 0.3 mg/cm². The rate of improvement then slows up to 0.35 mg/cm², beyond which, the performance declines. Therefore, both packing schemes suggest an optimal Pt loading of about 0.35 mg/cm². Figures 4.9b and 4.9c match qualitatively the trends seen in experiments [69, 70, 71]. The drop in performance for Pt loading > 0.35 mg/cm² in Figs. 4.9b and 4.9c can be attributed to decreased porosity at higher Pt loadings which reduces the effective surface area. Such a trend can be observed in the experimental results of [71] for the activation region, and in [69, 70] for the diffusion loss region. In contrast, the polarization curves in Fig. 4.9a obtained with Eq. (4.22) [55], indicate that performance declines monotonically with Pt loading in all the regions of polarization curve. The main reason for this monotonic trend is that Eq. (4.22) predicts the highest effective surface area at a porosity of 0.5, with the surface area declining continuously for porosities below 0.5 as illustrated in Fig. 4.5. In our

simulation, we have used the CL composition and thickness data provided in [71]; the typical CL porosity is less than 0.5 as reported in [71]. Accordingly, for porosities less than 0.5, a monotonically decreasing performance is observed in Fig. 4.9a.

To further investigate the behavior of our sphere-packing approach with varying catalyst loading, we examined the effect of Pt|C weight ratio for rhombohedral packing. First, the Pt|C weight ratio is changed from 20 to 40% and the effect of Pt loading on performance is presented in Fig. 4.10. Figure 4.10 shows that the performance increases monotonically with Pt loading in contrast to the non-monotonic variation for 20% Pt|C observed in Figs 4.9b and 4.9c. Similar to the trend reported in experiments [69], a higher Pt loading is required to achieve the best performance when the Pt|C ratio is changed from 20 to 40%. Next, the performance of 20 and 40% Pt|C vs. Pt loading are compared at a constant operating voltage of 0.6 V in Fig. 4.11 as in [69]. In agreement with the experimental trend of [69], it is seen that Pt|C = 20% consistently performs better than Pt|C = 40% except at very high Pt loading. Therefore, using 20% Pt|C may be a good option for cost-effective catalysts.

Next, we examine the effect of varying the Pt|C weight ratio from 10% to 40% at a constant Pt loading of 0.2 mg/cm^2 in Fig. 4.12. In agreement with the experimental results of Paganin et al. [70] the performance is seen to vary non-monotonically with Pt|C ratio. In agreement with the results of [70], smaller limiting currents are observed for high Pt|C ratios. Because the CL thickness is fixed in this simulation, porosity becomes the dominant factor in determining the effective surface area, and hence the limiting current. For Pt|C > 15%, the amount of carbon decreases which increases the overall porosity, which in turn leads to a lower effective surface area, and hence the limiting current is reached earlier.

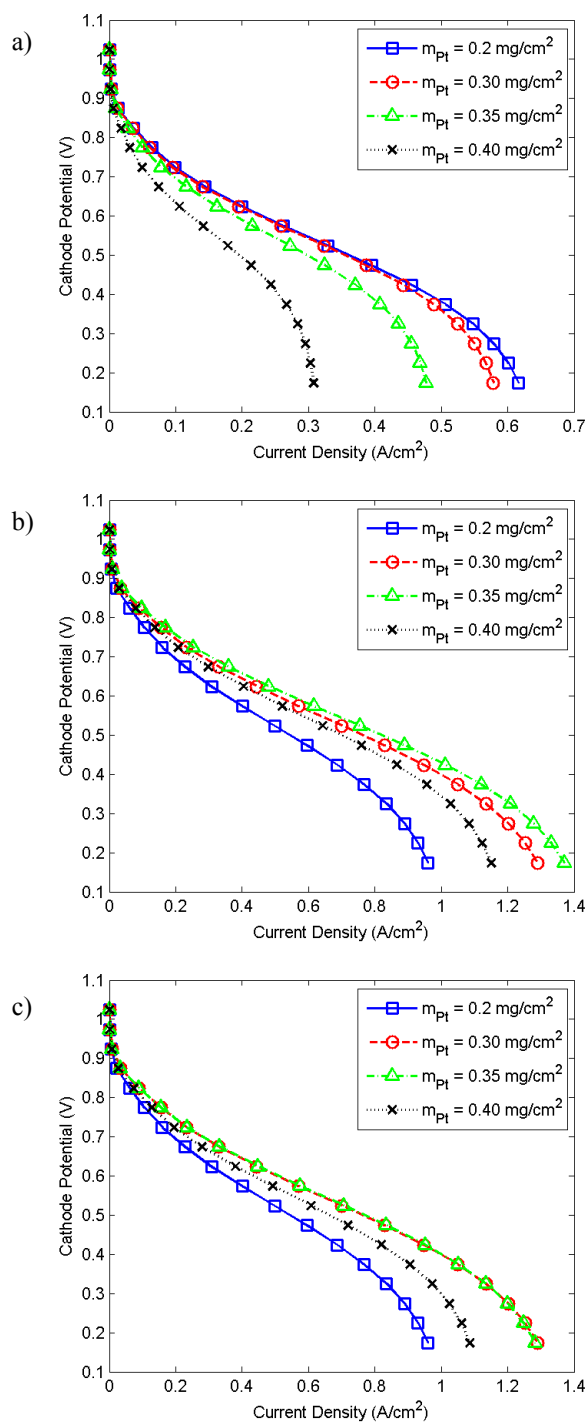


Figure 4.9. Effect of Pt loading with $NFP = 33\%$ and $Pt|C = 20\%$ for effective surface area calculation with (a) Eq. 4.22 [55], (b) rhombohedral sphere packing, and (c) tetragonal sphere packing

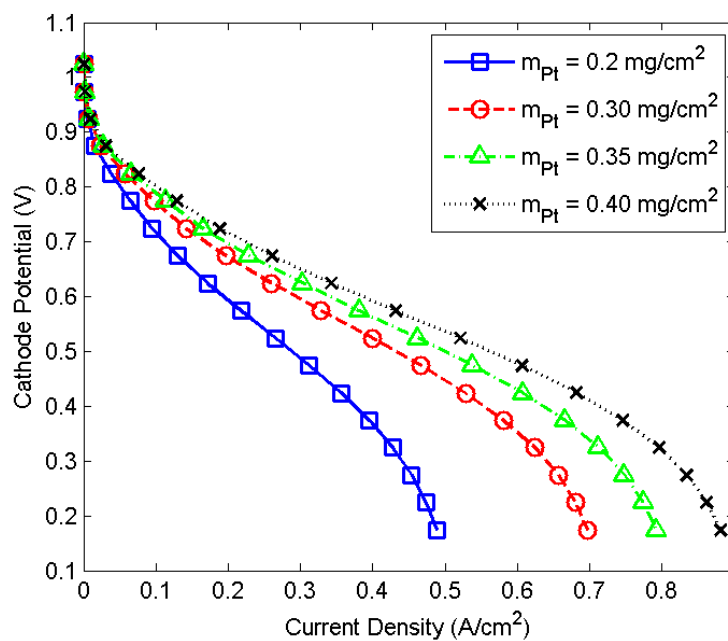


Figure 4.10. Effect of Pt loading with $NFP = 33\%$ and $Pt|C = 40\%$ for the rhombohedral packing scheme

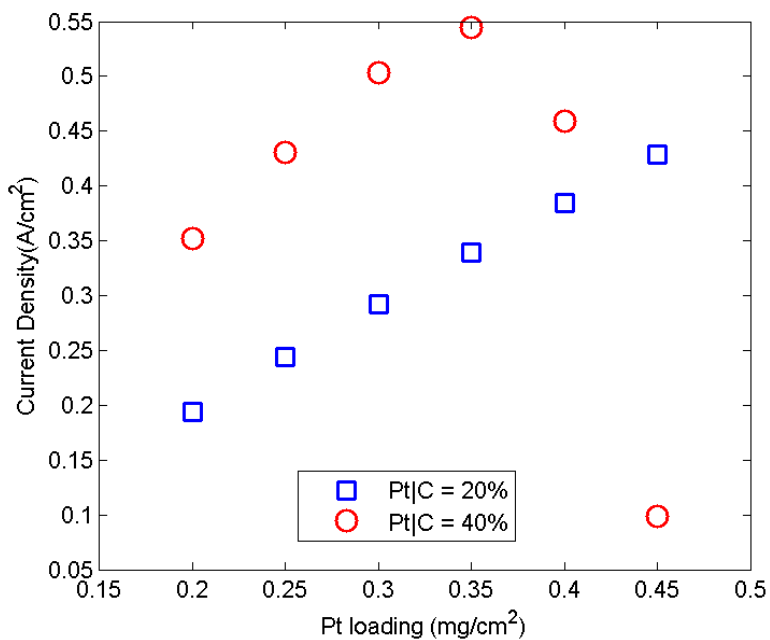


Figure 4.11. Current density variation at $V_c = 0.6$ V for $Pt|C = 20\%$ and 40%

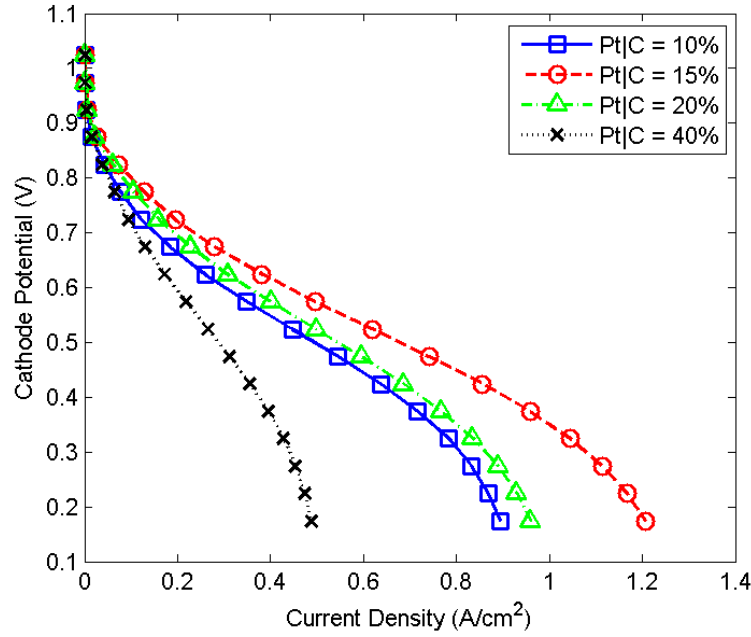


Figure 4.12. Effect of Pt|C weight ratio on polarization curves for $m_{Pt} = 0.2 \text{ mg/cm}^2$

Next, we investigate the effect of ionomer loading. In this study, the ionomer loading is determined by the ionomer weight fraction (NFP), which is reported in [72] to unify the results in the literature [70,73-75] for ionomer loading. The polarization curves in Fig. 4.13 are obtained with different effective surface area calculation method as NFP is varied from 25% to 45%. In Fig. 4.13b, the performance improves with NFP up to 35% for rhombohedral packing scheme, beyond which excessive ionomer content decreases performance by decreasing porosity. Similarly, for the tetragonal packing scheme in Fig. 4.13c, the optimal value of NFP is 33%. Both packing arrangements suggest optimum NFP values for the CL in agreement with experimental studies [69-71, 72-76]. Passalacqua et al. [72], Uchida et al. [74] and Russel et al. [71] reported an optimal NFP of 33% which is identical to the value obtained here for the tetragonal packing scheme. In addition, the optimum NFP values

deduced from the experimental data of [70] and [73] are between 30-35% and 40%, respectively. In contrast, Fig. 4.13a shows a monotonically decreasing performance with NFP . This situation can again be explained by porosity values less than 0.5 and the behavior of the effective surface area expression proposed by [55].

The effect of ionomer loading is shown in Fig. 4.14 for the three effective surface area calculation methods for a fixed operating voltage of 0.6 V. Figure 4.14 indicates that all three methods predict an optimal value of NFP for the ohmic loss region. The improvement in performance with NFP can be attributed to the improvement in proton conductivity which is proportional to NFP according to the Bruggeman approximation. On the other hand, increased NFP can have an adverse effect on electron transport and the diffusion of reactants. In this study, only the latter effect is modeled, hence the optimal NFP values for the ohmic loss region may be slightly overestimated. Even so, both sphere-packing methods properly capture the performance improvement with increasing ionic conductivity, followed by the adverse effect of decreasing porosity in Fig. 4.14. The rhombohedral and tetragonal schemes predict optimum NFP values of 35% and 33%, respectively, which are in very good agreement with the experimental results [69-72, 74]. In contrast, the use of Eq. (4.22) places the optimum NFP at around 27%; moreover, the trend of the curve with Eq. (4.22) in Fig. 4.14 also does not match experimental observations. It should be recalled that the main handicap of Eq. (4.22) is its unphysical modeling of porosity, whereas the sphere-packing method represents a more realistic approach.

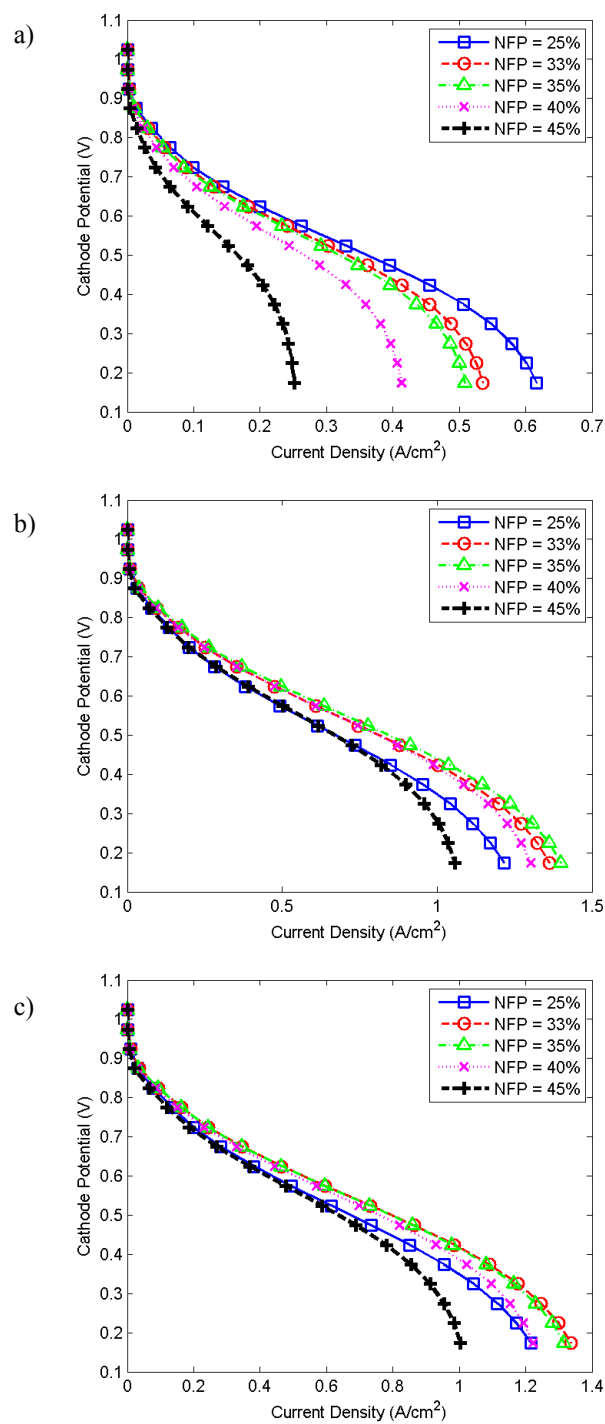


Figure 4.13. Effect of NFP with $m_{Pt} = 0.325 \text{ mg/cm}^2$ and $Pt|C = 20\%$ for effective surface area calculation with (a) Eq. 4.22 [55], (b) rhombohedral sphere packing, and (c) tetragonal sphere packing

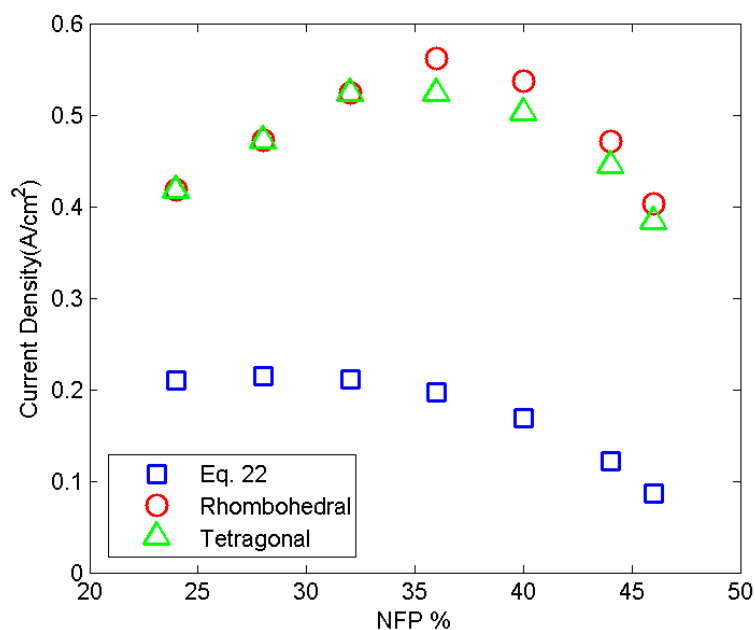


Figure 4.14. Current density variation at $V_c = 0.6$ V for $m_{Pt} = 0.325$ mg/cm² and Pt/C = 20% with Eq. 4.22 [55], rhombohedral sphere packing, and tetragonal sphere packing

The effect of Pt loading on the optimal value of NFP was also investigated for the rhombohedral packing scheme in Fig. 4.15 by studying a low ($m_{Pt} = 0.25$ mg/cm²) and a high ($m_{Pt} = 0.5$ mg/cm²) catalyst loading case. For the low Pt loading case, the optimal NFP value was 50% as seen in Fig. 4.15a. For the high Pt loading case in Fig. 4.15b, the optimal NFP was 20%. In addition, it may be recalled that for the moderate Pt loading of 0.325 mg/cm² in Fig. 4.13b, the optimal NFP was 35%. In general, this suggests that as the Pt loading decreases the optimal NFP value increases, which is consistent with the results reported in [77].

Finally, we investigated the effect of CL thickness by utilizing the rhombohedral packing scheme in Fig. 4.16. Figure 4.16 shows that the performance improves with CL thickness from 6 to 10 μ m. Beyond 10 μ m, the performance falls.

As t_{CL} is increased from 6 to 10 μm , the porosity increases from 3.5% to 42% and it promotes reactant transport so the performance improves mainly in the diffusion loss region. On the other hand, charge transfer losses are linearly proportional to t_{CL} . For $t_{CL} > 10 \mu\text{m}$, the slope of the curves in the ohmic region in Fig. 4.16 increases, confirming higher charge transfer losses.

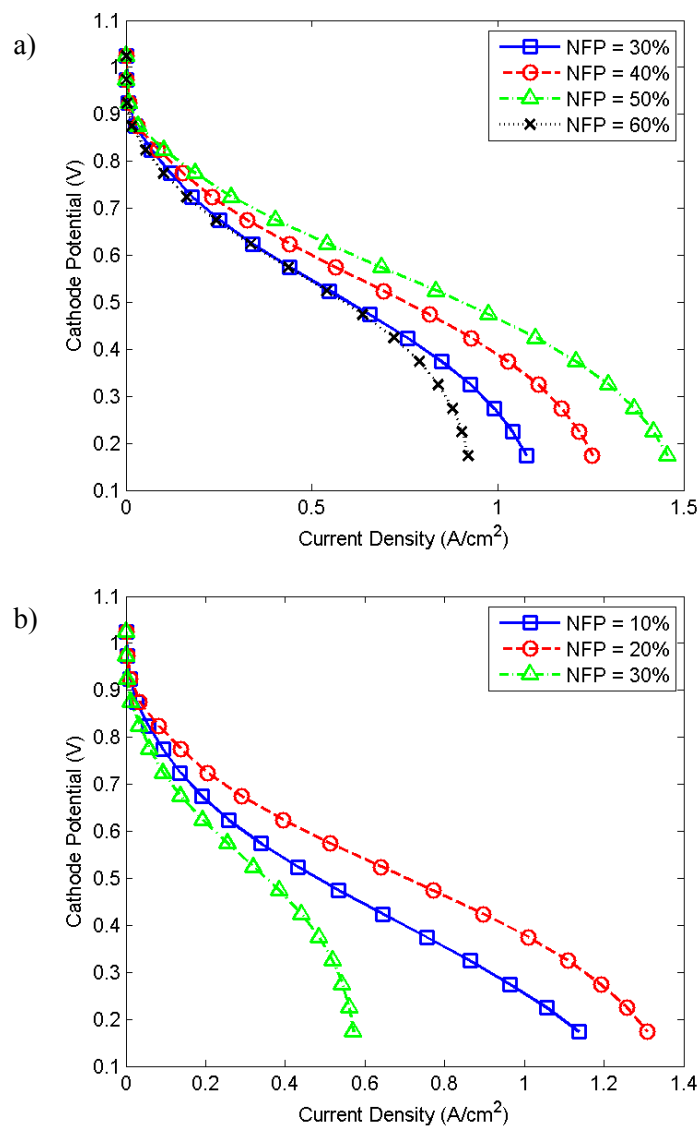


Figure 4.15. Effect of Pt loading on NFP with the rhombohedral packing scheme for $t_{cl} = 15 \mu\text{m}$; (a) $m_{Pt} = 0.25 \text{ mg}/\text{cm}^2$, (b) $m_{Pt} = 0.5 \text{ mg}/\text{cm}^2$

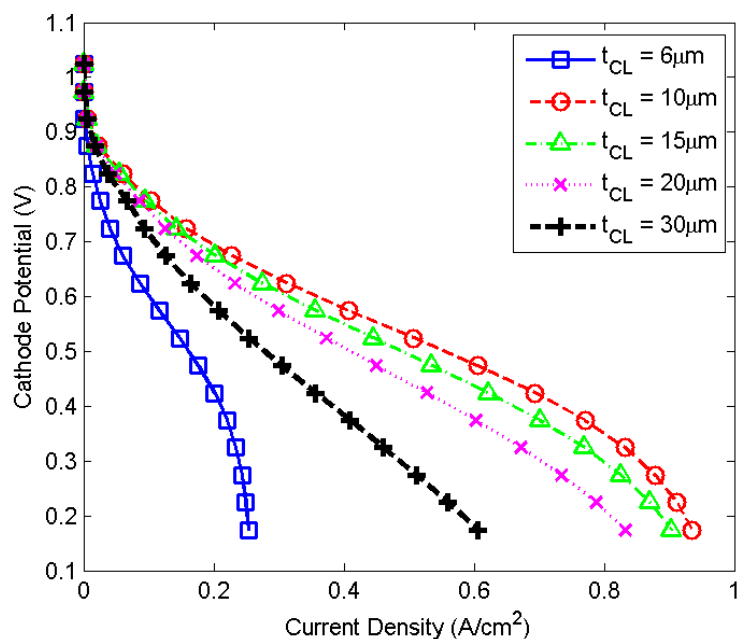


Figure 4.16. Effect of catalyst layer thickness with the rhombohedral packing scheme for $NFP = 30\%$ and $m_{Pt} = 0.2 \text{ mg/cm}^2$

4.4 Summary

As discussed in Chapter 2, the effective agglomerate surface area is a critically important parameter for accurately determining diffusion losses in the classical agglomerate model. Chapter 4 presents a new approach to model the variation of the effective agglomerate surface area with catalyst layer composition based on two regular sphere-packing schemes: rhombohedral, and tetragonal. It is shown that the sphere-packing methods provide an agglomerate surface area term that varies in a realistic manner with catalyst layer porosity. The results of the new approach are compared with the previously suggested expression in [55].

The effects of Pt and ionomer loading were investigated by using the sphere-packing approach, and the results for both were found to be in excellent agreement with experimentally-observed trends. The results confirm that the sphere-packing

method's success can be attributed to the physically rigorous manner in which the effective surface area is calculated in contrast to the previous expression of [55]. In addition, the model was used to study the effect of Pt|C weight ratio and Pt loading on the optimum ionomer loading, as well as the effect of catalyst layer thickness on performance. In all cases, the model predictions matched experimentally observed trends.

Next, In Chapter 5, we apply our improved agglomerate model to optimize the spatial distribution of the various CL constituents to obtain the best performance.

Chapter 5

OPTIMIZATION OF FUNCTIONALLY GRADED PEM FUEL CELL CATALYST LAYER COMPOSITION

Commercialization of PEM fuel cells can be realized only when high performance is achieved at low cost. The cathode catalyst layer of PEM fuel cells remains a major limiter of performance due to sluggish reaction kinetics while also being a significant cost-driver due to the use of expensive platinum catalyst. Therefore, proper design of the PEM fuel cell cathode catalyst layer by optimizing the loading and spatial distribution of its constituent materials is essential to promote commercialization by improving performance and reducing cost.

In Chapter 4, we developed an agglomerate model which correctly accounts for variations in the agglomerate surface area as the CL constituents are varied to provide a better estimate of diffusion losses. Here, this improved agglomerate model is employed to investigate a PEM fuel cell catalyst layer with a functionally-graded composition.

Utilizing the 2D cathode model in Chapter 4, we studied the effects of through-thickness and in-plane grading of CL constituents on polarization behavior. Then we investigated the idea of bidirectionally-graded (simultaneous grading in both in-plane and through-thickness directions) CL composition. Finally, the bidirectionally-graded CL composition is optimized under different operating regimes.

5.1 Investigation of Functionally Graded Catalyst Layer Composition

The CL is a 10-30 μm thick composite structure containing platinum (Pt), carbon support, ionomer electrolyte, gas pores, and liquid water. Within this structure, reactions are catalyzed by Pt while the carbon support and ionomer phase conduct electrons and protons, respectively, and the pores create pathways for reactant gas access and product removal. Consequently, the CL activity consists of multiple competing transport processes which require an optimum loading of catalyst, carbon support, and ionomer distributed within a layer of adequate porosity. For example, whereas a higher Pt loading would improve the reaction rate, it would adversely impact reactant transport due to decreased porosity. Similarly, a higher volume fraction of ionomer would improve proton transport, but also at the cost of reduced reactant transport due to a lower porosity. In this context, several experimental studies [69, 70, 72-75] have been performed to optimize the CL composition to improve the overall PEM fuel cell efficiency.

Uchida et al. [74] experimentally studied the effects of ionomer loading and reported an optimum value for ionomer loading that gave better performance over the entire operating regime. Similarly, Antolini et al. [73] reported an optimum Nafion loading which minimizes activation and ohmic losses. Paganin et al. [70] examined both platinum-to-carbon weight ratio (%Pt|C) and Nafion loading and also reported optimum values for these quantities. Passalacqua et al. [72] unified the optimum Nafion loading results of [2-4] by defining a parameter called NFP (Nafion percentage). They also performed experiments and reported an optimum NFP value of 33% which agrees with the optimum NFP loading of about 33-40% given by [70, 73, 74]. Qi and Kaufman [69] studied the effects of Pt loading and %Pt|C for a CL with

33% NFP which was the optimal Nafion loading according to their experimental data. They reported optimum Pt loadings for 20% and 40% Pt|C ratios.

The literature contains many other experimental studies that focus on the optimization of the CL composition. However, most of these consider a spatially-uniform CL composition. Relatively few experimental studies exist [78-81] that have attempted to investigate spatially-graded CL compositions. [78-80] studied the effect of a graded catalyst loading through the thickness of the CL. Ticianelli et al. [78, 79] reported performance improvement when the catalyst concentration was increased at the membrane/CL interface. Antoine et al. [80] investigated porous and non-porous active layers. For the porous case, they observed performance improvement when the catalyst loading was increased adjacent to the membrane. On the other hand, they reported better performance when the catalyst loading was higher at the gas diffusion layer (GDL)/CL interface for the non-porous electrode. Wilkinson and Pierre [82] studied graded catalyst loading along the length of the gas channel and reported enhanced performance when the catalyst loading was higher towards the inlet. In addition, Xie et al. [81] examined the effect of an NFP gradient through the thickness of the CL and reported improved performance for a higher NFP towards the membrane/CL interface.

Determining an optimal CL composition requires a good understanding of the physical phenomena occurring within the CL. Numerical models serve as a valuable tool to provide detailed insight that might be difficult to observe experimentally. The literature contains several numerical studies [39, 53, 91, 108-110] that have investigated functionally-graded CL compositions. Wang et al. [39] developed a 1D cathode model based on percolation theory that characterizes effective CL properties

and the active reaction area. Employing a macro-homogeneous model for the CL, they investigated the effects of graded NFP through the CL thickness. In agreement with experimental results [81], they reported better performance for high NFP close to the membrane/CL interface. However, their use of the macro-homogeneous approach to model the CL prevented them from predicting the effects of the graded CL in the mass transport regime. Using the classical agglomerate approach, Sun et al. [53] reported improved performance for higher Nafion loading towards the membrane with their 2D cathode model. Song et al. [91] optimized the Pt and NFP distributions through the thickness of the CL with their 1D cathode model which employs a macro-homogeneous approach by considering the effect of liquid water saturation. They obtained the optimum NFP distribution as a linearly increasing function from the membrane to the GDL. For the optimum Pt loading distribution, they obtained a convex increasing function from the membrane to the GDL.

Schwarz and Djilali [55] developed a multiple thin-film agglomerate model to account for the effect of liquid water in the CL. With their improved agglomerate approach they investigated graded catalyst loading cases in three separate directions with a 3D fuel cell model. They reported improved performance when the catalyst loading was higher towards the channel inlet, and when it was higher towards the channel in the lateral in-plane direction. Srinivasarao et al. [109] investigated the graded CL composition in the through-thickness direction by considering multiple stacked CLs within their 2D cathode model. They used the multiple thin-film agglomerate model as in [108] and investigated graded catalyst, NFP and Pt|C distributions separately. In addition, Mukherjee and Wang [110] studied a bi-layer CL with direct numerical simulation. In agreement with the previous studies they also

reported increased performance when the Nafion loading was higher towards the membrane/CL interface.

It should be noted that the fidelity of PEM fuel cell simulations depends critically on the employed CL modeling approach. Employing the improved agglomerate model presented in Chapter 4, in-plane, through-thickness, and bidirectionally-graded CLs were studied as depicted schematically in Fig. 5.1. It should be noted that the effect of CL porosity on surface area, which is captured by the improved agglomerate model, was not accounted for in previous agglomerate models [53, 108, 109] while investigating the graded CL composition. Moreover, none of the previous studies provided guidelines for the range of variation in loading within the graded CL. Most importantly, the multidirectionally-graded CL composition as shown in Fig. 5.1c has not been studied to date.

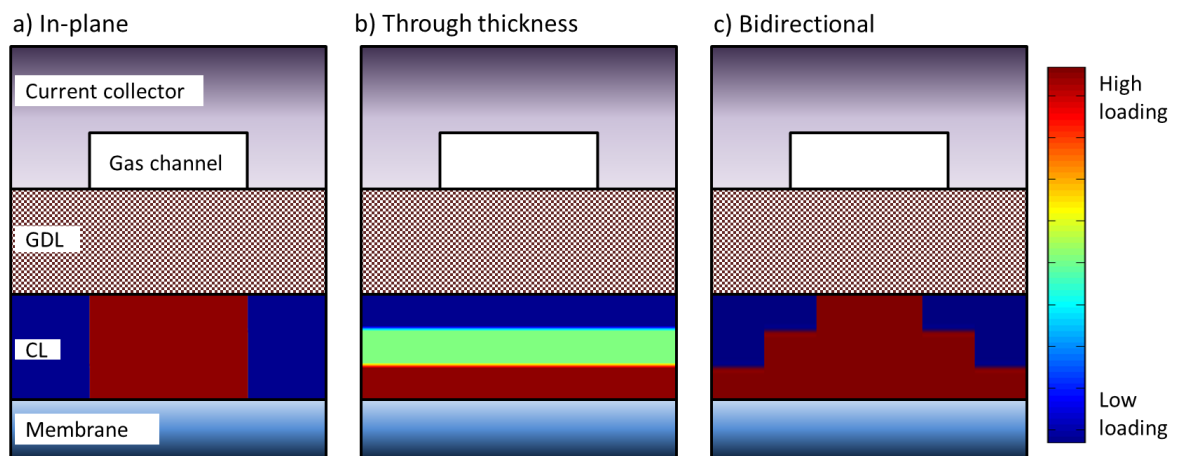


Figure 5.1. Schematic representation of graded CL composition in various directions.

5.1.1 Results and Discussion

Here, we employ the 2D cathode model from Chapter 4 to investigate the effect of graded CL composition on performance. The parameters for the baseline case are listed in Table 5.1.

Table 5.1. Parameter values used in the cathode simulation for the baseline case

Channel width	w_{ch}	1.5 mm
Land width	w_l	1.5 mm
GDL thickness	t_{GDL}	250 μm
CL thickness	t_{CL}	15 μm
Pressure	P	2.04 atm (30 psi)
Temperature	T	353 K
Relative humidity	RH	0.5
Platinum loading	m_{Pt}	0.003 kg m ⁻²
Pt to C weight ratio	Pt C	0.2
Ionomer weight fraction	NFP	0.30
Agglomerate radius	r_{agg}	3E - 6 m
Ionomer film thickness	δ	145E - 9 m
Henry's constant	H	31663 Pa m ³ mol ⁻¹
Reference exchange current density	$i_{0,ref}$	0.00105 A m ⁻² for $V_c \geq 0.8 V$ 0.06948 A m ⁻² for $V_c \leq 0.8 V$
Cathode charge transfer coefficient	α_c	1 for $V_c \geq 0.8 V$ 0.61 for $V_c \leq 0.8 V$
Electron conductivity	σ_s	150 S m ⁻¹
Diffusivities	D_{O_2, N_2}	1.86E - 5 m ² s ⁻¹
	D_{H_2O, N_2}	2.58E - 5 m ² s ⁻¹
	D_{O_2, H_2O}	2.47E - 5 m ² s ⁻¹

It is evident that the concentration and transport of reacting species (ions, electrons, O₂) in the CL is not spatially uniform either in the through-thickness or in-plane directions. For instance, the proton flux is the highest at the membrane/CL interface and drops to zero at the GDL/CL interface. Similarly, the reactant flux is highest at the GDL/CL interface and drops to zero at the membrane/CL interface. Consequently, the reaction rate is also not spatially uniform within the CL. These

observations suggest that more efficient reactions and higher catalyst utilization could be achieved by functionally grading the CL composition to fit the requirements imposed by these non-uniform reaction rates. Increasing the effectiveness of the CL by grading its composition requires a good understanding of the effects of the charge and species transport mechanisms on the reaction rate. In addition, the reaction rate distribution and the overpotential in the CL are highly dependent on the operating regime.

O_2 mass fraction distributions for activation ($V_c = 0.9$ V), ohmic ($V_c = 0.6$ V), and mass transport ($V_c = 0.2$ V) regimes are shown in Fig. 5.2 for the spatially-uniform CL composition case. In the activation regime, the O_2 concentration throughout the CL is high and uniform as the O_2 consumption rate is small compared to the rate of diffusion (Fig. 5.2a). In contrast, the reaction rate greatly exceeds the rate of diffusion in the mass transport regime due to which the under-land region experiences greatly reduced O_2 concentrations (Fig. 5.2c).

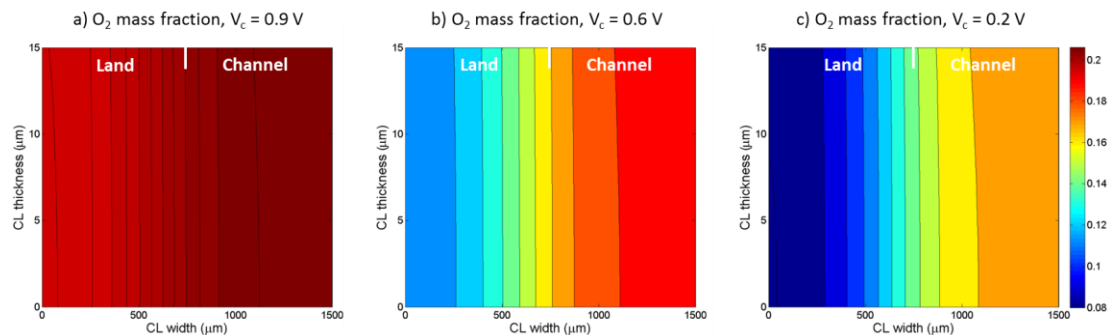


Figure 5.2. O_2 mass fraction distributions in the CL for different operating regimes (spatially-uniform CL composition).

The overpotential is the difference between electron and ionic potentials. It conveys information about the effects of both the electron and ion transport. Figure 5.3 illustrates the overpotential distribution in the CL for activation, ohmic, and mass transport regimes. The overall trend in Fig. 5.3 indicates that the overpotentials are always higher under the land (due to shorter electron paths) and close to the membrane/CL interface (due to higher ion concentrations). In the activation regime, the spatial differences in overpotential are very small; the overpotential is slightly higher under the land than under the channel due to shorter electron paths. Furthermore, the electrolyte potential only varies in the through-thickness direction in the activation regime as can be seen in Fig. 5.4a. In the ohmic loss region, the spatial variations in overpotential become greater mainly due to a higher ionic potential drop as illustrated in Fig. 5.4b. Figure 5.4b indicates that the ionic potential greatly decreases under the channel due to an abundance of reactant which results in higher ion consumption under the channel. In the mass transport regime, the overpotential distribution in Fig. 5.3c closely follows the ionic potential distribution in Fig. 5.4c which shows that ions cannot be consumed under the land at high reaction rates due to a lack of reactant.

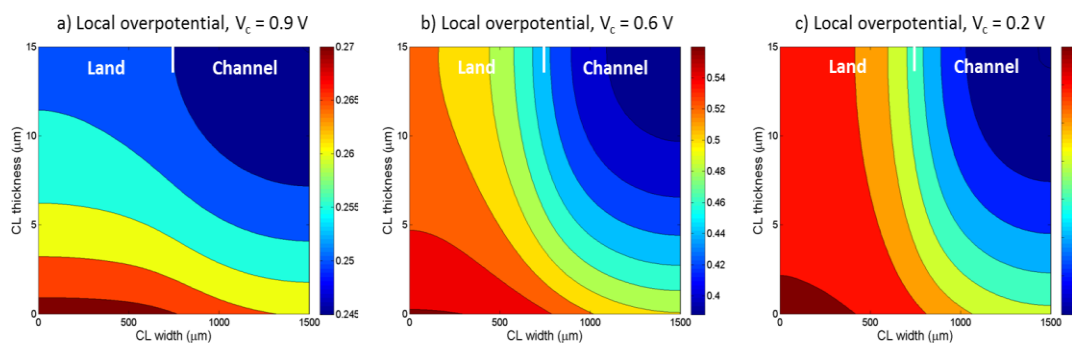


Figure 5.3. Absolute values of overpotential (V) distribution in the CL for different operating regimes (spatially-uniform CL composition).

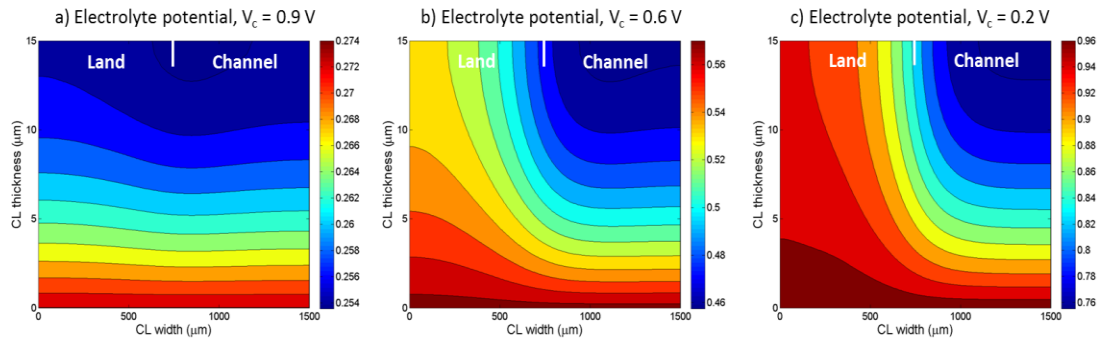


Figure 5.4. Ionic potential (V) distribution in the CL for different operating regimes (spatially-uniform CL composition).

The reaction rate distribution for the spatially-uniform CL composition is shown in Fig. 5.5 for the same three operating regimes. The location of the highest reaction rate can be explained by combining the effects of mass and charge transport presented in Figs. 5.2-5.4. The reaction rate distribution in Fig. 5.5a is almost identical to the overpotential distribution in Fig. 5.3a which implies that the reactions are dominated by local overpotentials in the activation region as the reactant concentration is almost uniform throughout the CL. In the ohmic loss regime, the highest reaction rate is observed at the junction of the land and the channel at the membrane/CL interface (Fig. 5.5b). Thus, it can be inferred that the ohmic loss region is almost equally dominated by both reactant and charge transport such that the highest reaction rate is obtained where all species can be transported easily. When the reaction rate increases further, reactant transport begins to dominate and the highest reaction rate is obtained under the channel (Fig. 5.5c). In Fig. 5.5c, it is also observed that the reaction rate changes only in the in-plane direction under the land due to severe reactant starvation there. Furthermore, close to the GDL/CL interface in Fig. 5.5, higher reaction rates are observed at the channel/land junction which can be attributed to shorter electron paths.

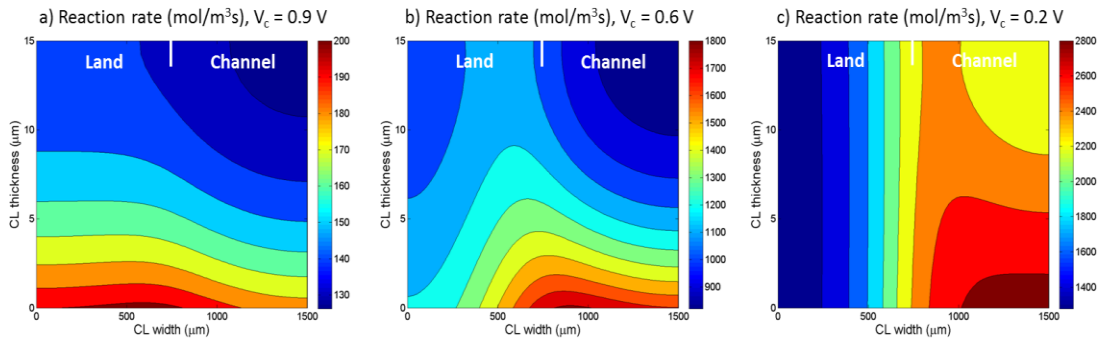


Figure 5.5. Reaction rate ($\text{mol}/\text{m}^3\text{s}$) distribution in the CL for different operating regimes (spatially-uniform CL composition).

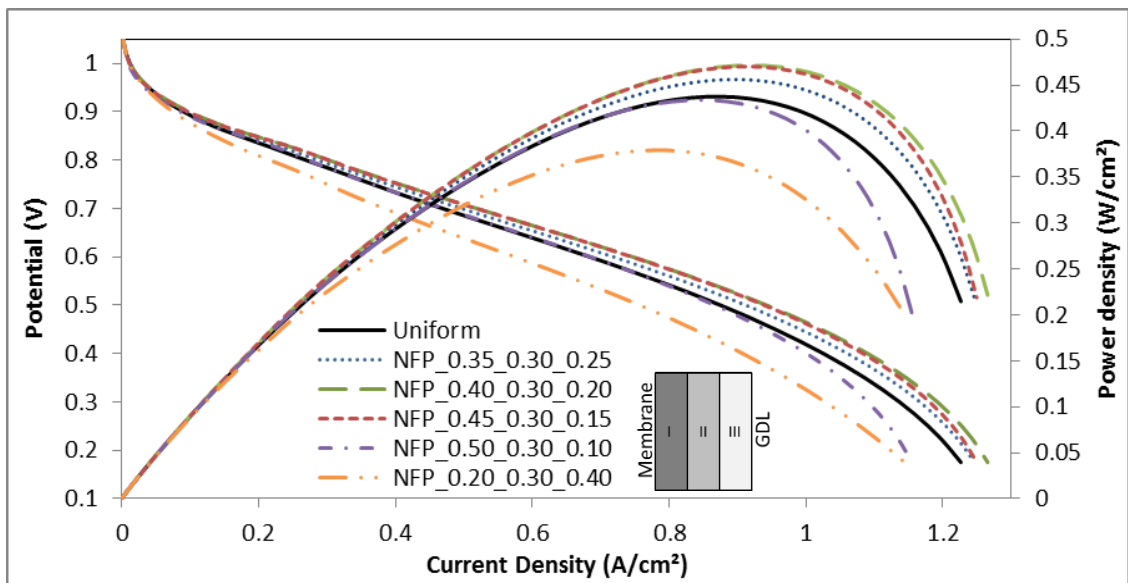


Figure 5.6. Effect of NFP grading in the through-thickness direction on cathode performance; the average NFP is fixed at 30%.

It is important to note that the highest reaction rates are always obtained at the membrane/CL interface showing the importance of ion concentration on reactions. This observation suggests that the CL composition could be graded to improve ion transport. Accordingly, we first investigate the case with graded NFP in the through-thickness direction while fixing the total Nafion content. The CL is divided into three layers of equal thickness, each with a different NFP, but with a constant average NFP

of 30%. The resulting performance curves are presented in Fig. 5.6. Figure 5.6 indicates that the performance is significantly affected by the NFP gradient in through-thickness direction. A higher NFP close to the membrane results in improved performance as was experimentally observed in [81]. Most of the improvement is observed in the ohmic loss region because higher NFP close to the membrane improves the transport of ions migrating into the CL from the membrane. In addition, decreasing NFP close to the GDL improves reactant transport by increasing the porosity. Due to these effects, the maximum power density is improved by about 7% over the baseline case. On the other hand, if we increase the NFP content close to the GDL and decrease the NFP close to the membrane, both the ion and reactant transport are negatively affected, and hence the performance decreases as seen in Fig. 5.6. Furthermore, Fig. 5.6 shows that the NFP close to the membrane should not be increased beyond about 40% due to diffusion limitations. In other words, there is an optimal NFP gradient in the through-thickness direction. In Fig. 5.6 it is observed that diffusion losses first decrease the current generation only in the mass transport region for the high NFP gradient configuration of 0.45_0.30_0.15, whereas they affect the entire polarization curve for the 0.50_0.30_0.10 NFP configuration.

Next, we investigated the graded catalyst loading in through-thickness direction. Similar to the NFP gradient case, the CL is divided into three layers of equal thickness, each with a different catalyst loading, but with a constant average loading of 0.30 mg/cm^2 . The resulting performance curves in Fig. 5.7 indicate that concentrating the catalyst towards the membrane (the ion-enriched region in the CL) increases Pt utilization and improves performance in agreement with the experimental observations of [78-80]. The maximum power density is improved by about 3.2% over

the baseline case. In contrast, biasing the catalyst concentration towards the GDL lowers the performance as well as catalyst utilization as the reaction rates are always lower at the GDL/CL interface. Attempting to improve Pt utilization by further concentrating catalyst at the membrane/CL interface is not feasible because excessive catalyst loading can block the pores and reduce reactant access leading to diffusion losses as observed in Fig. 5.7.

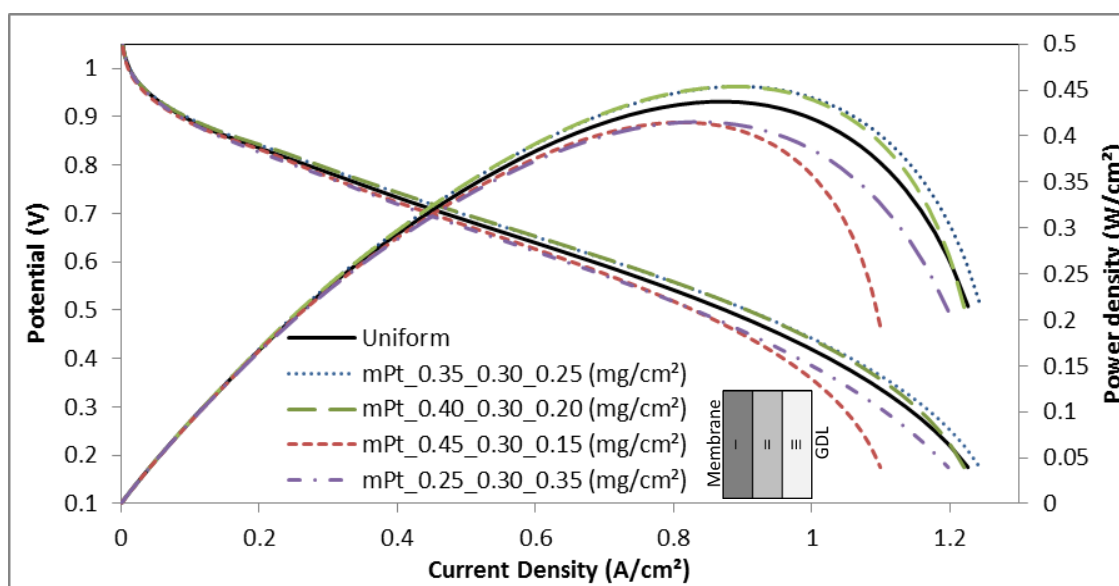


Figure 5.7. Effect of catalyst grading in the through-thickness direction on cathode performance; the average catalyst loading is fixed at 0.30 mg/cm^2 .

We also studied the effect of graded Pt|C weight ratio in the through-thickness direction while fixing the Pt loading, NFP and overall Pt|C ratio. The resulting polarization curves are illustrated in Fig. 5.8. It is important to note that, for the same NFP and Pt loading, a higher Pt|C weight ratio implies lower Nafion and carbon loadings which result in higher porosity. Hence, higher Pt|C would improve reactant transport, whereas lower Pt|C would benefit the ohmic region. Figure 5.8 shows that a lower Pt|C close to the membrane improves performance in agreement with our

previous findings because a lower Pt|C corresponds to a higher Nafion loading which improves ion transport. Concurrently, a higher Pt|C close to the GDL enhances porosity and improves diffusion. The maximum power density is improved by about 12% over baseline for the 0.15_0.25_0.35 Pt|C configuration. This performance improvement is higher than that seen in Fig. 5.6 due to the combined effects of highly improved reactant transport (higher porosity) close to the GDL and higher Nafion loading close to the membrane. On the other hand, the inverse configuration lowers performance as shown in Fig. 5.8.

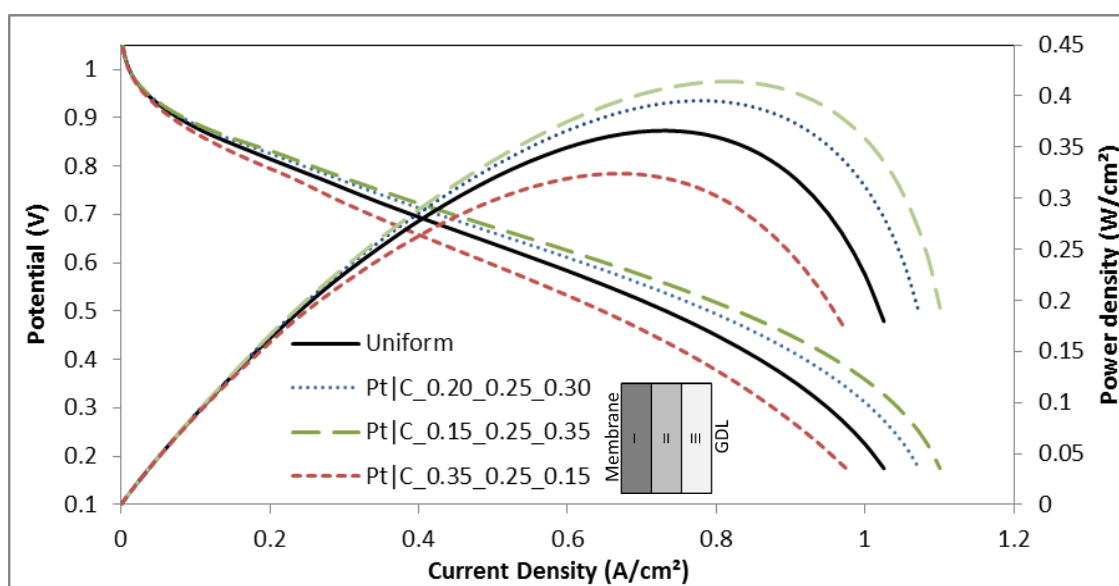


Figure 5.8. Effect of Pt|C grading in the through-thickness direction on cathode performance for constant catalyst loading and NFP. The average Pt|C is fixed at 0.25.

In addition, we studied the case for varying Pt|C ratio but with fixed Pt and Nafion loadings. In this case, varying Pt|C only changes the carbon loading and the porosity. The performance curves in Fig. 5.9 indicate that the diffusion loss region is improved for both configurations. It should be noted that the average porosity

decreases for both configurations from 0.55 to around 0.5 which increases the effective surface area and improves performance in the diffusion loss region. The ohmic loss region is not noticeably improved for either configuration as the electron potential drop in the through-thickness direction is insignificant. Figure 5.9 indicates that a greater performance improvement is observed for the configuration with higher Pt|C ratio close to the GDL; higher Pt|C close to the GDL provides more pathways for reactant access to the active area and improves mass transport.

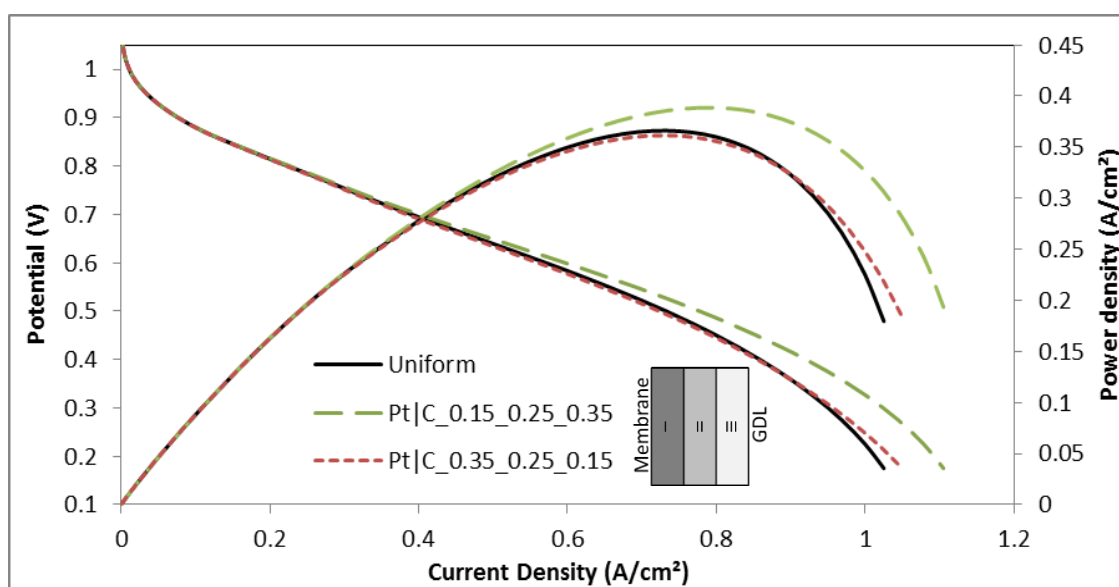


Figure 5.9. Effect of Pt|C grading in the through-thickness direction on cathode performance for constant catalyst and Nafion loadings ($m_{Pt} = 0.3 \text{ mg/cm}^2$, $m_N = 0.514 \text{ mg/cm}^2$). The average Pt|C is fixed at 0.25.

Another important observation from Figs. 5.2-5.5 is that the reaction rates are always higher under the channel than under the land in the mass transport regime. This suggests that the CL composition could be functionally graded in the in-plane direction to improve reactant transport.

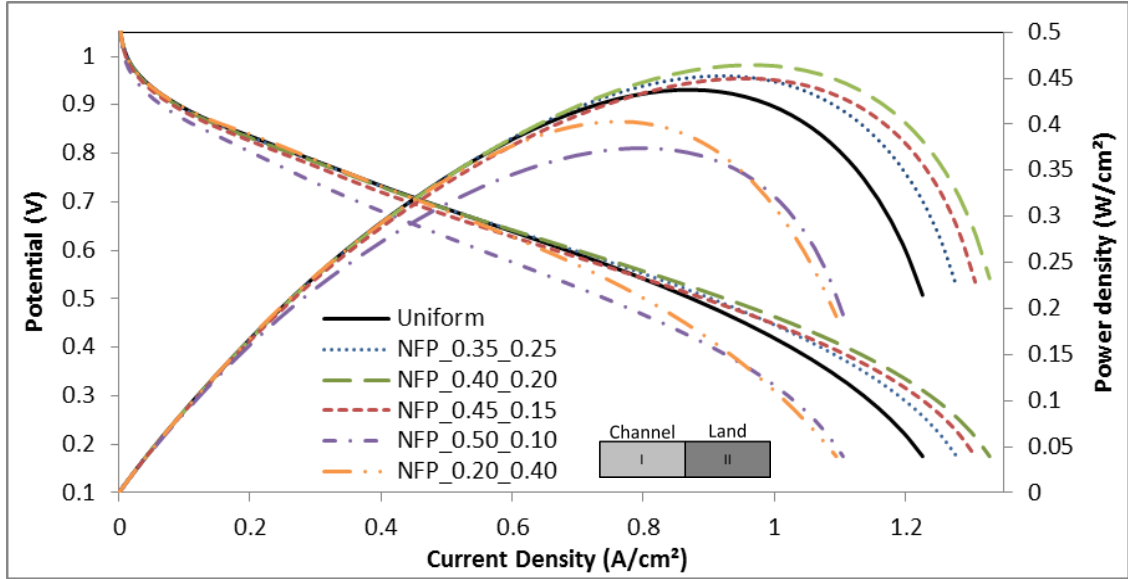


Figure 5.10. Effect of NFP grading in the in-plane direction on cathode performance; the average NFP is fixed at 30%.

We investigate this idea by first grading the NFP in the in-plane direction while fixing the average NFP in the CL at 30%. We consider the case where the CL is divided into two parts (under-channel and under-land) each with different NFP values. The resulting polarization curves in Fig. 5.10 show that higher NFP under the channel improves performance in the diffusion-loss region. Increasing the under-channel NFP improves ion conductivity in the through-thickness direction leading to higher ion transport towards the GDL interface under the channel where the reactant concentration is high enough to consume these ions. Increasing the under-channel NFP improves the power density by about 6.5% over baseline. In contrast, increasing the NFP under the land results in poor performance especially in the diffusion loss region because the under-land region suffers from insufficient O_2 concentration to consume the ions. Figure 5.10 also indicates that increasing the under-channel NFP beyond about 40% exacerbates diffusion losses. The effect of decreased porosity is

first felt only in the diffusion loss region for NFP_0.45_0.15 configuration; further NFP grading causes diffusion losses throughout the polarization curve as see for the NFP_0.50_0.10 configuration.

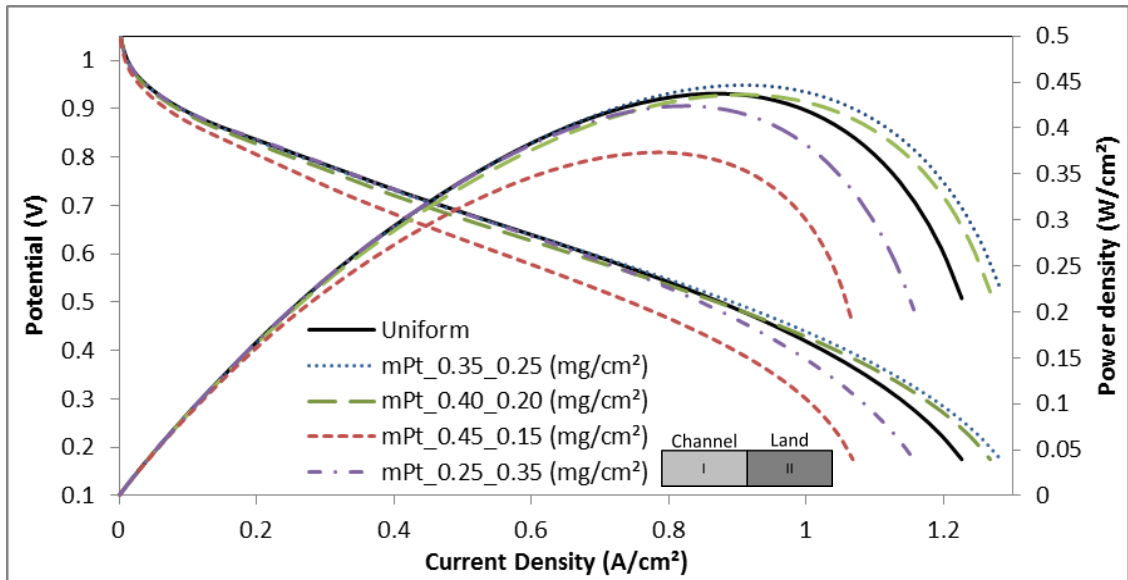


Figure 5.11. Effect of catalyst grading in the in-plane direction on cathode performance; the average catalyst loading is fixed at 0.30 mg/cm^2 .

Next, we examine the effect of catalyst grading in the in-plane direction to improve reactant transport in the mass transport regime. Similar to the laterally-graded NFP case, we divided the CL into under-channel and under-land regions, each with a different catalyst loading. The effect of in-plane catalyst gradient on performance in Fig. 5.11 shows that concentrating the catalyst under the channel improves performance in the diffusion-loss region. The improvement can be attributed to increased catalyst utilization because the under-channel region is enriched with reactant compared to the under-land region especially in the mass transport regime. The maximum power density is increased about 2.5% over baseline by concentrating

the catalyst under the channel. Similar to previous results, there is an optimum gradient for the Pt loading due to diffusion limitations.

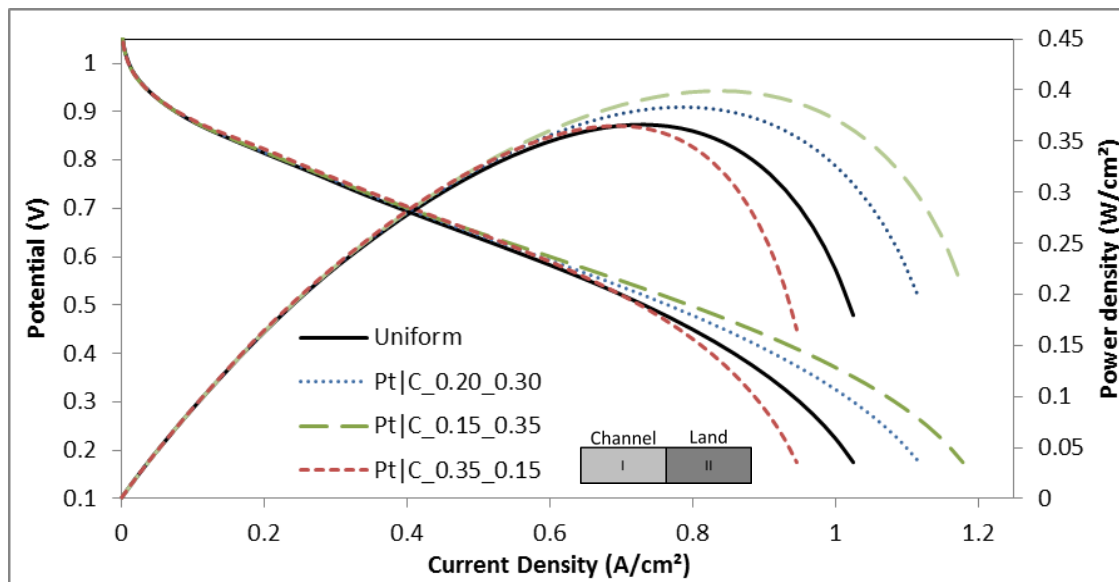


Figure 5.12. Effect of Pt|C grading in the in-plane direction on cathode performance for constant catalyst loading and NFP. The average Pt|C is fixed at 0.25.

Next, we study the effect of Pt|C grading in the in-plane direction while keeping the Pt loading and NFP content constant in the CL. Again, the under-land and under-channel regions of the CL are loaded with different Pt|C ratios. The resulting polarization curves presented in Fig. 5.12 indicate that a lower Pt|C ratio under the channel improves performance especially in the diffusion-loss region. The performance improvement in Fig. 5.12 can be attributed to higher Nafion and carbon loadings under the channel corresponding to a lower Pt|C ratio; then, improved ion conduction under the channel increases performance. The maximum power density is improved about 9.5% over baseline as shown in Fig. 5.12. Although Fig. 5.12 reveals the same trends as in Fig. 5.10, the former yields higher performance improvement

due to better reactant transport under higher porosity. As expected, the inverse configuration results in lower current densities in the mass transport regime.

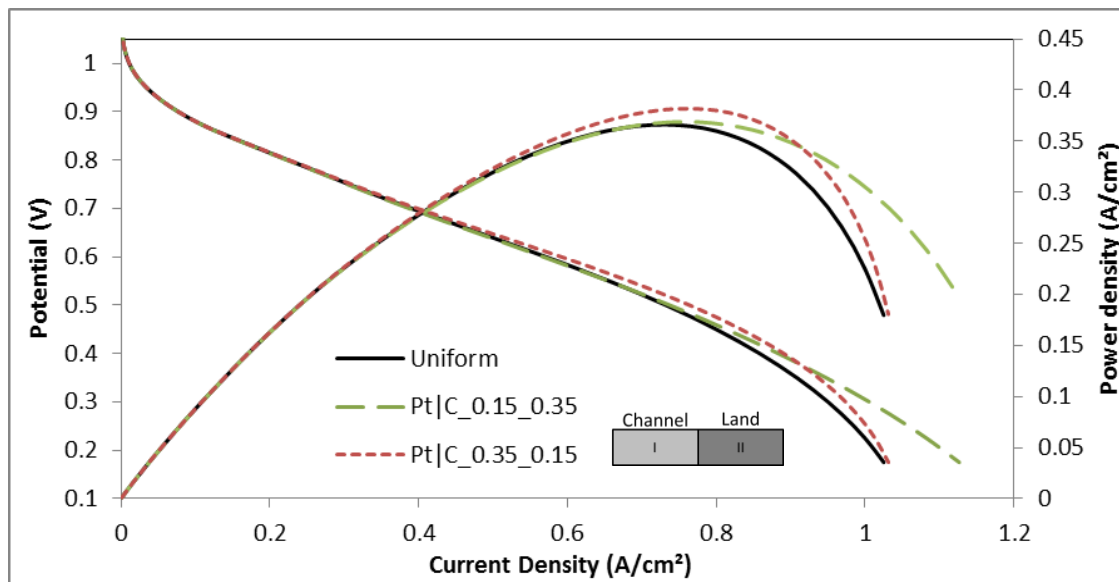


Figure 5.13. Effect of Pt|C grading in the in-plane direction on cathode performance for constant catalyst and Nafion loadings ($mPt = 0.3 \text{ mg/cm}^2$, $mN = 0.514 \text{ mg/cm}^2$). The average Pt|C is fixed at 0.25.

In Fig. 5.12 the effect of graded Pt|C is dominated by the effect of Nafion loading (similar to the case in Fig. 5.10) which varies due to the constant NFP assumption. Therefore, we next isolate the effect of laterally grading the carbon loading by varying the Pt|C ratio at a fixed Nafion loading. The resulting performance curves presented in Fig. 5.13 show that the configuration with higher Pt|C under the land does not experience a noticeable mass transport loss due to a locally lower carbon loading and higher porosity. Hence, such a Pt|C grading improves reactant transport under the land which typically suffers from diffusion losses at high reaction rates. In contrast, the inverse case of lower Pt|C under the land reveals a distinct mass transport loss region. However, the case of lower Pt|C under the land performs slightly better in

the ohmic loss region as the effective under-land surface area is increased over the baseline case. Higher effective surface area under the land increases current generation in the ohmic loss regime leading to higher reaction rates under the land as illustrated in Fig. 5.5b. Due to this improvement in the ohmic loss region, the maximum power density is increased by about 4% over baseline.

So far, we studied the effects of graded CL composition in the through-thickness and in-plane directions separately. Graded composition in the through-thickness direction mainly improves performance in the ohmic loss regime by improving ion transport. Graded CL composition in the in-plane direction mainly improves performance in the mass transport regime by improving reactant transport. It is worthwhile to investigate if grading the CL composition in both directions simultaneously can provide a performance that exceeds the benefits of CL grading solely in either individual direction.

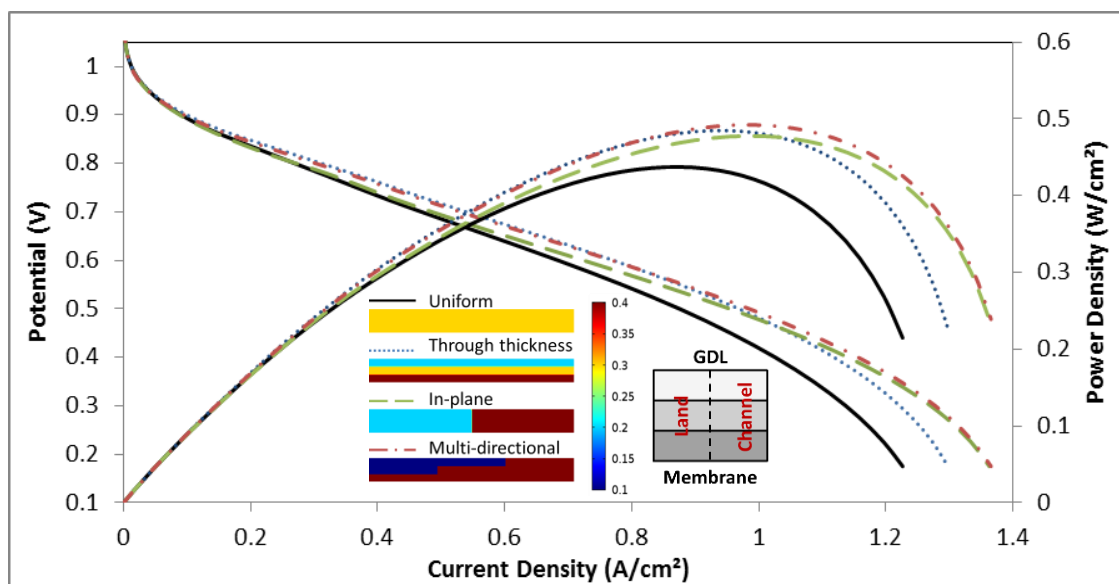


Figure 5.14. Effect of bidirectional NFP grading on performance; the average NFP is fixed at 30%.

Accordingly, we first examined the benefit of grading NFP in the through-thickness direction, the in-plane direction, and bidirectionally as illustrated in Fig. 5.14 while keeping the average NFP constant at 30%. Figure 5.14 indicates that grading the NFP bidirectionally improves performance both in the ohmic and mass transport loss regimes. Bidirectional grading improves ion transport in the through-thickness direction concentrating Nafion close to the membrane. At the same time, concentrating Nafion under the channel improves ion transport and reactant consumption in the mass transport regime for which the reactant is abundant only under the channel.

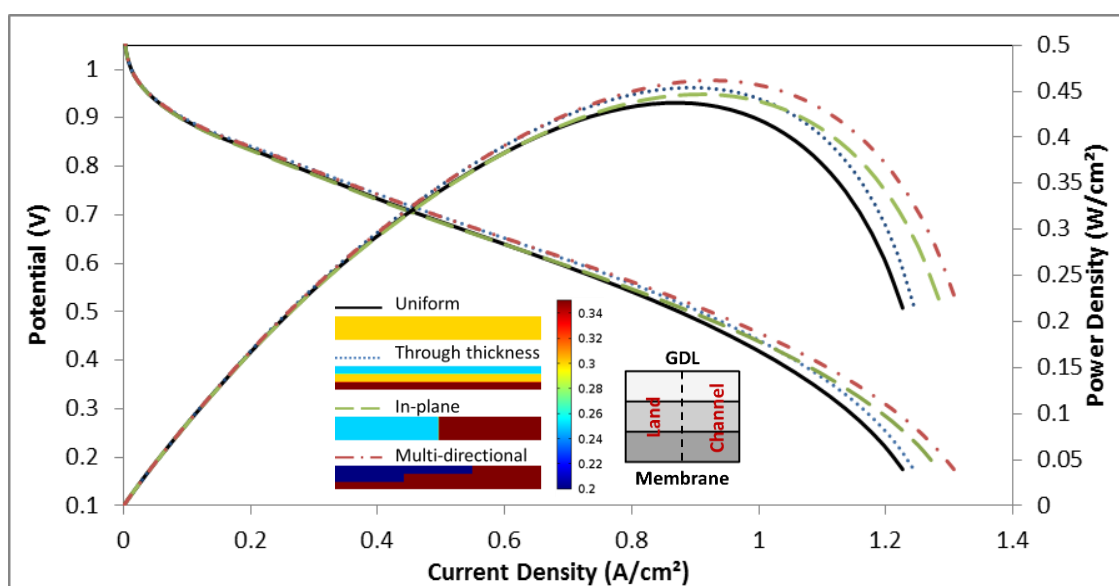


Figure 5.15. Effect of bidirectional catalyst grading on performance; the average catalyst loading is fixed at 0.30 mg/cm^2 .

Finally, we compare the performance obtained by grading the catalyst in the through-thickness direction, the in-plane direction, and bidirectionally as illustrated in Fig. 5.15 while keeping the average catalyst loading constant at 0.30 mg/cm^2 . As expected, the bidirectional grading superposes the positive effects of the through-

thickness and in-plane cases. Therefore, bidirectionally-graded catalyst loading provides improved performance in both ohmic and diffusion-loss regions.

Figures 5.14 and 5.15 indicate that bidirectional grading would be a desirable option if such a CL could be manufactured. In this study, we have only considered one out of several possible multi-directional grading configurations. The results are promising, and suggest that performance could be improved further by simultaneously optimizing the CL composition gradients along multiple directions. Further study is required to optimize the CL topology for superior performance over a range of operating conditions.

5.2 Optimization of Bidirectionally-Graded Catalyst Layer Composition

Numerical models represent a quick and cost-effective way to investigate fuel cell performance and have also played a vital role in improving CL design. Several researchers have used numerical modeling to study the effect of varying CL composition [48, 53, 56, 54, 60], and its spatially-graded distribution [39, 108-110]. On the other hand, only a limited number of studies have attempted to mathematically optimize CL composition and the spatial distribution of its constituent materials as pointed out in previous work section of Chapter 1.

To date, many researchers have investigated spatially-graded CL composition in the through-thickness [39, 91, 93, 109, 110], in-plane [108], or along the channel directions [108]. Only two of these studies optimized the distribution in through thickness direction by dividing the CL in to several zones. In the previous section, we obtained better performance with a bidirectionally-graded CL composition and concluded that the performance could be further improved by optimizing the CL composition gradients along multiple directions.

In this section, employing the improved agglomerate approach in Chapter 4, the CL composition is optimized simultaneously in both the in-plane and through-thickness directions. Furthermore, unlike the previous 1D composition optimization studies [91, 93], employing 2D cathode model in Chapter 4, we consider a continuous distribution of CL materials instead of dividing the CL into discrete sublayers. Employing a gradient-based algorithm, we optimized the bidirectionally-graded catalyst loading, NFP and C loading separately to maximize the current density in the activation, ohmic, and diffusion-loss regions. Performance improvements from bidirectional grading are compared with results from unidirectional grading options (in-plane and through-thickness grading). Next, we perform two-variable optimization for the bidirectionally-graded CL by optimizing NFP-Pt and NFP-C loadings. Finally, we compare the performance improvements from two-variable optimization with the single-variable optimization cases.

5.2.1 Optimization Problem Formulation

The physical model in Chapter 4 describes the CL in terms of agglomerate dimensions, CL thickness (t_{CL}), and three design parameters: catalyst loading (m_{Pt}), Nafion content (NFP), and C loading (m_C). The volume fractions of Pt (ϵ_{Pt}), C (ϵ_C), ionomer (ϵ_N), ionomer in the agglomerate (ϵ_{agg}), and CL porosity (ϵ_v) are calculated as:

$$\epsilon_{Pt} = \frac{m_{Pt}}{t_{CL}\rho_{Pt}} \quad (5.1)$$

$$\epsilon_C = \frac{m_C}{t_{CL}\rho_C} \quad (5.2)$$

$$\epsilon_N = \frac{m_{Pt}(NFP)}{Pt|C(1 - NFP)t_{CL}\rho_N} \text{ where } Pt|C = \frac{m_{Pt}}{m_C + m_{Pt}} \quad (5.3)$$

$$\epsilon_{agg} = 1 - \left(\frac{\epsilon_{Pt} + \epsilon_C}{\frac{4\pi}{3} n \pi r_{agg}^3} \right) \quad (5.4)$$

$$\epsilon_v = 1 - \epsilon_{Pt} - \epsilon_C - \epsilon_N \quad (5.5)$$

The goal of this study is to improve performance by optimizing the bidirectional distribution of these design parameters, whose range of values is selected to be consistent with the catalyst ink formulations reported in experimental studies.

Fuel cell performance is usually assessed from its polarization curve which plots current density against operating voltage. In this study, the fuel cell performance is assessed by the current (I_{CD}) at a fixed operating voltage which can be calculated as:

$$I_{CD} = \frac{2}{(w_l + w_{ch})} \int_0^{(w_l + w_{ch})/2} \int_0^{t_{CL}} \nabla \cdot i \, dx dy \quad (5.6)$$

Therefore, the objective is to maximize the current density at a given operating voltage by optimizing the bidirectionally-graded CL composition for the selected design variables. For a single-variable (x_v) optimization, the optimization statement can be mathematically stated as:

$$\text{maximize: } I_{CD}(x_v) \text{ at } V_c = V_{op} \quad (5.7)$$

$$\text{subject to: } 0 < \epsilon_v < 1; 0 < \epsilon_{Pt} < 1; 0 < \epsilon_C < 1; \quad (5.8)$$

$$0 < \epsilon_N < 1; \frac{1}{n_g} \sum_1^{n_g} x_v = x_{base}$$

where x_v is the variable being optimized, x_{base} is its baseline value (which is set equal to the spatial average of x_v), n_g is total the number of grid points, and V_{op} is the fixed cathode potential. Equation 5.8 ensures that while the spatial distribution of a CL constituent is being optimized, its total loading remains fixed at the baseline value. In addition, we also imposed upper and lower bounds for each variable. The baseline value and range for the three design variables are listed in Table 5.2.

Table 5.2. Baseline value and range for the three optimization variables

Optimization variable	Baseline value	Range
m_{pt} ($kg\ m^{-2}$)	0.003	$0.001 < m_{pt} < 0.015$
m_c ($kg\ m^{-2}$)	0.012	$0.001 < m_c < 0.025$
NFP	0.3	$0.01 < NFP < 0.70$

The CL model is solved using the finite element analysis software COMSOL. Sensitivities for the design variables must be provided in order to conduct a gradient-based optimization. Sensitivity, defined as the change in the objective function due to a change in the design variable, is obtained by differentiating the objective function given in Eq. 5.6 with respect to the optimization variable. The adjoint method is used to calculate sensitivities with linear discretization. Then, the calculated sensitivities and the COMSOL numerical solution are coupled with the MATLAB gradient-based optimization solver “fmincon”. It is also important to note that the sensitivities are filtered to ensure smoothness and mesh-independence as follows [84]:

$$S_f = \frac{1}{x_v \sum_{i=1}^N H_i} \sum_{i=1}^{n_g} H_i x_v \frac{dI_{CD}}{dx_v} \quad (5.9)$$

where H_i is the convolution operator (weight factor) which is expressed as [84]:

$$H_i = r_{min} - dist(k, i), \quad \{i \in n_g \mid dist(k, i) \leq r_{min}\} \quad (5.10)$$

where r_{min} is the filter radius, k and i are the indices for the grid points, and $dist(k, i)$ is the separation between the two points.

The parameter values used in the numerical simulations are given in Table 5.1.

5.2.2 Results and Discussion

As previously mentioned in the previous section, the reaction rate is non-uniformly distributed in as in Fig. 5.5 depending on the concentration of the reacting species (O_2 , H^+ , e^-). The reaction rates are always higher at the membrane/CL interface irrespective of the operating regime because of high ion concentration as in Fig. 5.5. In the lateral direction, the reaction rate is dominated by the O_2 and e^- transport and shifts from under-land to under-channel region.

So the non-uniform nature of the reactions facilitates to improve performance by grading the CL composition as illustrated in the previous section. Here, the continuous distribution of bidirectionally-graded CL composition is optimized to improve fuel cell performance. It is important to note that for all cases although the local volume fraction of each constituent is being varied to maximize performance, the spatially-averaged volume fraction of each CL constituent is set equal to the baseline value in Table 5.2.

First, we optimize NFP under three different operating regimes for uniform Pt and C loadings. Figure 5.16 shows the optimum bidirectional NFP distributions for the activation ($V_c = 0.9$ V), ohmic ($V_c = 0.6$ V), and diffusion loss ($V_c = 0.2$ V) regions. It is apparent that the optimum NFP distribution depends strongly on the operating regime. NFP values are found to vary between 1% and 40% which means that some zones require very little NFP whereas others require high NFP loadings. The overall trend in Fig. 5.16 indicates that the zone of high NFP shifts from under the land to

under the channel with the decreasing cathode potential. In the activation regime, the NFP loading is concentrated towards the membrane/CL interface in the through-thickness direction with a slight bias towards the under-land region in the in-plane direction. In the ohmic loss regime, the NFP loading while still higher along the membrane/CL interface becomes most concentrated under the channel/land junction. In the diffusion loss regime, the NFP loading does not vary much in the through-thickness direction, but becomes strongly concentrated under the channel in the in-plane direction.

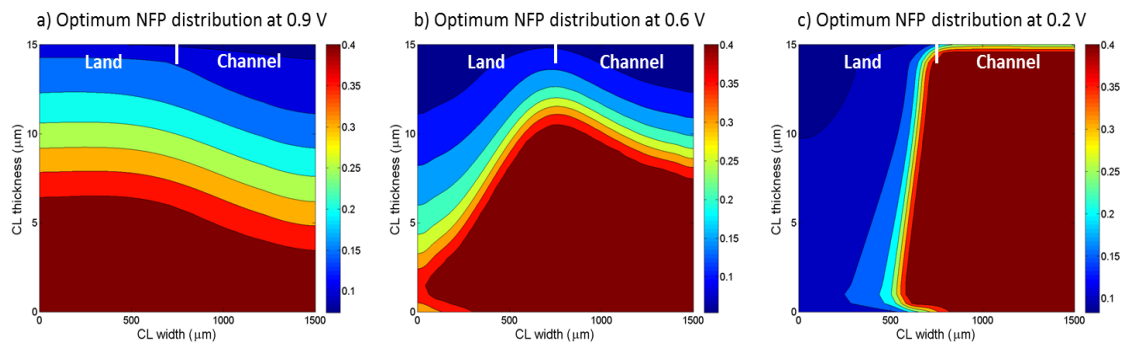


Figure 5.16. Optimum NFP distributions under different operating regimes for uniform Pt and C loadings

Performance improvements over the baseline case resulting from the bidirectionally-optimized NFP distributions in Fig. 5.16 are compared next in Fig. 5.17 with three unidirectionally-graded CL cases. The three unidirectionally-graded cases in Fig. 5.17 are: (1) Lateral-channel which refers to NFP grading in the lateral direction with NFP = 0.2 under the land, and NFP = 0.4 under the channel; (2) lateral-land which also refers to NFP grading in the lateral direction but with NFP = 0.4 under the land, and NFP = 0.2 under the channel; and (3) through-thickness which refers to three discrete CL sublayers with NFP loadings of 0.4, 0.3, and 0.2, with the highest

loading at the membrane/CL interface. Figure 5.17 confirms that bidirectionally-optimized grading is superior to all the unidirectional grading options under all operating regimes with a performance improvement over baseline of about 12-15%. It is also important to realize that the highest improvement is observed under the ohmic loss regime as NFP improves ion transport which is responsible for the majority of ohmic losses. Through-thickness grading with higher NFP close to the membrane improves performance by improving ion conduction from the membrane/CL interface and reactant transport at the GDL/CL interface, while lateral-channel grading improves performance by facilitating ion transport under the channel where O_2 concentration is high (for the diffusion loss regime). On the other hand, bidirectional grading of NFP facilitates improved ion transport where all the reacting species are abundant and reaction rates are high.

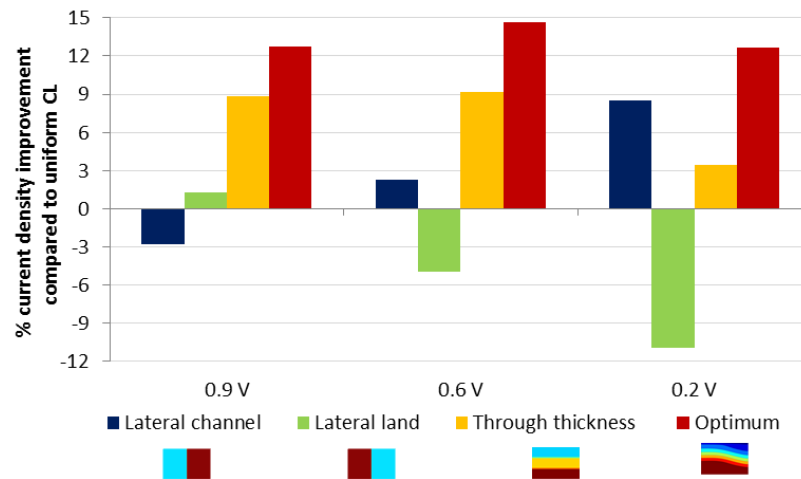


Figure 5.17. Performance improvement over the baseline case for two in-plane, through-thickness, and bidirectionally-optimized NFP distributions under different operating regimes for uniform Pt and C loadings

Reaction rates corresponding to the optimum NFP distributions in Fig. 5.16 are illustrated in Fig. 5.18. The beneficial effect of optimizing NFP grading can be assessed by comparing the reaction rates in Fig. 5.18 with those of the spatially-uniform case in Fig. 5.5. Figure 5.18 indicates a greater range of performance (higher highs and lower lows) for each operating regime compared to Fig. 5.5. For example, higher reaction rates are observed in the mid-section of the CL in Figs. 5.18a and 5.18b compared to Figs. 5.5a and 5.5c. This can be attributed to better ion transport which is improved by locating more NFP at the high and intermediate reaction-rate zones for the spatially-uniform baseline case. Figure 5.18c shows laterally decreasing reaction rates from under the channel to under the land. While Fig. 5.5c shows a through-thickness reaction-rate gradient under the channel, Fig. 5.18c indicates a uniformly high reaction-rate zone under the channel. This can be attributed to improved ion transport in the O_2 -abundant under-channel region for the optimized case. This effect is primarily responsible for the performance improvement.

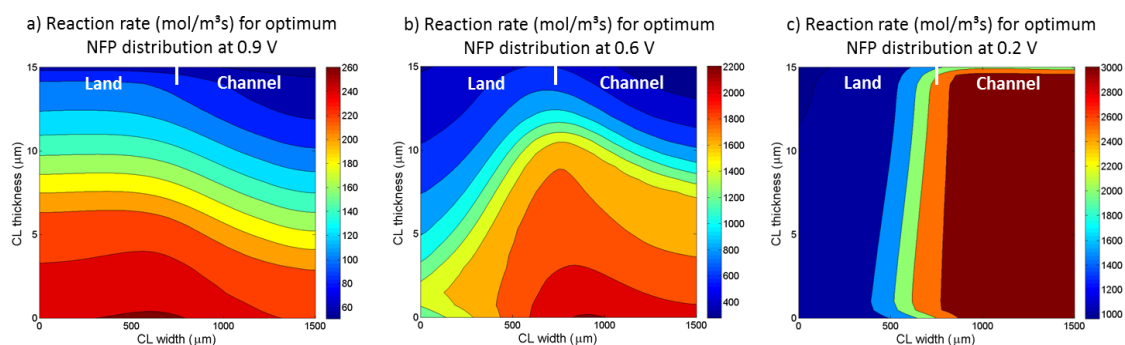


Figure 5.18. Reaction rate (mol/m^3s) distributions corresponding to the optimum NFP distributions in Fig. 5.16

Next, catalyst loading is bidirectionally-optimized for uniform NFP and C loadings under the three operating regimes as shown in Fig. 5.19. Figure 5.19 indicates

that optimal catalyst distribution also depends strongly on the operating regime. The optimized catalyst loading is found to vary between 0.1 to 0.35 mg cm^{-2} across all operating regimes, Similar to the trend for optimal NFP distribution, catalyst loading shifts from under the land to under the channel as the cathode potential decreases. In the activation regime, the zone of high catalyst concentration is observed to extend from the membrane/CL interface to beyond the CL midplane, with a bias towards the under-land region. Catalyst concentration increases under the channel/land junction under the ohmic-loss regime. Finally, Fig. 5.19c shows that the optimum Pt distribution for the diffusion-loss regime reflects a mostly lateral grading with higher Pt loading under the channel.

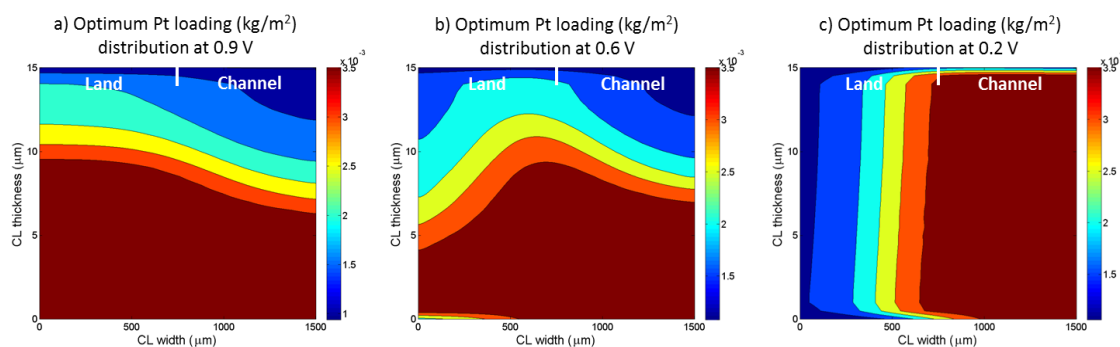


Figure 5.19. Optimum Pt distributions under different operating regimes for uniform NFP and C loadings

Performance improvements obtained with the bidirectionally-optimized catalyst loading are compared with unidirectionally-graded catalyst loadings in Fig. 5.20. The three unidirectionally-graded cases in Fig. 5.20 are: (1) Lateral-channel with a Pt loading of 0.25 mg cm^{-2} under the land, and 0.35 mg cm^{-2} under the channel; (2) lateral-land with a Pt loading of 0.35 mg cm^{-2} under the land, and 0.25 mg cm^{-2} under the channel; and (3) through-thickness with three discrete CL sublayers with Pt

loadings of 0.35, 0.30, and 0.25 mg cm⁻², with the highest loading at the membrane/CL interface. Results show that for all operating regimes the bidirectionally-graded catalyst performs better than any unidirectional grading option with a performance improvement of about 8-10%. It is not surprising that the highest improvement is seen for the activation regime as catalyst's role is to reduce the activation energy for the chemical reactions. Through-thickness catalyst grading improves catalyst utilization by concentrating Pt in the ion-enriched region close to the membrane, thereby improving the performance. Lateral catalyst grading also improves catalyst utilization by concentrating Pt in the O₂-enriched region (under the channel for the diffusion-loss regime), or e⁻-enriched region (under the land for the activation regime). However, bidirectional grading of Pt improves catalyst utilization even further by selectively placing catalyst at the highly reactive regions in the CL.

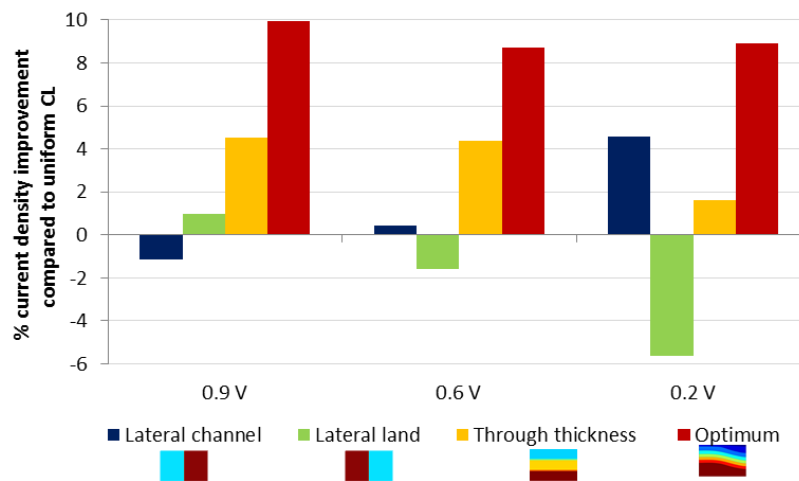


Figure 5.20. Performance improvement over the baseline case for two in-plane, through-thickness, and bidirectionally-optimized Pt distributions under different operating regimes for uniform NFP and C loadings

Reaction rates corresponding to the optimum catalyst loading distributions in Fig. 5.19 are shown in Fig. 5.21. In comparison with the reaction rates for the baseline

case in Fig. 5.5, the reaction rates in Fig. 5.21 display a greater range of values under all operating regimes. In the activation and ohmic loss regimes (Figs. 5.21a and 5.21b) reaction rates close to the membrane/CL interface and in the mid-section of the CL improved with respect to Figs. 5.5a and 5.5b. This can be attributed to improved catalyst utilization by concentrating Pt in the high and intermediate reaction-rate zones in Figs. 5.5a and 5.5b. Similarly, concentrating Pt in the high and intermediate reaction-rate regions in Fig. 5.5c improves the catalyst utilization and hence the reaction rates as seen in Fig. 5.21c.

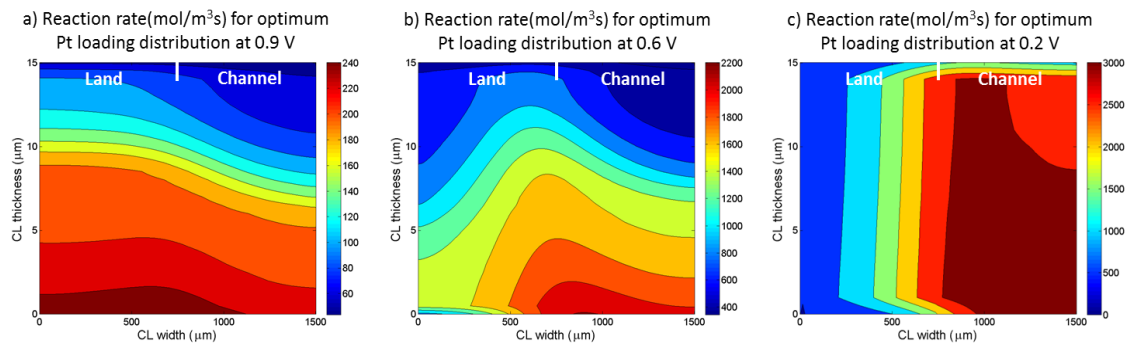


Figure 5.21. Reaction rate (mol/m^3s) distributions corresponding to the optimum Pt distributions in Fig. 5.19

Next, we optimized the spatial distribution of C for uniform NFP and Pt loadings as shown in Fig. 5.22. Similar to the previously obtained optimum NFP and Pt distributions, Fig. 5.22 indicates that the optimum C distribution also depends strongly on the operating regime. In addition, the high C zone shifts from under the land to under the channel with decreasing cathode potential in response to the shifting reaction-rate profile. In the activation loss regime (Fig. 5.22a), the C loading gradient is primarily in the through-thickness direction from the membrane to the GDL with slightly higher concentration under the land. In the ohmic loss regime (Fig. 5.22b), C

loading is concentrated under the channel/land junction with a gradient from the membrane to the GDL interface. Figure 5.22c indicates higher C loading under the channel and close to membrane/CL interface in diffusion-loss regime. In addition, Fig. 5.22c shows both lateral and through-thickness gradients from channel to land and membrane to GDL interfaces, respectively.

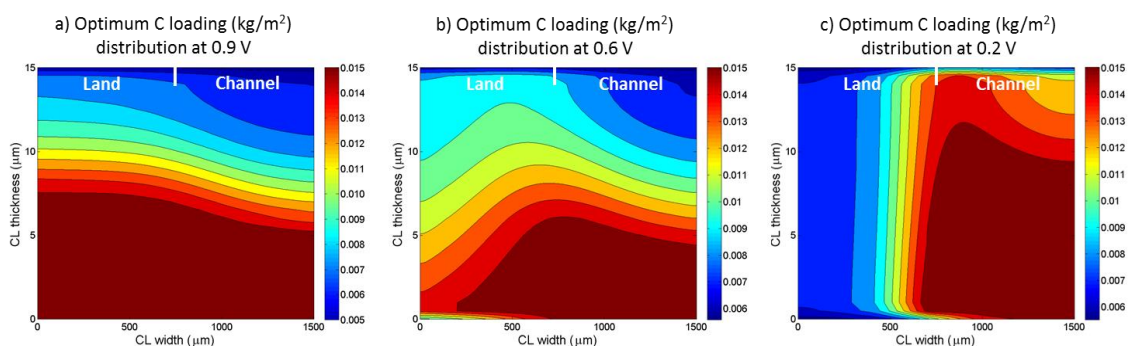


Figure 5.22. Optimum C distributions under different operating regimes for uniform NFP and Pt loadings

The corresponding performance improvements over the baseline case are shown in Fig. 5.23 along with the improvements obtained for three unidirectionally-graded C loadings. The three unidirectionally-graded cases in Fig. 5.23 are: (1) Lateral-channel with a C loading of 0.9 mg cm^{-2} under the land, and 1.5 mg cm^{-2} under the channel; (2) lateral-land with a C loading of 1.5 mg cm^{-2} under the land, and 0.9 mg cm^{-2} under the channel; and (3) through-thickness with three discrete CL sublayers with C loadings of 1.5, 1.2, and 0.9 mg cm^{-2} , with the highest loading at the membrane/CL interface. Figure 5.23 indicates that the bidirectionally-graded C distribution improves the performance by more than 6% in all operating regimes. Through-thickness grading of C towards the membrane/CL interface facilitates better reactant transport (by decreasing the porosity at the GDL/CL interface) while the

lateral grading improves e^- transport at the O_2 -enriched region (by concentrating C under the channel). Overall, bidirectional grading utilizes C better by locating it in the high reaction-rate zones in any direction under each operating regime. Therefore, the bidirectionally-graded C distributions are superior to the unidirectional grading options in terms of performance improvement.

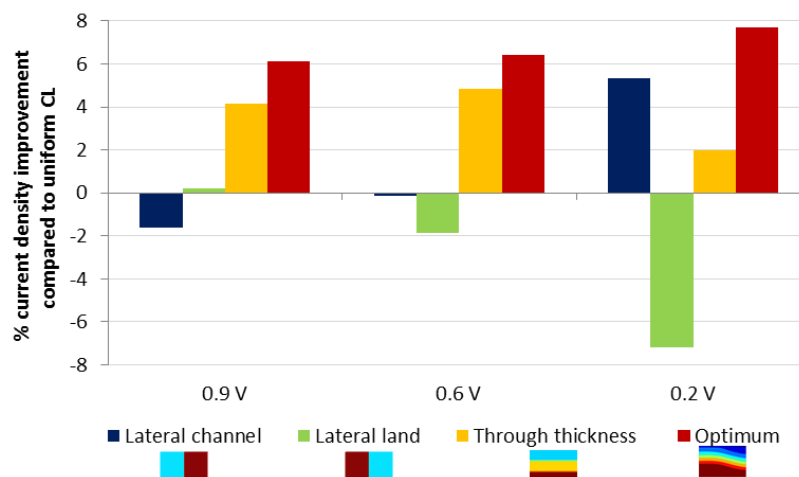


Figure 5.23. Performance improvement over the baseline case for two in-plane, through-thickness, and bidirectionally-optimized C distributions under different operating regimes for uniform NFP and Pt loadings

Reaction rates corresponding to the optimum C distributions in Fig. 5.22 are illustrated in Fig. 5.24. In comparison with Fig. 5.5, it is seen that high and intermediate reaction rates are improved under all operating regimes in Fig. 5.24. In addition, high and intermediate reaction-rate zones are enlarged with respect to the baseline case of spatially-uniform CL. Due to improved reactant transport at the GDL/CL interface and better e^- transport in the ion-enriched zones, higher reaction rates are observed at the membrane/CL interface, and in the mid-section of the CL for the activation and ohmic-loss regimes. In the diffusion-loss regime, e^- transport is improved at the ion- and O_2 -enriched zones, hence higher reaction rates are obtained

under the channel close to the membrane. In addition, a lighter C loading close to the GDL/CL interface (Fig. 5.22c) improves reactant transport which increases the reaction rate.

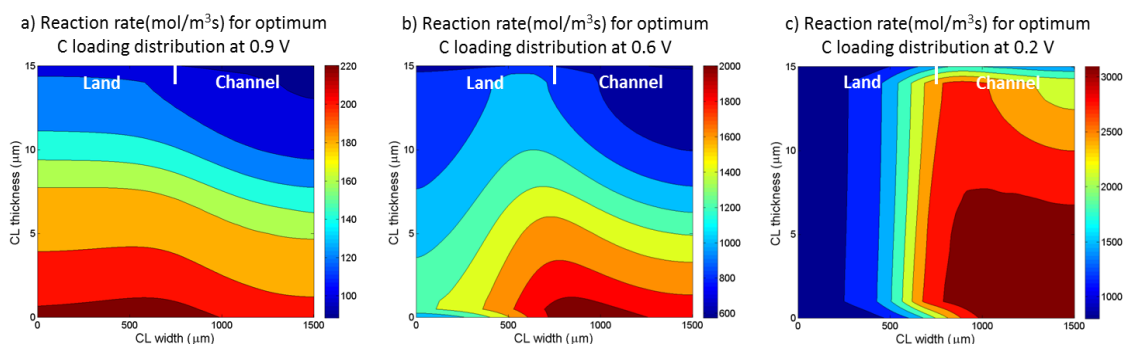


Figure 5.24. Reaction rate (mol/m^3s) distributions corresponding to the optimum C distributions in Fig. 5.22.

So far we have investigated optimal distributions of CL constituents individually, and shown that the highest performance improvement is obtained by bidirectionally optimizing NFP. Next, we examine the joint optimization of two constituents: NFP with Pt, and NFP with C.

For uniform C loading, optimal NFP/Pt distributions under the three operating regimes are shown in Fig. 5.25. Figure 5.25b shows that zone of high NFP concentration adjacent to the membrane/CL interface shifts from under the land to under the channel in a manner similar to Fig. 5.13. On the other hand, the Pt distribution is quite different from the one in Fig. 5.19. For the first time, we see that the highest Pt concentration is located not at the edge of the CL, but rather at its mid-section. Moreover, the catalyst contours exhibit some curvature in the through-thickness direction in Figs. 5.25a and 5.25b, and in the lateral direction in Fig. 5.25c. It can be inferred that the catalyst loading is slightly decreased in the high NFP zones,

and the highest catalyst concentration occurs in the intermediate NFP zones. A similar trend was also reported in the 1D optimization study of Song et al. [91]. This interaction can be explained by the effect of porosity and the dominant nature of the NFP distribution over the catalyst distribution. NFP can be considered as dominant because a higher performance improvement was obtained with the optimum NFP distribution than the catalyst distribution. Therefore, the catalyst loading is decreased in the high NFP zones to maintain the porosity above a certain level. Performance begins to fall when the porosity is too small due to insufficient reactant transport; the effect of porosity is modeled here based on effective diffusivities and the effective agglomerate surface area calculation method presented in Chapter 4.

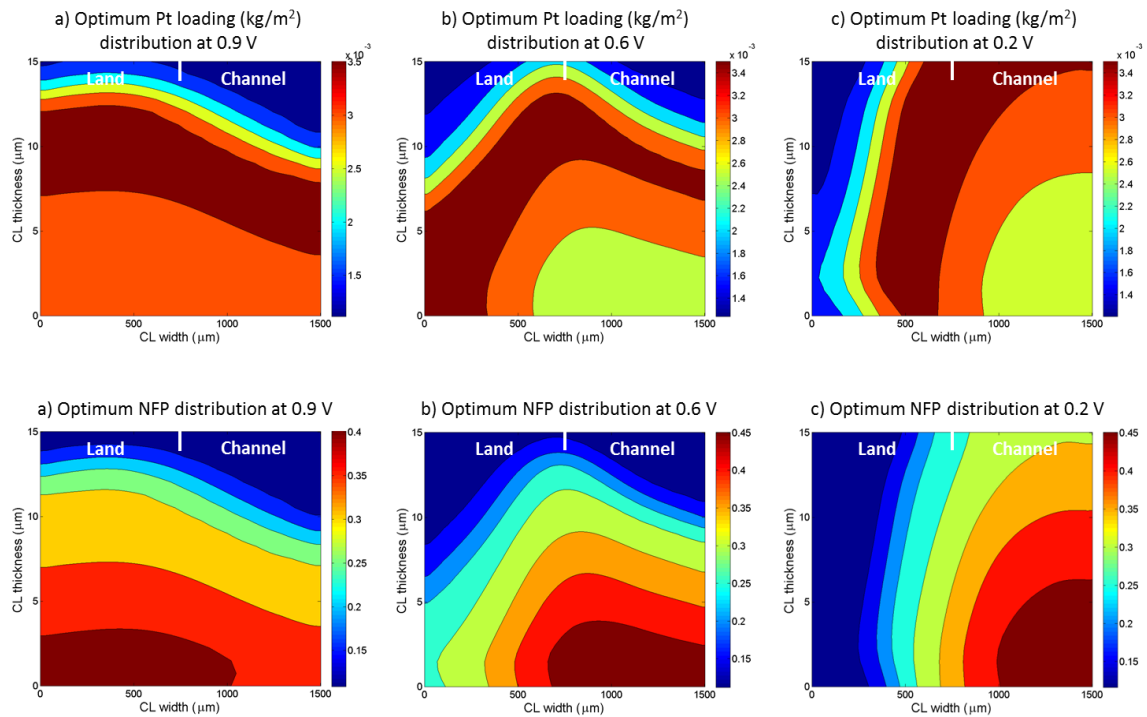


Figure 5.25. Bidirectionally-optimized (a) Pt, and (b) NFP distributions under different operating regimes obtained by two-variable Pt/NFP optimization for uniform C loading

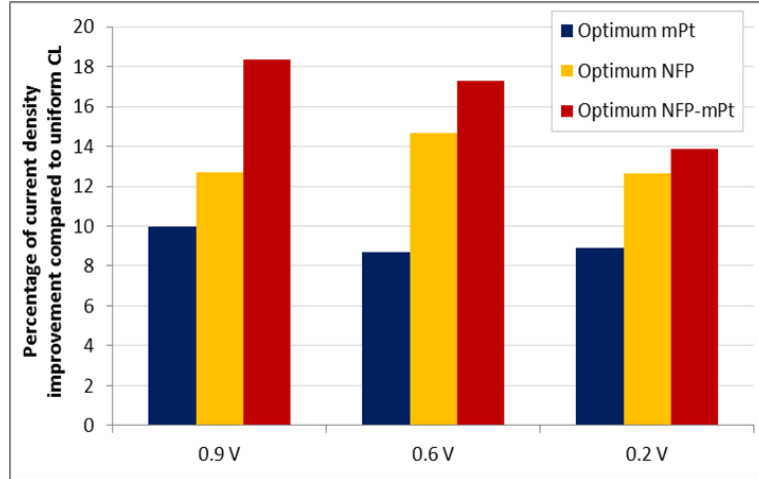


Figure 5.26. Performance improvement over the baseline case for single-variable Pt and NFP optimization, and two-variable NFP/Pt optimization under different operating regimes

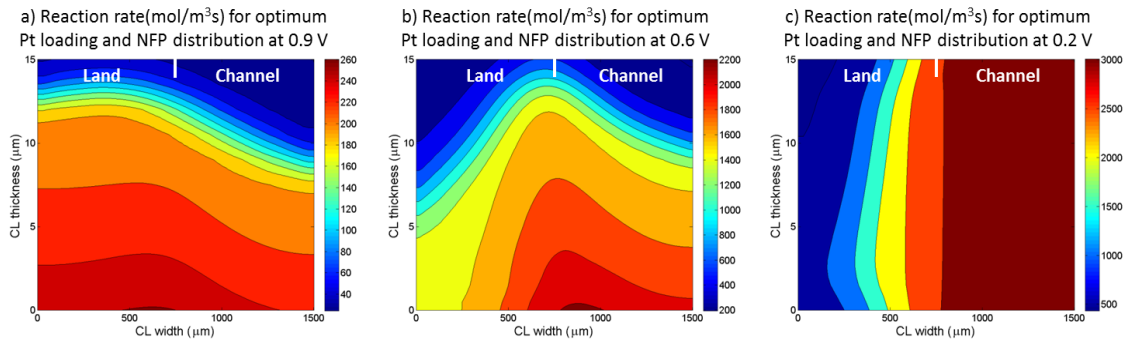


Figure 5.27. Reaction rate ($\text{mol}/\text{m}^3\text{s}$) distributions corresponding to the optimum NFP/Pt distributions in Fig. 5.25

Performance improvements corresponding to the optimized NFP/Pt distributions in Fig. 5.25 are presented in Fig. 5.26 along with the improvements obtained with single-variable optimizations. Figure 5.26 shows higher performance for the two-variable optimization in comparison to either single-variable optimization. The highest improvement for the optimum NFP/Pt case is obtained for the activation regime. The band of high Pt concentration in the mid-section of the CL decreases the

activation energy in the region where ion concentration is improved by better ion transport resulting from higher NFP at the membrane/CL interface.

Figure 5.27 shows the reaction rate distributions corresponding to the optimum NFP/Pt distributions in Fig. 5.25. The reaction rate distributions in Fig. 5.27 look very similar to those obtained for the optimum NFP in Fig. 5.18. In comparison to Fig. 5.18a, reaction rates in the mid-section of the CL are improved significantly due to the high catalyst loading there. In addition, slightly higher intermediate reaction rates are observed in Figs. 5.27b and 5.27c with respect to Figs. 5.18b and 5.18c which can be attributed to the high concentration of catalyst at the intermediate reaction-rate zones.

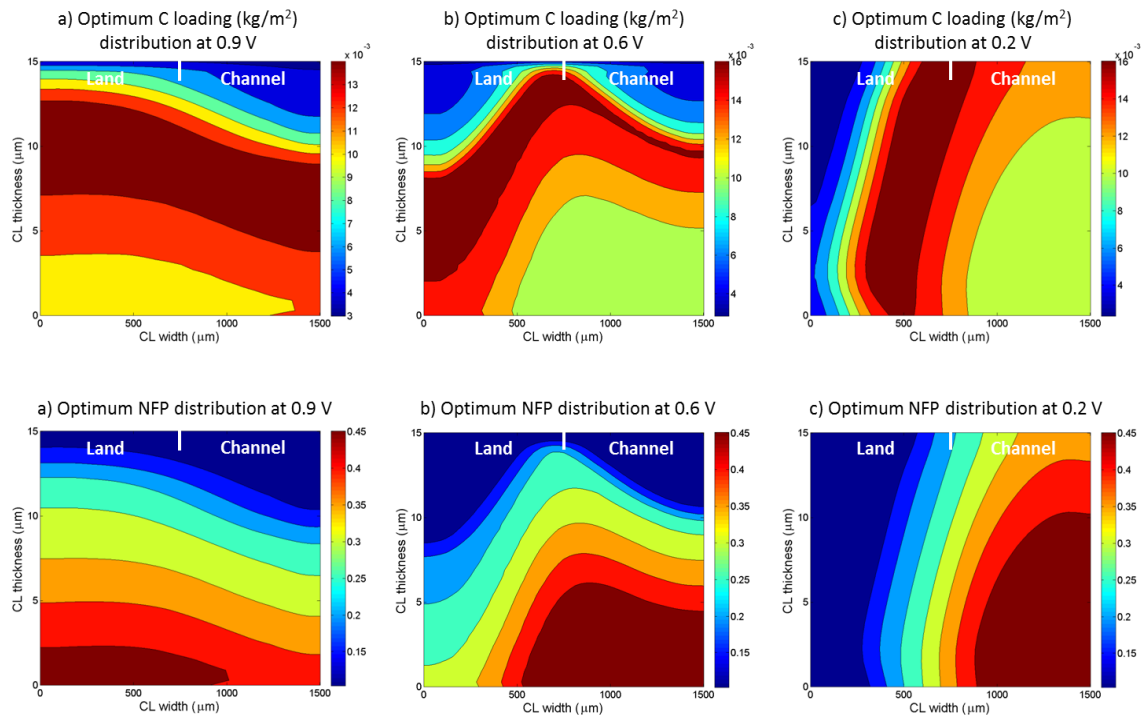


Figure 5.28. Bidirectionally-optimized (a) C, and (b) NFP distributions under different operating regimes obtained by two-variable C/NFP optimization for uniform Pt loading

Finally, results for the optimal NFP/C distributions with uniform Pt loading are presented in Fig. 5.28. Following the trend in Fig. 5.25, the NFP distribution primarily determines the overall CL composition for the NFP/C optimization. Therefore, the NFP distribution in Fig. 5.28b is similar to the single-variable NFP optimization result in Fig. 5.16. In order to maintain an adequate porosity, the C contours again exhibit curvature in the through-thickness direction for the activation and ohmic-loss regimes, and in the lateral direction for the diffusion-loss regime.

Reaction rate improvements are presented in Fig. 5.29 for the optimum NFP/C distributions along with the single-variable optimization results. Two-variable NFP/C optimization clearly improves performances over the single-variable cases under all three operating regimes. In addition, the highest improvement is obtained for the ohmic-loss regime because the jointly optimized NFP and C distributions work together to further improve charge transport.

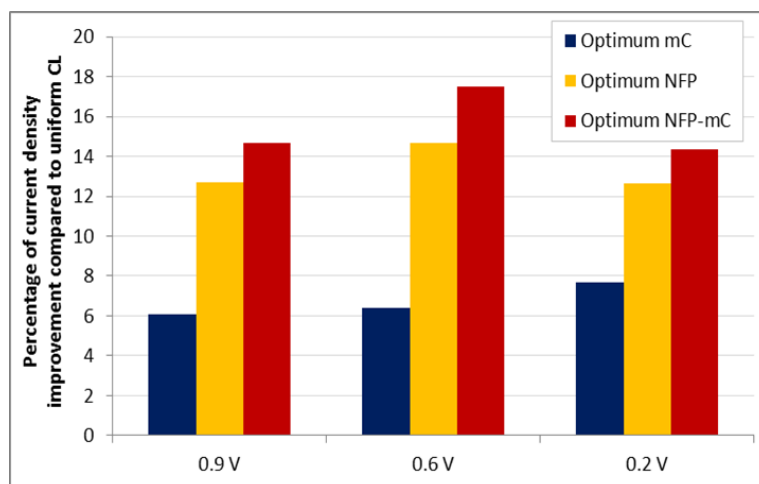


Figure 5.29. Performance improvement over the baseline case for single-variable C and NFP optimization, and two-variable NFP/C optimization under different operating regimes

The reaction rates corresponding to the optimum NFP/C distributions in Fig. 5.28 are shown in Fig. 5.30. Since the NFP distribution is the dominant factor in the two-variable optimization, the reaction rate distributions look similar to Figs. 5.18 and 5.27. In comparison to Fig. 5.27, a larger high reaction-rate zone is observed for the ohmic-loss regime. This can be attributed to the beneficial effect of C optimization on e^- transport which is significant in the ohmic-loss regime. In the activation regime, smaller intermediate reaction-rate zones are observed in Fig. 5.30a when compared to Fig. 5.27a. This clarifies the importance of the catalyst in lowering the activation energy for the reactions. As previously mentioned, porosity is highly important for reactant transport especially in the diffusion-loss regime. The Pt and C distributions in Figs. 5.27c and 5.30c, respectively, are graded such that they provide optimum porosity in conjunction with the dominant NFP configuration. Therefore, Figs. 5.27c and 5.30c look very similar to each other.

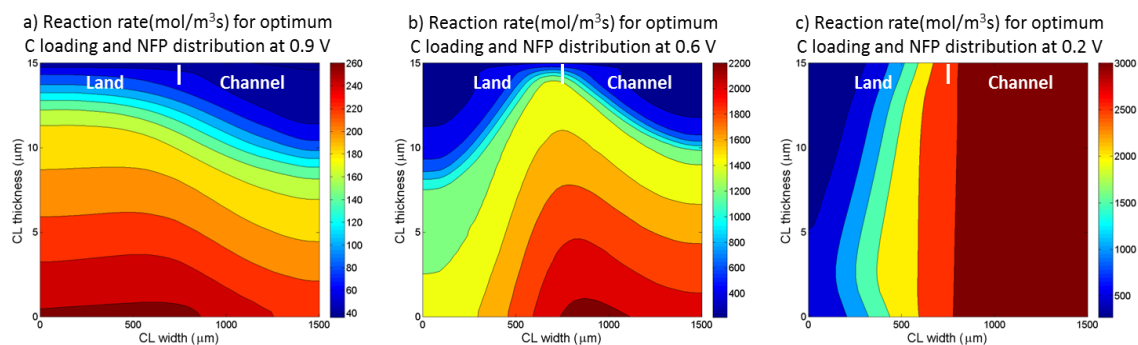


Figure 5.30. Reaction rate (mol/m^3s) distributions corresponding to the optimum NFP/C distributions in Fig. 5.28

So far, we optimized the constituent distribution for the baseline composition listed in Table 5.2. In order to explore the effect of a different baseline composition, we decided to optimize the Pt loading distribution for an average Pt loading of 0.1

mg/cm² at 0.6 V (as opposed to 0.3 mg/cm² for the baseline case) while retaining all the other constituent loading values from Table 5.2. This reduction in Pt loading causes a sharp drop in performance as shown in Fig. 5.31. It should be noted that for this lower Pt loading, the polarization curve is very different from the baseline case. Therefore, it may no longer be accurate to claim that 0.6 V still corresponds to the ohmic loss region; it is possible that diffusion effects are already being felt at 0.6 V for the low Pt loading of 0.1 mg/cm².

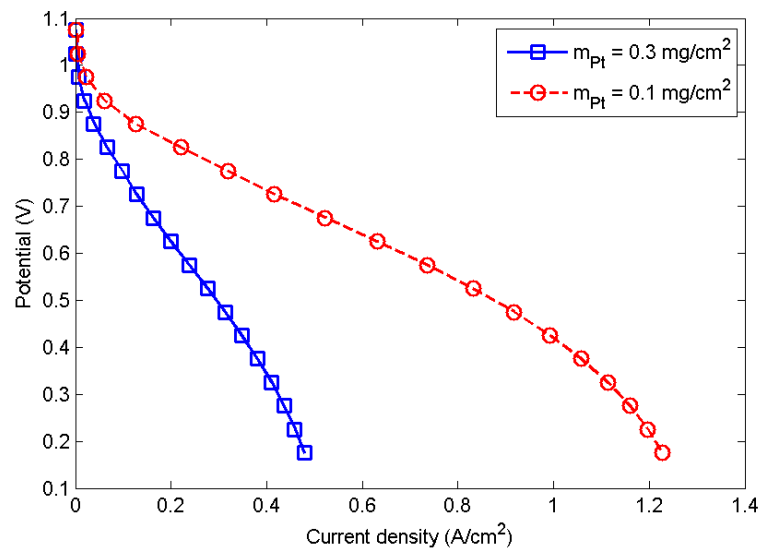


Figure 5.31. Comparison of polarization curves for two Pt loadings while retaining all of the other constituent loading values in Table 5.2

The reaction rate distribution for the spatially-uniform Pt loading of 0.1 mg/cm² shown in Fig. 5.32 is clearly quite different from the baseline case in Fig. 5.5b. Therefore, the optimal Pt distribution obtained for this low Pt loading case is also significantly different as can be seen by comparing Fig. 5.33 with Fig 5.19b. In comparison with the spatially-uniform case, about 40% performance improvement is obtained with the optimal Pt distribution for the 0.1 mg/cm² case (the current density

increases from 0.22 to 0.31 A/cm²). This huge improvement can be explained by referring to the sphere-packing model that is used to determine the agglomerate surface area. For low Pt loading, the porosity increases as the agglomerate surface area decreases according to the linear portion of the surface area vs. porosity curve shown in Fig. 4.5. High porosity is associated with very low agglomerate surface area, and the optimization improves performance by concentrating the Pt at the highly reactive zones. However, it should be noted that although spatial optimization improves performance by 40%, the actual performance as measured by the current density is still poor for the 0.1 mg/cm² Pt case compared with the 0.3 mg/cm² Pt baseline case as shown by the polarization curves in Fig. 5.31.

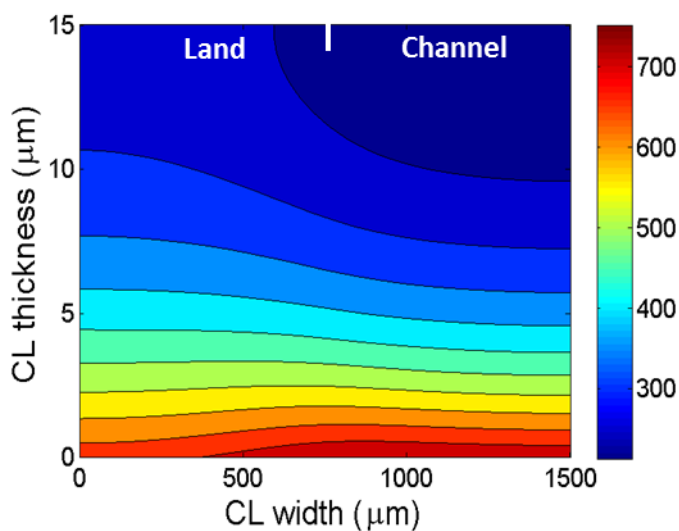


Figure 5.32. Reaction rate distribution (mol/m³s) for the spatially-uniform Pt loading of 0.1 mg/cm²

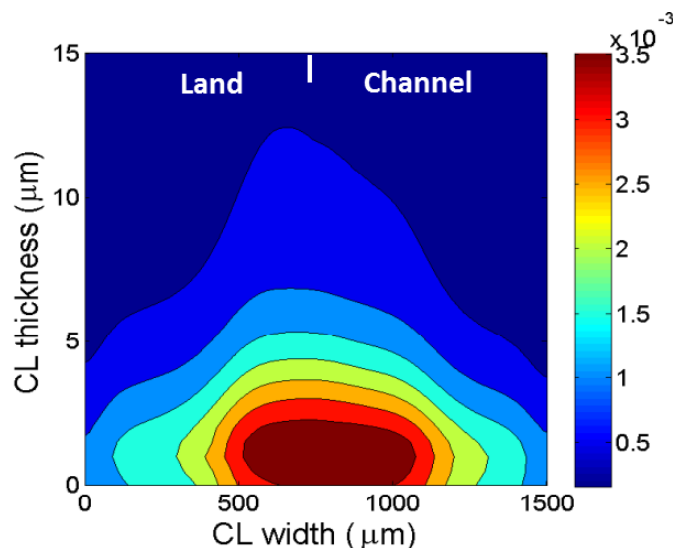


Figure 5.33. Optimal Pt distribution at 0.6V for an average Pt loading of 0.1 mg/cm^2

5.3 Summary

In this chapter, we examined through thickness, in-plane and bidirectionally (both in the in-plane and through-thickness directions) graded catalyst layer compositions. Then using a gradient-based approach, continuous distributions of NFP, Pt, and C in the 2D CL were optimized individually to maximize current density in activation, ohmic and diffusion-loss regimes.

Investigating the functionally-graded CL composition, it was found out that a higher NFP close to the membrane improves ion transport and performance in the ohmic loss region. Higher NFP under the channel improves performance in the mass transport region due to both improved ion and reactant transport. Concentrating Pt close to the membrane improves performance by increasing catalyst utilization in this ion-rich region. In addition, higher catalyst loading under the channel improves performance in the mass transport regime in this reactant-rich region. Optimum gradients were found for both NFP and catalyst loading. Increasing the gradient beyond a critical value results in decreased performance due to diffusion limitations.

In addition, it was pointed out that the bidirectional grading yields superior performance over unidirectional grading due to simultaneous improvements in both the ohmic loss and mass transport regimes.

The optimization results showed that the optimum CL composition distributions are strongly dependent on the operating regime. For all the components it was observed that the zones of high concentration shift from under the land to under the channel with decreasing operating voltage. Highest performance improvements in all operating regimes were obtained by optimizing NFP which indicates the relative importance of ion transport. Bidirectionally-graded distributions were found to give significantly higher performances in comparison to the unidirectionally-graded CL. Bidirectional grading superposes the beneficial effects in both directions and improves transport properties as desired exactly at the high reaction-rate zones.

Two-variable optimization of NFP/Pt and NFP/C distributions showed that NFP is the dominant factor. Thus it forces smaller Pt and C loadings at the high NFP zones to maintain an adequate porosity. Due to superposition of benefits from two constituents, higher performances are obtained with respect to single-variable optimization. The highest performance improvement is obtained in the activation regime for NFP/Pt optimization, while NFP/C optimization provides the highest improvement in ohmic-loss regime.

Chapter 6

CONCLUSIONS AND FUTURE WORK

6.1 Conclusions

The ultimate goal in CL research is minimize Pt loading without compromising overall performance. Maximizing Pt utilization in this manner requires a thorough understanding of the various physical phenomena within the complex porous structure of the CL. The key to improving Pt utilization is to optimize the spatial distribution of Pt and other CL constituents. To this end, accurate and robust numerical models can play a major role in finding the optimal CL composition and its spatial distribution which could be fabricated in the future with the advent of next-generation manufacturing techniques. The objective of this dissertation was to develop accurate CL modeling approaches in order to optimize the CL composition.

A comprehensive literature review revealed that the most commonly used CL modeling approach- the agglomerate model- suffers from several shortcomings that limit its ability to predict the effect of catalyst loading on performance in the mass transport loss regime. The shortcomings of the classical agglomerate model were studied by conducting macro and microscale simulations in Chapter 2. A numerical investigation of the single agglomerate revealed that the classical agglomerate approach is unable to accurately represent the underlying physics because the highly reactive nature of the agglomerate core restricts all diffusion losses to just the ionomer film. Therefore, the dominant role played by the ionomer film forces the same limiting current irrespective of Pt loading in the agglomerate core. The single C|Pt particle and

2D cathode models suggested two possible ways to improve the agglomerate model's predictions: (i) modeling discrete catalyst particles inside the agglomerate core in order to capture local diffusion losses, and (ii) setting relations between the agglomerate parameters (δ , a_{agg}) and CL compositional variables.

In Chapter 3, a novel multiscale CL modeling approach was presented. The limitations of the classical agglomerate approach were resolved by accounting for discrete Pt particles in the agglomerate core instead of using the homogenous mixture assumption. In comparison to the classical model, accounting for discrete Pt particles provided a more realistic representation of the physical process and facilitated a better estimation of the effects of catalyst utilization in the agglomerate core. Therefore, unlike the classical approach, the modified particle model was found to be sensitive to catalyst loading and its distribution in the agglomerate core. In addition, it was also shown that catalyst utilization could be improved by concentrating the Pt particles close to the periphery of the agglomerate. Finally, a framework was presented to show how to employ the modified agglomerate approach to build a 3D model for the PEM fuel cell cathode. The modified model's predictions were compared against the classical agglomerate and macro-homogeneous approaches. It was shown that the modified approach is as good as the classical agglomerate model in predicting current density distributions, and it is superior to the classical agglomerate model in predicting the effect of catalyst loading on cathode performance.

In Chapter 4, the agglomerate model was further improved by incorporating a sphere-packing approach to accurately calculate the agglomerate surface area (a_{agg}) as a function of the CL constituents. Specifically, the reduction in the effective surface area due to overlapping particles was modeled geometrically based on two sphere-

packing schemes: rhombohedral, and tetragonal. The new model's predictions were compared with the previously suggested expression in [55] in which the surface area was modeled as an arbitrary function of CL porosity by only considering two limiting cases of CL porosity. It was shown that the sphere-packing approach is superior in predicting the effects of compositional variations on performance and matched the experimentally-observed trends.

In Chapter 5, functionally-graded CL compositions were studied by employing the 2D cathode model with the improved agglomerate model in Chapter 4. First, the effects of in-plane, through-thickness, and bidirectional grading on performance curves were investigated. In agreement with the previous studies [39, 53, 78-81, 91, 108-110], improved performance was obtained with the graded CL composition. In addition, it was shown that there are optimum gradients for NFP and catalyst loading implying that the gradients cannot be increased beyond a certain point. More importantly, the bidirectional grading study showed that the performance could be further improved by optimizing the CL composition gradients along multiple directions. Then a numerical optimization study was performed for bidirectionally-graded (both in the in-plane and through-thickness directions) CL constituents (NFP, Pt and C). It was found that the optimum profiles depend significantly on the operating regime for all constituents. Significant performance improvements were obtained with the optimal CL compositions in comparison to the unidirectionally-graded CLs; the continuous bidirectional grading facilitates better utilization by improving transport properties exactly at the high reaction-rate zones. In addition, further performance improvement was obtained with two-variable optimization of NFP/Pt and NFP/C distributions due to the superposition of benefits from both constituents.

6.2 Future Work

In Chapter 5, the spatial distribution of CL constituents was optimized at three specific operating voltages and it was found that the optimal distribution depends significantly on the operating regime. The desired operating regime is, of course, a function of the intended application of the fuel cell. Therefore, one avenue for future work would be to conduct a multi-objective optimization of the CL constituent distribution for a range of operating voltages that matches the intended application.

The existence of liquid water in the CL was not considered in this research study. At its extreme, the presence of liquid water can cause CL flooding and block reactant access to the catalyst sites. Even in the absence of total flooding, the fuel cell's performance would be significantly affected because the reactant gas must first dissolve in the liquid water in order to reach the catalyst sites. On the other hand, very low water content can cause membrane dryout which adversely affects the membrane's proton conductivity, and lowers the performance. In this context, the research presented here can be extended in the future by incorporating the effects of liquid water within the improved agglomerate model. The resulting model would be more sensitive to operating conditions such as relative humidity, operating pressure and temperature. Furthermore, a detailed optimization study can be performed to obtain the optimal CL and GDL topologies for better performance and liquid water transport.

In addition, the particle approach presented in Chapter 3 could be further improved. For instance, the effects of deviations from the ideal spherical shape of the agglomerate could be investigated, or C particles could be modeled within the agglomerate core to account for more realistic reactant and electron transport.

Another important avenue for future research would be to use the modified particle model to study catalyst degradation. The acid electrolyte used in the CL causes catalyst particle dissolution at high operating voltages. Therefore, catalyst dissolution can be considered as the main degradation mechanism that results in a loss of electrochemical surface area. Furthermore, the dissolved particles may precipitate on other particles leading to larger particles with correspondingly lower surface area and Pt utilization. Catalyst dissolution and particle growth mechanisms can be modeled using the modified particle approach developed in Chapter 3. The multiscale nature of the particle approach, would allow one to investigate the interactions between the macroscopic transport phenomena and degradation mechanisms. For instance, one might be able to predict the effect of O₂ concentration or relative humidity on aging whereas most degradation studies to date have only addressed voltage drop with time.

REFERENCES

- [1] IEA, "World energy outlook," tech. rep., International Energy Agency, (2011)
- [2] W.R. Grove, Philosophical Magazine, Ser. III., XV. (1839)
- [3] B. Cook IEEE Proc. (2002), 205-16
- [4] L. Carrette, K.A. Friedrich, and U. Stimming, Fuel Cells, 1 (2001) 5-39
- [5] H. Tsuchiya and O. Kobayashi, Int. J. Hydrogen Energy, 29 (2004) 985-990
- [6] S. Gottesfeld, and T. Zawodzinski, Adv. Electrochem. Sci. Eng., Weinheim, Wiley-VCH, 5 (1997) 198-203
- [7] J.C. Amphlett, R.M. Baumert, R.F. Mann, B.A. Peppley, and P.R. Roberge, J. Electrochem. Soc., 142(1) (1995) 1-8
- [8] R.F. Mann, J.C. Amphlett, M.A.I Hooper, H.M. Jensen, B.A. Peppley, and P. R. Roberge, J. Power Sources, 86 (2000) 173-180
- [9] T.E. Springer, T.A. Zawodzinski, and S. Gottesfeld, J. Electrochem. Soc., 138(8) (1991) 2334-2342
- [10] D.M. Bernardi, and M.W. Verbrugge, J. Electrochem. Soc., 139(9) (1992) 2477-2491
- [11] V. Gurau, H. Liu, and S. Kakac, AIChE J., 44(11) (1998) 2410-2422
- [12] D. Singh, D.M. Lu, and N. Djilali, Int. J. Eng. Sci., 37(4) (1999) 431-452
- [13] Z. Shi, X. Wang and Z. Zhang, Proceedings of Comsol Conference (2006)
- [14] S. Dutta, S. Shimpalee, and J.W. Van Zee, Int. J. Heat Mass Transfer, 44(11), (2001) 2029-2042
- [15] T. Berning, D.M. Lu, and N. Djilali, J. Power Sources, 106 (1/2) (2002) 284 - 294
- [16] D. Natarajan, and T.V. Nguyen, J. Electrochem. Soc., 148 (12) (2001) A1324-A1335
- [17] G. Lin, W. He, and T. Nguyen, J. Electrochem. Soc., 151 (12) (2004) A1999-A2006
- [18] U. Pasaogullari, and C.-Y. Wang, J. Electrochem. Soc., 152 (2) (2005) A380-A390
- [19] T. Fuller, J. Newman, J. Electrochem. Soc., 140(5) (1993) 1218-1225
- [20] T.V. Nguyen, R.E. White, J. Electrochem. Soc., 140 (8) (1998) 2178-2186
- [21] S. Paddison, R. Paul, T. Zawodzinski, (2000), J. Electrochem. Soc., 147(2) (2000) 617-626
- [22] P. Khalatur, S. Talitskikh, A. Khokhlov, Macromol. Theor. Sim., 11(5) (2002) 566-586
- [23] Y. Bultel, P. Ozil, R. Durand, and D. Simonsson, Electrochem. Soc. Proceed., 95 (1995) 34-47

- [24] Y. Bultel, P. Ozil, and R. Durand, *J. Appl. Electrochem.*, 29 (1999) 1025-1033
- [25] Y. Bultel, P. Ozil, and R. Durand, *J. Appl. Electrochem.*, 28 (1998) 269-276
- [26] O. Antoine, Y. Bultel, R. Durand, and P. Ozil, *Electrochem. Acta*, 43(1998) 3681-3691
- [27] G. Wang, P.P. Mukherjee, C-Y. Wang, *Electrochim. Acta* 51 (2006) 3139-3150
- [28] G. Wang, P.P. Mukherjee, C-Y. Wang, *Electrochim. Acta* 51 (2006) 3151-3160
- [29] G. Wang, P.P. Mukherjee, C-Y. Wang, *Electrochim. Acta* 52 (2007) 6367-6377
- [30] N.A. Siddique, F. Liu, *Electrochim. Acta* 55 (2010) 5357-5366
- [31] J. Zhang, W. Yang, L. Xu, Y. Wang, *Electrochim. Acta* 56 (2011) 6912- 6918
- [32] T. Hattori, A. Suzuki, R. Sahnoun, M. Koyama, H. Tsuboi, N. Hatakeyama, A. En-dou, H. Takaba, M. Kubo, C. A. D. Carpio, et al., *Appl. Surf. Sci.*, 254 (2008).
- [33] S. H. Kim and H. Pitsch, *J. Electrochem. Soc.*, 156 (2009) 673-681
- [34] K.J. Lange, P-C. Sui and N.Djilali, *J. Electrochem. Soc.*, 157 (2010) 1434-1442
- [35] K.J. Lange, P-C. Sui and N.Djilali, *J. Power Sources* 208 (2012) 354- 365
- [36] Q. Yan, J. Wu, *Energy Convers. Manage.*, 49 (2008) 2425-2433
- [37] D. Harvey, J.G. Pharoah, K. Karan, *J. Power Sources* 179 (2008) 209-219
- [38] Y.W. Rho, S. Srinivasan, Y.T. Kho, *J. Electrochem. Soc.* 141 (8) (1994) 2089-2096
- [39] Q. Wang, M. Eikerling, D. Song, Z. Liu, T. Navessin, Z. Xie and S. Holdcroft, *J. Electrochem. Soc.*, 151 (7) (2004) A950-A957
- [40] M. Eikerling, A.A. Kornyshev, *J. Electroanal. Chem.* 453 (1-2) (1998) 89-106
- [41] D.M. Bernardi, M.W. Verbrugge, *AIChE J.* 37 (8) (1991) 1151-1163
- [42] C. Marr, X. Li, *J. Power Sources* 77 (1) (1999) 17-27
- [43] D. Song, Q. Wang, Z. Liu, T. Navessin, M. Eikerling, S. Holdcroft, *J. Power Sources*, 126 (12) (2004) 104
- [44] T.E. Springer, M.S. Wilson, S. Gottesfeld, *J. Electrochem. Soc.*, 140 (12) (1993) 3513-3526
- [45] T. Springer, I. Raistrick, *J. Electrochem. Soc.*, 136 (6) (1989) 1594-1603
- [46] S.J. Ridge, R.E. White, Y. Tsou, R.N. Beaver, G.A. Eisman, *J. Electrochem. Soc.*, 136 (7) (1989) 1902-1909
- [47] K. Broka, P. Ekdunge, *J. Appl. Electrochem.* 27 (3) (1997) 281-289
- [48] S. H. R. M. Rao and W. A. Tun, *Chem. Eng. Technol.* 24 (2001) 1, 51-57
- [49] F. Jaouen, G. Lindbergh, and G. Sundholm, *J. Electrochem. Soc.*, 149 (4) A437-A447 (2002)
- [50] F. Jaouen, G. Lindbergh, K. Wiezell, *J. Electrochem. Soc.*, 150 (12) (2003) A1711-A1717.
- [51] N.P. Siegel, M.W. Ellis, D.J. Nelson, M.R. Von Spakovsky, *J. Power Sources* 115 (2003) 81-89
- [52] Q. Wang, M. Eikerling, D. Song, Z. Liu, *J. Electroanal. Chem.* 573 (2004) 61- 69
- [53] W. Sun, B.A. Peppley, K. Karana, *Electrochim. Acta* 50 (2005) 3359 - 3374
- [54] M. Yin, *J. Electrochem. Soc.*, 152 (3) A583-A593 (2005)
- [55] M. Secanell, K. Karan, A. Suleman, N. Djilali, *Electrochim. Acta* 52 (2007) 6318-6337

- [56] R. M. Rao, R. Rengaswamy, *J. Power Sources*, 158 (2006) 110-123
- [57] P.K. Das, X. Li, Z-S. Liu, *J. Power Sources*, 179 (2008) 186-199
- [58] D. H. Schwarz and N. Djilali, *J. Electrochem. Soc.*, 154 (11) B1167-B1178 (2007)
- [59] J.J. Baschuk and X. Li, *J. Power Sources*, 86 (2000), 181-196
- [60] S. Kamarajugadda and S. Mazumder, *J. Power Sources*, 183 (2008) 629 - 642
- [61] P. Jain, L.T. Biegler, and M. S. Jhona, *J. Electrochem. Soc.*, 157 (8) B1222-B1229 (2010)
- [62] Y. Tabe, M. Nishino, H. Takamatsu, and T. Chikahisa, *J. Electrochem. Soc.*, 158 (10) B1246-B1254 (2011)
- [63] W. Yoon and A. Z. Weber, *J. Electrochem. Soc.*, 158 (8) B1007-B1018 (2011)
- [64] W.K. Epting, S. Litster, *Int. J. Hydrogen Energ.*, 37 (2012) 8505-8511
- [65] S. Kamarajugadda, S. Mazumder, *J. Power Sources* 208 (2012) 328- 339
- [66] T. Swamy, E.C. Kumbur, M.M. Mench, *J. Electrochem. Soc.*, 157 (1) (2010) B77-85.
- [67] A.A. Kulikovskiy, *Electrochim. Acta*, 55 (22) (2010) 6391-6401.
- [68] S. Obut, E. Alper, *J. Power Sources* 196 (2011) 1920-1931
- [69] Z. Qi, A. Kaufman, *J. Power Sources*, 113 (2003) 37-43
- [70] V.A. Paganin, E.A. Ticianelli, E.R. Gonzalez, *J. Appl. Electrochem.*, 26 (1996) 297-304
- [71] J.B. Russel, M.S. Thesis, Virginia Polytechnic Institute and State University, (2003)
- [72] E. Passalacqua, F. Lufrano G. Squadrito A. Patti , L. Giorgi, *Electrochim. Acta*, 46 (2001) 799-805
- [73] E. Antolini, L. Giorgi, A. Pozio, E. Passalacqua, *J. Power Sources*, 77 (1999) 136-142
- [74] M. Uchida, Y. Aoyama, N. Eda, A. Ohta, *J. Electrochem. Soc.*, 142 (12) (1995) 4143-4149
- [75] A. Ticianelli, C.R. Derouin, A. Redondo, S. Srinivasan, *J. Electrochem. Soc.*, 135 (9) (1988) 2209-2214
- [76] S. J. Lee, S. Mukerjee, J. McBreen, Y.W. Rho, Y.T. Kho, T.H. Lee, *Electrochim. Acta*, 43 (1998) 3693-3701
- [77] G. Sasikumar, J.W. Ihm, H. Ryua, *J. Power Sources*, 132 (2004) 11-17
- [78] E.A. Ticianelli, J.G. Beery, S.J. Srinivasan, *Appl. Electrochem.*, 21 (1991) 597-605
- [79] E.A. Ticianelli , C.R. Derouin , S.J. Srinivasan, *J. Electroanal. Chem.*, 251 (1988) 275-295
- [80] O. Antoine, Y. Butel, P. Ozil, R. Burand, *Electrochim. Acta*, 45 (2000) 4493-4500
- [81] Z. Xie, R. Chow, K. Shi, T. Navessin, Q. Wang, D. Song, B. Andreaus, M. Eikerling, Z. Liu, S. Holdcroft, *J. Electrochem. Soc.*, 152 (6) A1171-A1179 (2005)
- [82] D.P. Wilkinson, J. St-Pierre, *J. Power Sources*, 113 (2003) 101-108
- [83] M. Secanell, A. Suleman, *AIAA Journal* 43 (10) (2005) 2262-2267

- [84] M. Bendsoe, O. Sigmund, *Topology Optimization*, 2nd ed., Springer-Verlag, 2003
- [85] M. Grujicic, K. Chittajallu, *Chem. Eng. Sci.* 59 (2004) 5883-5895.
- [86] K.-H. Lin, C.-H. Cheng, C.-Y. Soong, F. Chen, W.-M. Yan, *J. Power Sources* 162 (2006) 246-254.
- [87] C.-H. Cheng, H.-H. Lin, G.-J. Lai, *J. Power Sources* 165 (2007) 803-813.
- [88] C.-H. Huang, J.-W. Lin, *J. Electrochem. Soc.*, 156 (1) (2009) B178-B187.
- [89] G. Catlin, S.G. Advani, A.K. Prasad, *J. Power Sources*, 196 (2011) 9407-9418
- [90] D. Song, Q. Wang, Z. Liu, Z. Xie, T. Navessin, M. Eikerling, S. Holdcroft, *J. Power Sources*, 126 (2004) 104-111
- [91] D. Song, Q. Wang, Z. Liu, M. Eikerling, Z. Xie, T. Navessin, S. Holdcroft, *Electrochim. Acta*, 50 (2005) 3347-3358
- [92] R. M. Rao and R. Rengaswamy, *Chem. Eng. Res. Des.*, 84 (2006) A10: 952-964
- [93] P. Jain, L. T. Biegler, and M. S. Jhon, *Electrochem. Solid-State Lett.*, 11 (10) (2008) B193-B196
- [94] H.S. Fogler, *Elements of Chemical Reaction Engineering* 3rd Edition, Prentice Hall PTR, 2000
- [95] Y. Bultel, P. Ozil, and R. Durand, *J. Appl. Electrochem.*, 30 (2000) 1369-1376
- [96] A.A. Kulikovskiy, *J. Electroanalytical Chemistry*, 652 (2011) 66-70
- [97] J. Zhang, *PEM Fuel Cell Electrocatalysts and Catalyst Layers Fundamentals and Applications*, Springer, 2008
- [98] E.L. Cussler, *Diffusion-Mass Transfer in Fluid Systems*, 2nd ed., Cambridge University Press, Cambridge (1997)
- [99] A. Parthasarathy, S. Srinivasan, A.J. Appleby, C.R. Martin, *J. Electrochem. Soc.* 139 (9) (1992) 2530-2537
- [100] A. Parthasarathy, C.R. Martin, S. Srinivasan, *J. Electrochem. Soc.*, 138 (4) (1991) 916-921
- [101] T. Sobolyeva, Ph.D. dissertation, Simon Fraser University, (2010)
- [102] S.W. Taylor, P.C.D. Milly, P.R. Jaffe, *Water Resour. Res.*, 26, 9 (1990) 2161-2169
- [103] E-TEK. Specifications for c-1: Hp Platinum on Vulcan XC-72, www.etekinc.com
- [104] S. Ma, C.-H. Solterbeck, M. Odgaard, and E. Skou, *Appl Phys A*, 96, 581 (2009) 581-589
- [105] M. Secanell, Ph.D. dissertation, University of Victoria, (2007)
- [106] A.J. Cooke, R.K. Rowe, *J. Environ. Eng.*, 125(2), (1999) 126-145.
- [107] Y. Yu, R.K. Rowe, *J. Environ. Eng.*, 138 (2012) 436-445.
- [108] D. H. Schwarz, N. Djilali, *Int. J. Energy Res.*, 33 (2009) 631-644
- [109] M. Srinivasarao, D. Bhattacharyya, R. Rengaswamy, S. Narasimhan, *Int. J. Hydrogen Energ.*, 35 (2010) 6356-6365
- [110] P.P. Mukherjee and C-Y. Wang, *J. Electrochem. Soc.*, 154 (11) B1121-B1131 (2007)

Appendix A

COPYRIGHT PERMISSIONS

Request for Permission to Reproduce or Re-Publish ECS Material

Please fax this form to: The Electrochemical Society (ECS), Attn: Permissions Requests, 1.609.730.0629.
You may also e-mail your request to: copyright@electrochem.org. Include all the information as required on this form. Please allow 3-7 days for your request to be processed.

I am preparing a (choose one): paper chapter book thesis

entitled: Modeling and Optimization of the PEM Fuel Cell Catalyst Layer
to be published by: _____

in an upcoming publication entitled: _____

I request permission to use the following material in the publication noted above, and request nonexclusive rights for all subsequent editions and in all foreign language translations for distribution throughout the world.

Description of material to be used—Indicate what material you wish to use (figures, tables, text, etc.) and give the full bibliographic reference for the source publication. You may attach a separate list, organized by ECS title.

Firat C. Cetinbas, Suresh G. Advani, Ajay K. Prasad, Journal of Electrochemical Society, 160 (8) F750-F756 (2013)
I would like to reuse all the material in my dissertation.

Signature: F. C. Cetinbas Date: 7/30/14

Name: Firat Cetinbas

Address: 126 Spencer Lab Newark DE 19716

Telephone: 302-740-7464 Fax: _____

E-mail: cetinbas@udel.edu

Permission is granted to reproduce the above-referenced material. Please acknowledge the author(s) and publication data of the original material, and include the words: "Reproduced by permission of The Electrochemical Society."

8/4/14
Date

[Signature]
John Lewis, Associate Director of Publications

**ELSEVIER LICENSE
TERMS AND CONDITIONS**

Jul 24, 2014

This is a License Agreement between Firat C Cetinbas ("You") and Elsevier ("Elsevier") provided by Copyright Clearance Center ("CCC"). The license consists of your order details, the terms and conditions provided by Elsevier, and the payment terms and conditions.

All payments must be made in full to CCC. For payment instructions, please see information listed at the bottom of this form.

Supplier	Elsevier Limited The Boulevard, Langford Lane Kidlington, Oxford, OX5 1GB, UK
Registered Company Number	1982084
Customer name	Firat C Cetinbas
Customer address	126 Spencer Lab NEWARK, DE 19716
License number	3435400372838
License date	Jul 24, 2014
Licensed content publisher	Elsevier
Licensed content publication	Journal of Power Sources
Licensed content title	Three dimensional proton exchange membrane fuel cell cathode model using a modified agglomerate approach based on discrete catalyst particles
Licensed content author	Firat C. Cetinbas, Suresh G. Advani, Ajay K. Prasad
Licensed content date	15 March 2014
Licensed content volume number	250
Licensed content issue number	None
Number of pages	10
Start Page	110
End Page	119
Type of Use	reuse in a thesis/dissertation
Portion	full article
Format	electronic
Are you the author of this Elsevier article?	Yes
Will you be translating?	No

7/24/2014

Rightslink Printable License

Title of your thesis/dissertation	Modeling and Optimization of the PEM Fuel Cell Catalyst Layer
Expected completion date	Aug 2014
Estimated size (number of pages)	184
Elsevier VAT number	GB 494 6272 12
Permissions price	0.00 USD
VAT/Local Sales Tax	0.00 USD / 0.00 GBP
Total	0.00 USD
Terms and Conditions	

INTRODUCTION

1. The publisher for this copyrighted material is Elsevier. By clicking "accept" in connection with completing this licensing transaction, you agree that the following terms and conditions apply to this transaction (along with the Billing and Payment terms and conditions established by Copyright Clearance Center, Inc. ("CCC"), at the time that you opened your Rightslink account and that are available at any time at <http://myaccount.copyright.com>).

GENERAL TERMS

2. Elsevier hereby grants you permission to reproduce the aforementioned material subject to the terms and conditions indicated.

3. Acknowledgement: If any part of the material to be used (for example, figures) has appeared in our publication with credit or acknowledgement to another source, permission must also be sought from that source. If such permission is not obtained then that material may not be included in your publication/copies. Suitable acknowledgement to the source must be made, either as a footnote or in a reference list at the end of your publication, as follows:

"Reprinted from Publication title, Vol /edition number, Author(s), Title of article / title of chapter, Pages No., Copyright (Year), with permission from Elsevier [OR APPLICABLE SOCIETY COPYRIGHT OWNER]." Also Lancet special credit - "Reprinted from The Lancet, Vol. number, Author(s), Title of article, Pages No., Copyright (Year), with permission from Elsevier."

4. Reproduction of this material is confined to the purpose and/or media for which permission is hereby given.

5. Altering/Modifying Material: Not Permitted. However figures and illustrations may be altered/adapted minimally to serve your work. Any other abbreviations, additions, deletions and/or any other alterations shall be made only with prior written authorization of Elsevier Ltd. (Please contact Elsevier at permissions@elsevier.com)

6. If the permission fee for the requested use of our material is waived in this instance, please be advised that your future requests for Elsevier materials may attract a fee.

7. Reservation of Rights: Publisher reserves all rights not specifically granted in the combination of (i) the license details provided by you and accepted in the course of this licensing transaction, (ii)

<https://s100.copyright.com/AppDispatchServlet>

2/7

these terms and conditions and (iii) CCC's Billing and Payment terms and conditions.

8. **License Contingent Upon Payment:** While you may exercise the rights licensed immediately upon issuance of the license at the end of the licensing process for the transaction, provided that you have disclosed complete and accurate details of your proposed use, no license is finally effective unless and until full payment is received from you (either by publisher or by CCC) as provided in CCC's Billing and Payment terms and conditions. If full payment is not received on a timely basis, then any license preliminarily granted shall be deemed automatically revoked and shall be void as if never granted. Further, in the event that you breach any of these terms and conditions or any of CCC's Billing and Payment terms and conditions, the license is automatically revoked and shall be void as if never granted. Use of materials as described in a revoked license, as well as any use of the materials beyond the scope of an unrevoked license, may constitute copyright infringement and publisher reserves the right to take any and all action to protect its copyright in the materials.

9. **Warranties:** Publisher makes no representations or warranties with respect to the licensed material.

10. **Indemnity:** You hereby indemnify and agree to hold harmless publisher and CCC, and their respective officers, directors, employees and agents, from and against any and all claims arising out of your use of the licensed material other than as specifically authorized pursuant to this license.

11. **No Transfer of License:** This license is personal to you and may not be sublicensed, assigned, or transferred by you to any other person without publisher's written permission.

12. **No Amendment Except in Writing:** This license may not be amended except in a writing signed by both parties (or, in the case of publisher, by CCC on publisher's behalf).

13. **Objection to Contrary Terms:** Publisher hereby objects to any terms contained in any purchase order, acknowledgment, check endorsement or other writing prepared by you, which terms are inconsistent with these terms and conditions or CCC's Billing and Payment terms and conditions. These terms and conditions, together with CCC's Billing and Payment terms and conditions (which are incorporated herein), comprise the entire agreement between you and publisher (and CCC) concerning this licensing transaction. In the event of any conflict between your obligations established by these terms and conditions and those established by CCC's Billing and Payment terms and conditions, these terms and conditions shall control.

14. **Revocation:** Elsevier or Copyright Clearance Center may deny the permissions described in this License at their sole discretion, for any reason or no reason, with a full refund payable to you. Notice of such denial will be made using the contact information provided by you. Failure to receive such notice will not alter or invalidate the denial. In no event will Elsevier or Copyright Clearance Center be responsible or liable for any costs, expenses or damage incurred by you as a result of a denial of your permission request, other than a refund of the amount(s) paid by you to Elsevier and/or Copyright Clearance Center for denied permissions.

LIMITED LICENSE

The following terms and conditions apply only to specific license types:

15. **Translation:** This permission is granted for non-exclusive world **English** rights only unless your license was granted for translation rights. If you licensed translation rights you may only translate this content into the languages you requested. A professional translator must perform all translations and reproduce the content word for word preserving the integrity of the article. If this license is to re-use 1 or 2 figures then permission is granted for non-exclusive world rights in all languages.

16. **Posting licensed content on any Website:** The following terms and conditions apply as follows: Licensing material from an Elsevier journal: All content posted to the web site must maintain the copyright information line on the bottom of each image; A hyper-text must be included to the Homepage of the journal from which you are licensing at <http://www.sciencedirect.com/science/journal/xxxxx> or the Elsevier homepage for books at <http://www.elsevier.com>; Central Storage: This license does not include permission for a scanned version of the material to be stored in a central repository such as that provided by Heron/XanEdu.

Licensing material from an Elsevier book: A hyper-text link must be included to the Elsevier homepage at <http://www.elsevier.com>. All content posted to the web site must maintain the copyright information line on the bottom of each image.

Posting licensed content on Electronic reserve: In addition to the above the following clauses are applicable: The web site must be password-protected and made available only to bona fide students registered on a relevant course. This permission is granted for 1 year only. You may obtain a new license for future website posting.

For journal authors: the following clauses are applicable in addition to the above: Permission granted is limited to the author accepted manuscript version* of your paper.

* **Accepted Author Manuscript (AAM) Definition:** An accepted author manuscript (AAM) is the author's version of the manuscript of an article that has been accepted for publication and which may include any author-incorporated changes suggested through the processes of submission processing, peer review, and editor-author communications. AAMs do not include other publisher value-added contributions such as copy-editing, formatting, technical enhancements and (if relevant) pagination.

You are not allowed to download and post the published journal article (whether PDF or HTML, proof or final version), nor may you scan the printed edition to create an electronic version. A hyper-text must be included to the Homepage of the journal from which you are licensing at <http://www.sciencedirect.com/science/journal/xxxxx>. As part of our normal production process, you will receive an e-mail notice when your article appears on Elsevier's online service ScienceDirect (www.sciencedirect.com). That e-mail will include the article's Digital Object Identifier (DOI). This number provides the electronic link to the published article and should be included in the posting of your personal version. We ask that you wait until you receive this e-mail and have the DOI to do any posting.

Posting to a repository: Authors may post their AAM immediately to their employer's institutional repository for internal use only and may make their manuscript publically available after the journal-specific embargo period has ended.

Please also refer to [Elsevier's Article Posting Policy](#) for further information.

18. **For book authors** the following clauses are applicable in addition to the above: Authors are permitted to place a brief summary of their work online only. You are not allowed to download and post the published electronic version of your chapter, nor may you scan the printed edition to create an electronic version. **Posting to a repository:** Authors are permitted to post a summary of their chapter only in their institution's repository.

20. **Thesis/Dissertation:** If your license is for use in a thesis/dissertation your thesis may be submitted to your institution in either print or electronic form. Should your thesis be published commercially, please reapply for permission. These requirements include permission for the Library and Archives of Canada to supply single copies, on demand, of the complete thesis and include permission for UMI to supply single copies, on demand, of the complete thesis. Should your thesis be published commercially, please reapply for permission.

Elsevier Open Access Terms and Conditions

Elsevier publishes Open Access articles in both its Open Access journals and via its Open Access articles option in subscription journals.

Authors publishing in an Open Access journal or who choose to make their article Open Access in an Elsevier subscription journal select one of the following Creative Commons user licenses, which define how a reader may reuse their work: Creative Commons Attribution License (CC BY), Creative Commons Attribution – Non Commercial - ShareAlike (CC BY NC SA) and Creative Commons Attribution – Non Commercial – No Derivatives (CC BY NC ND)

Terms & Conditions applicable to all Elsevier Open Access articles:

Any reuse of the article must not represent the author as endorsing the adaptation of the article nor should the article be modified in such a way as to damage the author's honour or reputation.

The author(s) must be appropriately credited.

If any part of the material to be used (for example, figures) has appeared in our publication with credit or acknowledgement to another source it is the responsibility of the user to ensure their reuse complies with the terms and conditions determined by the rights holder.

Additional Terms & Conditions applicable to each Creative Commons user license:

CC BY: You may distribute and copy the article, create extracts, abstracts, and other revised versions, adaptations or derivative works of or from an article (such as a translation), to include in a collective work (such as an anthology), to text or data mine the article, including for commercial purposes without permission from Elsevier

CC BY NC SA: For non-commercial purposes you may distribute and copy the article, create extracts, abstracts and other revised versions, adaptations or derivative works of or from an article

(such as a translation), to include in a collective work (such as an anthology), to text and data mine the article and license new adaptations or creations under identical terms without permission from Elsevier

CC BY NC ND: For non-commercial purposes you may distribute and copy the article and include it in a collective work (such as an anthology), provided you do not alter or modify the article, without permission from Elsevier

Any commercial reuse of Open Access articles published with a CC BY NC SA or CC BY NC ND license requires permission from Elsevier and will be subject to a fee.

Commercial reuse includes:

- Promotional purposes (advertising or marketing)
- Commercial exploitation (e.g. a product for sale or loan)
- Systematic distribution (for a fee or free of charge)

Please refer to [Elsevier's Open Access Policy](#) for further information.

21. Other Conditions:

v1.7

If you would like to pay for this license now, please remit this license along with your payment made payable to "COPYRIGHT CLEARANCE CENTER" otherwise you will be invoiced within 48 hours of the license date. Payment should be in the form of a check or money order referencing your account number and this invoice number 501360635. Once you receive your invoice for this order, you may pay your invoice by credit card. Please follow instructions provided at that time.

Make Payment To:
Copyright Clearance Center
Dept 001
P.O. Box 843006
Boston, MA 02284-3006

For suggestions or comments regarding this order, contact RightsLink Customer Support: customer@copyright.com or +1-877-622-5543 (toll free in the US) or +1-978-646-2777.

Gratis licenses (referencing \$0 in the Total field) are free. Please retain this printable license for your reference. No payment is required.

**ELSEVIER LICENSE
TERMS AND CONDITIONS**

Aug 11, 2014

This is a License Agreement between Firat C Cetinbas ("You") and Elsevier ("Elsevier") provided by Copyright Clearance Center ("CCC"). The license consists of your order details, the terms and conditions provided by Elsevier, and the payment terms and conditions.

All payments must be made in full to CCC. For payment instructions, please see information listed at the bottom of this form.

Supplier	Elsevier Limited The Boulevard, Langford Lane Kidlington, Oxford, OX5 1GB, UK
Registered Company Number	1982084
Customer name	Firat C Cetinbas
Customer address	126 Spencer Lab NEWARK, DE 19716
License number	3446041040093
License date	Aug 11, 2014
Licensed content publisher	Elsevier
Licensed content publication	Journal of Power Sources
Licensed content title	Investigation of a polymer electrolyte membrane fuel cell catalyst layer with bidirectionally-graded composition
Licensed content author	Firat C. Cetinbas, Suresh G. Advani, Ajay K. Prasad
Licensed content date	15 December 2014
Licensed content volume number	270
Licensed content issue number	n/a
Number of pages	9
Start Page	594
End Page	602
Type of Use	reuse in a thesis/dissertation
Portion	full article
Format	electronic
Are you the author of this Elsevier article?	Yes
Will you be translating?	No
Title of your	Modeling and Optimization of the PEM Fuel Cell Catalyst Layer

thesis/dissertation

Expected completion date Aug 2014

Estimated size (number of pages) 184

Elsevier VAT number GB 494 6272 12

Permissions price 0.00 USD

VAT/Local Sales Tax 0.00 USD / 0.00 GBP

Total 0.00 USD

Terms and Conditions

INTRODUCTION

1. The publisher for this copyrighted material is Elsevier. By clicking "accept" in connection with completing this licensing transaction, you agree that the following terms and conditions apply to this transaction (along with the Billing and Payment terms and conditions established by Copyright Clearance Center, Inc. ("CCC"), at the time that you opened your Rightslink account and that are available at any time at <http://myaccount.copyright.com>).

GENERAL TERMS

2. Elsevier hereby grants you permission to reproduce the aforementioned material subject to the terms and conditions indicated.

3. Acknowledgement: If any part of the material to be used (for example, figures) has appeared in our publication with credit or acknowledgement to another source, permission must also be sought from that source. If such permission is not obtained then that material may not be included in your publication/copies. Suitable acknowledgement to the source must be made, either as a footnote or in a reference list at the end of your publication, as follows:

"Reprinted from Publication title, Vol/edition number, Author(s), Title of article / title of chapter, Pages No., Copyright (Year), with permission from Elsevier [OR APPLICABLE SOCIETY COPYRIGHT OWNER]." Also Lancet special credit - "Reprinted from The Lancet, Vol number, Author(s), Title of article, Pages No., Copyright (Year), with permission from Elsevier."

4. Reproduction of this material is confined to the purpose and/or media for which permission is hereby given.

5. Altering/Modifying Material: Not Permitted. However figures and illustrations may be altered/adapted minimally to serve your work. Any other abbreviations, additions, deletions and/or any other alterations shall be made only with prior written authorization of Elsevier Ltd. (Please contact Elsevier at permissions@elsevier.com)

6. If the permission fee for the requested use of our material is waived in this instance, please be advised that your future requests for Elsevier materials may attract a fee.

7. Reservation of Rights: Publisher reserves all rights not specifically granted in the combination of (i) the license details provided by you and accepted in the course of this licensing transaction, (ii)

these terms and conditions and (iii) CCC's Billing and Payment terms and conditions.

8. **License Contingent Upon Payment:** While you may exercise the rights licensed immediately upon issuance of the license at the end of the licensing process for the transaction, provided that you have disclosed complete and accurate details of your proposed use, no license is finally effective unless and until full payment is received from you (either by publisher or by CCC) as provided in CCC's Billing and Payment terms and conditions. If full payment is not received on a timely basis, then any license preliminarily granted shall be deemed automatically revoked and shall be void as if never granted. Further, in the event that you breach any of these terms and conditions or any of CCC's Billing and Payment terms and conditions, the license is automatically revoked and shall be void as if never granted. Use of materials as described in a revoked license, as well as any use of the materials beyond the scope of an unrevoked license, may constitute copyright infringement and publisher reserves the right to take any and all action to protect its copyright in the materials.

9. **Warranties:** Publisher makes no representations or warranties with respect to the licensed material.

10. **Indemnity:** You hereby indemnify and agree to hold harmless publisher and CCC, and their respective officers, directors, employees and agents, from and against any and all claims arising out of your use of the licensed material other than as specifically authorized pursuant to this license.

11. **No Transfer of License:** This license is personal to you and may not be sublicensed, assigned, or transferred by you to any other person without publisher's written permission.

12. **No Amendment Except in Writing:** This license may not be amended except in a writing signed by both parties (or, in the case of publisher, by CCC on publisher's behalf).

13. **Objection to Contrary Terms:** Publisher hereby objects to any terms contained in any purchase order, acknowledgment, check endorsement or other writing prepared by you, which terms are inconsistent with these terms and conditions or CCC's Billing and Payment terms and conditions. These terms and conditions, together with CCC's Billing and Payment terms and conditions (which are incorporated herein), comprise the entire agreement between you and publisher (and CCC) concerning this licensing transaction. In the event of any conflict between your obligations established by these terms and conditions and those established by CCC's Billing and Payment terms and conditions, these terms and conditions shall control.

14. **Revocation:** Elsevier or Copyright Clearance Center may deny the permissions described in this License at their sole discretion, for any reason or no reason, with a full refund payable to you. Notice of such denial will be made using the contact information provided by you. Failure to receive such notice will not alter or invalidate the denial. In no event will Elsevier or Copyright Clearance Center be responsible or liable for any costs, expenses or damage incurred by you as a result of a denial of your permission request, other than a refund of the amount(s) paid by you to Elsevier and/or Copyright Clearance Center for denied permissions.

LIMITED LICENSE

The following terms and conditions apply only to specific license types:

15. Translation: This permission is granted for non-exclusive world **English** rights only unless your license was granted for translation rights. If you licensed translation rights you may only translate this content into the languages you requested. A professional translator must perform all translations and reproduce the content word for word preserving the integrity of the article. If this license is to re-use 1 or 2 figures then permission is granted for non-exclusive world rights in all languages.

16. Posting licensed content on any Website: The following terms and conditions apply as follows: Licensing material from an Elsevier journal: All content posted to the web site must maintain the copyright information line on the bottom of each image; A hyper-text must be included to the Homepage of the journal from which you are licensing at <http://www.sciencedirect.com/science/journal/xxxxx> or the Elsevier homepage for books at <http://www.elsevier.com>; Central Storage: This license does not include permission for a scanned version of the material to be stored in a central repository such as that provided by Heron/XanEdu.

Licensing material from an Elsevier book: A hyper-text link must be included to the Elsevier homepage at <http://www.elsevier.com>. All content posted to the web site must maintain the copyright information line on the bottom of each image.

Posting licensed content on Electronic reserve: In addition to the above the following clauses are applicable: The web site must be password-protected and made available only to bona fide students registered on a relevant course. This permission is granted for 1 year only. You may obtain a new license for future website posting.

For journal authors: the following clauses are applicable in addition to the above: Permission granted is limited to the author accepted manuscript version* of your paper.

*** Accepted Author Manuscript (AAM) Definition:** An accepted author manuscript (AAM) is the author's version of the manuscript of an article that has been accepted for publication and which may include any author-incorporated changes suggested through the processes of submission processing, peer review, and editor-author communications. AAMs do not include other publisher value-added contributions such as copy-editing, formatting, technical enhancements and (if relevant) pagination.

You are not allowed to download and post the published journal article (whether PDF or HTML, proof or final version), nor may you scan the printed edition to create an electronic version. A hyper-text must be included to the Homepage of the journal from which you are licensing at <http://www.sciencedirect.com/science/journal/xxxxx>. As part of our normal production process, you will receive an e-mail notice when your article appears on Elsevier's online service ScienceDirect (www.sciencedirect.com). That e-mail will include the article's Digital Object Identifier (DOI). This number provides the electronic link to the published article and should be included in the posting of your personal version. We ask that you wait until you receive this e-mail and have the DOI to do any posting.

Posting to a repository: Authors may post their AAM immediately to their employer's institutional repository for internal use only and may make their manuscript publically available after the journal-specific embargo period has ended.

Please also refer to [Elsevier's Article Posting Policy](#) for further information.

18. **For book authors** the following clauses are applicable in addition to the above: Authors are permitted to place a brief summary of their work online only. You are not allowed to download and post the published electronic version of your chapter, nor may you scan the printed edition to create an electronic version. **Posting to a repository:** Authors are permitted to post a summary of their chapter only in their institution's repository.

20. **Thesis/Dissertation:** If your license is for use in a thesis/dissertation your thesis may be submitted to your institution in either print or electronic form. Should your thesis be published commercially, please reapply for permission. These requirements include permission for the Library and Archives of Canada to supply single copies, on demand, of the complete thesis and include permission for UMI to supply single copies, on demand, of the complete thesis. Should your thesis be published commercially, please reapply for permission.

Elsevier Open Access Terms and Conditions

Elsevier publishes Open Access articles in both its Open Access journals and via its Open Access articles option in subscription journals.

Authors publishing in an Open Access journal or who choose to make their article Open Access in an Elsevier subscription journal select one of the following Creative Commons user licenses, which define how a reader may reuse their work: Creative Commons Attribution License (CC BY), Creative Commons Attribution – Non Commercial - ShareAlike (CC BY NC SA) and Creative Commons Attribution – Non Commercial – No Derivatives (CC BY NC ND)

Terms & Conditions applicable to all Elsevier Open Access articles:

Any reuse of the article must not represent the author as endorsing the adaptation of the article nor should the article be modified in such a way as to damage the author's honour or reputation.

The author(s) must be appropriately credited.

If any part of the material to be used (for example, figures) has appeared in our publication with credit or acknowledgement to another source it is the responsibility of the user to ensure their reuse complies with the terms and conditions determined by the rights holder.

Additional Terms & Conditions applicable to each Creative Commons user license:

CC BY: You may distribute and copy the article, create extracts, abstracts, and other revised versions, adaptations or derivative works of or from an article (such as a translation), to include in a collective work (such as an anthology), to text or data mine the article, including for commercial purposes without permission from Elsevier

CC BY NC SA: For non-commercial purposes you may distribute and copy the article, create extracts, abstracts and other revised versions, adaptations or derivative works of or from an article

(such as a translation), to include in a collective work (such as an anthology), to text and data mine the article and license new adaptations or creations under identical terms without permission from Elsevier

CC BY NC ND: For non-commercial purposes you may distribute and copy the article and include it in a collective work (such as an anthology), provided you do not alter or modify the article, without permission from Elsevier

Any commercial reuse of Open Access articles published with a CC BY NC SA or CC BY NC ND license requires permission from Elsevier and will be subject to a fee.

Commercial reuse includes:

- Promotional purposes (advertising or marketing)
- Commercial exploitation (e.g. a product for sale or loan)
- Systematic distribution (for a fee or free of charge)

Please refer to [Elsevier's Open Access Policy](#) for further information.

21. Other Conditions:

v1.6

You will be invoiced within 48 hours of this transaction date. You may pay your invoice by credit card upon receipt of the invoice for this transaction. Please follow instructions provided at that time.

To pay for this transaction now; please remit a copy of this document along with your payment. Payment should be in the form of a check or money order referencing your account number and this invoice number RLNK501374631.

Make payments to "COPYRIGHT CLEARANCE CENTER" and send to:

Copyright Clearance Center

Dept 001

P.O. Box 843006

Boston, MA 02284-3006

Please disregard electronic and mailed copies if you remit payment in advance.

Questions? customercare@copyright.com or +1-855-239-3415 (toll free in the US) or +1-978-646-2777.

Gratis licenses (referencing \$0 in the Total field) are free. Please retain this printable license for your reference. No payment is required.